

The Influence of Molecular Ion Characteristics on Room Temperature Ionic Liquid Structure and Transport Properties

by

Heidrun Veronika Spohr

A THESIS SUBMITTED IN PARTIAL FULFILLMENT OF
THE REQUIREMENTS FOR THE DEGREE OF

DOCTOR OF PHILOSOPHY

in

The Faculty of Graduate Studies

(Chemistry)

THE UNIVERSITY OF BRITISH COLUMBIA

(Vancouver)

May 2010

© Heidrun Veronika Spohr 2010

Abstract

Room temperature ionic liquids (RTILs) are pure, organic salts, that are liquid at ambient temperatures. RTILs are highly customizable, with a wide choice of ion types and varying substituents. The customizability of RTILs also poses the greatest challenge, rational design of liquid properties from molecular structure.

The influence of RTIL ion characteristics on liquid structure and transport properties is systematically investigated employing molecular dynamics simulations. The characteristics investigated include size disparity, ion charges that are displaced from the center of mass, and variation of the cation-anion charge separation σ'_{+-} . Different simple spherical ionic liquid models are developed that isolate each of these characteristics.

Statistical mechanical analysis shows that more size disparate models have decreased coordination numbers, the diffusion coefficients and electrical conductivity increase, and the viscosity decreases. The effects of size disparity can be canceled to a large extent by decreasing σ'_{+-} . An increasing displacement of the ion charge leads to the formation of directional ion pairs of increasing strength. Weak pairing results in non-uniform ion distributions and reduced caging, with similar liquid property trends as size disparate systems. A large charge displacement and short σ'_{+-} leads to increasing numbers of strong, long-lived directional ion pairs that dominate the liquid behavior. Increasing viscosities and decreasing electrical conductivities are observed in this regime. The temperature behavior of the ionic liquid models deviates from linear Arrhenius behavior, especially for the conductivity. The relationship between diffusion and viscosity conforms to the fractional Stokes-Einstein equation. The qualitative conclusions of our calculations suggest the utilization of ions with moderate charge displacement, and large size disparities, for desired low-viscosity RTILs with large ion mobilities.

Mixtures of water with ionic liquid models generally show increased diffusion coefficients and electrical conductivities, and decreased viscosities. The increased mobility of the ions can be mainly ascribed to dynamical effects due to light water replacing heavy ions in the ion coordination shell. We observe deviating behavior when water can form strong, directional interactions with at least one ion, in the case of small, or of strongly charge displaced ions. In both cases the viscosity increases with increasing water concentration.

Table of Contents

Abstract	ii
Table of Contents	iii
List of Tables	vi
List of Figures	viii
Acknowledgements	xiii
Statement of Co-Authorship	xiv
1 Introduction	1
1.1 Introduction to Room Temperature Ionic Liquids	1
1.1.1 Ionic Liquid Properties	2
1.1.2 Utilization and Applications	3
1.1.3 Environmental Acceptability	3
1.2 The Influence of Ion Characteristics on RTIL Liquid Properties	4
1.2.1 Melting Point	4
1.2.2 Shear Viscosity	5
1.2.3 Electrical Conductivity	5
1.2.4 Impurities and Mixtures	6
1.2.5 Opportunities and Challenges	7
1.3 Computer Simulations of Ionic Liquids	8
1.3.1 Quantum Chemical Calculations	8
1.3.2 Atomistic Simulations	9
1.3.3 Coarse Graining Approach	11
1.3.4 Progress and Limitations of Ionic Liquid Simulations	12
1.4 The Present Approach	12
1.4.1 Choice of RTIL Ion Characteristics	12
1.4.2 Advantages of this Approach	15
Bibliography	17
2 The Influence of Ion Size Disparity	24
2.1 Introduction	24
2.2 The Model and Simulation Method	26
2.3 Results and Discussion	29
2.3.1 Structural and Thermodynamic Properties	29

2.3.2	Transport Properties	33
2.3.3	Temperature Dependence of Transport Properties	42
2.4	Summary and Conclusions	44
Bibliography		47
3	The Influence of Charge Location	49
3.1	Introduction	49
3.2	Models and Simulation	50
3.3	Results and Discussion	55
3.3.1	Structural and Thermodynamic Properties	55
3.3.2	Transport Properties	62
3.3.3	Cation Rotation, Reorientation, and Ion-Pair Lifetimes	69
3.3.4	Temperature Dependence and Comparison with Experiment	72
3.4	Summary and Conclusions	76
Bibliography		79
4	Competing Influences of Molecular Properties	81
4.1	Introduction	81
4.2	Ionic Liquid Models and Simulation Method	84
4.3	Results and Discussion	90
4.3.1	Structural Properties	90
4.3.2	Transport Properties	103
4.4	Summary and Conclusions	112
Bibliography		115
5	The Influence of Water on Model Ionic Liquids	117
5.1	Introduction	117
5.2	Models and Simulation Method	119
5.3	Results and Discussion	122
5.3.1	Structural Properties	122
5.3.2	Transport Properties	132
5.4	Summary and Conclusions	151
Bibliography		155
6	Conclusion	158
6.1	Analysis	158
6.2	Comparison with Experimental Work	160
6.3	Future Work	163
Bibliography		166

Appendices

A Simulation methods	168
A.1 The Simulation Model	168
A.1.1 Interaction Potentials	168
A.1.2 Interaction Site Models and Quaternions	172
A.2 Time Evolution of Model Systems	174
A.2.1 The Gear Predictor-Corrector Algorithm	174
A.2.2 Simulation Constraints	177
A.3 Statistical Analysis of Model Systems	179
A.3.1 Structural Properties	179
A.3.2 Dynamical Properties	180
A.4 Nomenclature Variations in Different Chapters	185
Bibliography	186

List of Tables

2.1	σ_i is the LJ length parameter, U is the average configurational energy (standard deviation $< 0.6\%$), and P the average pressure (standard deviation $< 0.5\%$). Also, in all simulations, $\epsilon = 6 \times 10^{-21}J$, the mass $m = 1.99265 \times 10^{-25}kg$, and the reduced density $\rho^* = 0.8$	27
3.1	Systems with off-center charge. l_q is the distance of the cationic charge from the center of mass, U is the average configurational energy, P is the average pressure, D_R is the rotational diffusion coefficient of the cation, τ_μ is the orientational relaxation time of the cation, τ_{ip} is the average lifetime of bonded ion pairs, and % p.c. is the percentage of paired cations. The numbers in brackets indicate the standard deviations of the quantities. All results are for 1200 K. Other parameters used in the simulations are: the LJ parameters, $\sigma = 5 \text{ \AA}$, $\epsilon = 6 \times 10^{-21}J$, the charges $q = \pm 1e$, the mass $m = 1.99265 \times 10^{-25}kg$, the moments of inertia of the cation $I_{xx} = I_{yy} = 2.8 \times 10^{-46}kgm^2$, and the reduced density $\rho^* = 0.8$	51
3.2	Systems with centered charge. σ is the LJ parameter, U is the average configurational energy, P is the average pressure, and the numbers in brackets indicate the standard deviations. The results are for 1200 K and the reduced density $\rho^* = 0.8$	52
3.3	Bonded ion-pair lifetimes and percentages of paired cations for different temperatures. Standard deviations are as in Table 3.1.	72
3.4	Experimental data [9] for different cations with $(Tf)_2N^-$ counterions.	76
4.1	Parameters and results for the charge-centered models $XC5$, XCY and $1CY$. Here X is the size disparity σ_+/σ_- , Y is σ'_{+-} (rounded), and σ_+ and σ_- are the LJ length parameters for the respective ions. s_{+-} is the position of the first peak in the cation-anion radial distribution function, and δ is the percentage difference between σ'_{+-} and s_{+-} . All ions considered are univalent, and for all particles the LJ energy parameter $\epsilon = 6 \times 10^{-21}J$, the masses $m = 1.99265 \times 10^{-25}kg$	85

4.2	Parameters and results for the charge-off-center models 1OCY, 2OCY and 3OCY. σ_+ and σ_- , interaction parameters, and masses are as for systems 1C5, 2C5 and 3C5, respectively (Table 4.1). X , Y , and δ are as in Table 4.1. l_q/R_+ indicates the charge displacement (Fig. 4.1), and s_{+-} is the position of the first peak in CC+- . D_R and τ_μ are the rotational diffusion coefficient and the orientational relaxation time of the cation, respectively, τ_{ip} is the average ion-pair lifetime, and % <i>p.c.</i> is the percentage of paired cations. The superscripts <i>a</i> and <i>b</i> denote results obtained with cation moments of inertia $I_{xx} = I_{yy} = 2.8 \times 10^{-45}$, and 2.8×10^{-44} kg m ² , respectively. All other results were obtained using $I_{xx} = I_{yy} = 2.8 \times 10^{-46}$ kg m ²	86
5.1	System parameters for the size disparate and charge-off-center models. σ_+ and σ_- are the LJ length parameters, l_q/R_+ is the normalized charge displacement. The LJ energy parameter is $\epsilon = 6 \times 10^{-21} J$ for all ions, the charges $q = \pm 1e$, the ion mass $m = 1.99265 \times 10^{-25} kg$, the moment of inertia of charge-off-center cations is $I_{xx} = I_{yy} = 2.8 \times 10^{-46} kg m^2$. Test simulations were also carried out with $I_{xx} = I_{yy} = 2.8 \times 10^{-45} kg m^2$ and $I_{xx} = I_{yy} = 2.8 \times 10^{-44} kg m^2$	120
A.1	Different Nomenclature used for the charge-centered size disparate ionic liquid model, with constant σ_{+-} , in Chapters 2, 4, and 5.	185
A.2	Different Nomenclature used for the charge-centered same size ion model, where σ_{+-} decreases, in Chapters 3 and 4.	185
A.3	Different Nomenclature used for the charge-off-center model, with same size anions and cations, in Chapters 3, 4, and 5.	185

List of Figures

1.1	Chemical structure of various room temperature ionic liquid cations: imidazolium (1), pyridinium (2), piperidinium (3), pyrrolidinium (4), ammonium (5) and phosphonium (6) cations.	2
1.2	Diagram of the size disparate ionic liquid model with constant counterion distance σ_{+-}	13
1.3	Diagram of the charge displaced ionic liquid model. The cation center of mass is shown as a dot and the cation center of charge is depicted as +. The anion center of mass and center of charge are at the same position (-). σ_{+-} is the center of mass counterion distance, σ'_{+-} is the center of charge counterion distance and l_q is the cation “charge arm”, its center of mass to center of charge distance.	14
1.4	Schematic overview of all simulation models. We label the charge-centered and charge-off-center models “XCY” and “XOCY”, where $X = \sigma_+/\sigma_-$ indicates the size disparity, and $Y = \sigma'_{+-}$ (in Å) is the minimum distance between the cation and anion charges.	16
2.1	Radial distribution functions of ionic systems of different size disparity. . .	30
2.2	Radial distribution functions of LJ systems of different size disparity. . . .	31
2.3	Radial charge distribution functions of systems of different size disparity, plotted as $rQ(r)$	33
2.4	Top: Off-diagonal pressure tensor autocorrelation functions for ionic fluids of different size disparity. Bottom: Viscosities as functions of the upper limit, t_{UL} , used in the numerical integration of the autocorrelation functions shown above.	34
2.5	Viscosities for ionic and LJ fluids as functions of size disparity. The triangles represent results obtained with 512 ions. The error bars indicate one standard deviation.	35
2.6	Diffusion coefficients as functions of size disparity for ionic (Top) and LJ (Bottom) fluids. The simulation results are compared with diffusion coefficients given by the Stokes-Einstein formula. In the top panel, the symbols, \triangle and ∇ , are the cation and anion values, respectively, obtained with 512 ions. The error bars indicate one standard deviation.	36
2.7	Normalized velocity autocorrelation functions for the ionic fluids of different size disparity.	38
2.8	Top: Current autocorrelation functions for ionic fluids of different size disparity. Bottom: Conductivities as functions of the upper limit, t_{UL} , used in the numerical integration of the autocorrelation functions shown above. . .	40

2.9	Conductivities of ionic fluids as functions of size disparity. Simulation results (solid line) are compared with Nernst-Einstein values (dashed line). The triangles represent results obtained with 512 ions. The error bars indicate one standard deviation.	41
2.10	Logarithms (base 10) of diffusion coefficients, viscosities and electrical conductivities as functions of $1/T$ for systems 1:1 and 3:1. The solid lines are fits to the VFT equation. The error bars indicate one standard deviation. . .	43
2.11	Diffusion coefficients as functions of T/η for systems 1:1 and 3:1. The lines are fits to Eq. (2.12). The error bars indicate one standard deviation. . . .	44
3.1	Center of mass radial distribution functions for the <i>OC</i> systems.	56
3.2	Charge-charge radial distribution functions for the <i>OC</i> systems.	57
3.3	Running coordination numbers for the <i>OC0</i> and <i>OC0.75</i> systems. For the <i>OC0.75</i> case results obtained using radial distributions about the center of mass (middle) and center of charge (bottom) are included. The contributions from counterions and coions as well as the total coordination number are shown.	59
3.4	The function $rQ_+(r)$ for <i>OC</i> systems plotted on linear and logarithmic scales. Screening lengths were estimated from the slopes of the dotted lines.	61
3.5	Top: Off-diagonal pressure tensor autocorrelation functions for <i>OC</i> systems at 1200 K. Bottom: Shear viscosities as functions of the upper integration limit t_{UL}	63
3.6	Top: Current autocorrelation functions for <i>OC</i> systems at 1200 K. Bottom: Conductivities as functions of the upper integration limit t_{UL}	64
3.7	Normalized velocity autocorrelation functions of <i>OC</i> and corresponding <i>C</i> systems.	66
3.8	Diffusion coefficients, viscosities and electrical conductivities for <i>OC</i> (black) and <i>C</i> (yellow) systems. The corresponding Stokes (diffusion) and Nernst-Einstein (conductivity) results are given by dashed lines. The triangles represent results obtained with 512 ions. The error bars indicate one standard deviation.	68
3.9	Normalized cation angular velocity autocorrelation functions.	70
3.10	Normalized cation reorientational autocorrelation functions.	71
3.11	Logarithms (base 10) of transport properties for <i>OC</i> systems as functions of $1/T$. The solid lines are fits to the VFT equation. The error bars indicate one standard deviation.	73
3.12	Diffusion coefficients for <i>OC</i> systems as functions of T/η . The solid lines are fits to the fractional Stokes-Einstein relationship given by Eq. (3.16). The error bars indicate one standard deviation.	74
4.1	Sketch of the geometry used for the charge-off-center (<i>XOCY</i>) model. l_q is the distance of the charge from the center of mass, σ_{+-} is the distance between the centers of mass, and σ'_{+-} is the charge separation.	82
4.2	Center of mass radial distribution functions for model <i>XCY</i>	92
4.3	Cation-anion center of charge radial distribution functions for models <i>1OCY</i> (top), <i>2OCY</i> (middle), and <i>3OCY</i> (bottom).	94
4.4	Cation-anion center of mass radial distribution functions for models <i>1OCY</i> (top), <i>2OCY</i> (middle), and <i>3OCY</i> (bottom).	95

4.5	Cation-cation center of mass radial distribution functions for models <i>1OCY</i> (top), <i>2OCY</i> (middle), and <i>3OCY</i> (bottom).	97
4.6	Cation-cation center of charge radial distribution functions for models <i>1OCY</i> (top), <i>2OCY</i> (middle), and <i>3OCY</i> (bottom).	98
4.7	Anion-anion center of mass radial distribution functions for models <i>1OCY</i> (top), <i>2OCY</i> (middle), and <i>3OCY</i> (bottom).	99
4.8	Radial charge distribution functions for models <i>1OCY</i> (top) and <i>3OCY</i> (middle and bottom).	101
4.9	Running coordination numbers of the cations for models <i>XC5</i> , <i>XCY</i> (top), and <i>3OCY</i> (bottom).	102
4.10	Transport properties versus size disparity for models <i>XC5</i> and <i>XCY</i>	104
4.11	Transport properties versus σ'_{+-} for models <i>XCY</i> and <i>1CY</i>	105
4.12	Transport properties versus charge displacement for models <i>1OCY</i> , <i>2OCY</i> , and <i>3OCY</i> . The diamonds (orange) and squares (blue) represent the results obtained for model <i>1OCY</i> with cation moments of inertia of 2.8×10^{-45} , and 2.8×10^{-44} kg m ² , respectively. All other results were obtained using 2.8×10^{-46} kg m ² . Note that for clarity the dependence of the diffusion coefficients on the moment of inertia is shown only for the positive ion.	107
4.13	Transport properties versus σ'_{+-} for models <i>1OCY</i> , <i>2OCY</i> , <i>3OCY</i> , and <i>1CY</i> . The open, black diamonds, triangles, and squares indicate results obtained with 512 ions for systems <i>1CY</i> , <i>1OCY</i> , and <i>3OCY</i> , respectively.	108
4.14	Angular velocity autocorrelation functions for model <i>3OCY</i>	110
4.15	Reorientational time correlation functions for model <i>3OCY</i>	110
5.1	Cation-anion rdfs for charge-centered models at different water concentrations. Results are shown for <i>1C5</i> -water (top panel), <i>3C5</i> -water (middle panel), and <i>1C5</i> -LJ-particles (bottom panel).	123
5.2	Cation-water(O) (top panel) and anion-water(O) (bottom panel) rdfs for charge-centered models at 30 mol% water. For model <i>1C5</i> , ion-LJ-particle results are included for comparison.	125
5.3	Water(O)-water(O) rdfs for <i>1C5</i> -water (top panel) and <i>3C5</i> -water (bottom panel) at different water concentrations. The dashed black line is the water(O)-water(O) rdf for pure water at the same ρ^* and temperature.	126
5.4	The reduced occupied volume $V_-(R)$ [Eq. (5.2)] for charge-centered models at different water concentrations. Both the total $V_-(R)$ (top panel) and its ionic contribution (bottom panel) are shown.	127
5.5	Cation-anion center of mass rdfs for <i>1OC3.1</i> -water mixtures at different water concentrations.	129
5.6	Ion-water rdfs for charge-off-center models at 30 mol% water. Included are the cation(CC)-water(O) (top panel), anion-water(O) (middle panel), and anion-water(H) (bottom panel) functions. For <i>1OC5</i> and <i>1OC3.1</i> some LJ particle results are shown for comparison.	130

5.7	A configurational snapshot of the 1OC3.8-water system at 30 mol% water. One cation-water-anion triple is indicated, others can be clearly seen. The anions are blue, the cations turquoise, the water oxygen atoms are red, and the water hydrogen atoms are white. All particles are shown with somewhat reduced diameters to reveal the hydrogen sites of the water molecules, and the charged site of the cations (dark turquoise).	131
5.8	Water(O)-water(O) rdfs for 1OC3.8-water (top panel) and 1OC3.1-water (bottom panel) at different water concentrations. The dashed black line is the water(O)-water(O) rdf for pure water at the same ρ^* and temperature.	133
5.9	The reduced occupied volume $V_+(R)$ [Eq. (5.2)] for charge-off-center models at different water concentrations. Both the total $V_+(R)$ (top panel) and its ionic contribution (bottom panel) are shown.	134
5.10	Diffusion coefficients versus water (LJ particle) concentration for 1C5-water (or LJ particles), 2C5-water, and 3C5-water systems. Results are shown for the cations (top panel), anions (middle panel), and water (LJ particles) (bottom panel). The orange squares indicate results obtained with a total of 512 particles, all other results shown were obtained with 216 particles. The error bars represent one standard deviation.	136
5.11	Dependence of the diffusion coefficients on the molecular mass of water for systems 1C5-water and 3C5-water. Results are shown for real water (w18, solid lines) and a heavier species (w120, dash-dot lines) having the same molecular mass as the ions. The panels are as in Fig. 5.10. The error bars represent one standard deviation.	137
5.12	Velocity autocorrelation functions for 3C5-water systems at 50 mol% water. The cation and anion functions are shown in the top and bottom panels, respectively. Results are included for real water (w18) and the heavier species (w120). Curves for the pure ionic liquid are shown for comparison.	138
5.13	Viscosity (top panel) and σ_{el}/ρ_+ (bottom panel) versus water (LJ particle) concentration for 1C5-water (or LJ particles), 2C5-water, and 3C5-water systems. The orange squares (water mixtures) and orange diamonds (LJ particle mixtures) indicate results obtained with a total of 512 particles, all other results shown were obtained with 216 particles. The error bars represent one standard deviation.	140
5.14	A configurational snapshot of the 3C5-water system at 50 mol% water. One of the chain-like, anion-water structures is indicated. The colors are as in Fig. 7, and again the diameters are somewhat reduced to reveal the hydrogen sites of the water molecules.	141
5.15	Dependence of the viscosity (top panel) and σ_{el}/ρ_+ (bottom panel) on the molecular mass of water for systems 1C5-water and 3C5-water. Results are shown for real water (w18, solid lines) and a heavier species (w120, dash-dot lines) having the same molecular mass as the ions. The error bars represent one standard deviation.	143
5.16	Diffusion coefficients of the cations (top panel), anions (middle panel), and water (LJ particles) (bottom panel) versus water (LJ particle) concentration for charge-off-center models mixed with water (solid lines) or LJ particles (dashed lines). The error bars represent one standard deviation.	145

5.17	Viscosity (top panel) and σ_{el}/ρ_+ (bottom panel) versus water (LJ particle) concentration for charge-off-center models mixed with water (solid lines) or LJ particles (dashed lines). The lightly dotted lines (top panel) show the linear behavior expected for all ideal 1OCY-water mixtures. The error bars represent one standard deviation.	146
5.18	Diffusion coefficients of the cations (top panel), anions (middle panel), and water (LJ particles) (bottom panel) versus water (LJ particle) concentration for model 1OC3.1 mixed with water (solid lines) or LJ particles (dashed lines). Results for some corresponding mixtures with the different ionic liquid models indicated on the figure are included for comparison. The error bars represent one standard deviation.	149
5.19	Viscosity (top panel) and σ_{el}/ρ_+ (bottom panel) versus water (LJ particle) concentration for model 1OC3.1 mixed with water (solid lines) or LJ particles (dashed lines). Corresponding results for 1OC3.8-water systems are included for comparison. The error bars represent one standard deviation.	150
6.1	Schematic overview of all simulation results. The black arrows indicate an increase or decrease in the RTIL characteristic, the red (green) arrows indicate a corresponding increase (decrease) in transport properties. Here, SD stands for size disparity, OC for a displacement of the cation charge from the center of mass (off-center model) and σ'_{+-} is the positive-negative center of charge distance.	160

Acknowledgements

I would like to thank all those, from whom I learned so much these last years:

Gren Patey, Lars Rose, Glenn Torrie, Abbas Parsafar, Tim Croteau, Erin Lindenberg, Jingyi Yan, Chris Hemming, Greg Lakatos, and Sandip Paul.

Statement of Co-Authorship

Chapters 2-5 are co-authored publications of H. V. Spohr and Prof. G. N. Patey. The research programs were designed by H. V. Spohr and G. N. Patey. The research and data analysis was performed by H. V. Spohr with guidance and suggestions from Prof. G. N. Patey. The manuscripts were written by H. V. Spohr with revisions and additions by Prof. G. N. Patey.

Chapter 1

Introduction

The objective of this thesis is to understand how the structural and transport properties of room temperature ionic liquids (RTILs) are influenced by the fundamental molecular characteristics of the constituent ions.

This thesis is organized into a Chapter to introduce the motivation and subject matter, followed by four Chapters describing the research performed, and finally a conclusion and outlook on further work that is motivated by the results of this research. The method and computational approach are discussed in the Appendix.

The introductory Chapter 1.1 gives a basic overview of ionic liquids, their structure, physical, and chemical properties and some examples for RTIL applications. In Chapter 1.2, an overview of present knowledge is presented on the influence of molecular structure on RTIL properties, and on their mixture properties. In Chapter 1.3, a brief outline is drawn of some computational approaches for the simulation of RTILs. Finally, Chapter 1.4 discusses the present computational approach and the choice of basic ionic liquid characteristics investigated.

1.1 Introduction to Room Temperature Ionic Liquids

RTILs are fascinating substances of increasing importance in academic research and in industry. RTILs are pure salts, formed of organic cations and inorganic or organic anions. In contrast to inorganic, crystalline salts, such as common table salt, RTILs are liquid at ambient temperatures, displaying melting points that are lower than those of inorganic salts by one to two orders of magnitude (on the Celsius temperature scale). Common RTILs melt between 100 and minus 100 degree Celsius.

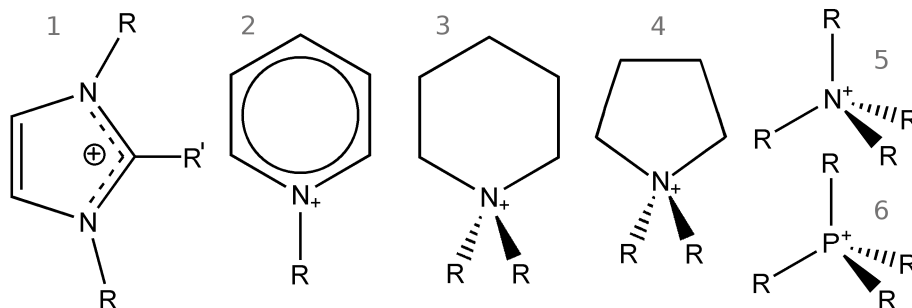


Figure 1.1: Chemical structure of various room temperature ionic liquid cations: imidazolium (1), pyridinium (2), piperidinium (3), pyrrolidinium (4), ammonium (5) and phosphonium (6) cations.

Some common RTIL cations are shown in Fig. 1.1: imidazolium (1), pyridinium (2), piperidinium (3), pyrrolidinium (4), ammonium (5) or phosphonium ions (6) are commonly used. The RTIL anions are often simple inorganic ions, for example halides, tetrafluoroborate (BF_4^-) or hexafluorophosphate (PF_6^-), but in current practice often larger organic ions are selected such as tosylate ($\text{CH}_3\text{C}_6\text{H}_4\text{SO}_3^-$ or TsO^-), dicyanimide ($(\text{NC})_2\text{N}^-$), trifluoromethanesulfonate (CF_3SO_3^- or TfO^-), bis(trifluoromethanesulfonyl)amide (Tf_2N^- or $(\text{CF}_3\text{SO}_2)_2\text{N}^-$), and others. New ion choices can be made to meet specific RTIL property targets, for example different azolium(+) and azolate(-) ions (five membered rings with 2-4 nitrogen atoms in the ring) were suggested for the production of energetic materials [1]. Amino acids were proposed as functionalized cations or anions for low cost, biodegradable RTILs [2, 3].

1.1.1 Ionic Liquid Properties

The general RTIL properties that are thought to be of capital importance are a negligible vapor pressure, excellent thermal stability, low flammability, an ability to conduct electricity, and strong and selective solubilities of other substances. One major disadvantage for chemical reactions in RTILs is that they generally have high viscosities, on the order of two magnitudes higher than organic solvents. This leads to slow mechanical mixing and slower reaction rates. These fundamental trends in RTIL properties can be mainly attributed to the strong Coulombic interactions among the ions [17–19], but large variations exist for

different types of ion combinations. For instance, the solvation behavior and miscibility of RTILs varies widely [20, 21]. It was observed that many RTILs are hygroscopic, both hydrophilic (for example 1,3-dimethylimidazolium (Fig. 1.1, 1) with halogen, NO_3^- or TfN^- anions), and hydrophobic RTILs (for example 1,3-dimethylimidazolium with PF_6^- or Tf_2N^- anions) [22, 23].

1.1.2 Utilization and Applications

RTILs are of importance in various research areas and have been proposed to improve diverse applications. They are used as reaction media, for surface modifications and synthesis of nanoparticles [4, 5], as catalysts [6], for chemical separation technology, and as sensors [7]. RTILs are utilized in electrochemical processes for deposition of metals and alloys, in electrosynthesis, and in a variety of electrochemical devices such as fuel cells, dye sensitized solar cells, batteries and double-layer capacitors [8–11]. Due to their ability to dissolve the bio-renewable resource cellulose, specific RTILs are employed in cellulose processing such as the production of fuel from biological sources, spinning of cellulose fibers and recycling of cellulose waste such as tissue paper [11–13]. Another promising application of RTILs is as lubricants and hydraulic fluids [14, 15]. Mostly these applications are not yet commercialised, but promise to be of great interest to industry. The first commercialisation of RTILs was the BASIL process (Biphasic Acid Scavenging utilizing Ionic Liquids) by the company BASF in 2004 [16], other large scale chemical production plants are in current use.

1.1.3 Environmental Acceptability

RTILs are also praised as new, more sustainable alternatives to commonly used organic solvents. There are several arguments for the environmental compatibility of RTILs. The negligible vapor pressure of RTILs eliminates one pathway of environmental release and reduces inhalative exposure of workers [24]. The low flammability lowers the risk of fast, exothermic oxidations in case of an accident [24]. Until recently, RTILs were thought to be relatively non-toxic, but recent studies have shown that environmental compatibility

strongly depends on the choice of RTIL ions [24–26]. Furthermore, RTILs can be recycled in a number of different ways [27], for example through biphasic separation, membrane separation, washing with liquids or gases, distillation or electro dialysis.

1.2 The Influence of Ion Characteristics on RTIL Liquid Properties

Because the choice of constituting ions is so crucial to the resulting RTIL properties, the following paragraphs give an overview of present knowledge on the influence of molecular shape and functionality on a selection of RTIL properties.

1.2.1 Melting Point

In general, ionic liquids with exceptionally low melting points consist of a combination of large anions and cations that have a diffuse distribution of charge, and that have weak intermolecular interactions (such as the avoidance of hydrogen bonds) [6]. The melting points of RTILs are also lowered by lengthening the alkyl side chains of the cation [28, 29], and by choosing asymmetric ions to prevent orderly packing into crystal structures [4, 30]. The general correlations of molecular structure to melting point described above can be contradicted by particular RTIL types. In some imidazolium RTILs the elimination of a hydrogen bond, by exchanging a hydrogen for a methyl group (R' in Fig. 1.1, 1), leads to an increase in melting point [22, 31, 32].

Many RTILs form glasses upon cooling. Glasses can be classified as ‘strong’ or ‘fragile’, depending on their dynamical behavior close to the solidification point [33]. The dynamical behavior of strong glasses follows an Arrhenius temperature dependence when plotted as the logarithm of viscosity versus T_g/T (where T_g is the glass transition temperature). Fragile glasses display non-Arrhenius temperature dependences. Glass-forming RTILs can also be classified in this way, and these concepts may aid in understanding the link between molecular structure, interactions and fluidity of RTILs [34, 35]. In this work, we are generally far from the glass transition temperature and we have not attempted to investigate

these concepts.

1.2.2 Shear Viscosity

Research on the shear viscosity of RTILs has mainly focused on the substituents of the ions. (In the subsequent document, whenever the term “viscosity” is used, this term denotes the shear viscosity.) Ions that form a stronger hydrogen bonding network through their substituents have increased viscosities [6, 8, 22]. Longer or more numerous alkyl side chains on the cation [8, 28, 36], and fluorination and lengthening of anion substituents [6, 22] increase van der Waals interactions and so viscosity. Flexibility introduced into the cation side chains reduces RTIL viscosity [6, 22, 37]. It has been reported that anions with an asymmetric molecular shape have especially low viscosities [4]. Pyridinium salts (Fig. 1.1, 4) were found to be slightly more viscous than imidazolium salts (Fig. 1.1, 1) [36]. The viscosity of ionic liquids is reported to be strongly dependant on the temperature, with viscosity changes up to 20% for a change of 5 K close to room temperature [6, 8]. Addition of a small amount of organic solvent or water (as an impurity) strongly decreases viscosity [6, 36], necessitating a strict control of water levels when measuring the viscosity of RTILs. Halogen impurities, such as chloride originating from RTIL synthesis, can increase the liquid viscosity [36]. Finally, as an exception to the trends reported in this paragraph, replacing a hydrogen for a methyl group on an imidazole carbon that is commonly able to hydrogen bond (R' in Fig. 1.1, 1), leads to an increase in viscosity [22]. The most likely explanation for this phenomenon is that the hydrogen bonding disturbs the uniformity of Coulombic interactions [38].

1.2.3 Electrical Conductivity

Pure RTILs are moderate to poor electrical conductors, of similar strength to solutions of inorganic electrolytes in organic liquids, one order of magnitude smaller than aqueous inorganic electrolytes [8, 9]. The electrical conductivity is limited by the number of charge carriers per unit volume and their mobility. Due to large ion sizes and strong interactions among the ions, diffusion in ionic liquids is hindered [8, 39, 40]. The number of

charge carriers is effectively reduced through correlated motion of ion pairs or larger aggregates (aggregation and pairing can also increase the vapour pressure of RTILs) [19, 39–43]. Lengthening of the cationic alkyl side chains decreases the conductivity through increased interactions among the ions [28]. In general, 1-alkyl-3-methylimidazolium (Fig. 1.1, 1) ions have larger electrical conductivities than N,N-dialkylpyrrolidinium (Fig. 1.1, 4) than tetraalkylammonium ions (Fig. 1.1, 5). This is attributed to shape; flat, disk-like ions being more mobile than tetrahedral ions [8]. Conductivity can be improved by mixing different ionic liquids, or by adding water or organic solvents [8, 9]. RTILs have wide electrochemical windows, meaning that they do not degrade within a large voltage range [8, 39]. This is an important prerequisite for a solvent in which electrochemical reactions are conducted.

1.2.4 Impurities and Mixtures

Mixing of RTILs with other substances reveals their complicated, widely varied physical behavior. Solvation of solvatochromic and fluorescent molecular probes (such as Reichardt’s betaine dye, Nile red or pyrenes) in RTILs exemplifies this. Solvation was found to depend on molecular ion sizes, strength of Coulombic interactions, electrical polarizability, dipole interaction strength, hydrogen bonding acidity or basicity, and ability to form aromatic π interactions [21, 42, 44–46]. Some RTILs show surfactant-like behavior, the charged groups and the non-polar alkyl substituents aggregate in separate domains [47]. These types of RTILs are inhomogeneous solvents, where the length scale of the heterogeneity depends on the alkyl substituent length and is temperature dependent [48]. Accordingly, some RTILs can display “dual” solvation behavior towards both polar and non-polar compounds, which accumulate in the respective domains of the heterogeneous ionic liquid [46, 49]. Some imidazolium RTILs are reported to form three dimensional polymeric supramolecules through hydrogen bonds [50]. The introduction of other molecules leads to disruption of the network to the formation of smaller structures, triples, contact ion pairs, and finally single solvated ions [50].

Mixtures of RTILs with water are extensively studied, most RTILs are hygroscopic, even those that are largely immiscible with water [23, 43]. The miscibility with water is

largely determined by the anions, forming anion-water complexes [43, 44]. Miscibility can be temperature dependant [51]. Even a small amount of water (or other solvents) strongly decreases the RTIL viscosity and increases the electrical conductivity [52, 53].

Mixtures of RTILs with different organic solvents have been studied. Saturated hydrocarbons have low solubilities in RTILs, that increase with the length of the alkyl substituent of the RTIL cation [21, 44, 53]. RTILs often have asymmetric miscibility gaps with organic solvents, where the ionic liquid is able to dissolve much more of the molecular solvent, than the solvent can dissolve RTIL molecules [43]. An advantage of ionic liquids is their generally high densities, which facilitate rapid phase separations with conventional (low density) solvents [21].

The solubility of gases in RTILs strongly depends on the type of interactions the gases can have with the RTIL ions. Gases with weak dispersion interactions are little soluble ($\text{H}_2 < \text{O}_2 < \text{CH}_4 < \text{C}_2\text{H}_6$), gases with quadrupole moments are more soluble (ethene, CO_2), and polar gases are very soluble (SO_2 , water vapor) in RTILs [43]. It has been observed that ionic liquids display almost no volume expansion upon the addition of CO_2 , indicating that the RTIL structure is only slightly disturbed. CO_2 inserts into gaps of the RTIL structure, coordinating mainly to the anions [43, 54].

1.2.5 Opportunities and Challenges

In summary, the main advantage of RTILs is the customizability of their liquid properties through combining a wide choice of different ion types, and by attaching different (functionalized) side chains to an ion “base”. On the other hand, this also poses the greatest challenge of RTILs. In order to design RTILs rationally one needs to be able to predict the macroscopic liquid properties from the molecular structure of the ions.

1.3 Computer Simulations of Ionic Liquids

Computer simulations are an ideal tool for studying RTILs because a direct connection can be drawn between the molecular structure and macroscopic properties. In this way, computer simulations can assist in the molecular interpretation of experimental observations. Computer simulations can explore changes in model systems systematically and can probe extreme physical conditions. Computer simulations can also be used to test theoretical models and to make predictions based on these models, linking theory and experiment. Many different simulation approaches have been applied to ionic liquids, each with its limitations, and consequently simulation results must be interpreted carefully. The following paragraphs give an overview of some different computational methods that have been applied to pure RTILs and RTIL mixtures, arranged by scale from quantum chemical, to atomistic, to coarse grained simulation methods.

1.3.1 Quantum Chemical Calculations

Quantum chemical calculations are able to probe the electronic structure of RTILs. They have been used to develop intramolecular interaction potentials for molecular simulations [55–57], and to determine the charge distribution and polarizability of RTIL molecules [58, 59]. Correlations were found between the interaction energies of gas phase ion pairs (and ion pair dimers) and melting points [60, 61], viscosity and vapor pressure [62, 63], and conductivity and ion mobility [18]. It has been determined that the main contributor to the ion pair interaction energy are the electrostatic Coulombic attractions [18, 64, 65]. Some studies found that hydrogen bonds [18] or charge transfer complexes [64] contribute little to the stabilization energy of 1,3-alkylimidazolium ionic liquids, whereas dispersion and induction interactions are not negligible [18, 65]. Several quantum chemical studies have suggested that hydrogen bonding in RTILs is of great importance to the (experimentally determined) transport properties [31, 32, 38, 66–69].

The inherent disadvantage of quantum chemical calculations to the goal of clarifying the relationship between molecular structure and RTIL properties is the limited scope of

quantum chemical calculations to one (or a few) ion pairs. The transfer of conclusions from ion pair calculations in the gas phase to the dense liquid phase must be made with care.

1.3.2 Atomistic Simulations

Atomistic simulations generally use empirically developed force fields to determine the equilibrium and dynamical properties of a system of molecules. The advantage of these atomistic simulations, in comparison to quantum mechanical calculations, is the simple additivity of the molecular interactions, speeding up the calculations and facilitating long simulation sequences. Simulations of ionic liquids mostly use either all atom or united atom force fields, the latter model treats some CH_2 and CH_3 groups as single atomic units.

The structure and the thermodynamic properties of ionic liquids have been investigated by several atomistic simulation studies, probing the orientation of the ions [70–72], and the influence of anion size and alkyl side chain length [73, 74]. Long alkyl side chains, containing more than four carbon atoms, have been observed to result in the formation of structural heterogeneity due to tail aggregation and clustering of counterions [75–78].

The direct calculation of transport properties such as viscosity and electrical conductivity in RTILs is difficult because of long-time correlations that lead to large statistical uncertainties, especially close to glass formation temperatures [57, 76, 79–81]. Often, the viscosity and electrical conductivity are estimated from the diffusion coefficients, few researchers have obtained the viscosity [82, 83], or the electrical conductivity [79, 82–84] from the fundamental Green-Kubo relations (see Appendix A.3.2). Very long simulation times are needed, and accordingly the simpler united atom models have often been employed to calculate transport properties. The accuracy of all-atom versus united atom models [77, 79], rigid versus flexible models [83], of polarizability of RTIL molecules [70, 85], and the influence of different partial charges on RTIL ions [86, 87] have been tested. All these factors were found to play a role in determining RTIL structure, and especially the dynamical properties. Accordingly, the results of atomistic simulations depend critically on the quality of the force field employed. The influences of anion type and alkyl side chain length of imidazolium RTIL on diffusion coefficients, viscosity, and electrical conductivity have been

investigated [69, 83, 84, 88–90]. Often, strong correlations among ions have been found, such as ion pairs or clusters [79, 82, 85, 91], resulting in relatively low conductivities of RTILs in comparison to the expected electrical conductivity calculated from their diffusion coefficients through the Nernst-Einstein equation (see Appendix A.3.2).

The majority of RTIL atomistic simulations is on the structure, thermodynamic and transport properties of imidazolium cations with plain alkyl substituents. Few studies examine other RTIL types, such as pyrrolidinium RTILs [85] or imidazolium RTIL with ether [92], and amino [67] functionalities. Other work investigates RTIL gas-liquid and RTIL-water interfaces [56, 93–98, 100], confined liquids between electrodes [56, 99, 101, 102], solutes in RTILs, and RTIL solvent properties [45, 56, 104–109].

Another area of atomistic simulation research is that of RTIL mixtures with water, alcohols, aromatic compounds, or gases. RTIL diffusion coefficients increase and viscosity decreases with the addition of water or alcohols [110–113]. Water and alcohol molecules interact mainly with the small RTIL anions [103, 111, 113–118], cation-anion and water-water interactions are also of importance, cation-water, and ion-cation interactions were found to be weak [116]. RTILs with long alkyl side chains were observed to change their structure upon dilution, from ordered ionic headgroups and aggregated tails in RTIL rich mixtures, to micelle formation, and finally to disordered ions in water [115]. The aggregate size and structure were found to strongly depend on the side chain length of the cations [119].

Organic solvents, such as aromatic compounds and alkenes, on the other hand, preferably interact with the cation through its alkyl substituents or aromatic ring interactions [120, 121]. The mixture segregates into polar and non-polar structures, which can result in the formation of drops and chains of RTIL surrounded by organic solvent [122]. The addition of moderate amounts of non-ionic solvent decreases the viscosity and increases the electrical conductivity, whereas a high amount of non-ionic solvent decreases the electrical conductivity [122] due to a decreasing density of charge carriers. A study of mixtures with acetonitrile shows the same trends for transport properties upon dilution [123].

The addition of gases to RTILs has also been studied in simulations, especially the

addition of CO₂. CO₂ was found to be far more soluble in RTILs than other gases, for example nitrogen or oxygen [124, 125]. Upon addition of CO₂ the volume of the RTIL-CO₂ mixture stays nearly constant, whereas the density increases [54, 126]. Little structural change is observed, CO₂ inserts into the free volume of the RTIL network, interacting mainly with the anion [54, 124, 127]. At high CO₂ concentrations, the alkyl side chains were observed to extend, and the cation-anion distances increased slightly [127]. Addition of CO₂ to amine functionalized RTILs leads to an increased number of hydrogen bonds and a strong increase in viscosity and decrease in ionic diffusion coefficients [126].

1.3.3 Coarse Graining Approach

In the coarse graining technique several (typically three) heavy (non-hydrogen) atoms are combined into one united particle bead, greatly simplifying the molecular structure. The coarse graining parameters are chosen to reproduce the structure (for example radial distribution functions) of a particular RTIL at a specific temperature, density and composition. Coarse grained simulations are much more efficient and faster than atomistic simulations and accordingly processes that take place across large spatial and temporal scales can be investigated. On the other hand, they can suffer from transferability due to fitting of the effective pair potential to a specific state. Coarse grained models sometimes exhibit faster translational and rotational timescales, and so it may not be possible to quantitatively predict the dynamical properties [128, 129].

Coarse graining simulations of RTILs found tail group aggregation, the formation of non-ionic domains, and so spatial heterogeneity [130–133]. Aggregation into micelles was observed in aqueous solution [134]. Furthermore, gas-liquid interfaces of RTILs were simulated, again separation of non-polar and ionic domains was observed, with alkyl groups pointing from the surface into vacuum [132, 135]. A comparison was made between molecular dynamics simulations of all-atom and coarse grained models of ion velocities and electrical conductivity in high electrical fields [136]. The coarse grained simulation was found to produce less accurate results, but was significantly faster, and so simulations with large numbers of particles are feasible.

1.3.4 Progress and Limitations of Ionic Liquid Simulations

In summary, computer simulations of RTILs have been used to good effect to gain new insights into the details of molecular orientation and structure in ionic liquids. The importance of different RTIL molecular interactions, and the effects of some molecular features on macromolecular RTIL properties have been determined.

On the other hand, the system size of quantum mechanical calculations, and the approximations and fitting of force field parameters of atomic and coarse grained simulations, can lead to doubts about the applicability of some of these results. This argument is supported by the sometimes contradictory results of some simulations. Even though many studies closely mimic particular RTILs down to atomic or even electronic level, they still cannot reproduce the transport properties accurately. The strong correlations of ions, and accordingly slow dynamics and long-time correlations, result in problematic transport property calculations with large uncertainties. Some studies provide little value because they simply provide a comparison of calculated to experimental properties, with few new insights. We note a lack of systematic approaches to study the effect of specific molecular features on RTIL liquid properties.

1.4 The Present Approach

1.4.1 Choice of RTIL Ion Characteristics

We try to approach the challenge of predicting RTIL properties from characteristic molecular features in a very systematic way. First, we identify molecular characteristics that distinguish RTILs from molten salts. We isolate each molecular characteristic from other factors by designing simplified, specific RTIL models that vary only in this molecular characteristic. Then we explore the time evolution of the RTIL model systems through molecular dynamics simulations (Appendix A.2), and through statistical analysis find the structure and time dependant properties (Appendix A.3).

To identify some of the important molecular characteristics, we compare the structure of high temperature molten salts with ionic liquids that melt at ambient temperatures. Com-

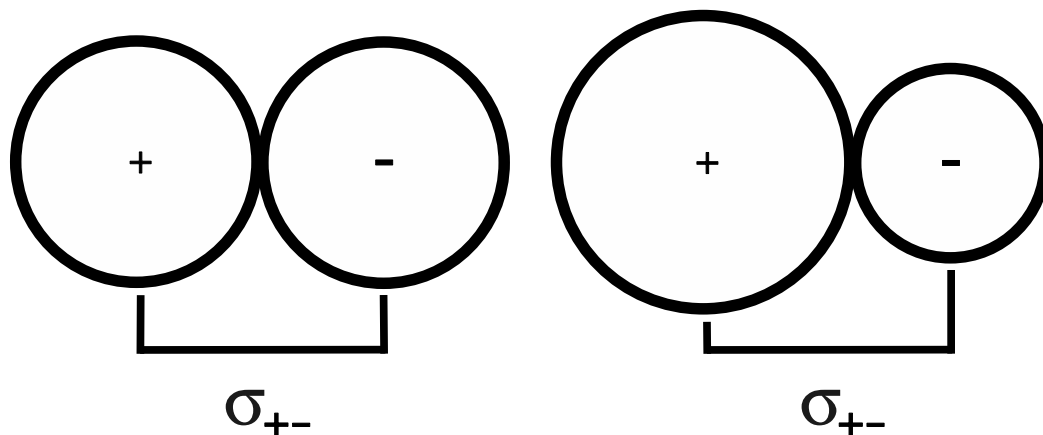


Figure 1.2: Diagram of the size disparate ionic liquid model with constant counterion distance σ_{+-} .

mon salts such as NaCl, KCl, CaSO₄, CaCO₃ or MgSO₄ all consist of small inorganic ions. Ionic liquids consist of much larger organic cations in combination with inorganic anions, so RTILs often have large ion size disparities. Size disparity is the first molecular characteristic that we investigate, the results are presented in Chapter 2. Using simple spherical models that interact via Lennard-Jones and Coulombic potentials (for the computational approach see Appendix A.1), we increase the size of the cation, while decreasing the size of the anion at the same time. The simultaneous change ensures a constant distance of positive to negative charge centers σ_{+-} , and we avoid changing the strong attractive Coulombic interactions that have a large influence on ionic systems (see Fig. 1.2). Other factors are also held constant, for example, reduced density (packing fraction) and mass.

RTIL cations also differ from simple inorganic cations of common salts in the distribution of their charge. Many ionic liquid cations consist of delocalized ring structures with heteroatoms (usually nitrogen). Here the charge is distributed, not centered on a single atom as in inorganic cations. For these cyclic cations and also for quaternary ammonium ions with asymmetric substituents, the center of charge is not necessarily the same as the center of mass. We chose this displacement of the charge as the second characteristic for our investigation. Kobrak and Sandalow propose a theoretical framework for the treatment of RTIL charge arms in their work, and show some examples of the influence of RTIL ion

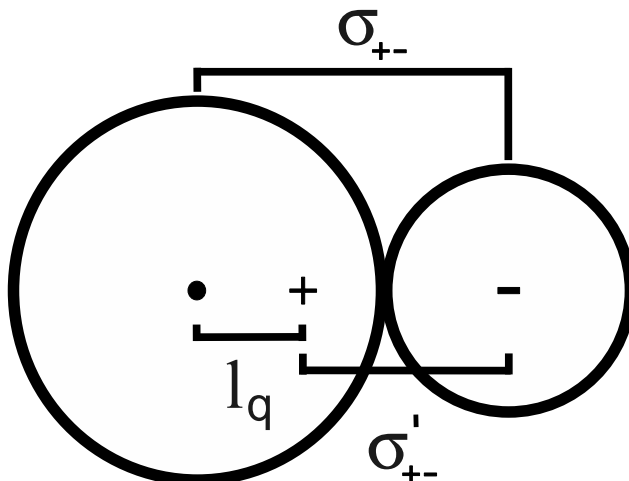


Figure 1.3: Diagram of the charge displaced ionic liquid model. The cation center of mass is shown as a dot and the cation center of charge is depicted as +. The anion center of mass and center of charge are at the same position (-). σ_{+-} is the center of mass counterion distance, σ'_{+-} is the center of charge counterion distance and l_q is the cation “charge arm”, its center of mass to center of charge distance.

charge arms on liquid properties [137]. To isolate the charge displacement from all other influences, we employ a model that consists of spheres of the same size, where the cation charge is displaced from the center of the sphere, its center of mass (see Fig. 1.3 and Appendix A.1.2). The investigation of the charge displaced model is described in Chapter 3.

We also investigate a combination of both models, with size disparity and charge displacement, to determine the relative importance of these characteristics. This study also highlights the important influence of variation in the cation-anion charge distance, and so of the strong Coulombic attraction. These results are presented in Chapter 4. A schematic overview of all simulation models used in this work is shown in Fig 1.4. *

There are many other influences worth considering that distinguish ionic liquids from molten salts, for example shape (spherical versus disk- or rod-like), variation of substituents, or more complicated intermolecular interactions due to delocalized charges, polarizability,

*Note that different nomenclature has been used for the same models in subsequently published Chapters. The nomenclature of each Chapter is described in the respective “Models and Simulation Method” part, and used consistently throughout each Chapter. Tables A.1-A.3 in Appendix A.4 summarize the different nomenclatures used.

directional hydrogen bonds, or varying strength of van der Waals interactions. These would be interesting to investigate, but exceed the scope of this thesis. However, some of these characteristics will be dealt with in future work of this group, which is described in more detail in Chapter 6.3.

As water plays an important role on RTILs due to their hygroscopic nature, the final investigation of this thesis considers the impact that water has on the liquid properties of the above RTIL models. This investigation is described in Chapter 5.

1.4.2 Advantages of this Approach

Simulations of these relatively simple RTIL models provide several advantages in comparison to detailed atomistic models. Firstly, these models allow different molecular influences to be decoupled, and so produce well-defined, and physically comprehensible results. The qualitative importance of different molecular characteristics can be distinguished, and the fundamental features that govern RTILs clarified. More complex models do not provide explicit and coherent insights on the influence of single molecular features on the liquid properties of RTILs. We note that even the simple models investigated in this work can display astonishingly complex liquid behavior. Additionally, our models facilitate fast simulations and accordingly enable us to carry out the long simulation sequences that are needed to resolve the long time correlations and slow dynamics of ionic systems.

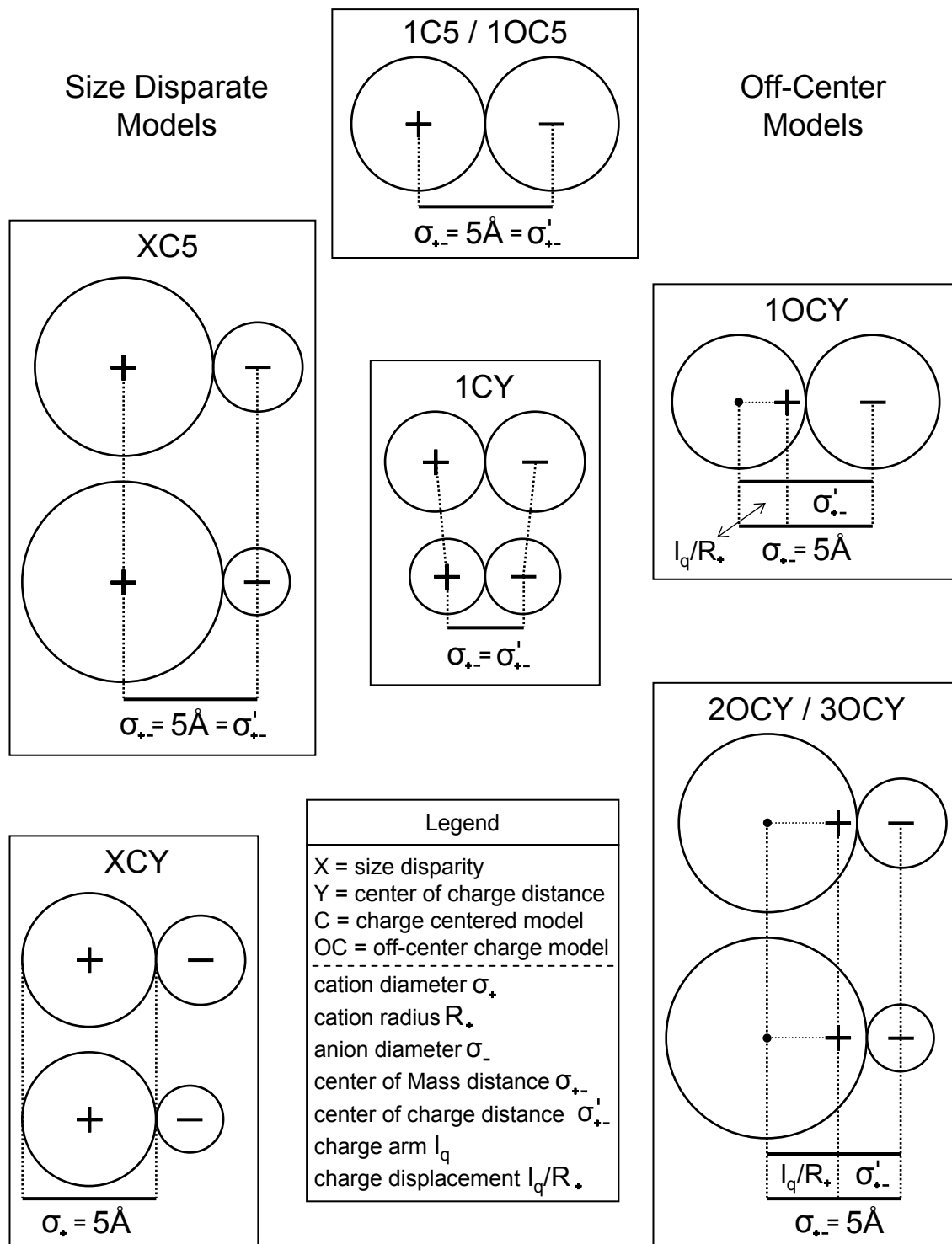


Figure 1.4: Schematic overview of all simulation models. We label the charge-centered and charge-off-center models “XCY” and “XOCY”, where $X = \sigma_+/\sigma_-$ indicates the size disparity, and $Y = \sigma'_{+-}$ (in \AA) is the minimum distance between the cation and anion charges.

Bibliography

- [1] M. Smiglak, A. Metlen and R. Rogers, *Acc. Chem. Res.* **40**, 1182 (2007).
- [2] H. Ohno and K. Fukumoto, *Acc. Chem. Res.* **40**, 1122 (2007).
- [3] Y. Y. Jiang, G. N. Wang, Z. Zhou, Y. T. Wu, J. Geng and Z. B. Zhang, *Chem. Commun.* **4**, 505 (2008).
- [4] Z. Fei, T. J. Geldbach, D. Zhao and P. J. Dyson, *Chem. Eur. J.* **12**, 2122 (2006) and references therein.
- [5] H. Olivier-Bourbigou and L. Magna, *J. Mol. Catal. A* **182-183**, 419 (2002).
- [6] P. Wasserscheid and W. Keim, *Angewandte Chemie - International Edition* **39**, 3772 (2000) and references therein.
- [7] J.F. Liu, J. A. Jönsson and G. B. Jiang, *Trends Anal. Chem.* **24**, 20 (2005).
- [8] M. Buzzeo, R. Evans and R. G. Compton, *Chemphyschem* **5**, 1106 (2004) and references therein.
- [9] M. Galinski, A. Lewandowski and I. Stepniak, *Electrochim. Acta* **51**, 5567 (2006) and references therein.
- [10] S. Z. El Abedin and F. Endres, *Acc. Chem. Res.* **40**, 2101 (2007).
- [11] J. F. Wishart, *Energy Environ. Sci.* **2**, 956 (2009) and references therein.
- [12] H. Ohno and Y. Fukaya, *Chem. Lett.* **38**, 2 (2009).
- [13] C. J. Raa, K. A. Venkatesana, K. Nagarajana, T. G. Srinivasan and P. R. V. Rao, *Electrochim. Acta* **53**, 1911 (2007).
- [14] I. Minami, *Molecules* **14**, 6, 2286 (2009).
- [15] M. D. Bermudez, A. E. Jimenez, J. Sanes and F. J. Carrion, *Molecules* **14**, 8, 2888 (2009).
- [16] <http://www.basf.com/group/corporate/en/innovations/innovation-award/2004/basil>
- [17] H. Shirota and E. W. Castner Jr., *J. Phys. Chem. A* **109**, 42, 9388 (2005).
- [18] S. Tsuzuki, H. Tokuda, K. Hayamizu and M. Watanabe, *J. Phys. Chem. B* **109**, 16474 (2005).
- [19] C. A. Angell, N. Byrne and J. P. Belieres, *Acc. Chem. Res.* **40**, 1228 (2007).

- [20] T. Kakiuchi, *Anal. Sci.* **24**, 1221 (2008).
- [21] C. F. Poole, *J. Chromatogr. A* **1037**, 49 (2004) and references therein.
- [22] P. Bonhôte, A. Dias, N. Papageorgiou, K. Kalyanasundaram and M. Grätzel, *Inorg. Chem.* **35**, 5, 1168 (1996) and references therein.
- [23] K. R. Seddon, A. Stark and M.-J. Torres, *Pure Appl. Chem.* **72**, 12, 2275 (2000).
- [24] J. Ranke, S. Stolte, R. Störmann, J. Arning and B. Jastorff, *Chem. Rev.* **107**, 2183 (2007).
- [25] D. Zhao, Y. Liao and Z. Zhang, *Clean* **35**, 1, 42 (2007).
- [26] S. Stolte, M. Matzke, J. Arning, A. Bösch, W. R. Pitner, U. Welz-Biermann, B. Jastorff and J. Ranke, *Green Chemistry* **9**, 1170 (2007).
- [27] B. Wu, W. W. Liu, Y. M. Zhang and H. P. Wang, *Chem. Eur. J.* **15**, 1804 (2009).
- [28] H. Tokuda, K. Hayamizy, K. Ishii, A. Susan and M. Watanabe, *J. Phys. Chem. B* **109**, 6103 (2005).
- [29] W. A. Henderson, V. G. Young Jr., W. Pearson, S. Passerini, H. C. DeLong and P. C. Trulove, *J. Phys.: Condens. Matter* **18**, 10377 (2006).
- [30] J. E. Gordon and G. N. SubbaRao, *J. Am. Chem. Soc.* **100**, 24, 7445 (1978).
- [31] P. Hunt, *J. Phys. Chem. B* **111**, 4844 (2007) and references therein.
- [32] S. Zahn, G. Bruns, J. Thar and B. Kirchner, *Phys. Chem. Chem. Phys.* **10**, 6921 (2008).
- [33] C. A. Angell, *J. Phys. Chem. Solids* **49**, 863 (1988).
- [34] W. Xu, E. I. Cooper and C. A. Angell, *J. Phys. Chem. B* **107**, 6170 (2003).
- [35] J. P. Belieres and C. A. Angell, *J. Phys. Chem. B* **111**, 4926 (2007).
- [36] J. Crosthwaite, M. Muldoon, J. Dixon, J. Anderson and J. Brennecke, *J. Chem. Thermodynamics* **37**, 559 (2005).
- [37] E. W. Castner Jr., J. F. Wishart and H. Shirota, *Acc. Chem. Res.* **40**, 1217 (2007) and references therein.
- [38] K. Fumino, A. Wulf and R. Ludwig, *Angew. Chem. Int. Ed.* **47**, 8731 (2008).
- [39] P. Hapiot and C. Lagrost, *Chem. Rev.* **108**, 2238 (2008).
- [40] F. Endres and S. Z. El Abedin, *Phys.Chem.Chem.Phys.* **8**, 2101 (2006).
- [41] K. J. Fraser, E. I. Izgorodina, M. Forsyth, J. L. Scott and D. R. MacFarlane, *Chem. Commun.*, 3817 (2009).
- [42] M. N. Kobra, *Adv. Chem. Phys.* **139**, 83 (2008) and references therein.

- [43] H. Weingärtner, *Angew. Chem. Int. Ed.* **47**, 654 (2008) and references therein.
- [44] J. Dupont and P. A. Z. Suarez, *Phys. Chem. Chem. Phys.* **8**, 2441 (2006).
- [45] C. Chiappe, M. Malvaldi and C. S. Pomelli, *Pure Appl. Chem.* **81**, 4, 767 (2009).
- [46] J. L. Anderson, J. Ding, T. Welton and D. W. Armstrong, *J. Am. Soc.* **124**, 14247 (2002).
- [47] J. Luczak, J. Hupka, J. Thöming and C. Jungnickel, *Colloids and Surfaces A: Physicochem. Eng. Aspects* **329**, 125 (2008).
- [48] A. Triolo, O. Russina, H. J. Bleif and E. Di Cola, *J. Phys. Chem. B* **111**, 4641 (2007).
- [49] C. Chiappe, *Monatsh. Chem.* **138**, 1035 (2007).
- [50] J. Dupont, *J. Braz. Chem. Soc.* **15**, 341 (2004).
- [51] P. Nockemann, K. Binnemans, B. Thijs, T. N. Parac-Vogt, K. Merz, A. W. Mudring, P. C. Menon, R. N. Rajesh, G. Cordoyiannis, J. Thoen, J. Leys and C. Glorieux, *J. Phys. Chem. B* **113**, 1429 (2009).
- [52] J. Widegren, E. Saurer, K. Marsh and J. Magee, *J. Chem. Thermodynamics* **37**, 6, 569 (2005).
- [53] A. Heintz, *J. Chem. Thermodynamics* **37**, 6, 525 (2005).
- [54] C. Cadena, J. L. Anthony, J. K. Shah, T. I. Morrow, J. F. Brennecke and E. J. Maginn, *J. Am. Chem. Soc.* **126**, 5300 (2004).
- [55] P. A. Hunt, *Mol. Simul.* **32**, 1, 1 (2006).
- [56] R. M. Lynden-Bell, M. G. Del Popolo, T. G. A. Youngs, J. Kohanoff, C. G. Hanke, J. B. Harper and C. C. Pinilla, *Acc. Chem. Res.* **40**, 1138 (2007).
- [57] E. J. Maginn, *Acc. Chem. Res.* **40**, 1200 (2007).
- [58] T. Yan, C. J. Burnham, M. G. Del Popolo and G. A. Voth, *J. Phys. Chem. B* **108**, 11877 (2004).
- [59] T. Yan, S. Li, W. Jiang, X. Gao, B. Xiang and G. A. Voth, *J. Phys. Chem. B* **110**, 1800 (2006).
- [60] E. A. Turner, C. C. Pye and R. D. Singer, *J. Phys. Chem. A* **107**, 2277 (2003).
- [61] P. A. Hunt, I. R. Gould and B. Kirchner, *Aust. J. Chem. A* **60**, 9 (2007).
- [62] H. Li, M. Ibrahim, I. Agberemi and M. N. Kobrak, *J. Chem. Phys.* **129**, 124507 (2008).
- [63] H. Jin, B. O'Hare, J. Dong, S. Arzhantsev, G. A. Baker, J. F. Wishart, A. J. Benesi and M. Maroncelli, *J. Phys. Chem. B* **112**, 81 (2008).
- [64] R. Katoh, M. Hara and S. Tsuzuki, *J. Phys. Chem. B* **112**, 15426 (2008).

- [65] S. Zahn, F. Uhling, J. Thar, C. Spickermann and B. Kirchner, *Angew. Chem. Int. Ed.* **47** 3639 (2008).
- [66] T. Köddermann, C. Wertz, A. Heintz and R. Ludwig, *ChemPhysChem* **7**, 1944 (2006).
- [67] G. Yu, S. Zhang, G. Zhou, X. Liu and X. Chen, *AIChE* **53**, 12, 3210 (2007).
- [68] M. F. Del Popolo, J. Kohanoff, R. M. Lynden-Bell and C. Pinilla, *Acc. Chem. Res.* **40**, 1156 (2007).
- [69] B. Qiao, C. Krekeler, R. Berger, L. D. Site and C. Holm, *J. Phys. Chem. B* **112**, 1743 (2008).
- [70] M. G. Del Popolo and G. A. Voth, *J. Phys. Chem. B* **108**, 1744 (2004).
- [71] C. Schröder, T. Rudas and O. Steinhauser, *J. Chem. Phys.* **125**, 244506 (2006).
- [72] C. Schröder, T. Rudas, G. Neumayr, W. Gansterer and O. Steinhauser, *J. Chem. Phys.* **127**, 044505 (2007).
- [73] S. M. Urahata and M. C. C. Ribeiro, *J. Chem. Phys.* **120**, 4, 1855 (2004).
- [74] C. J. Margulis, *Mol. Phys.* **102**, 829 (2004).
- [75] J. N. A. C. Lopes and A. A. H. Pádua **110**, 3330 (2006).
- [76] Z. Hu and C. J. Margulis, *Acc. Chem. Res.* **40**, 1097 (2007).
- [77] G. Raabe and J. Köhler, *J. Chem. Phys.* **128**, 154509 (2008).
- [78] T. Köddermann, D. Paschek and R. Ludwig, *Chemphyschem* **9**, 549 (2008).
- [79] J. Picalek and J. Kolafa, *J. Mol. Liq.* **134**, 29 (2007).
- [80] Z. Hu and C. J. Margulis, *J. Phys. Chem. B* **111**, 4705 (2007).
- [81] C. Schröder, M. Haberler and O. Steinhauser, *J. Chem. Phys.* **128**, 134501 (2008).
- [82] B. Bhargava and S. Balasubramanian, *J. Chem. Phys.* **123**, 144505 (2005).
- [83] C. Rey-Castro, A. L. Tormo and L. F. Vega, *Fluid Phase Equilibr.* **256**, 62 (2007).
- [84] M. H. Kowsari, S. Alavi, M. Ashrafizaadeh and B. Najafi, *J. Chem. Phys.* **130**, 014703 (2009).
- [85] O. Borodin and G. Smith, *J. Phys. Chem. B* **110**, 11481 (2006).
- [86] R. M. Lynden-Bell and T. G. A. Youngs, *Mol. Sim.* **32**, 1025 (2006).
- [87] C. Schröder and O. Steinhauser, *J. Chem. Phys.* **128**, 224508 (2008).
- [88] S. M. Urahata and M. C. C. Ribeiro, *J. Chem. Phys.* **122**, 024511 (2004).
- [89] C. Rey-Castro and L. F. Vega, *J. Phys. Chem B* **110**, 14426 (2006).

- [90] M. H. Kowsari, S. Alavi, M. Ashrafizaadeh and B. Najafi, *J. Chem. Phys.* **129**, 224508 (2008).
- [91] H. A. Every, A. G. Bishop, D. R. MacFarlane, G. Orädd and M. Forsyth, *Phys. Chem. Chem. Phys.* **6**, 1758 (2004).
- [92] G. D. Smith, O. Borodin, L. Li, H. Kim, Q. Liu, J. E. Bara, D. L. Gin and R. Nobel, *Phys. Chem. Chem. Phys.* **10**, 6301 (2008).
- [93] R. M. Lynden-Bell, *Mol. Phys.* **101**, 2625 (2003).
- [94] R. M. Lynden-Bell, J. Kohanoff and M. F. Del Popolo, *Faraday Discuss.* **129**, 57 (2004).
- [95] M. Gonzalez-Melchior, F. Bresme and J. Alexandre, *J. Chem. Phys.* **122**, 104710 (2005).
- [96] A. Chaumont, R. Schurhammer and G. Wipff, *J. Phys. Chem. B* **109**, 18964 (2005).
- [97] B. L. Bhargava and S. Balasubramanian, *J. Am. Chem. Soc.* **128**, 10073 (2006).
- [98] N. Sieffert and G. Wipff, *J. Phys. Chem. B* **110**, 26, 13076 (2006).
- [99] C. Pinilla, M. G. Del Popolo, J. Kohanoff and R. M. Lynden-Bell, *J. Phys. Chem. B* **111**, 4877 (2007).
- [100] B. L. Bhargava and M. L. Klein, *J. Phys. Chem. A* **113**, 1898 (2009).
- [101] A. A. Kornyshev, *J. Phys. Chem. B* **111**, 5545 (2007).
- [102] S. K. Reed, P. A. Madden and A. Papadopoulos, *J. Chem. Phys.* **128**, 124701 (2008).
- [103] G. Raabe and J. Köhler, *J. Chem. Phys.* **129**, 144503 (2008).
- [104] M. N. Kobrak and V. Znamenskiy, *Chem. Phys. Lett.* **395**, 127 (2004).
- [105] Y. Shim, M. Y. Choi and H. J. Kim, *J. Chem. Phys.* **122**, 044510 (2005).
- [106] Y. Shim, M. Y. Choi and H. J. Kim, *J. Chem. Phys.* **122**, 044511 (2005).
- [107] M. N. Kobrak, *J. Chem. Phys.* **125**, 064502 (2006).
- [108] A. A. H. Padua, M. F. Costa Gomes and J. N. A. Canongia Lopes, *Acc. Chem. Res.* **40**, 1087 (2007).
- [109] M. N. Kobrak, *J. Phys. Chem. B* **111**, 4755 (2007).
- [110] C. G. Hanke and R. M. Lynden-Bell **107**, 10873 (2003).
- [111] M. S. Kelkar and E. J. Maginn, *J. Phys. Chem. B* **111**, 4867 (2007).
- [112] M. Moreno, F. Castiglione, A. Mele, C. Pasqui and G. Raos, *J. Phys. Chem. B* **112**, 7826 (2008).

- [113] A. R. Porter, S. Y Liem and P. L. A. Popelier, *Phys. Chem. Chem. Phys.* **10**, 4240 (2008).
- [114] C. G. Hanke, N. A. Atamas and R. M. Lynden-Bell, *Green Chemistry* **4**, 107 (2002).
- [115] W. Jiang, Y. Wang and G. A. Voth, *J. Phys. Chem. B* **111**, 4812 (2007).
- [116] C. Schröder, T. Rudas, G. Neumayr, S. Benkner and O. Steinhauser, *J. Chem. Phys.* **127**, 234503 (2007).
- [117] S. Jahangiri, M. Taghikhani, H. Behnejad and S. J. Ahmadi, *Mol. Phys.* **106**, 8, 1015 (2008).
- [118] Y. Danten, M. I. Cabaco and M. Besnard, *J. Phys. Chem. A* **113**, 2873 (2009).
- [119] B. L. Bhargava and M. L. Klein, *J. Phys. Chem. B* **113**, 9499 (2009).
- [120] C. G. Hanke, A. Johansson, J. B. Harper and R. M. Lynden-Bell, *Chem. Phys. Lett.* **374**, 85 (2002).
- [121] J. B. Harper and R. M. Lynden-Bell, *Mol. Phys.* **102**, 85 (2004).
- [122] M. G. Del Popolo, C. L. Mullan, J. D. Holbrey, C. Hardacre and P. Ballone, *J. Am. Chem. Soc.* **130**, 7032 (2008).
- [123] X. P. Wu, Z. P. Liu, S. P. Huang and W. C. Wang, *Phys. Chem. Chem. Phys.* **7**, 2771 (2005).
- [124] J. Deschamps, M. F. Costa Gomes and A. A. H. Pádua *ChemPhysChem* **5**, 1049 (2004).
- [125] W. Shi and E. J. Maginn, *J. Phys. Chem. B* **112**, 16710 (2008).
- [126] K. E. Gutowski and E. J. Maginn, *J. Am. Chem. Soc.* **130**, 14690 (2008).
- [127] W. Shi and E. J. Maginn, *J. Phys. Chem. B* **112**, 2045 (2008).
- [128] S. O. Nielsen, C. F. Lopez, G. Srinivas and M. L. Klein, *J. Phys.: Condens. Matter* **16**, 481 (2004).
- [129] B. L. Bhargava, S. Balasubramanian and M. L. Klein, *Chem. Commun.*, 3339 (2008).
- [130] Y. Wang and G. A. Voth, *J. Am. Chem. Soc.* **127**, 12192 (2005).
- [131] Y. Wang, S. Izvekov, T. Yan and G. A. Voth, *J. Phys. Chem. B* **110**, 3564 (2006).
- [132] Y. Wang, W. Jiang, T. Yan and G. A. Voth, *Acc. Chem. Res.* **40**, 1193 (2007).
- [133] B. L. Bhargava, R. Devane, M. L. Klein and S. Balasubramanian, *Soft Matter* **3**, 11, 1395 (2007).
- [134] B. L. Bhargava and M. L. Klein, *Mol. Phys.* **107**, 4-6, 393 (2009).
- [135] W. Jiang, Y.T. Wang, T.Y. Yan and G. A. Voth, *J. Phys. Chem. C* **112**, 4, 1132 (2008).

- [136] J. W. Daily and M. M. Micci, *J. Chem. Phys.* **131**, 9, 094501 (2009).
- [137] M. N. KobraK and N. Sandalow, in *Molten Salts XIV* (The Electrochemical Society, Pennington, NJ, 2006).

Chapter 2

Structural and Dynamical Properties of Ionic Liquids: The Influence of Ion Size Disparity

*

2.1 Introduction

Ionic liquids range from molten salts, consisting of simple inorganic ions, to room temperature ionic liquids, which are composed of large organic cations, for example, quaternary amines, imidazoles or other heterocyclic molecules and organic or inorganic anions [1–3]. There are many possibilities of assembling ionic liquids due to the variety of ions and the variations in side chains of the ions. Room temperature ionic liquids are of importance for two reasons. Firstly, they have very different properties than common organic solvents and therefore are used as alternate solvents in chemical reactions. Secondly, they have the advantage of flexibility, because the solvent properties can be adjusted by altering the ionic liquid molecules, for example adding side chains or functional groups. Tuning can also be achieved by changing the composition of ionic liquid mixtures.

The variety of ionic liquid building blocks is an advantage, but also brings difficulties for researchers trying to tailor make new ionic liquids. For example, for use in chemical or electrochemical reactions low melting points and viscosities are desired. However, it is difficult to accurately predict ionic liquid properties from the molecular structure. Some insight into ionic liquid properties has been gained. For example, as one would expect, melting points are especially low for ionic liquids that are combinations of large anions and

*A version of this chapter has been published. H. V. Spohr and G. N. Patey, “Structural and Dynamical Properties of Ionic Liquids: The Influence of Ion Size Disparity”, *J. Chem. Phys.* **129**, 064517 (2008).

large cations. Low molecular symmetry is also observed to decrease melting points [4, 5]. Viscosities tend to increase with the introduction of longer side chains and/or hydrogen bonding groups [5, 6]. Furthermore, the viscosity of some room temperature ionic liquids decreases strongly with increasing temperature [5, 6]. However, it is not yet possible to draw a consistent picture that includes all molecular characteristics of ionic liquids.

Our objective is to find and separate the features of ionic liquids that govern their solution properties. In contrast to many simulation studies of ionic liquids, which employ all atom models, we focus on simpler model systems in order to isolate the influences of different molecular traits. In this Chapter we employ molecular dynamics (MD) simulations to investigate the importance of ion size disparity on structural and dynamical properties of ionic liquids. In room temperature ionic liquids the cations are often much larger than the anions. For example, quaternary amines have van der Waals radii of 2.8 Å for the smallest Me_4N^+ , 4.13 Å for Bu_4N^+ and even larger values for longer side chains [7]. Imidazoles and other heterocyclic rings are of the same size or larger. In contrast, the van der Waals radius of the chloride ion is 1.8 Å, the other halogenides and anions such as BF_4^- or PF_6^- have radii of about 2.5 Å or smaller.

Previous investigations aimed at isolating the influence of particle size disparity on structural and dynamical properties of liquids are relatively few. There have been studies of melting in 2D Lennard-Jones (LJ) systems [8, 9], and of structure and dynamics in 3D soft-sphere systems [10]. There have also been MD studies of structure and transport in models of particular molten salts [11–13], but the size-disparity range of these models is very limited, also several parameters are varied simultaneously, making it near impossible to identify specific influences. One recent simulation study has focused on size disparity, investigating a binary mixture of particles having a 5:1 size ratio and interacting through Yukawa potentials [14]. No other size ratio was considered and only structural information was reported. The main finding was that as the temperature was decreased, the large particles first crystallized onto a face-centered-cubic lattice while the small particles remained fluid. The smaller particles crystallized upon further cooling.

Here we report structural and dynamical results for charged LJ particles. The size disparity is varied systematically, while holding other model parameters fixed, so that the influence of particle size disparity can be clearly identified and understood. The temperature dependence of the transport properties is examined, and compared with experiment wherever possible. The remainder of the Chapter is divided into three parts. The model and simulation method are described in Chapter 2.2, the results are presented and discussed in Chapter 2.3, and our conclusions are summarized in Chapter 2.4.

2.2 The Model and Simulation Method

We consider simple model ionic fluids characterized by the pair interaction

$$u(r_{ij}) = 4\epsilon_{ij} \left[\left(\frac{\sigma_{ij}}{r_{ij}} \right)^{12} - \left(\frac{\sigma_{ij}}{r_{ij}} \right)^6 \right] + \frac{q_i q_j}{4\pi\epsilon_0 r_{ij}}, \quad (2.1)$$

where ϵ_{ij} and σ_{ij} are the energy and length parameters of the LJ potential, q_i is the charge of the ion i (all ions are univalent), r_{ij} is the interionic separation, and ϵ_0 is the permittivity of free space. In the MD simulations the LJ potential is truncated and shifted in the usual way to avoid discontinuity [15]. The LJ parameters for cross interactions are calculated according to the Lorentz-Berthelot mixing rules. Periodic boundary conditions are employed and the long-range Coulombic interactions are handled with Ewald sums [16, 17].

We are interested in isolating as far as possible the influence of ion size disparity on the properties of ionic liquids. Therefore, we vary the cation and anion “diameters”, σ_+ and σ_- , while holding as many other variables as possible fixed. To avoid obviously large effects that would come through changing the strong cation-anion attraction, $\sigma_{+-} = (\sigma_+ + \sigma_-)/2$ is held constant. The reduced density, $\rho^* = \rho_+ \sigma_+^3 + \rho_- \sigma_-^3$ (this fixes the packing fraction) is also kept constant by varying the sample volume. The ϵ_{ij} parameters are held fixed and set to the same value, ϵ , for all pair interactions, and the mass is taken to be a constant value for all ions. The values of the parameters employed in our simulations are given in Table 2.1. Note that the $\sigma_+ : \sigma_-$ ratio varies from 1:1 to 5:1 with $\sigma_{+-} = 5 \text{ \AA}$ for all systems. The value of ϵ and the constant mass were selected to be roughly in the range one would

expect for real ionic liquids, given the constraints imposed to better identify the influence of size disparity. Of course, if one wished to model a particular ionic liquid these constraints should be lifted, allowing the choice of more realistic parameters.

Ionic Systems	$\sigma_+(\text{\AA})$	$\sigma_-(\text{\AA})$	$U(kJ/mol)$	$P(bar)$
1 : 1	5.000	5.000	-445	-1679
2 : 1	6.667	3.333	-432	-1529
3 : 1	7.500	2.500	-415	-1121
4 : 1	8.000	2.000	-404	-881
5 : 1	8.333	1.667	-396	-740
LJ Systems	$\sigma_L(\text{\AA})$	$\sigma_S(\text{\AA})$	$U(kJ/mol)$	$P(bar)$
1 : 1	5.000	5.000	-27.7	3612
2 : 1	6.667	3.333	-25.1	2329
3 : 1	7.500	2.500	-22.7	1573
4 : 1	8.000	2.000	-21.5	1266
5 : 1	8.333	1.667	-20.6	1091

Table 2.1: σ_i is the LJ length parameter, U is the average configurational energy (standard deviation $< 0.6\%$), and P the average pressure (standard deviation $< 0.5\%$). Also, in all simulations, $\epsilon = 6 \times 10^{-21}J$, the mass $m = 1.99265 \times 10^{-25}kg$, and the reduced density $\rho^* = 0.8$.

Most simulations were carried out with 216 ions in a cubical box of length L , but tests were performed with 512 particles to ensure that our qualitative results were not strongly size dependent. All short-range interactions were truncated at $L/2$, the Ewald inverse-length parameter was set at $6.0/L$, and wavevectors with $k^2 \leq 50$ were included in the Fourier space sum. The equations of motion were integrated using a fifth order Gear predictor-corrector algorithm, with a timestep of 2×10^{-15} seconds. Each system was equilibrated with simple temperature scaling until equilibrium was achieved (usually runs of 2 ns were sufficient). Four production runs each of 2 ns were then carried out under NVT conditions at $1200K$ (unless otherwise specified), employing a Gaussian isokinetic thermostat [18]. Averages collected for each production run were used to estimate standard deviations in the overall averages for the physical properties reported in this Chapter.

For comparison purposes, simulations were also carried out for LJ fluids obtained by simply removing the ionic charges. The cations then become large LJ particles and the

anions smaller ones. Comparing the LJ and ionic liquid results helps reveal the role played by Coulombic interactions.

Diffusion coefficients are obtained employing the Einstein relationship [17]

$$D_\alpha = \frac{1}{6} \lim_{t \rightarrow \infty} \frac{d}{dt} \langle |\mathbf{r}_\alpha(0) - \mathbf{r}_\alpha(t)|^2 \rangle , \quad (2.2)$$

where $\mathbf{r}_\alpha(t)$ is the position vector of an ion of species α .

The shear viscosity η is given by the Green-Kubo relation [17, 19]

$$\eta = \frac{V}{k_B T} \int_0^\infty \langle P_{lk}(0) P_{lk}(t) \rangle dt , \quad (2.3)$$

where V is the volume, T the temperature, and k_B the Boltzmann constant. P_{lk} denotes an off-diagonal element ($l \neq k$) of the pressure tensor defined by

$$P_{lk}(t) = \frac{1}{V} \left(\sum_i v_{il}(t) v_{ik}(t) m_i + \sum_i r_{il}(t) F_{ik}(t) \right) , \quad (2.4)$$

where the summation on i is over all particles in the simulation cell and v_{il} , F_{il} and r_{il} denote the l components of the velocity, force, and position of particle i . In calculating the elements of the pressure tensor for Coulombic systems, care must be taken with the Fourier space contribution occurring in the Ewald sums. This requires special treatment of the Fourier space contribution to the forces as described by Heyes [20] and others [12]. We note that the average pressure, P , is obtained from the diagonal elements of the pressure tensor

$$P = \frac{1}{3} \sum_l \langle P_{ll} \rangle , \quad (2.5)$$

where the sum on l is over x , y , and z .

The static electrical conductivity is given by

$$\sigma_{el} = \frac{1}{3k_B T V} \int_0^\infty \langle \mathbf{J}(0) \cdot \mathbf{J}(t) \rangle dt , \quad (2.6)$$

where

$$\mathbf{J}(t) = \sum_{i=1}^N q_i \mathbf{v}_i(t) , \quad (2.7)$$

is the current.

2.3 Results and Discussion

Chapter 2.3 is divided into three parts. We first consider structural and thermodynamic aspects followed by a discussion of transport properties. Finally, we compare the temperature dependence of the transport properties to experimental observations.

2.3.1 Structural and Thermodynamic Properties

Ion-Ion radial distribution functions are given in Fig. 2.1, and, for comparison purposes, functions for corresponding LJ fluids are plotted in Fig. 2.2. In the cation-anion radial distribution functions the first peak is at the same distance for all systems. This is mainly due to the constraint that σ_{+-} has the same value for all systems considered. The peak height increases slightly from 4.4 for the 1:1 and 2:1 systems up to 4.9 for the 5:1 case. This small effect likely arises because as the size disparity increases anions can more readily approach the cation without hindering each other. The attractive Coulombic interactions reinforce the effect of constant σ_{+-} , pulling oppositely charged ions together as close as the repulsive core interactions allow. In the LJ system (Fig. 2.2) the first peak shifts to slightly longer distances and becomes broader reflecting the absence of strong attractive Coulombic interactions.

The first peak of the cation-cation radial distribution function is shifted to larger distances for more size disparate systems. The peak position is 6.8 Å for the 1:1 system and 8.8 Å for the 5:1 case. Also, the peaks increase in height and become narrower. In the LJ system the first peak of the large-large distribution function also shifts to larger distances from 5 Å for 1:1 to 8.8 Å for 5:1. The peak positions shift roughly in accordance with the LJ distance parameters ($\sigma_{++}(1:1) = 5$ Å, $\sigma_{++}(5:1) = 8.3$ Å). Comparing corresponding ionic and LJ fluid results, we note that the position of the first peak for the large LJ particles is

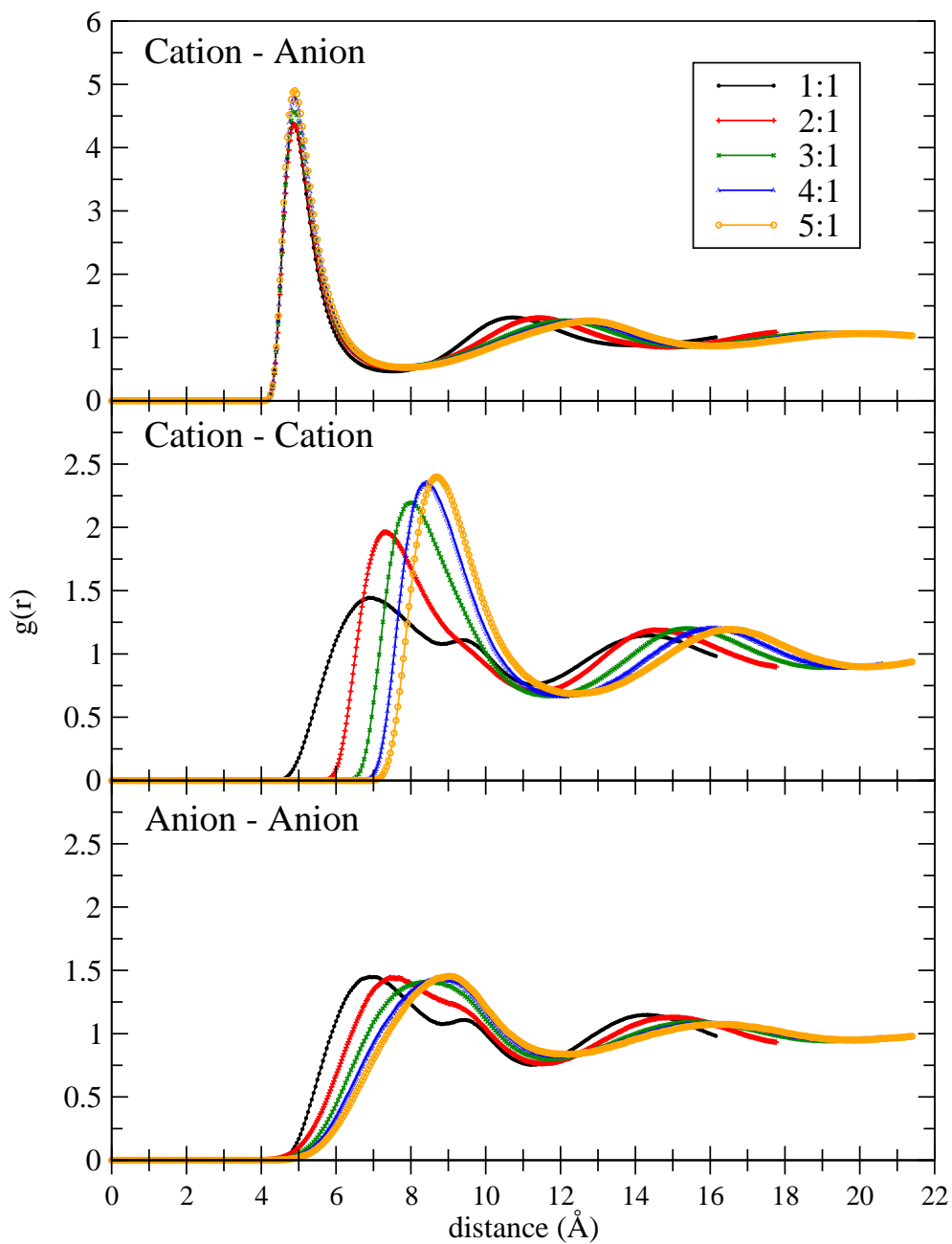


Figure 2.1: Radial distribution functions of ionic systems of different size disparity.

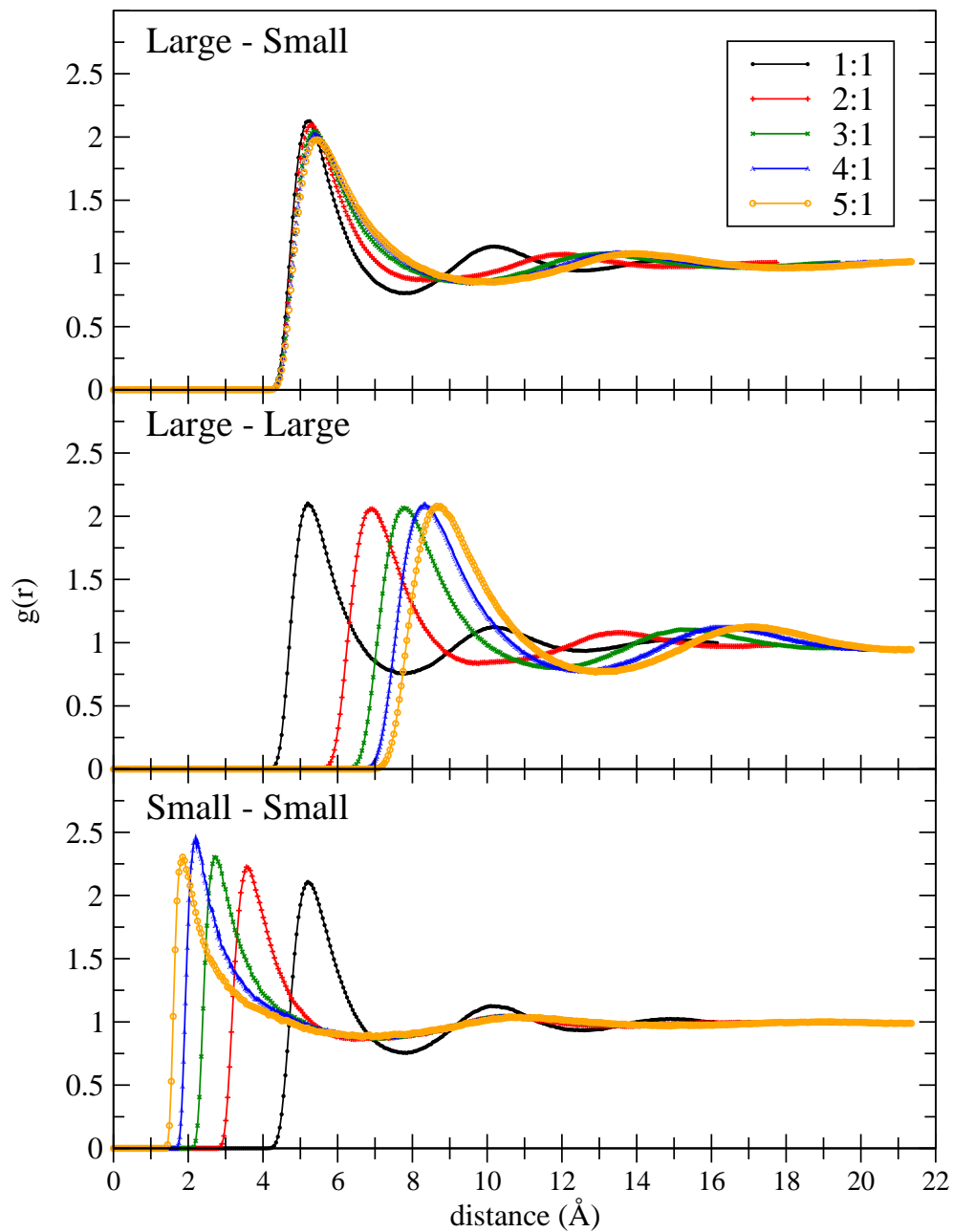


Figure 2.2: Radial distribution functions of LJ systems of different size disparity.

much smaller than that between cations (5 Å vs. 6.8 Å) in the 1:1 system, but essentially the same for the 5:1 case (8.8 Å). The smaller cations in the 1:1 and 2:1 systems have strong repulsive Coulombic interactions that push the cations apart, whereas the large LJ particles of the corresponding systems do not. For the larger cations the Coulombic interactions are less important and the core repulsions dominate. Therefore the peak position for the large cations is the same as that of the corresponding LJ particles. We do note that the height of the first peak in the cation-cation function increases with increasing size disparity, and actually exceeds that of the corresponding LJ function for size disparities of 3:1 and larger. This is somewhat unexpected due to the Coulombic repulsion, and clearly reflects the importance of anion-cation correlations in these strongly coupled systems.

In contrast with the cation-cation case, the anion-anion radial distribution functions display a trend opposite that of the small LJ particles. For the small-small distribution functions the first peak shifts to shorter distances with increasing size disparity, whereas the first peak of the anion-anion distribution function shifts to longer distances, displaying the same trend as the cation-cation radial distribution function. This suggests that the anion-anion distributions are strongly influenced by anion-cation correlations, with the direct anion-anion interactions playing a more minor role. The diffusion coefficients discussed in Chapter 2.3.2 also indicate strong anion-cation coupling.

In this regard, it is interesting to consider the radial charge distribution function [21]

$$Q(r) = Q_+(r) + Q_-(r) = \rho [g_{++}(r) + g_{--}(r) - 2g_{+-}(r)] , \quad (2.8)$$

where $\rho = \rho_+ = \rho_-$. Following Ref. [21] we plot the function $rQ(r)$ in Fig. 2.3. We note that for all liquids considered, this function displays the exponentially screened oscillatory decay characteristic of *strongly-coupled* ionic systems, with significant charge ordering. The screening length varies from ~ 27.4 Å for the 1:1 case to ~ 18.7 Å for 5:1. Thus, screening becomes more effective with increasing size disparity.

The average potential energies and pressures are given in Table 2.1. The energy varies smoothly from -445 kJ/mol for the 1:1 system to -396 kJ/mol for 5:1. We note that an

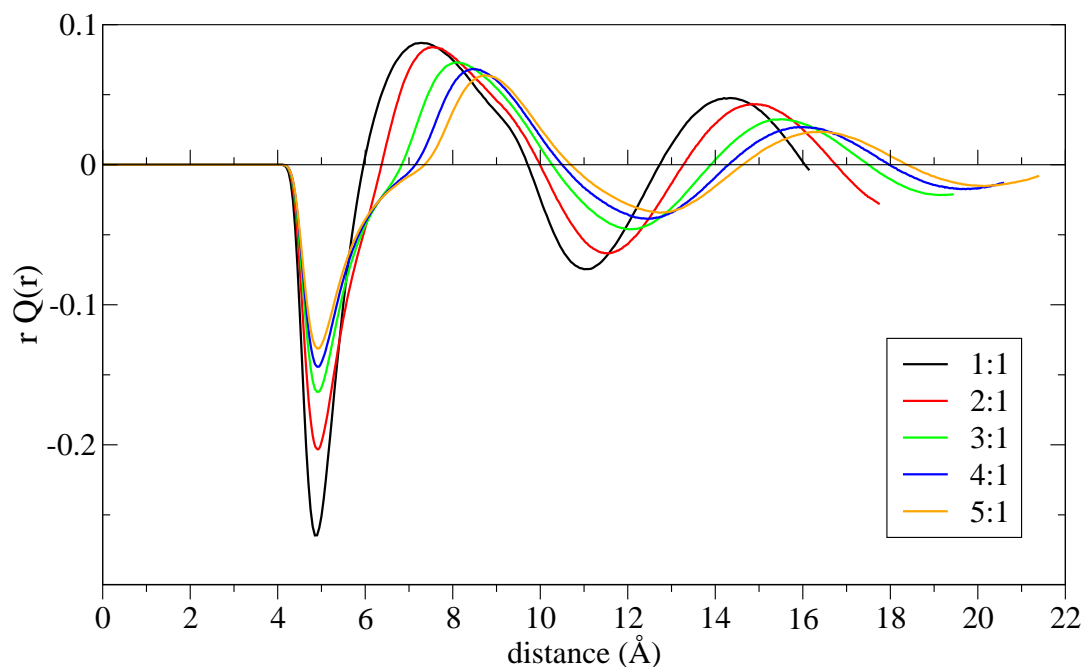


Figure 2.3: Radial charge distribution functions of systems of different size disparity, plotted as $rQ(r)$.

increase in energy with size disparity is also found for the LJ fluid, although the magnitude of the energy is much smaller in the LJ case. For the ionic fluids, the pressure increases from the 1:1 to the 5:1 system (see Table 2.1), whereas a continuous decrease occurs for LJ systems. Clearly, in the ionic systems the variation of pressure with size disparity appears to be dominated by increasing Coulombic repulsion.

2.3.2 Transport Properties

Viscosity and viscosity variation with size disparity is of interest for ionic liquids. We calculate the viscosity employing Eq. (2.3). The pressure tensor autocorrelation functions and their integrals as a function of the upper limit time, t_{UL} , are shown in Fig. 2.4. The viscosity is obtained in the $t_{UL} \rightarrow \infty$ limit. All viscosities are plotted in Fig. 2.5. It can be seen that the viscosities decrease with increasing size disparity. The viscosities decrease strongly from 1:1 to 2:1 to 3:1, then the rate of decrease diminishes, and by 5:1 the

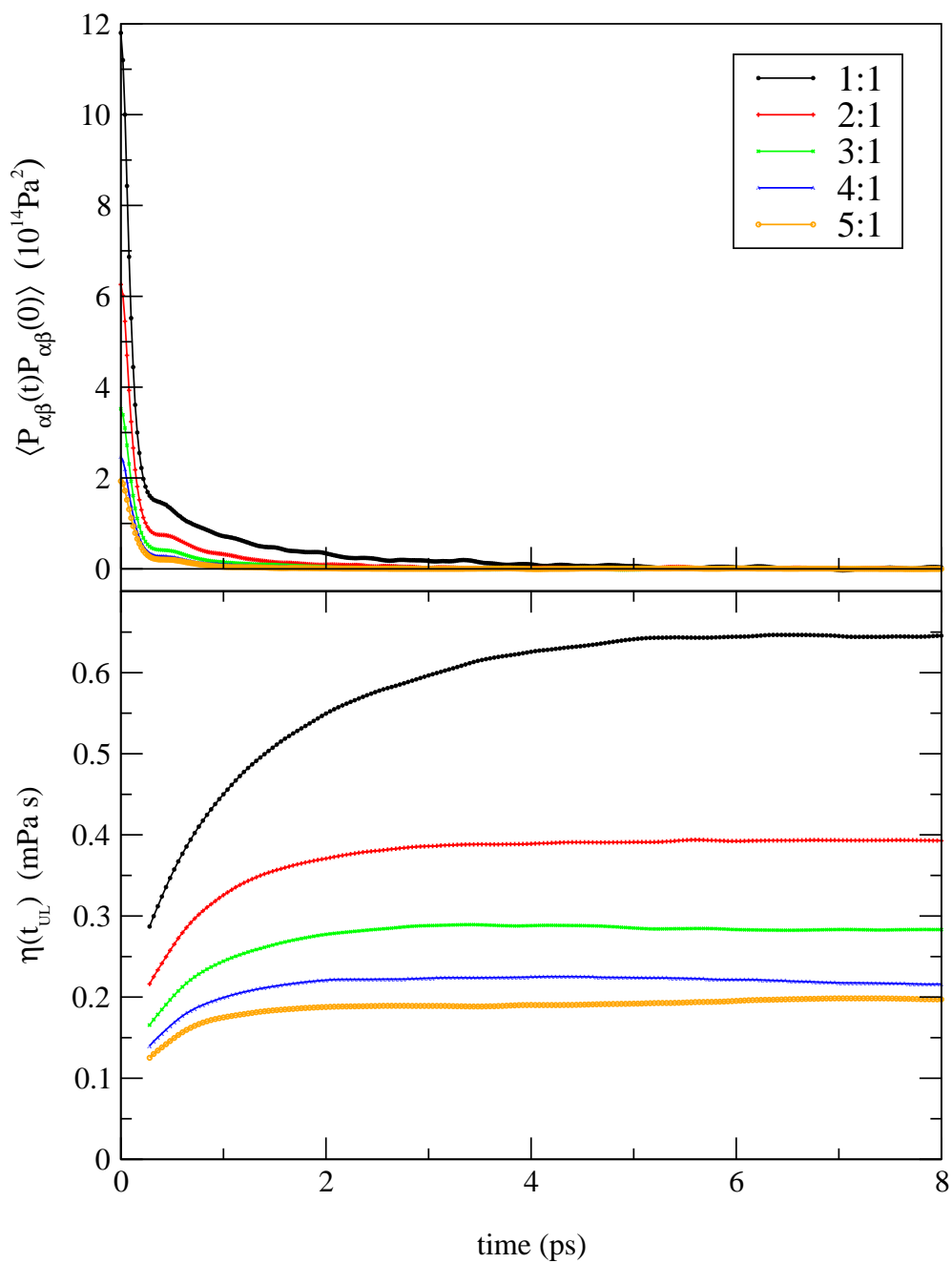


Figure 2.4: Top: Off-diagonal pressure tensor autocorrelation functions for ionic fluids of different size disparity. Bottom: Viscosities as functions of the upper limit, t_{UL} , used in the numerical integration of the autocorrelation functions shown above.

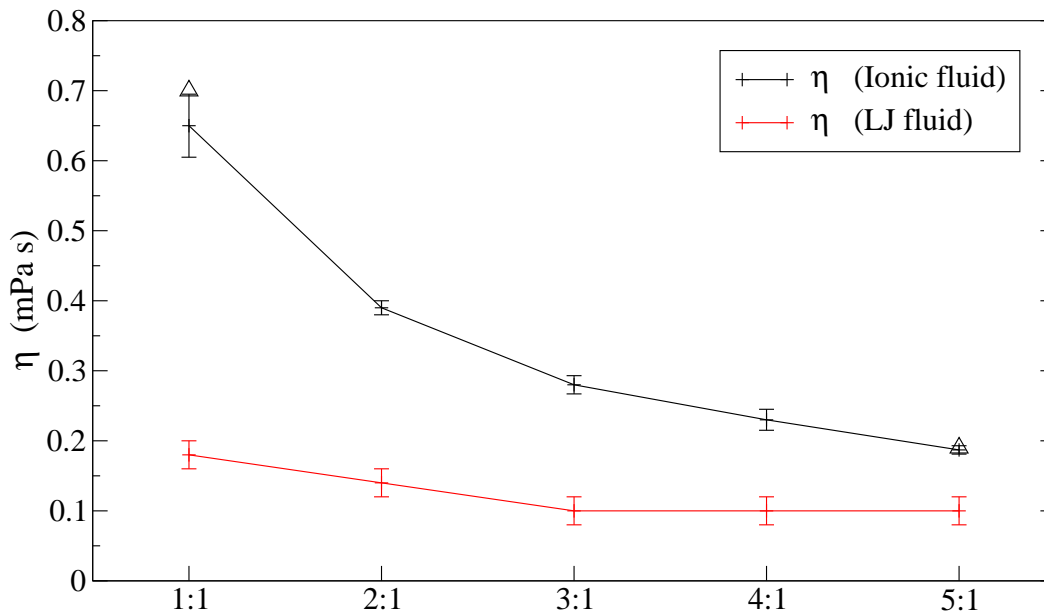


Figure 2.5: Viscosities for ionic and LJ fluids as functions of size disparity. The triangles represent results obtained with 512 ions. The error bars indicate one standard deviation.

viscosity appears to be approaching a limiting value. The viscosities of the LJ system are approximately three times smaller, but also decrease with increasing size disparity. Thus, size disparity decreases viscosity for fluids with or without charges, but the decrease is stronger in charged systems. Results obtained with 512 ions are included in Fig. 2.5 for 1:1 and 5:1 systems. We note that the same trend is evident and, if anything, the 216 particle system underestimates the decrease in viscosity with increasing size disparity.

The diffusion coefficients obtained from the mean square displacement through Eq. (2.2) are shown in Fig. 2.6. Ionic fluid results are displayed on top, those for the LJ system on the bottom. Some results obtained with 512 ions are included in the figure, and we note that they lie close to the values obtained with 216 particles. For the 1:1 system the diffusion coefficients of the cation and anion are obviously equal. For both ionic and LJ fluids, the diffusion of the small particles is faster than that of the large ones, as one would expect. The diffusion coefficients of both anions and cations increase up to size ratios of 3:1, but there

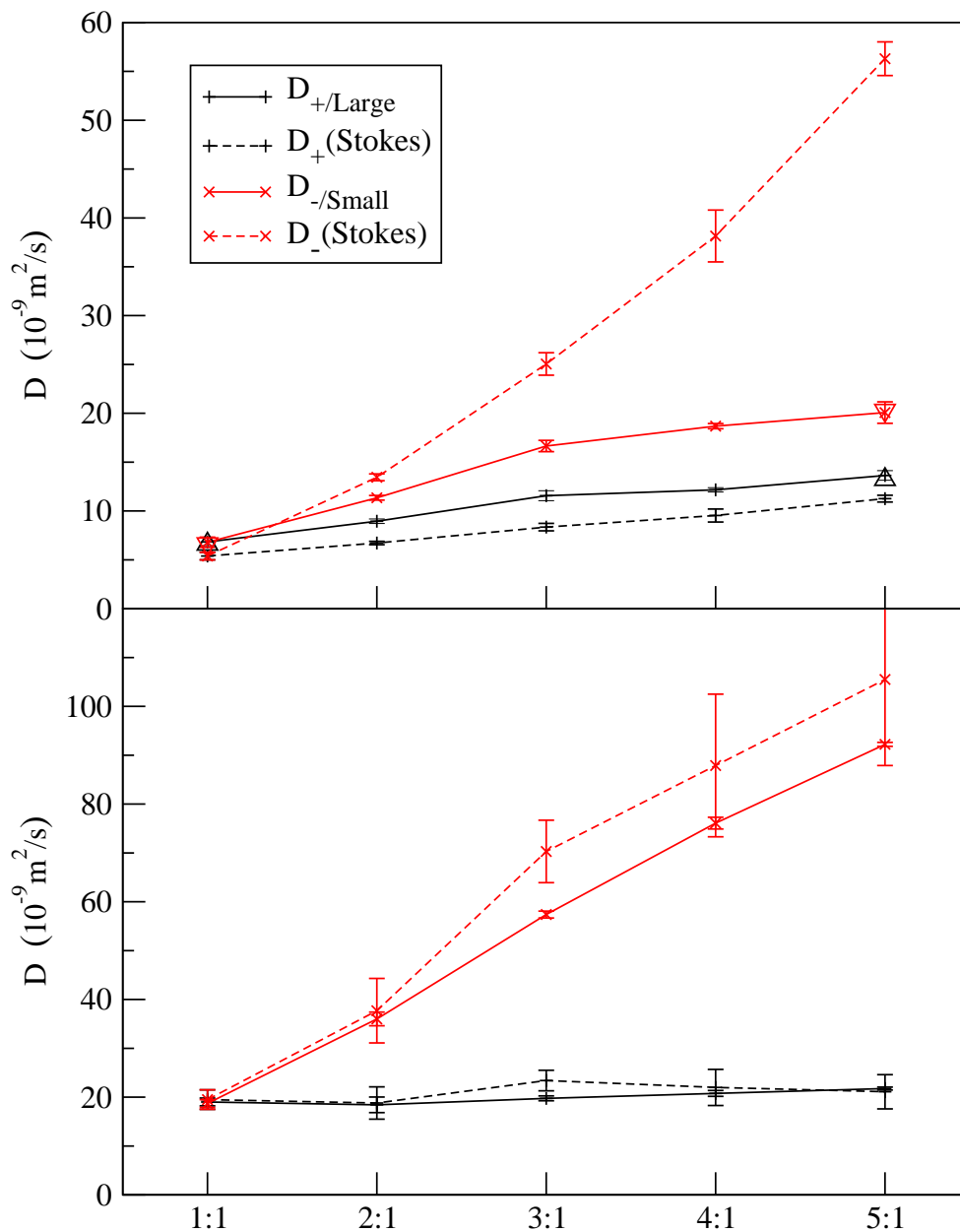


Figure 2.6: Diffusion coefficients as functions of size disparity for ionic (Top) and LJ (Bottom) fluids. The simulation results are compared with diffusion coefficients given by the Stokes-Einstein formula. In the top panel, the symbols, \triangle and ∇ , are the cation and anion values, respectively, obtained with 512 ions. The error bars indicate one standard deviation.

are no substantial variations in diffusion coefficients for more size disparate systems. In contrast, the diffusion coefficients of small LJ particles increase continually with increasing size disparity, while those of large LJ particles remain nearly constant. In the ionic fluid the motion of the positive and negative ions is clearly strongly correlated. This correlation reduces the diffusion for both ionic species relative to the corresponding LJ system, but is particularly important for the smaller anions in fluids with strong size disparity. The strong anion-cation coupling is also evident in the behavior of the anion-anion radial distribution functions, and in the radial charge distribution functions, as described in Chapter 2.3.1.

Further insight can be obtained by examining the diffusion coefficients given by the Stokes-Einstein formula (stick boundary conditions) [19]

$$D_{ST} = \frac{k_B T}{3\pi\eta d_{ST}}, \quad (2.9)$$

where d_{ST} is the Stokes diameter of the particle. In our calculations we take this diameter to be the LJ parameter σ_α . Of course, one could always find “hydrodynamic radii” that compel Eq. (2.9) to yield correct diffusion coefficients, but this is not particularly instructive for the present analysis. Also, the possible applicability of the so-called “fractional” Stokes-Einstein relationship is examined in Chapter 2.3.3 when we discuss the temperature dependence of the transport properties. Comparing the Stokes diffusion coefficients (Fig. 2.6, dashed lines) to those obtained directly from simulations (Fig. 2.6, solid lines), we note that the Stokes equation fails markedly for the small anions of the size-disparate systems. The slope of the Stokes-Einstein diffusion coefficients of the cations is also smaller. In contrast, the Stokes-Einstein formula performs relatively well for the LJ fluid (Fig. 2.6, bottom). This behavior is not unexpected and is again an indication of the strong anion-cation correlations that are not included in the Stokes-Einstein expression. In the LJ system the small-large correlations are not as strong and the Stokes-Einstein results are much improved.

Additional insight into diffusion in the ionic fluids can be obtained from the velocity autocorrelation functions plotted in Fig. 2.7. Of course, estimates of the diffusion coefficients can be obtained by integrating the velocity autocorrelation functions and applying

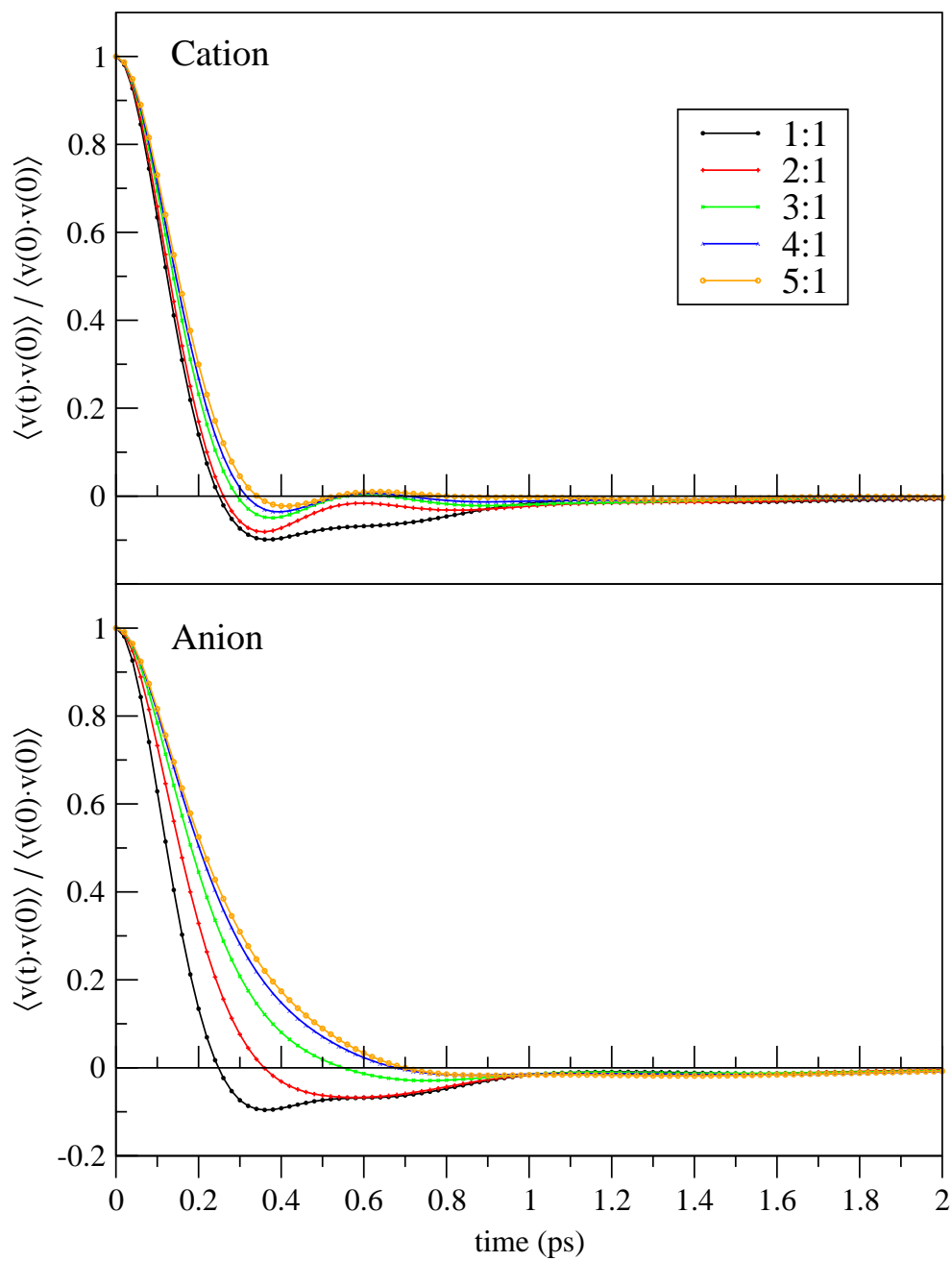


Figure 2.7: Normalized velocity autocorrelation functions for the ionic fluids of different size disparity.

the well-known Green-Kubo relationship [19]. Without making any attempt to treat the expected long-time tails, we find that the diffusion coefficients found this way are about 3% smaller than those given by Eq. (2.2), which is reasonable agreement. The behavior of the velocity autocorrelation functions is obviously consistent with the variation of the diffusion coefficients with size disparity discussed above. Note in particular that for both ionic species the correlation functions cut the time axis at longer times and that the negative portion diminishes in importance as size disparity increases. This gives rise to larger diffusion coefficients.

In many ionic liquids that have been studied experimentally the diffusion coefficients of cations and anions are similar, even though the ions differ markedly in size and mass [23, 24]. This is consistent with our observations for size disparate systems with strong Coulombic coupling. In other ionic liquids, the diffusion coefficient of the larger cation is found to be larger than that of the smaller anion [23, 24]. Our simulations do not provide any explanation of this phenomena, except that its origin appears to lie in factors other than strong coupling.

Another property of interest in ionic liquids is the electrical conductivity given by Eq. (2.7). The current autocorrelation function and $\sigma_{el}(t_{UL})$, where t_{UL} is again the upper limit of integration, are shown in Fig. 2.8. Note, the static conductivity is obtained as $t_{UL} \rightarrow \infty$. It can be seen from Fig. 2.8 (bottom) that the estimated $t_{UL} \rightarrow \infty$ limits are not as certain as those achieved for the viscosities. It is difficult (even with very long MD runs) to obtain sufficiently accurate current autocorrelation functions, and the accuracy of the integral is further compromised by the positive and negative contributions. Nevertheless, a definite trend in the conductivities can be identified, as shown in Fig. 2.9. The conductivity increases from 1:1 to 3:1, and then decreases over the range 3:1 to 5:1.

This behavior can be understood by comparing with Nernst-Einstein conductivities given by the expression [19]

$$\sigma_{NE} = \sum_{\alpha} \frac{\rho_{\alpha} D_{\alpha} q_{\alpha}^2}{k_B T}, \quad (2.10)$$

where $\rho_{\alpha} = N_{\alpha}/V$. From Fig. 2.9 (dashed line), it can be seen that the Nernst-Einstein

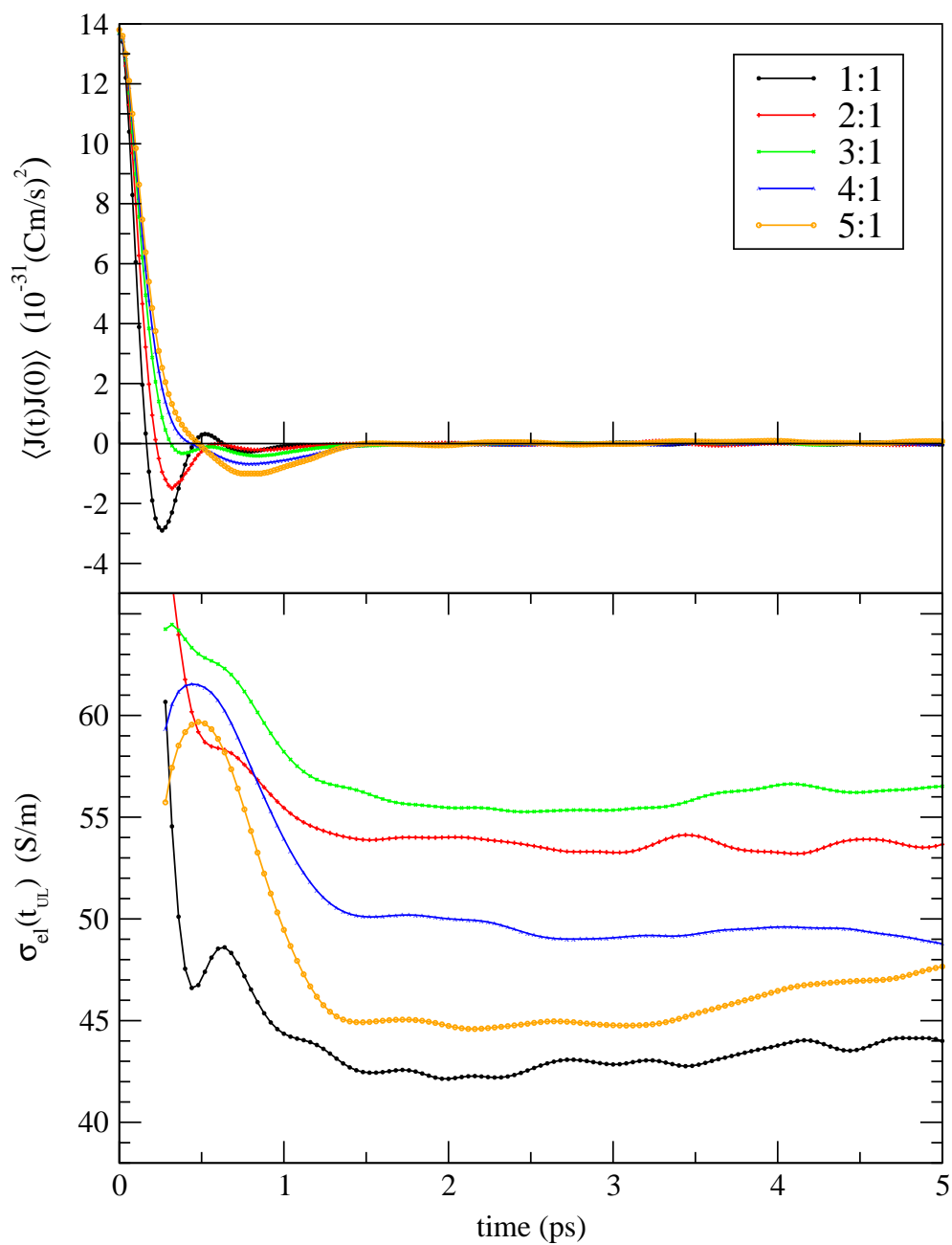


Figure 2.8: Top: Current autocorrelation functions for ionic fluids of different size disparity. Bottom: Conductivities as functions of the upper limit, t_{UL} , used in the numerical integration of the autocorrelation functions shown above.

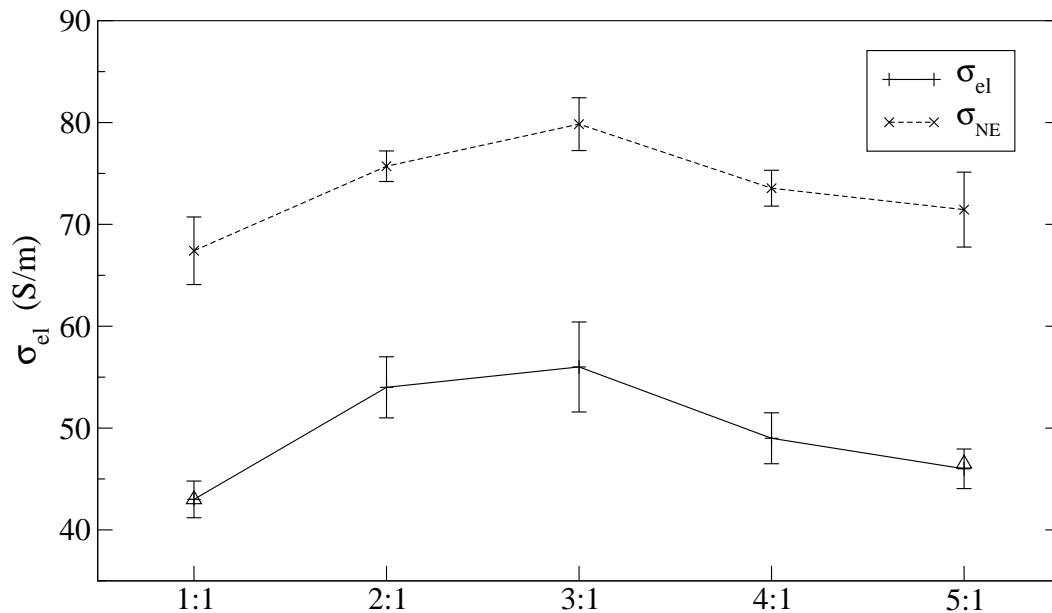


Figure 2.9: Conductivities of ionic fluids as functions of size disparity. Simulation results (solid line) are compared with Nernst-Einstein values (dashed line). The triangles represent results obtained with 512 ions. The error bars indicate one standard deviation.

formula overestimates the conductivity. This is likely because correlations amongst the ions are neglected. Nevertheless, the Nernst-Einstein values show the same trend with changing size disparity. This suggests that the non-monotonic behavior of the conductivity observed in our simulations is not due to ion correlation effects. Considering the Nernst-Einstein equation, we can easily rationalize the trend observed. The Nernst-Einstein formula includes the diffusion coefficients, which increase from 1:1 to 3:1. This results in increasing conductivities over this range of size disparity. The Nernst-Einstein formula also includes the number densities ρ_α of the ions. At constant packing fraction, the number (charge) densities decrease with increasing size disparity. The diffusion coefficients between 3:1 and 5:1 increase very little, whereas the number densities of the ions continue to decrease. This leads to reduced conductivities explaining the shape of the curves in Fig. 2.9.

2.3.3 Temperature Dependence of Transport Properties

The temperature dependence of the transport properties is of interest, and allows qualitative comparison with experiment. Here we focus on the 1:1 and 3:1 systems. The 1:1 system crystallized spontaneously at approximately 800 K into a CsCl structure. The crystallization was signalled by a sharp drop in the configurational and total energy at fixed temperature. The crystal structure could be easily identified in configurational “snapshots”. The 3:1 system was fluid at 800 K, and remained disordered at lower temperatures eventually becoming “glassy” (600 K), at least on simulation time scales. We did not observe any signs of spontaneous crystallization for the 3:1 case.

As expected, the diffusion coefficients and electrical conductivities decrease as the temperature is reduced, and the viscosities increase. The logarithm (base 10) of the diffusion coefficients, viscosities and conductivities are plotted versus $1/T$ in Fig. 2.10. We note that the deviations from linearity (Arrhenius behavior) are most noticeable for the conductivity. The temperature dependence of all three properties is well described by the Vogel-Fulcher-Tammann (VFT) equation

$$A = A_0 \exp\left(\frac{B}{T - T_0}\right), \quad (2.11)$$

where A represents the diffusion coefficient, viscosity or electric conductivity, and A_0 , B , and T_0 are fitting parameters. The fits obtained are shown in Fig. 2.10. We note that the VFT equation gives excellent fits to experimental results for the same transport properties [22–24], although more curvature is observed in the experimental plots.

We have also attempted to fit the diffusion coefficients to the “fractional” Stokes-Einstein expression [25–27]

$$D_\alpha = C \left(\frac{T}{\eta}\right)^\beta, \quad (2.12)$$

where C and β are the fitting parameters. Of course, in the conventional Stokes-Einstein formula $\beta = 1$, but other values have been reported for ionic liquids [26, 27]. The fits obtained for the 1:1 and 3:1 systems are shown in Fig. 2.11, and in all cases we find $\beta \approx 0.8$. This value is in good agreement with the exponents reported by Voronel *et al.*

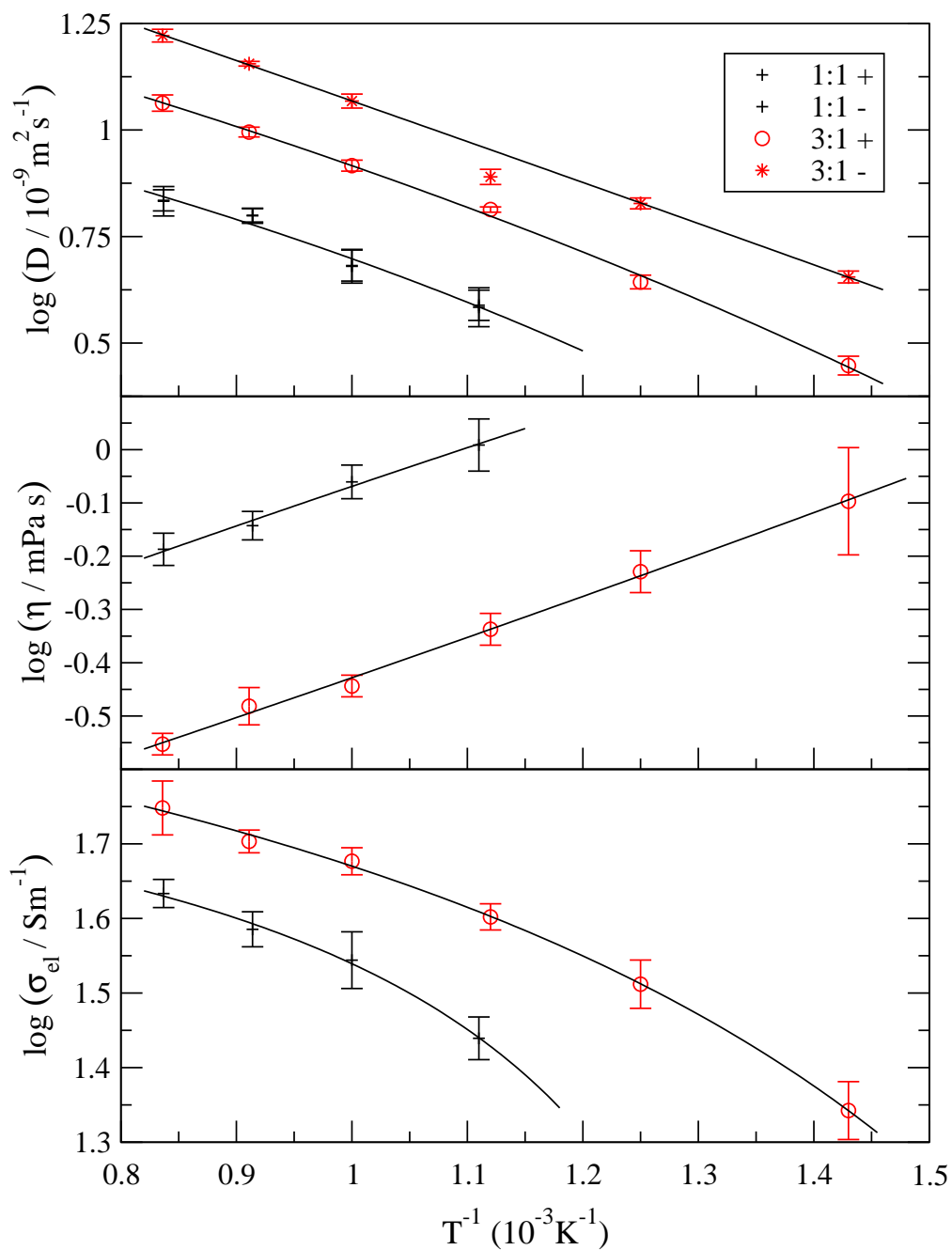


Figure 2.10: Logarithms (base 10) of diffusion coefficients, viscosities and electrical conductivities as functions of $1/T$ for systems 1:1 and 3:1. The solid lines are fits to the VFT equation. The error bars indicate one standard deviation.

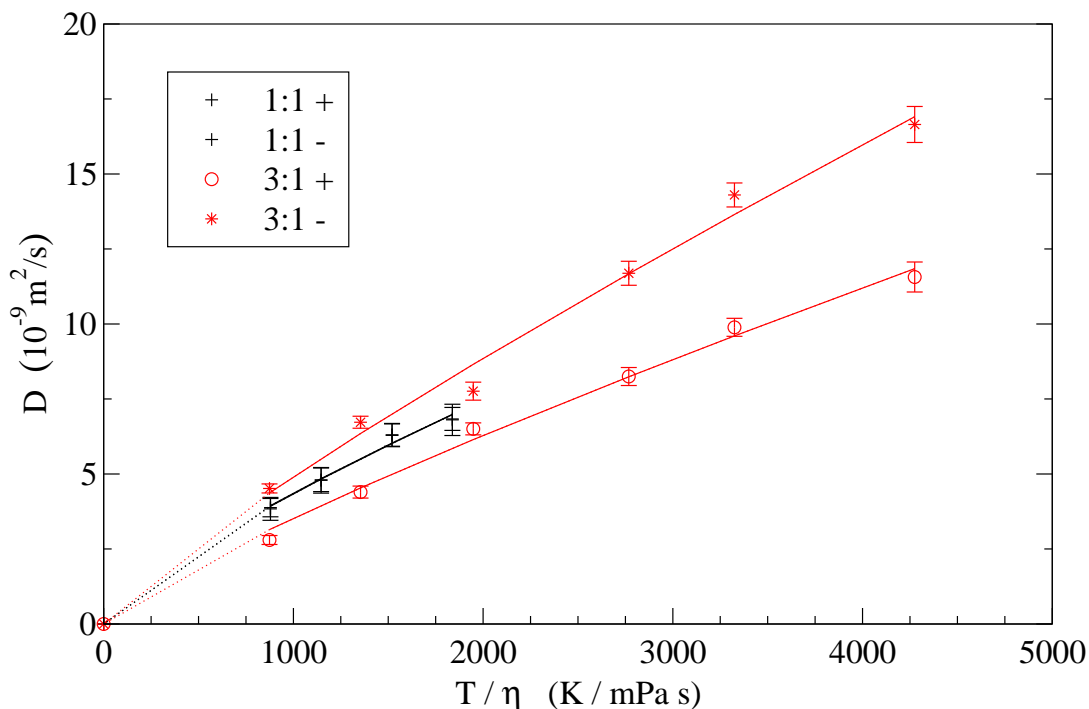


Figure 2.11: Diffusion coefficients as functions of T/η for systems 1:1 and 3:1. The lines are fits to Eq. (2.12). The error bars indicate one standard deviation.

[26] for a number of molten inorganic salts. However, we note that other values (e.g. ~ 0.9) have been reported for more complex ionic liquids [27]. It may be that the exponent ~ 0.8 is appropriate for molten salts comprised of simple inorganic ions, but that the value varies for the more complex non-spherical ions (with side chains etc.) that tend to form room temperature ionic liquids.

2.4 Summary and Conclusions

We have attempted to isolate the influence of ion size disparity on the properties of ionic liquids. This is done by varying the ion size ratio while holding other variables, most importantly, the characteristic interionic distance, σ_{+-} , and the packing fraction, fixed. For all systems considered, the radial charge distribution function exhibits oscillatory decay characteristic of Coulombic systems in the strongly coupled regime. The screening length

decreases with increasing size disparity. Structurally, for larger size disparities the cation-cation (the larger species) and cation-anion correlations appear to dominate. This view is supported by the anion-anion radial distribution function, where the first peak is broad and actually moves to larger separations as the anion decreases in size. This behavior contrasts with that observed for fluids of corresponding LJ particles, of the same size ratio, and indicates strong cation-anion correlations.

The fluid viscosity is also strongly influenced by varying the size disparity, decreasing by about a factor of three as the size ratio varies from 1:1 to 5:1. The decrease is rapid at first, then slows, and appears to be approaching a limiting value at 5:1.

The diffusion coefficients of both species increase over the range 1:1 to 3:1, but then become practically constant. The diffusion coefficient of the smaller anion is larger than that of the cation in the strongly size disparate systems, but the variation with size ratio is similar for both ions. The conventional Stokes-Einstein formula gives a reasonable approximation to the diffusion coefficient of the cations, but fails completely for the anions. This is not surprising since the Stokes-Einstein expression does not take explicit account of the strong anion-cation correlations in the size disparate systems.

The electrical conductivity is sensitive to ion size disparity, but less so than one might have expected. The conductivity increases by about 25% from 1:1 to 2:1, remains nearly constant up to 3:1, then decreases until at 5:1 it is only a little larger than the 1:1 case. The Nernst-Einstein formula (which does not directly include ion correlation effects) seriously overestimates the conductivities but does show the non-monotonic behavior. With aid of the Nernst-Einstein expression, the non-monotonic behavior of the conductivities can be explained in terms of competing effects. As the size ratio is increased, increasing diffusion coefficients act to increase the conductivity, but decreasing number densities tend to reduce it, resulting in the behavior observed.

In comparison with room temperature ionic liquids the model considered here is clearly oversimplified. The melting point remains well above room temperature even for large size disparities. Consequently, the viscosities of the model fluids are much below those observed in room temperature systems. Nevertheless, some features of the temperature dependence

of the transport properties do coincide with experimental observations. In particular, the temperature dependence of the diffusion coefficients, viscosities, and electrical conductivities is well represented by the VFT equation, as are corresponding experimental results. Also, we show that the diffusion coefficients follow the fractional Stokes-Einstein equation $D_\alpha \propto (T/\eta)^\beta$ with $\beta \approx 0.8$. This agrees with the experimental value obtained for many molten inorganic salts [26], but other values have been reported for room temperature ionic liquids [27]. This leads us to speculate that ~ 0.8 might be the “appropriate” exponent for strongly coupled molten salts comprised of relatively simple spherical ions, but that other factors (possibly weaker coupling due to the molecular structure of the ions) influence the exponent for some room temperature ionic liquids.

Finally, we believe that the present systematic investigation of ion size disparity is a necessary first step towards identifying the molecular factors that are important in real ionic liquids. Additional features are obviously important, and other aspects of ion geometry are investigated in the following Chapters, particularly, the effect of off-center charge location (Chapter 3), which is thought to be an important feature of some ionic liquids [28].

Bibliography

- [1] H. Weingärtner, *Angew. Chem. Int. Ed.* **47**, 654 (2008), and references therein.
- [2] M. N. Kobrak, *Adv. Chem. Phys.* **139**, 83 (2008).
- [3] E. W. Castner, Jr., J. F. Wishart, and H. Shirota, *Acc. Chem. Res.*, **40**, 1217 (2007).
- [4] J. Crosthwaite, M. Muldoon, J. Dixon, J. Anderson, and J. Brennecke, *J. Chem. Thermodyn.* **37**, 559 (2005).
- [5] P. Wasserscheid and W. Keim, *Angew. Chem., Int. Ed.* **39**, 3772 (2000).
- [6] M. Buzzeo, R. Evans, and R. Compton, *Chemphyschem* **5**, 1106 (2004).
- [7] B. Krungalz, *J. Chem. Soc., J. Chem. Soc. Faraday Trans. I* **437**, 78, (1982).
- [8] M. Sadr-Lahijany, P. Ray, and H. Stanley, *Physica A* **270**, 295 (1999).
- [9] T. Hamanaka and A. Onuki, *Phys. Rev. E* **74**, 011506 (2006).
- [10] A. Moreno and J. Colmenero, *Phys. Rev. E* **124**, 184906 (2006).
- [11] J. Trullas and J.A. Padro, *Phys. Rev. B* **55**, 12210 (1997).
- [12] N. Galamba, C.A. Nieto de Castro, and J.F. Ely, *J. Phys. Chem. B* **108**, 3658 (2004).
- [13] N. Galamba, C.A. Nieto de Castro, and J.F. Ely, *J. Chem. Phys.* **122**, 224501 (2005).
- [14] N. Kikuchi and J. Horbach, *Europhys. Lett.* **77**, 26001 (2007).
- [15] D. Frenkel and B. Smit, *Understanding Molecular Simulation: From Algorithms to Applications* (Academic Press, 1996).
- [16] M. Deserno and C. Holm, *J. Chem. Phys.* **109**, 18, 7678 (1998).
- [17] M. Allen and D. Tildesley, *Computer Simulations of Liquids* (Oxford, Clarendon, 1987).
- [18] D.J. Evans and G.P. Morriss, *Comput. Phys. Rep.* **1**, 297 (1984).
- [19] J. P. Hansen and I. R. McDonald, *Theory of Simple Liquids*, 2nd ed. (Academic, London, 1986).
- [20] D. Heyes, *Phys. Rev. B* **49**, 755, (1994).
- [21] P. Koblinski, J. Eggebrecht, D. Wolf, and S.R. Phillpot, *J. Chem. Phys.* **113**, 282 (2000).

- [22] H. Tokuda, K. Hayamizy, K. Ishii, A. Susan, M. Watanabe, *J. Phys. Chem. B* **108**, 16593, (2004).
- [23] H. Tokuda, K. Hayamizy, K. Ishii, A. Susan, M. Watanabe, *J. Phys. Chem. B* **109**, 6103, (2005).
- [24] H. Tokuda, K. Hayamizy, K. Ishii, A. Susan, M. Watanabe, *J. Phys. Chem. B* **110**, 2833, (2006).
- [25] R. Zwanzig and A. K. Harrison, *J. Chem. Phys.* **83**, 5861 (1985).
- [26] A. Voronel, E. Veliyulin, and V. Sh. Machavariani, *Phys. Rev. Lett.* **80**, 2630 (1998).
- [27] M. Kanakubo, K. R. Harris, N. Tsuchihashi, K. Ibuki, and M. Ueno, *J. Phys. Chem. B* **111**, 2062, (2007).
- [28] M.N. Kobrak, N. Sandalow, in *Molten Salts XIV* (The Electrochemical Society, Pennington, NJ, 2006).

Chapter 3

Structural and Dynamical Properties of Ionic Liquids: The Influence of Charge Location *

3.1 Introduction

Room temperature ionic liquids differ from simple molten inorganic salts in that they are not composed of simple spherical ions with a charge located at their center. Rather, such liquids consist of a wide variety of large organic cations combined with inorganic or organic anions, which might be simple or complex [1–3]. Consequently, the equation of state, viscosity, conductivity, and other properties of interest strongly depend on the chemical structure of the ions involved. Some correlations between ionic structure and liquid properties have been noted. For example, low melting points are favored by ion size disparity and by low molecular symmetry [1, 4, 5], the presence of side chains and the ability to form hydrogen bonds tend to result in more viscous liquids [5, 6]. However, despite such general observations many questions persist, and exactly how the chemical structure of the ions influences the liquid properties remains to be determined. The present Chapter is a contribution towards this end.

Our objective is to isolate the influence of particular features of the chemical structure by carrying out simulation studies of model systems where, insofar as possible, only one structural feature is varied at a time. There have been many “all-atom” simulations of room temperature ionic liquids [7], and while these provide much insight, it is difficult to relate specific features of the chemical structure of the ions to particular liquid properties, when everything is included at once. Furthermore, the determination of transport properties

*A version of this chapter has been published. H. V. Spohr and G. N. Patey, “Structural and Dynamical Properties of Ionic Liquids: The Influence of Charge Location”, *J. Chem. Phys.* **130**, 104506 (2009).

requires very long simulations, and these are more easily achieved with simplified models. As a first step, we focused on the influences of ion size disparity, showing that size disparity alone can increase ion diffusion, decrease the liquid viscosity, and increase the conductivity (see Chapter 2) [8]. In the present Chapter we investigate the influence of the ion charge location.

Kobrak and Sandalow [1, 9] have recently considered the issue of charge distribution in the complex ions that tend to form room temperature ionic liquids. They introduced the concept of a “charge arm”, defined as the distance of the charge from the center of mass multiplied by the charge. Based on theoretical analysis and experimental data, they argue that the charge arm is an important parameter influencing the dynamical properties of ionic liquids. In particular, they suggest that an increasing charge arm should lead to increased ion mobilities and lower liquid viscosities, in accord with some experimental observations [10]. In the present Chapter, we examine ionic models in which only the charge arm varies, thus allowing us to clearly isolate its influence.

We note that a simulation study aimed at determining the influence of ion shape and charge distribution on liquid properties has been recently reported by Malvaldi and Chiappe [11]. This is interesting work, but limited in that a systematic investigation of charge location was not carried out. The authors do find that locating the charge off center increases the ionic diffusion coefficients, which is in accord with the suggestions of Kobrak and Sandalow [9], but viscosities and conductivities were not reported.

The remainder of this Chapter is divided into three parts. The models and simulation methods employed are described in Chapter 3.2, the results are presented and discussed in Chapter 3.3, and our conclusions are given in Chapter 3.4.

3.2 Models and Simulation

We wish to isolate and examine the influence of charge location on the properties of ionic liquids. Therefore, we consider models consisting of univalent spherical ions of the same size, but the charge of the cation is located a distance l_q from the center of mass. The charge

of the anion remains at the center of mass for all systems considered. The ions interact through the pair potential

$$u(ij) = 4\epsilon \left[\left(\frac{\sigma}{r_{ij}} \right)^{12} - \left(\frac{\sigma}{r_{ij}} \right)^6 \right] + \frac{q_i q_j}{4\pi\epsilon_0 r'_{ij}}, \quad (3.1)$$

where σ and ϵ are the Lennard-Jones (LJ) parameters taken to be the same for all pair interactions, r_{ij} is the distance between the centers of mass of ions i and j , r'_{ij} is the charge-charge distance, q_i is the charge of ion i and ϵ_0 is the permittivity of free space.

The systems considered and parameters employed are summarized in Table 3.1. The systems are labelled $OCxx$, where OC indicates off-center charge and xx is the value of l_q/R_{ion} , where R_{ion} is the ionic radius taken to be $\sigma/2$ for the present model. All parameters were selected to be roughly in the range one might expect for ionic liquids. Note that in all cases the reduced density $\rho^* = \rho\sigma^3 = 0.8$, where $\rho = (N_+ + N_-)/V$ is the total number density.

	$l_q(\text{\AA})$	$U(kJ/mol)$ ($< 0.4\%$)	$P(bar)$ ($< 1\%$)	$D_R(10^{11}Hz)$ ($< 5\%$)	$\tau_\mu(ps)$ ($< 5\%$)	$\tau_{ip}(ps)$ ($< 5\%$)	% p.c. ($< 5\%$)
$OC0$	0	-445	-1679	-	-	-	-
$OC0.25$	0.625	-455	-2447	49.0	1.2	0.04	8
$OC0.5$	1.25	-488	-1541	7.5	1.3	0.08	20
$OC0.625$	1.563	-518	-414	4.2	1.6	0.17	36
$OC0.688$	1.719	-539	574	3.2	1.9	0.9	90
$OC0.75$	1.875	-566	2120	2.2	2.9	2.6	96
$OC0.875$	2.188	-651	7760	1.5	3.8	90	99

Table 3.1: Systems with off-center charge. l_q is the distance of the cationic charge from the center of mass, U is the average configurational energy, P is the average pressure, D_R is the rotational diffusion coefficient of the cation, τ_μ is the orientational relaxation time of the cation, τ_{ip} is the average lifetime of bonded ion pairs, and % p.c. is the percentage of paired cations. The numbers in brackets indicate the standard deviations of the quantities. All results are for 1200 K. Other parameters used in the simulations are: the LJ parameters, $\sigma = 5 \text{ \AA}$, $\epsilon = 6 \times 10^{-21} J$, the charges $q = \pm 1e$, the mass $m = 1.99265 \times 10^{-25} kg$, the moments of inertia of the cation $I_{xx} = I_{yy} = 2.8 \times 10^{-46} kgm^2$, and the reduced density $\rho^* = 0.8$.

In order to separate effects due to the off-center charge location from those coming simply through the stronger Coulombic attractions that result when unlike charges can get closer together, we also carried out calculations for ionic liquids with centered charges but smaller ionic radii to give similar Coulombic attractions. Specifically, for these systems σ_{+-} is defined as the minimum $+-$ separation possible in the corresponding off-center case when the center of mass separation is σ . The volume of the system is reduced for the smaller ions such that ρ^* remains fixed at 0.8. These charge-centered systems are labelled Cxx , where xx indicates that the system is comparable with the $OCxx$ case. The C systems considered are listed in Table 3.2 together with some of their properties. The parameters not included in Table 3.2 are the same as those given in Table 3.1.

	$\sigma(\text{\AA})$	$U(kJ/mol)$ ($< 0.3\%$)	$P(bar)$ ($< 0.5\%$)
$C0.5$	3.75	-599	-7768
$C0.625$	3.437	-655.8	-11793
$C0.75$	3.125	-724	-18062
$C0.875$	2.812	-812	-28210

Table 3.2: Systems with centered charge. σ is the LJ parameter, U is the average configurational energy, P is the average pressure, and the numbers in brackets indicate the standard deviations. The results are for 1200 K and the reduced density $\rho^* = 0.8$.

All simulations were carried out in the NVT ensemble employing a Gaussian isokinetic thermostat [12]. As in Chapter 2 [8], unless otherwise specified, all results reported are at 1200 K. Each system was first equilibrated for 1 ns using simple temperature scaling followed by a further 1 ns of equilibration with the thermostat turned on. Five production runs each of 2 ns were then carried out to give a total run time of 10 ns. Average physical properties of interest were obtained for each production run and standard deviations were estimated using these averages. The LJ potential was truncated at $L/2$, where L is the length of the cubic simulation cell, and shifted to avoid discontinuity [13]. The long-range Coulombic interactions were taken into account using Ewald sums [14] with an inverse length parameter of $6.0/L$ and 50 wavevectors. A fifth order Gear predictor-corrector algorithm was employed to integrate the equations of motion [14]. In all simulations the timestep was

$2 \times 10^{-15} s$, except for the OC0.875 system where $1 \times 10^{-15} s$ was used. In most simulations there were 216 ions in the central cell, but some calculations were performed with 512 ions to ensure that the number dependence was not qualitatively significant.

The transport properties were obtained in the usual way. The diffusion coefficients were found from the Einstein relation [14]

$$D_\alpha = \frac{1}{6} \lim_{t \rightarrow \infty} \frac{d}{dt} \langle |\mathbf{r}_\alpha(0) - \mathbf{r}_\alpha(t)|^2 \rangle , \quad (3.2)$$

where $\mathbf{r}_\alpha(t)$ is the position vector of an ion of species α .

The shear viscosity η is given by [14, 15]

$$\eta = \frac{V}{k_B T} \int_0^\infty \langle P_{lk}(0) P_{lk}(t) \rangle dt , \quad (3.3)$$

where V is the volume, T the temperature, and k_B the Boltzmann constant. P_{lk} ($l \neq k$) is an off-diagonal element of the pressure tensor defined by

$$P_{lk} = \frac{1}{V} \left(\sum_i v_{il} v_{ik} m_i + \sum_i r_{il} F_{ik} \right) , \quad (3.4)$$

where the summation on i is over all particles and v_{il} , F_{ik} , and r_{il} denote the l components of the velocity, force, and position vectors of particle i . Our system includes long-range interactions which are partly calculated in Fourier space, therefore, particular care must be taken in calculating the forces [16, 17]. The pressure P is obtained from the diagonal elements of the pressure tensor

$$P = \frac{1}{3} \sum_{l=x,y,z} P_{ll} . \quad (3.5)$$

The static electrical conductivity is obtained from the current-current correlation function [15]

$$\sigma_{el} = \frac{1}{3k_B T V} \int_0^\infty \langle \mathbf{J}(0) \cdot \mathbf{J}(t) \rangle dt , \quad (3.6)$$

where the current

$$\mathbf{J}(t) = \sum_{i=1}^N q_i \mathbf{v}_i , \quad (3.7)$$

with q_i being the charge of particle i , and \mathbf{v}_i its velocity.

For the positive ions with off-center charge it is of interest to calculate rotational diffusion coefficients defined as [15]

$$D_R = \frac{1}{2} \int_0^\infty \langle \boldsymbol{\omega}(0) \cdot \boldsymbol{\omega}(t) \rangle dt , \quad (3.8)$$

where $\boldsymbol{\omega}$ is the angular velocity of a cylindrically symmetric positive ion. Note that in our model the charge is placed on the z axis, such that it is an axis of cylindrical symmetry, and there is no torque about this axis. Therefore, the relevant components of $\boldsymbol{\omega}$ are ω_x and ω_y only. These are included in Eq. 3.8.

It is also of interest to examine the reorientational autocorrelation function

$$O(t) = \langle \boldsymbol{\mu}(0) \cdot \boldsymbol{\mu}(t) \rangle , \quad (3.9)$$

which describes the orientational decay of the vector $\boldsymbol{\mu}$ joining the center of mass and the charge of the cation. We note that this function is analogous to the dipole-dipole autocorrelation function familiar in the theory of dipolar liquids.

Finally, as the cation charge is moved further from the center, it interacts more strongly with the charge of the anion, and eventually we would expect “bonded” directional ion pairs (cations and anions tending to form dumbbells) to become a significant factor influencing the properties of ionic liquids. To explore this effect, we adopt a procedure sometimes used to investigate hydrogen-bond dynamics in liquids and solutions [18, 19]. This involves introducing two population variables $h(t)$ and $H(t)$ associated with bonded ion pairs. $h(t)$ is one if a “tagged” pair of ions are “bonded” at time t and is zero otherwise. $H(t)$ is one if the tagged pair remains continuously bonded from time 0 to time t , and otherwise zero. We then construct the continuous bonded ion-pair time correlation function

$$S_{ip}(t) = \frac{\langle h(0)H(t) \rangle}{\langle h \rangle}, \quad (3.10)$$

where the angular brackets denote an average over all ion pairs that are bonded at $t = 0$. $S_{ip}(t)$ describes the probability that an ion pair, which is bonded at $t = 0$, remains continuously bonded up to time t . $S_{ip}(t)$ decays as a single exponential (apart from a very brief inertial period at short times), and the characteristic relaxation time τ_{ip} is the average time that an ion pair persists after it is selected at $t = 0$, or, the average “lifetime” of a bonded ion pair.

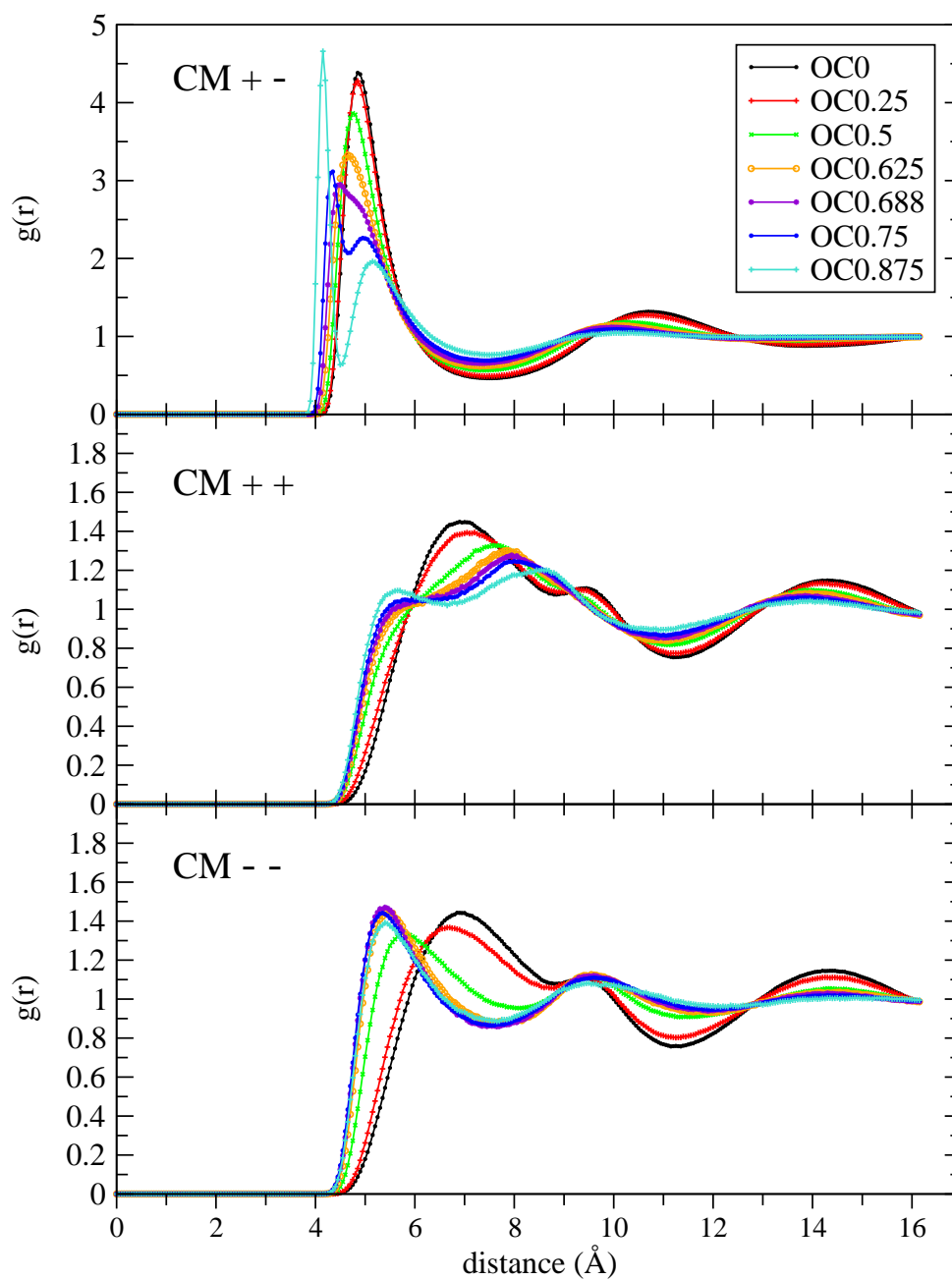
Of course the definition of a “bonded” ion pair is somewhat arbitrary, but here we use geometric criteria as is sometimes done for hydrogen bonds [18, 19]. An ion pair is said to be bonded if the ions are within a certain distance of each other, and if the angle between the vector $\boldsymbol{\mu}$ (defined above) and the vector \mathbf{r}_{CM} joining the centers of mass lies within a certain range. The distances and angles considered are discussed in Chapter 3.3.3.

3.3 Results and Discussion

3.3.1 Structural and Thermodynamic Properties

In Figs. 3.1 and 3.2 the radial distribution functions of the charge-centered system $OC0$ are compared to those of the off-center charge model. For the cations with off-center charge, radial distribution functions are given for the center of mass (CM) (Fig. 3.1) and the center of charge (CC) (Fig. 3.2). For convenience, we use abbreviated symbols for the radial distribution functions. For example, the radial distribution function between the cation charge and the anion is denoted $CC+-$, and that of the center of mass of the cations as $CM++$.

We see from Figs. 3.1 and 3.2 that $CM+-$ and $CC+-$ show similar trends, in that the first peak becomes slimmer and shifts to shorter distances as the charge is moved further off center. The positive charge is more exposed to the anion as it moves away from the CM, leading to stronger and more localized anion-cation interactions. For systems $OC0.75$ and

Figure 3.1: Center of mass radial distribution functions for the *OC* systems.

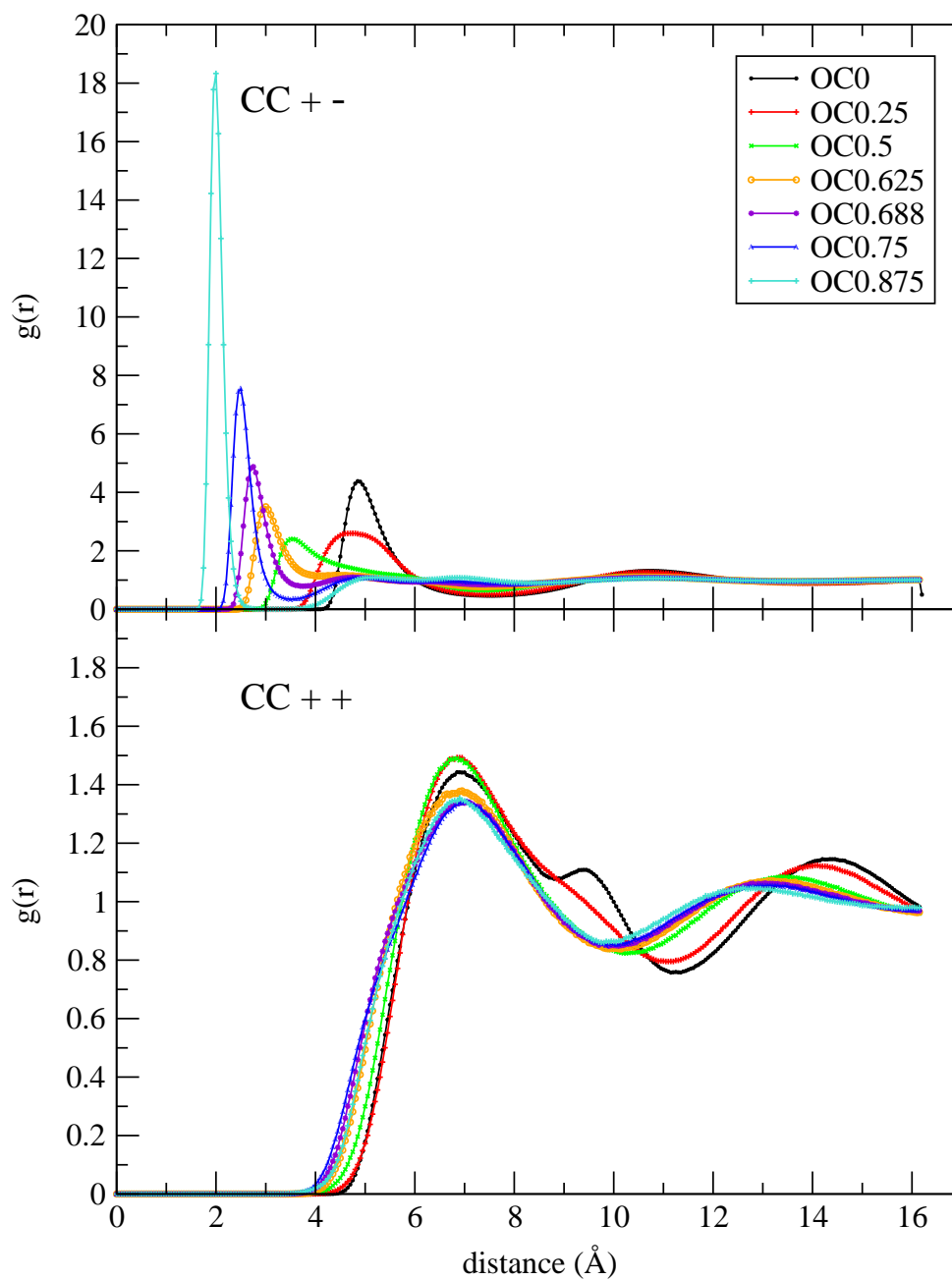


Figure 3.2: Charge-charge radial distribution functions for the *OC* systems.

OC0.875, the $CM+-$ splits into two peaks at small separations. The first, very narrow peak indicates the formation of strongly “bonded” ion pairs, whereas the outer peak, which is broader and smaller in magnitude is associated with “non-bonded” neighbors. For charges that are well off-center, we would expect the ion pairs to be highly directional, and their nature and lifetime are discussed in detail in Chapter 3.3.3.

For the *OC0* system, $CM++$ and $CM--$ must be identical, but moving the charge off center obviously breaks this symmetry. From Fig. 3.2, we see that the charge-charge function $CC++$ changes a little as the charge is initially moved, but that there are only small variations beyond *OC0.5*. This indicates that as the positive charges become more exposed, Coulombic repulsion dominates this function. $CM++$, on the other hand, shows significant dependence on charge location. As the charge is moved further away from the center, the first peak broadens, and shows two distinct maxima for the more off-center cases. This behavior reflects the fact that when the charges are off-center, cation pair interactions depend on the orientation of approach. The inner peak at $\sim 5.5 \text{ \AA}$ is associated with orientations where the charges are directed outward away from each other, and the outer peak where they are directed inward. The broadness of the peak comes from averaging over the different orientational possibilities. The anion function $CM--$ is surprisingly sensitive to the position of the charge of the cation. We see from Fig. 3.1 that the first peak moves to significantly smaller separations and becomes sharper as the charge is moved off center. The inward shift of the first peak likely indicates that once ion pairs are formed, favorable interactions with the positive charge act to significantly counter the anion-anion repulsion.

It is instructive to consider running coordination numbers defined as

$$CN_{\alpha}(R) = 4\pi \int_0^R (\rho_{\beta}g_{\alpha\beta} + \rho_{\alpha}g_{\alpha\alpha})r^2dr , \quad (3.11)$$

where ρ_{α} is the number density of species α , and $g_{\alpha\beta}$ and $g_{\alpha\alpha}$ are the counterion and coion radial distribution functions, respectively. The $CN_{\alpha}(R)$ together with the counterion and coion contributions are shown in Fig. 3.3 for systems *OC0* and *OC0.75*. For the off-center system *OC0.75*, two sets of results are included; one is obtained using radial distribution

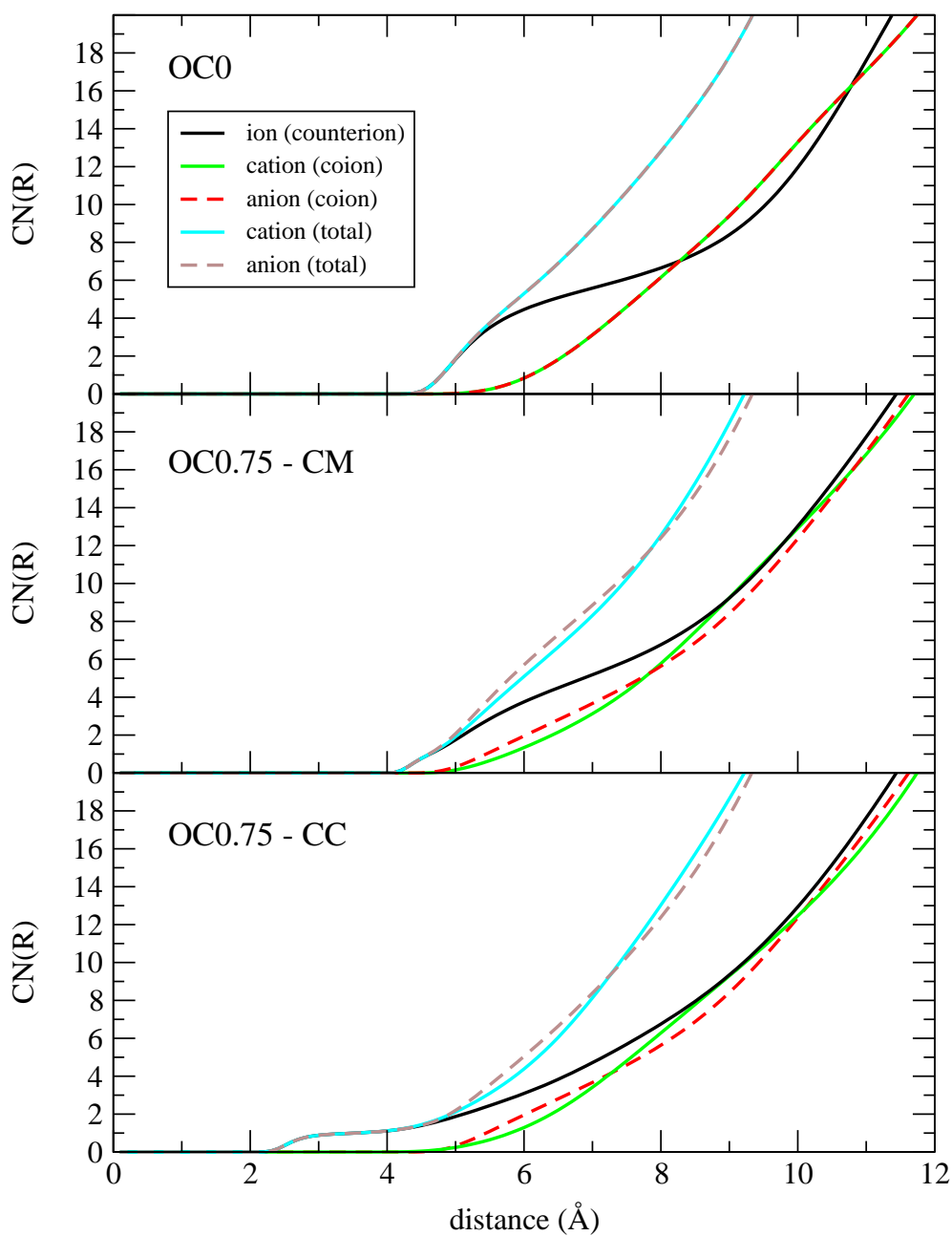


Figure 3.3: Running coordination numbers for the $OC0$ and $OC0.75$ systems. For the $OC0.75$ case results obtained using radial distributions about the center of mass (middle) and center of charge (bottom) are included. The contributions from counterions and coions as well as the total coordination number are shown.

functions about the center of mass and the other about the center of charge. We note that the center-of-mass curves are not very sensitive to charge location, and that the total number of neighbours in the “first shell” ($R \approx 7.5 - 8 \text{ \AA}$) is essentially the same for both systems, and for both ions. A distinct feature in the center-of-charge curves for *OC0.75* is the flat initial portion with $CN(R) \approx 1$, obviously coming from the counterion contribution. This is another manifestation of the strong directional ion pairing noted above. The results shown in Fig. 3.3 indicate that the influences of off-center charge on the transport properties discussed in Chapter 3.3.2 do not come simply through changes in coordination number. For the off-center systems all neighbors are obviously not equivalent. Some counterions interact more weakly with a central ion, others more strongly, in the limit forming strongly bound directional ion pairs. It is mainly this asymmetry of the of the interactions, not changes in the total coordination number, that influences the transport properties of systems with off-center charge.

It is interesting to examine charge ordering and Coulombic screening in these systems as revealed by the radial charge distribution functions [20, 21]

$$Q_\alpha(r) = \rho_\alpha [CM_{\alpha\alpha}(r) - CM_{\alpha\beta}(r)] , \quad (3.12)$$

where α and β denote the ionic species and CM is the center of mass radial distribution function. Results for $rQ_+(r)$ are plotted in Fig. 3.4 on both linear and logarithmic scales. The $rQ_-(r)$ plots are qualitatively similar and hence are not shown. For the *OC0* system we see the screened oscillatory behavior characteristic of strongly coupled Coulombic systems [20]. As the charge is moved significantly off center, the behavior of $rQ_+(r)$ changes rather dramatically, with a strong, sharp minimum appearing at the most probable $+ -$ charge separation. At larger separations an oscillatory structure still persists, but the amplitude of the oscillations becomes continually weaker as the charge is moved further off center. This behavior probably indicates that the system is moving from a strongly coupled Coulombic system towards a system of tightly bound neutral (dipolar) dumbbells. Assuming that at sufficiently large r , $Q_\alpha(r) = \frac{A_\alpha}{r} e^{-r/\lambda} \sin\left(\frac{2\pi r}{d} + \phi\right)$, where d and ϕ are the period and phase

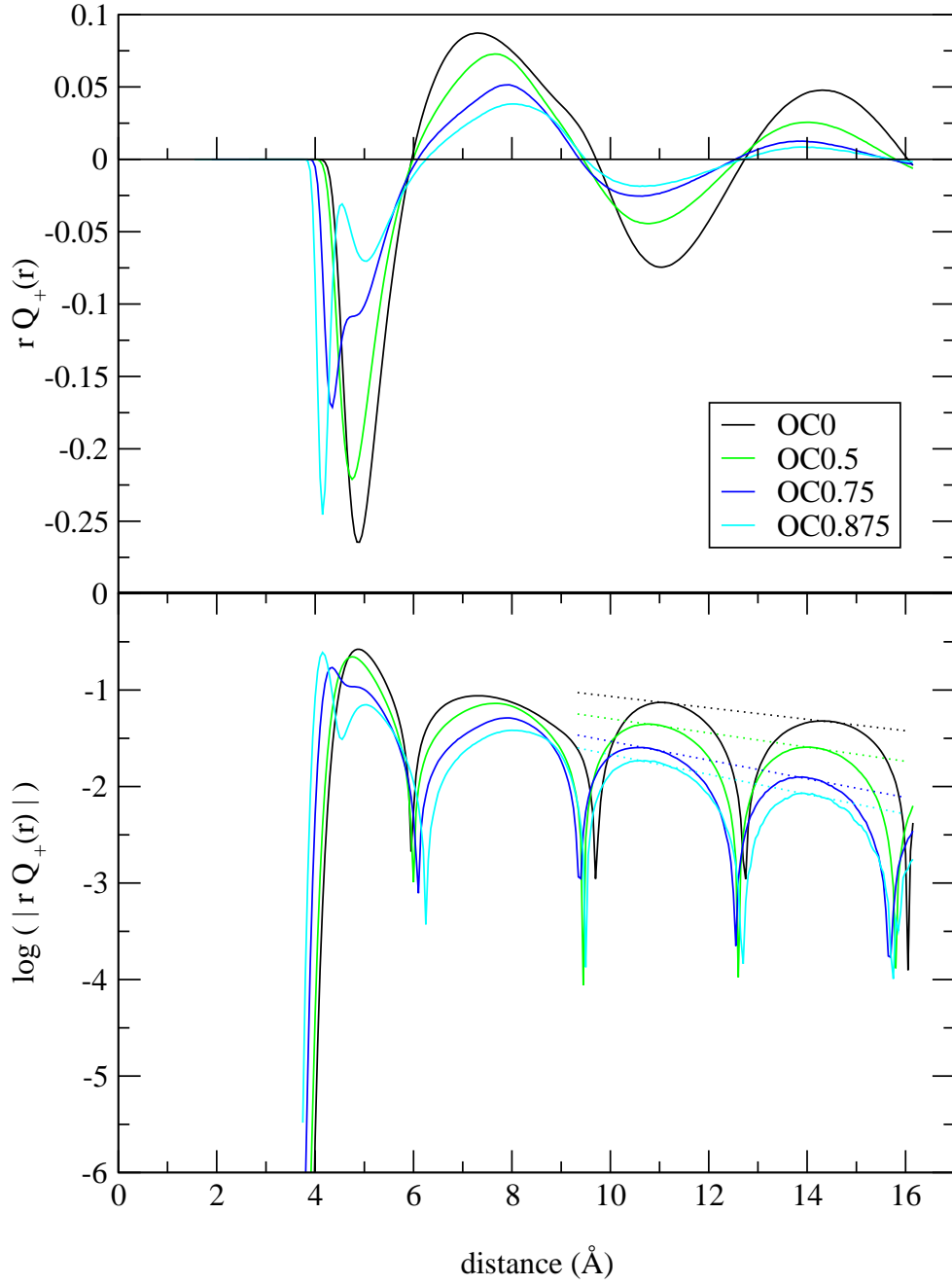


Figure 3.4: The function $rQ_+(r)$ for *OC* systems plotted on linear and logarithmic scales. Screening lengths were estimated from the slopes of the dotted lines.

shift of the charge oscillation, the screening length λ can be estimated [20, 21] from the logarithmic plot shown in Fig. 3.4. We find screening lengths ranging from $\sim 17 - 11 \text{ \AA}$ for systems $OC0 - OC0.875$, respectively. Estimates for the anion span approximately the same range. These screening lengths are comparable to those reported [21] for more realistic models of particular RTILs.

The average configurational energies and pressures (together with other quantities discussed in Chapter 3.3.3) are summarized in Table 3.1. Not surprisingly, we note that the energies become more negative as the positive charge is moved off center and can interact more strongly with the charge of the anion. The pressure initially decreases but then increases with increasing l_q . The initial decrease is due to the increased Coulombic attractions, but as oppositely charged ions are drawn more closely together, the negative contribution to the pressure is overcome by the positive contribution from the LJ potential, leading to the increasing values observed.

3.3.2 Transport Properties

The pressure tensor autocorrelation function (Fig. 3.5, upper panel) strongly increases near $t = 0$, and decays more slowly as the charge is moved off center. In addition, rapid oscillations appear for the more off-center systems. These oscillations also occur in other time correlation functions discussed in Chapter 3.3.2, and are associated with ion pairing. The viscosities obtained by integrating Eq. (3.3) are plotted in Fig. 3.5 (lower panel) as functions of the upper integration limit t_{UL} . The shear viscosity of the liquid is obtained in the limit $t_{UL} \rightarrow \infty$. We note that convergence to the infinite time result is slower in systems $OC0.75$ and $OC0.875$ where the charges are furthest from the center.

The electrical current autocorrelation functions are shown in Fig. 3.6. These functions also display rapid oscillations and decay more slowly as the charge is moved further off center. The conductivities $\sigma_{el}(t_{UL})$ obtained by integrating the current autocorrelation functions are included in Fig. 3.6 (bottom panel). The static conductivity is obtained as $t_{UL} \rightarrow \infty$. The more off-center systems decay very slowly to the limiting value. The slow decay is due to the persistent negative tails of the current autocorrelation functions, which

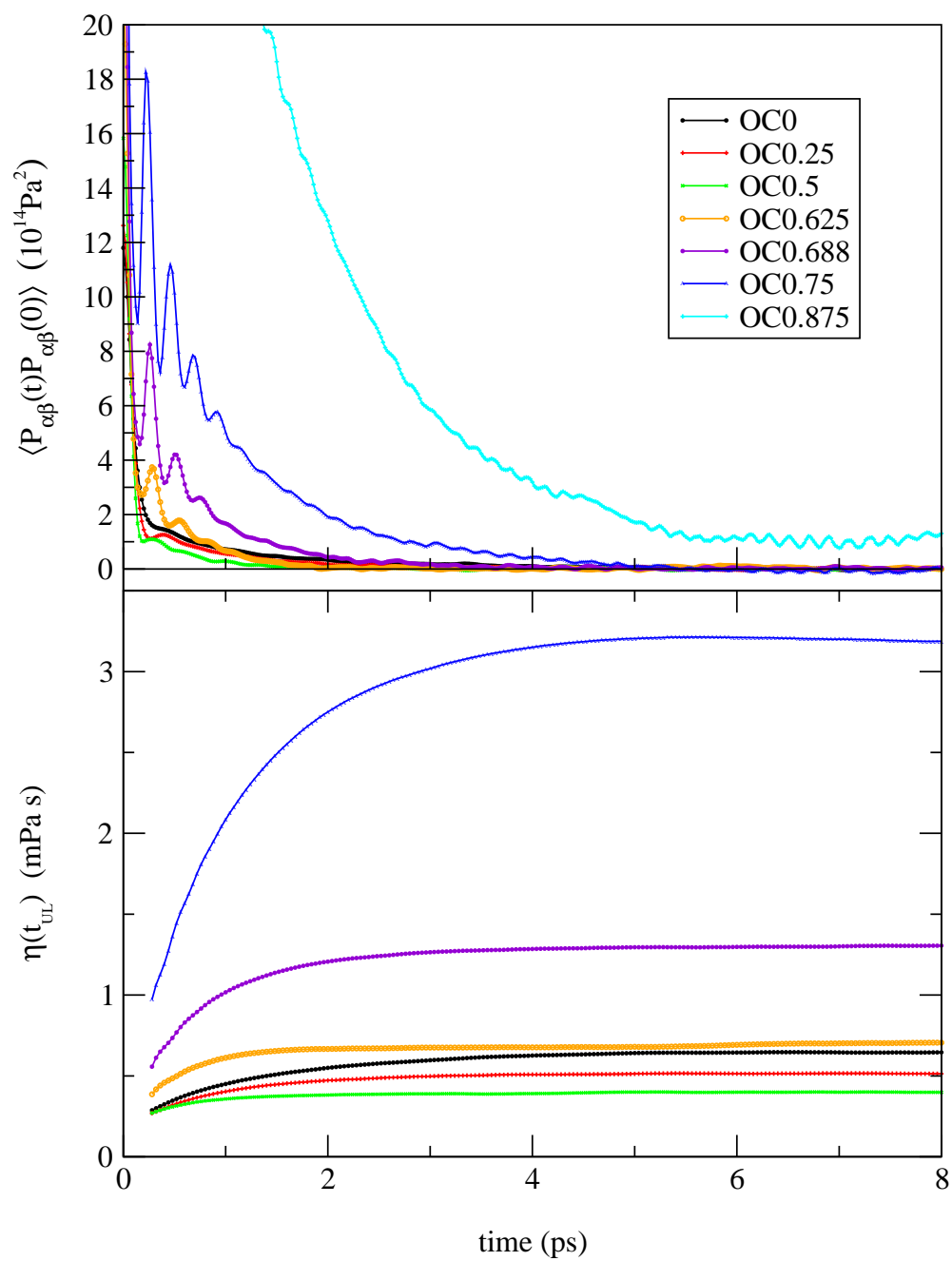


Figure 3.5: Top: Off-diagonal pressure tensor autocorrelation functions for *OC* systems at 1200 K. Bottom: Shear viscosities as functions of the upper integration limit t_{UL} .

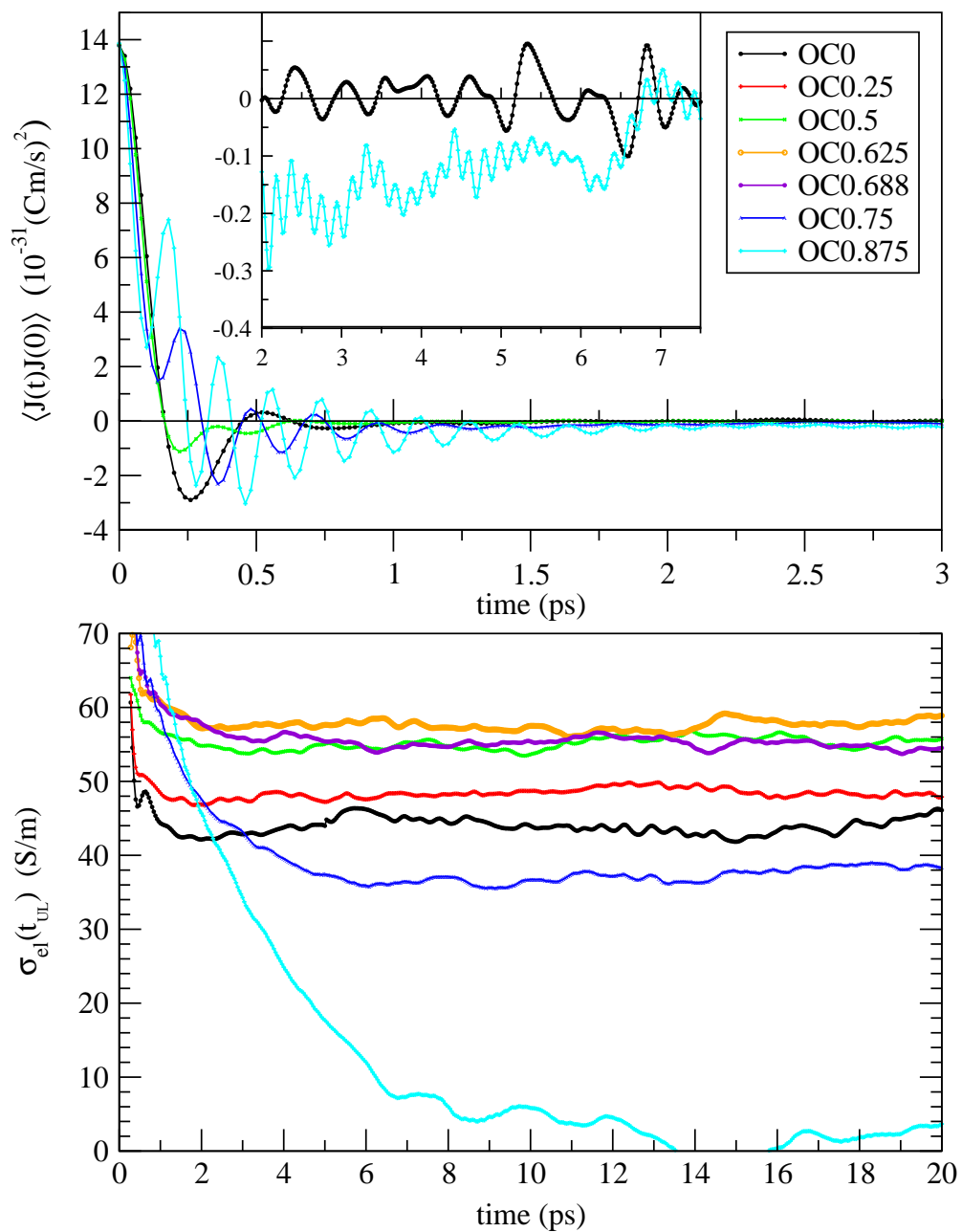


Figure 3.6: Top: Current autocorrelation functions for *OC* systems at 1200 K. Bottom: Conductivities as functions of the upper integration limit t_{UL} .

can be clearly seen in the magnified view shown in the inset (Fig. 3.6, top panel). We note that for the $OC0.875$ system the static conductivity is approaching zero, consistent with the insulating limit we would expect for strongly bound neutral ion pairs.

The velocity autocorrelation functions plotted in Fig. 3.7 are also instructive. We see that for both the cation and anion the so-called “caging” effect, signalled by negative values of the velocity autocorrelation function, becomes less pronounced and eventually disappears as the charge is moved off center. This leads to increased diffusion coefficients as discussed in the next paragraphs. It is interesting to note that for the C systems, where the charge remains centered, but the characteristic cation-anion distance parameter corresponds to that of the off-centered systems, caging effects are enhanced as the cation-anion interactions become stronger, and the diffusion coefficients decrease (see next paragraphs). This serves to illustrate the importance of the fact that the enhancement of the cation-anion interaction is highly directional when the charge is off-center, caging is only enhanced along the cation-anion “bond” and not in all directions as in the C system case. We note that oscillations develop in the velocity autocorrelation functions for the more off-center systems, and these can again be attributed to the ion pairs. The extent of the pairing is also evidenced by the fact that for system $OC0.875$ the cation and anion results are nearly identical, consistent with the ions moving as strongly bound pairs on the timescale (2 ps) shown in the plot. This is in complete agreement with the “bonded” ion pair lifetimes discussed in Chapter 3.3.3.

Diffusion coefficients, viscosities and conductivities are plotted in Fig. 3.8. Inspection of these plots shows that the OC systems separate into two categories with dramatically differing behavior. For systems $OC0 - OC0.625$, we observe relatively slow variation in the transport properties as the charge is positioned further from the center, whereas much more rapid change (particularly for the viscosity and conductivity) is evident in the range $OC0.625 - OC0.875$. These rapid variations are associated with the onset of significant directional ion pairing.

Considering the diffusion coefficients (top panel of Fig. 3.8) more closely, we note that for the OC systems the cation diffusion coefficient D_+ increases as the charge is moved further

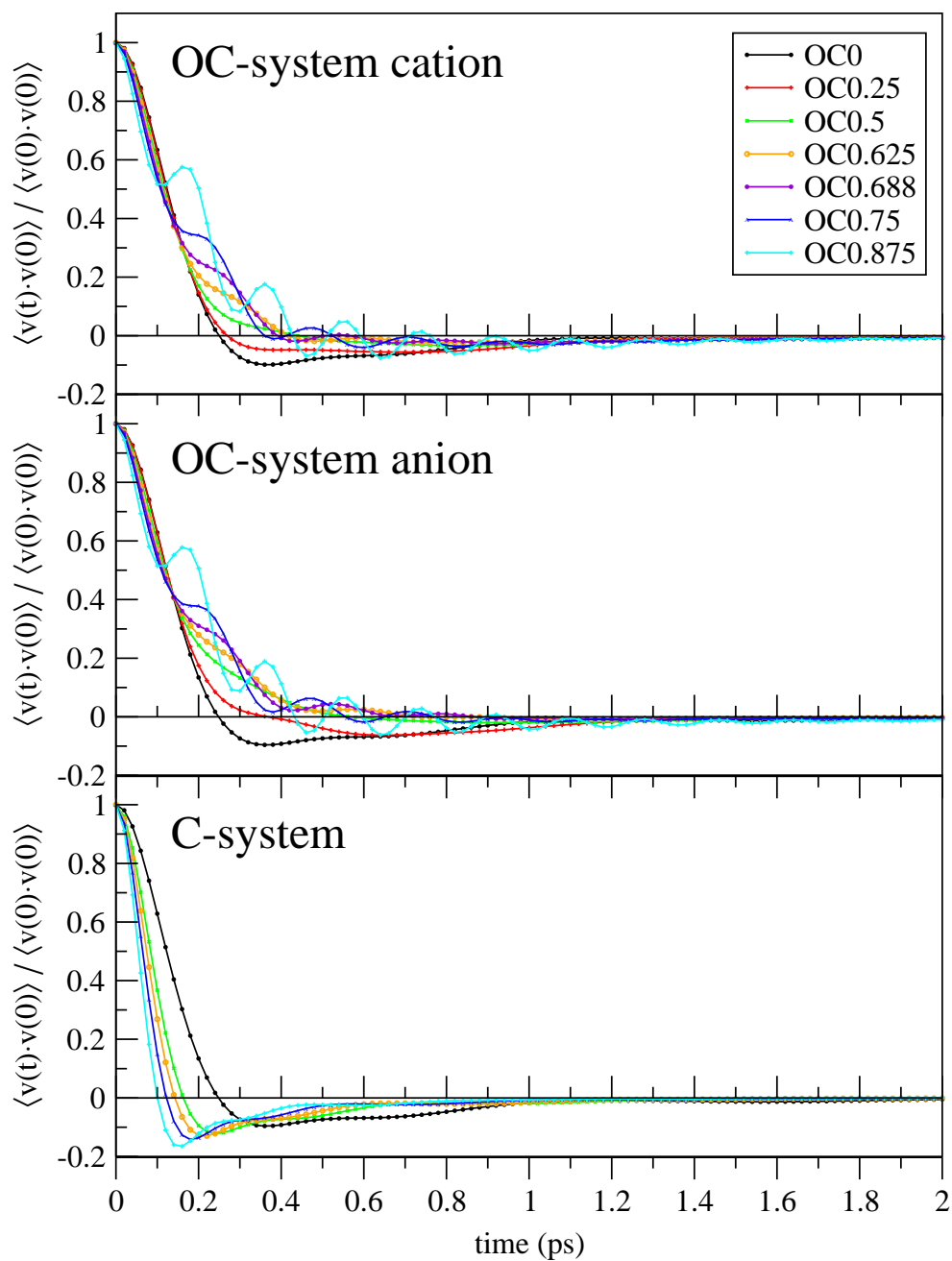


Figure 3.7: Normalized velocity autocorrelation functions of *OC* and corresponding *C* systems.

off center over the entire range considered; the anion diffusion coefficient D_- increases up to $OC0.625$ and then decreases slightly. For $OC0.875$, D_- and D_+ are nearly equal, which is as we would expect for tightly bound ion pairs. In contrast, for the C systems $D_+ = D_-$ decreases in a near linear fashion as σ_{+-} is decreased (top panel of Fig. 3.8). Thus the asymmetry of the Coulombic interactions in the OC systems allows the ions to diffuse more freely. We note that in the OC systems the diffusion constant of the anion is larger than that of the cation. Since the total average coordination numbers of the anions and cations are very similar to each other, and not strongly dependent on the charge location, the differences between the anion and cation diffusion constants are likely due to asymmetries in various multi-ion “clusters”. For example, if one considers linear triples, $+ - +$ will be more strongly “bonded” than $- + -$, because it is not possible for the two anions to bond equally strongly to a cation with off-center charge, whereas the cations can reorient such that both charges are as close as possible to the anion. Therefore, we would expect the more stable $+ - +$ cluster to slow the diffusion of two cations and one anion more than a $- + -$ slows the diffusion of two anions and one cation, thus contributing to a larger diffusion coefficient for the anion.

Stokes-Einstein (SE) results (stick boundary conditions) given by [15]

$$D_{ST} = \frac{k_B T}{3\pi\eta d_{ST}}, \quad (3.13)$$

where d_{ST} is taken to be the LJ parameter σ_α for an ion of species α , are also plotted in Fig. 3.8 (top panel, dashed lines). We note that for the OC systems, the SE curve is in fair agreement with the true diffusion coefficients up to $OC0.5$, but then the SE curve decreases rapidly as the viscosity increases (see middle panel), drastically parting company with the true diffusion coefficients. For the OC systems the increase in viscosity associated with directional ion pairing is not reflected in the diffusion coefficients. We show in the next paragraphs that the relationship between diffusion coefficients and viscosities is better represented by a “fractional” Stokes-Einstein equation, and that this is particularly true in the strongly paired regime. In contrast to the OC systems, for the C systems the SE

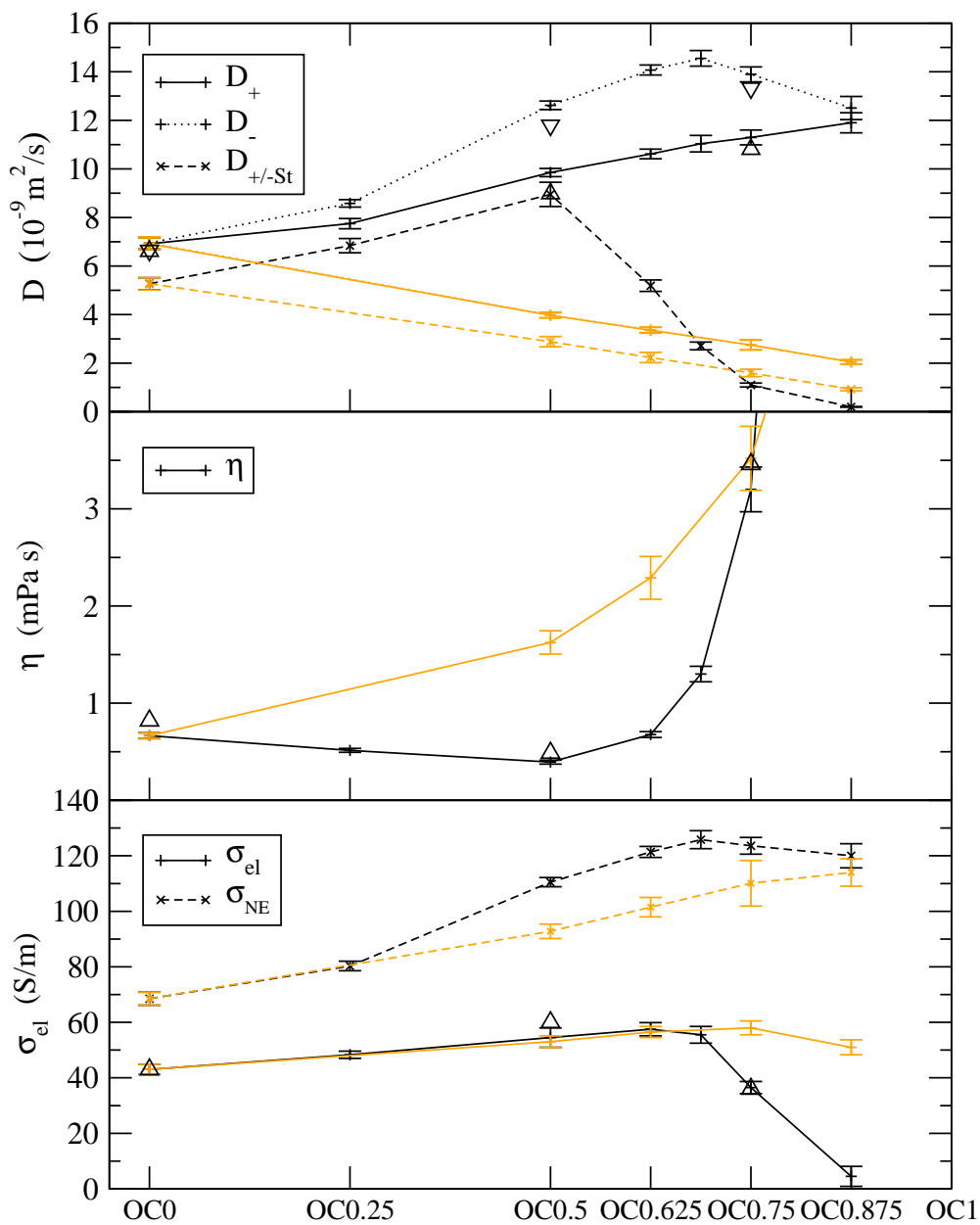


Figure 3.8: Diffusion coefficients, viscosities and electrical conductivities for *OC* (black) and *C* (yellow) systems. The corresponding Stokes (diffusion) and Nernst-Einstein (conductivity) results are given by dashed lines. The triangles represent results obtained with 512 ions. The error bars indicate one standard deviation.

equation gives a reasonable representation of the diffusion coefficients over the entire range of σ_{+-} considered.

Turning to the viscosity (middle panel, Fig. 3.8), we see that for the *OC* systems the viscosity first decreases up to *OC0.5*, but then increases, turning up rather sharply at *OC0.625* as directional ion pairing becomes important. For the *C* systems, the viscosity increases continually as σ_{+-} decreases.

The electrical conductivities are plotted in the lower panel and compared with values given by the Nernst-Einstein (NE) equation [15]

$$\sigma_{NE} = \sum_{\alpha} \frac{\rho_{\alpha} D_{\alpha} q_{\alpha}^2}{k_B T}, \quad (3.14)$$

where $\rho_{\alpha} = N_{\alpha}/V$. For the *OC* systems the conductivities increase slowly up to *OC0.625* and then decrease sharply towards zero. The decrease reflects the formation of ion pairs, and is reasonable considering that in the limit of all ions tightly paired the conductivity must approach zero. We note that the conductivities of the *C* systems are in close agreement with the *OC* results until ion pairing becomes important. In this region, the conductivities of the *C* systems also decrease but not nearly as rapidly as in the *OC* case. The NE conductivities are generally much larger than the true results and, not surprisingly, cannot capture the strong influence of ion pairs.

We note that the decrease in viscosity and increase in conductivity observed in the range *OC0*–*OC0.5* is completely consistent with the analysis of Kobrak and Sandalow [9]. However, these authors did not anticipate the possible influence of directional ion pairing. Effects consistent with ion pairing do show up in experimental results for some ionic liquids, and this is further discussed in the next paragraphs.

3.3.3 Cation Rotation, Reorientation, and Ion-Pair Lifetimes

The rotational motion and reorientation of the cations with off-center charge is of interest. If we take the vector $\boldsymbol{\mu}$ (drawn from the CM to the charge location) to be the z axis, then the autocorrelation function of the $\omega_x = \omega_y$ component of the angular velocity is

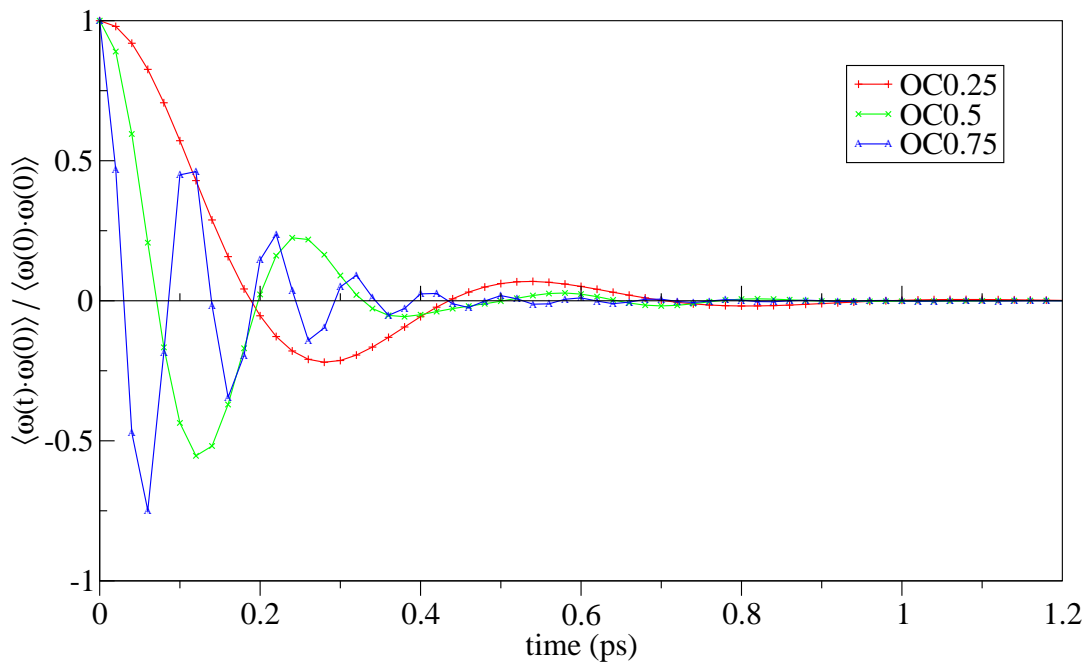


Figure 3.9: Normalized cation angular velocity autocorrelation functions.

shown in Fig. 3.9 for selected systems. The corresponding rotational diffusion coefficients obtained by integration (Eq. (3.8)) are given in Table 3.1. We note that the angular velocity autocorrelation function oscillates more and more rapidly as the charge is moved further off center. This is another indication of the formation of strongly directional ion pairs.

Further insight into the reorientational motion of the positive ion is provided by Fig. 3.10, where we plot the normalized time correlation function of the vector $\boldsymbol{\mu}$ (Eq. (3.9)). The corresponding relaxation times τ_{μ} (estimated assuming exponential decay at long times) are given in Table 3.1. We note that for the system *OC0.25*, where the charge is only a little off-center, $O(t)$ decays rapidly to zero exhibiting some structure with a first minimum occurring at ~ 0.25 ps. The oscillations are in all likelihood associated with weakly bound ion pairs. As the charge is moved further off center, $O(t)$ looks more and more like a single exponential decay with some weak structure at short times. This behavior is very similar to the decay of the dipole-dipole correlation function in strongly polar dielectric liquids and is consistent with strongly bound ion pairs. The relaxation time τ_{μ} increases from 1.2 to

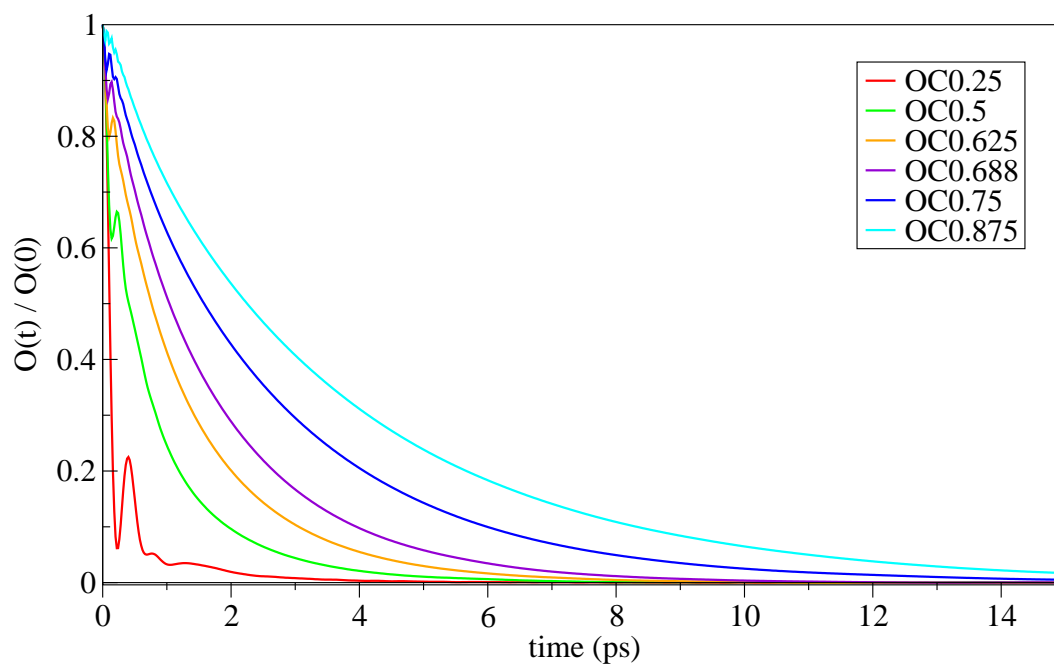


Figure 3.10: Normalized cation reorientational autocorrelation functions.

3.8 ps over the range of systems considered.

Since directional ion pairing is obviously important in the *OC* model, we have calculated the “bonded” ion pair correlation function, $S_{ip}(t)$, as described in Chapter 3.2. Ion pairs are defined if the angle between $\boldsymbol{\mu}$ and \mathbf{r}_{CM} is sufficiently small and if the intercharge distance is less than a certain value. We examined $S_{ip}(t)$ for angles of 10 – 20 degrees and distances corresponding to the first minimum in $CC + -$. In all cases, $S_{ip}(t)$ (not shown) exhibited single exponential behavior (except for small inertial contributions at short times), and the estimated ion-pair “lifetimes” did not exhibit significant dependence on the angle considered. The ion-pair lifetimes obtained for 15 degrees are given in Table 3.1, and we see that they vary from very short, 0.04 ps for *OC0.25* to very long, 90 ps for *OC0.875*. For *OC0.688-OC0.75*, the lifetimes (0.9-2.6 ps) are comparable to those of hydrogen bonds in water under ambient conditions.

3.3.4 Temperature Dependence and Comparison with Experiment

For systems *OC0*, *OC0.5*, *OC0.625* and *OC0.75* we have carried out calculations for different temperatures in the range 700-1200 K. Logarithms of the transport properties versus $1/T$ are plotted in Fig. 3.11 (the *OC0.625* results are not shown for clarity). The Vogel-Fulcher-Tammann (VFT) equation [1]

$$A = A_0 \exp\left(\frac{B}{T - T_0}\right), \quad (3.15)$$

where A is a transport property and A_0 , B and T_0 are fitting parameters, is commonly used to fit experimentally measured diffusion coefficients, viscosities and electrical conductivities [22]. It can be seen from Fig. 3.11 that the VFT equation gives good fits to the results for our model. The largest deviations from linear (Arrhenius) behavior occur for the conductivities. Additionally, the conductivity plot for system *OC0.75* exhibits curvature that is opposite that observed for the other systems. This is likely a manifestation of the fact that ion pairing is much more important in the *OC0.75* system. The ion-pair lifetimes are given in Table 3.3, and we see that these are short and increase only weakly with decreasing

$\tau_{ip}(ps)$	1200K	1100K	1000K	900K	800K	700K
<i>OC0.5</i>	0.08	0.08	0.09	0.10	0.10	0.10
<i>OC0.625</i>	0.17	0.19	0.19	0.21	0.23	0.25
<i>OC0.75</i>	2.2	3.3	4.1	5.6	7.9	13.3
% paired cations	1200K	1100K	1000K	900K	800K	700K
<i>OC0.5</i>	20	21	22	22	23	23
<i>OC0.625</i>	36	37	39	41	44	45
<i>OC0.75</i>	96	97	97	98	98	99

Table 3.3: Bonded ion-pair lifetimes and percentages of paired cations for different temperatures. Standard deviations are as in Table 3.1.

temperature for *OC0.5* and *OC0.625*, but are much longer and increase strongly at lower temperatures for *OC0.75*. Therefore, one might speculate that for *OC0.75* there are two distinct activation barriers to conductivity; one associated with the breaking of “bonded”

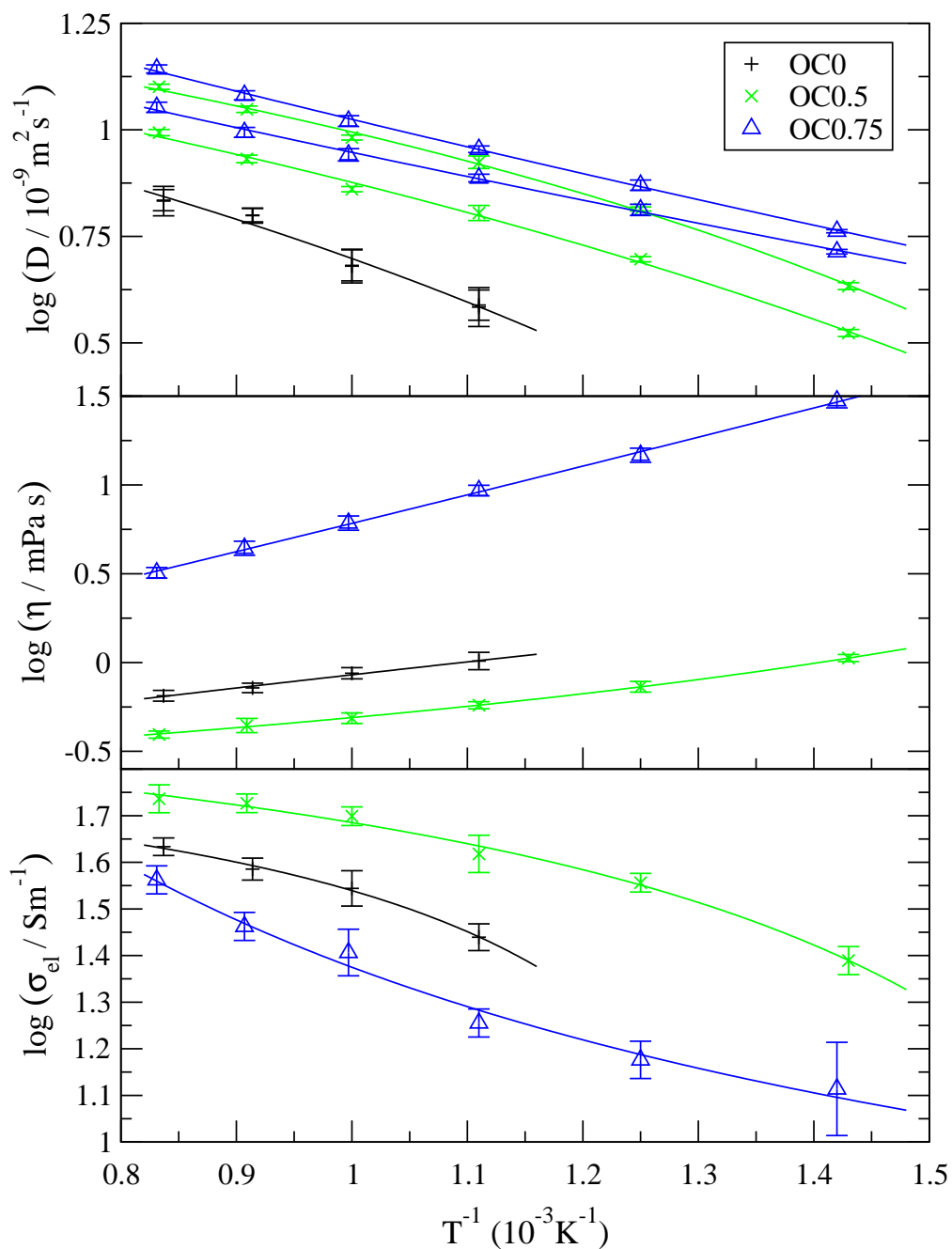


Figure 3.11: Logarithms (base 10) of transport properties for *OC* systems as functions of $1/T$. The solid lines are fits to the VFT equation. The error bars indicate one standard deviation.

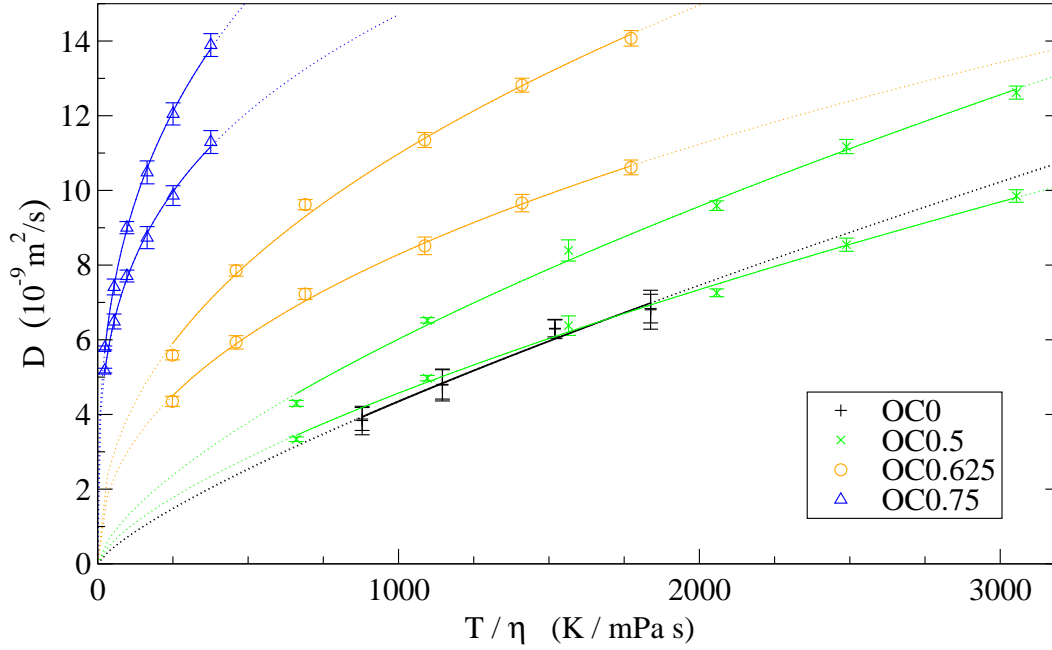


Figure 3.12: Diffusion coefficients for *OC* systems as functions of T/η . The solid lines are fits to the fractional Stokes-Einstein relationship given by Eq. (3.16). The error bars indicate one standard deviation.

ion pairs, and one with the movement (diffusion) of ions through the fluid. For the other systems where the charge is not so far off-center only the second barrier is operative. We note that a similar “ion association” barrier to conductivity in ionic liquids could be caused by other factors such as cation-anion hydrogen bonding [23].

In Fig. 3.12 the diffusion coefficients D_α are plotted versus T/η and the curves are fitted to the “fractional” Stokes-Einstein equation [24–26]

$$D_\alpha = C \left(\frac{T}{\eta} \right)^\beta, \quad (3.16)$$

where C and β are fitting parameters. In the conventional Stokes-Einstein formula $\beta = 1$. For common high temperature molten inorganic salts it is found [25] that $\beta \approx 0.8$, and we have obtained similar exponents for systems of spherically symmetric but size disparate ions (Chapter 2.3.3, Fig. 2.11) [8]. Here we find that the results for systems with off-center

charges are equally well described by the fractional Stokes-Einstein equation, but that the values of β become smaller as the charge is moved off center, we obtain approximately 0.7, 0.45 and 0.3 for systems *OC0.5*, *OC0.625* and *OC0.75*, respectively. Thus the systems with off-center charges deviate strongly from the conventional Stokes-Einstein equation, and also from common molten salts. We will discuss the implications of these and related results in a separate publication.

Comparing the transport properties of our model systems with those of real room temperature ionic liquids [1, 22], we note that the viscosities of our models are generally too low and the diffusion coefficients and conductivities are too high. This is mainly due to the fact that our simulations are carried out well above room temperature in order to avoid crystallization in some systems (the *OC0* system freezes at 700 K), or very slow convergence in others. It is difficult with present simulation methods to estimate the freezing-melting temperature of the systems with off-center charge because when cooled these systems tend to become trapped in “glassy” states and do not form crystals on simulation time scales. Also it must be noted that our models are oversimplified compared with real systems, lacking details of shape and structural features such as side chains. It is likely that such missing features also contribute to the quantitative discrepancies observed.

The simulation results can be used to directly test ideas recently put forward by Kobrak and Sandalow [1, 9]. As noted above, these authors suggest that the charge arm $L_c = |l_q Q|$, where l_q is the distance from the center of mass to the charge of magnitude Q , is an important parameter in determining the transport properties of ionic liquids. They predict lower viscosities and higher electrical conductivities for ions with larger charge arms. We find that for short to moderate charge arms this is exactly what happens, but that for more extreme charge arms precisely the opposite effect is observed, i.e., the viscosity increases steeply and the conductivity decreases sharply as the charge arm is further increased (see Fig. 3.8). This behavior can be traced to the formation of directional ion pairs.

Our results might possibly explain an inconsistency pointed out by Kobrak and Sandalow [9] between some experimental data and their charge arm analysis. Experimental results [9] for 1-butyl-3-methyl-imidazolium (BMIM), N-butyl-N-methyl-pyrrolidinium (P14), and

N-hexyl-N,N,N-trimethylammonium (N6111), all with the counterion bis(trifluoromethylsulfonyl)imide ((Tf)₂N⁻), are given in Table 3.4. These cations have comparable masses, and since BMIM and P14 have similar charge arms they are expected to have similar properties, as they do. On the other hand, N6111, which has a larger charge arm, has a higher viscosity and a lower conductivity than the other liquids, contrary to expectation. Kobrak and Sandalow attribute this discrepancy to the flexibility of N6111 and this might well be true, however, our simulations suggest that directional ion pairing might be an alternative explanation. To examine this possibility, we consider the normalized, dimensionless charge arm $L_c^* = L_c/eR_{ion}$, where R_{ion} is the total ion radius rather than L_c itself. The reason for this is that a large ion might have a large absolute charge arm but still not form ion pairs, whereas a smaller ion might form ion pairs with a shorter charge arm. Note that normalized charge arms defined in this way were used to label our systems, for example, $L_c^* = 0.5$ for OC0.5. Estimates of L_c^* for BMIM, P14 and N6111 are given in Table 3.4, and we note that the estimated L_c^* for N6111 lies in the range where the transport properties do show the influence of directional ion pairing, whereas the estimates for the other two cations do not.

	BMIM	P14	N6111
Cation Mol. Wt. (g/mol)	139.1	142.2	144.3
Charge Arm (eÅ)	1.0	0.9	2.5
Normalized Charge Arm (range)	0.18 – 0.24	0.16 – 0.22	0.63 – 0.89
Viscosity (<i>mPas</i> , 25°C)	69	85	153
Conductivity (10^{-1} S/m, 25°C)	3.9(20°C)	2.2	0.4
Melting Point (°C)	-22	-18	< 25

Table 3.4: Experimental data [9] for different cations with (Tf)₂N⁻ counterions.

3.4 Summary and Conclusions

We have investigated the influence of charge location on the properties of ionic liquids. The models considered consist of spherical univalent ions of the same size but with the charge of the cation located a distance l_q from the center of mass. It is found that the parameter

l_q has a significant influence on the liquid structure, and is particularly important for the transport properties.

Initially, as the charge is moved off center ($l_q \lesssim 0.6\sigma$), the diffusion coefficients increase, signaling that the ions have become more mobile. This is accompanied by increasing electrical conductivities, and decreasing viscosities. These observations confirm suggestions put forward by Kobrak and Sandalow [9], and are likely due to the fact that the off-center charge of the cation leads to spatially non-uniform distributions of neighboring counterions, reduced “caging” and consequently greater ion mobility. To confirm that the anisotropy of the interactions is crucial, we carried out calculations for charge-centered ionic liquids (C systems) with similar cation-anion interaction strengths, and for these systems exactly opposite behavior was observed.

As l_q is made larger ($\gtrsim 0.6\sigma$), the behavior of the transport properties changes dramatically. In this region, the diffusion coefficients increase no further, the electrical conductivity decreases sharply, and the viscosity shows a strong increase. We trace this behavior to the formation of directional ion pairs that are strongly “bonded”. In analogy with current treatments of hydrogen bonding, we introduce a geometric definition of “bonded” ion pairs, and a correlation function to describe their time dependence. It is found that both the number of directional ion pairs, and their estimated lifetime increase rapidly in the region where the strong increase in viscosity and decrease in conductivity is observed. We note that the influence of directional ion pairing might explain why some real ionic liquids have higher viscosities and lower conductivities than one would expect, if one assumed that the l_q -dependence of these properties is simply monotonic [9].

The rotational behavior of the cations was investigated by calculating their angular velocity autocorrelation function, and the reorientational time correlation function of the vector drawn from the center of mass to the charge (analogous to the dipole-dipole autocorrelation function in dipolar fluids). These functions, together with the associated rotational diffusion coefficients and relaxation times, also provide evidence of strong directional ion pairing.

The temperature dependence of the transport properties was examined for selected sys-

tems. Diffusion coefficients, viscosities, and conductivities were all well fit by the VFT equation, as are experimental results. The the biggest deviation from Arrhenius behavior is displayed by the conductivity. For larger values of l_q , the conductivity exhibits qualitatively different behavior than it does for smaller values, and again we attribute this to directional ion pair bonding. We speculate that in these systems there are two “barriers” to conductivity, the usual barrier associated with ion diffusion, and an additional barrier related to the breaking of ion pair bonds. Finally, we find that for all systems considered the fractional Stokes-Einstein equation holds extremely well. The exponent obtained decreases with increasing l_q , varying from ~ 0.8 for charge-centered systems to ~ 0.3 in our most extreme off-center case.

Bibliography

- [1] M. N. Kobrak, Adv. Chem. Phys. **139**, 83 (2008), and references therein.
- [2] H. Weingärtner, Angew. Chem. Int. Ed. **47**, 654 (2008), and references therein.
- [3] E. W. Castner, Jr., J. F. Wishart, and H. Shirota, Acc. Chem. Res., **40**, 1217 (2007), and references therein.
- [4] J. M. Crosthwaite, M. J. Muldoon, J. K. Dixon, J. L. Anderson, and J. F. Brennecke, J. Chem. Thermodyn. **37**, 559 (2005).
- [5] P. Wasserscheid and W. Keim, Angew. Chem., Int. Ed. **39**, 3773 (2000).
- [6] M. Buzzeo, R. Evans, and R. G. Compton, Chemphyschem **5**, 1106 (2004).
- [7] For examples see, C. Rey-Castro, A. L. Tormo, and L. F. Vega, Fluid Phase Equilib. **256**, 62 (2007);
B. Qiao, C. Krekeler, R. Berger, L. D. Site, and C. Holm, J. Phys. Chem. B **112**, 1743 (2008);
J. N. A. C. Lopes and A. A. H. Pádua, *ibid.*, **110**, 3330 (2006);
S. Schröder, T. Rudas, and O. Steinhauser, J. Chem. Phys. **125**, 244506 (2006).
- [8] H. V. Spohr and G. N. Patey, J. Chem. Phys. **129**, 064517 (2008).
- [9] M.N. Kobrak, N. Sandalow, in *Molten Salts XIV* (The Electrochemical Society, Pennington, NJ, 2006).
- [10] H. Shirota and E. W. Castner, J. Phys. Chem. B **110**, 21576 (2005).
- [11] M. Marvaldi, C. Chiappe, J. Phys.:Condens. Matter **20**, 035108 (2008).
- [12] D.J. Evans and G.P. Morriss, Comput. Phys. Rep. **1**, 297 (1984).
- [13] D. Frenkel and B. Smit, *Understanding Molecular Simulation: From Algorithms to Applications* (Academic Press, 1996).
- [14] M. P. Allen and D. J. Tildesley, *Computer Simulations of Liquids* (Oxford, Clarendon, 1987).
- [15] J. P. Hansen and I. R. McDonald, *Theory of Simple Liquids*, 2nd ed. (Academic, London, 1986).
- [16] D. M. Heyes, Phys. Rev. B **49**, 755 (1994).
- [17] N. Galamba, C. A. Nieto de Castro, J. F. Ely, J. Phys. Chem. B **108**, 3658 (2004).

- [18] A. Chandra, *J. Phys. Chem. B* **107**, 3899 (2008), and references therein.
- [19] A. Luzar, *J. Chem. Phys.* **113**, 10663 (2000), and references therein.
- [20] P. Keblinski, J. Eggebrecht, D. Wolf, and S.R. Phillpot, *J. Chem. Phys.* **113**, 282 (2000).
- [21] Y. Shim, M. Y. Choi, and H. J. Kim, *J. Chem. Phys.* **122**, 044510 (2005)
- [22] H. Tokuda, K. Hayamizy, K. Ishii, A. Susan, M. Watanabe, *J. Phys. Chem. B* **108**, 16593, (2004); **109**, 6103, (2005); **110**, 2833 (2006).
- [23] T. Köddermann, C. Wertz, A. Heintz, and R. Ludwig, *ChemPhysChem* **7**, 1944 (2006).
- [24] R. Zwanzig and A. K. Harrison, *J. Chem. Phys.* **83**, 5861 (1985).
- [25] A. Voronel, E. Veliyulin, and V. Sh. Machavariani, *Phys. Rev. Lett.* **80**, 2630 (1998).
- [26] M. Kanakubo, K. R. Harris, N. Tsuchihashi, K. Ibuki, and M. Ueno, *J. Phys. Chem. B* **111**, 2062 (2007).

Chapter 4

Structural and Dynamical Properties of Ionic Liquids: Competing Influences of Molecular Properties *

4.1 Introduction

There have been many attempts to link the molecular features of ionic liquids to their physicochemical properties, and these have been discussed in several recent reviews [1–3]. Several important molecular features distinguish so-called room temperature ionic liquids (RTILs) from molten salts. In RTILs, the cations tend to be organic in nature, and are generally much larger than the inorganic cations of molten salts, thus introducing large cation-anion size disparities. Additionally, in RTILs one or both ions is usually non-spherical in shape, and more complex electrostatic effects due to charge displacement, dipoles, higher multipoles etc., come into play. Finally, in particular systems, a variety of other influences such as π -system interactions, hydrogen bonding, or the clustering of aliphatic chains, can become important.

We are interested in focusing on some of the most basic molecular features of the ions, and systematically examining their influences on the liquid behavior, with particular emphasis on transport properties. In Chapter 2 [4], we considered the influence of ion size disparity in models where all other important variables, notably, the characteristic length parameter determining the Coulombic attraction (here called σ'_{+-} , see Fig. 4.1), dispersion interactions, the mass, and the packing fraction, were held fixed. The constant σ'_{+-} was achieved by

*A version of this chapter has been published. H. V. Spohr and G. N. Patey, “Structural and Dynamical Properties of Ionic Liquids: Competing Influences of Molecular Properties”, *J. Chem. Phys.* **132**, 154504 (2010).

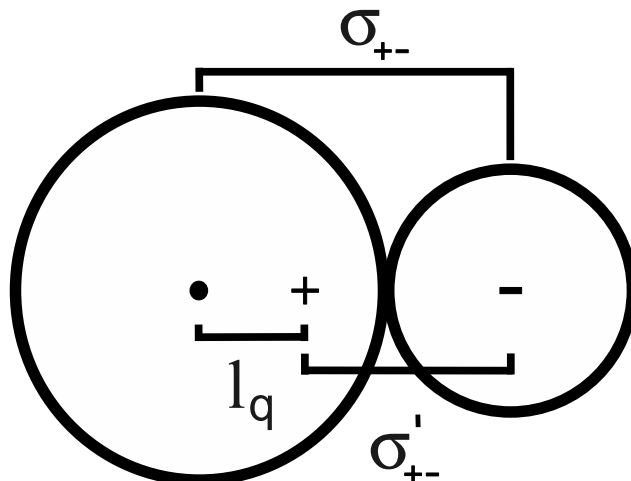


Figure 4.1: Sketch of the geometry used for the charge-off-center (*XOCY*) model. l_q is the distance of the charge from the center of mass, σ_{+-} is the distance between the centers of mass, and σ'_{+-} is the charge separation.

simultaneously enlarging the cation and shrinking the anion, while altering the ion densities to maintain a specified packing fraction. Under these conditions, increasing size disparity increases diffusion coefficients, and decreases the shear viscosity. The electrical conductivity is not a simple monotonic function of size disparity, but displays the competing influences of the changes in diffusion coefficients and charge density. The temperature dependence of all transport properties was well represented by the Vogel-Fulcher-Tamman (VFT) equation, in accord with many experimental observations. Not unexpectedly, comparing results for our rather simple model with experiment does not lead to unambiguous conclusions. For example, one experimental study [5] that considers the cations triethylpentylammonium and triethylpentylphosphonium coupled with the bis(trifluoromethanesulfonyl)amide anion, reports larger diffusion coefficients, higher electrical conductivity, and lower viscosity for the phosphonium case, where the size disparity is larger, in apparent agreement with our observations. However, another study [6] of 1-butyl-3-methylimidazolium coupled with the anions, PF_6^- , AsF_6^- and SbF_6^- , reports decreasing viscosities for the larger anions, where the size disparities are actually smaller (note that the cation is much larger than any of the anions). The authors [6] attribute their observations to weaker cation-anion interactions,

due to the increasing size of the anion, and indeed this is a factor not included in our model, where σ'_{+-} was held fixed in order to isolate the influence of size disparity. One purpose of the present Chapter is to extend our model calculations to include systems where both size disparity and σ'_{+-} can vary, and, in fact, we show that these parameters can have strongly competing effects on the transport properties.

Inspired by suggestions of Kobrak and Sandalow [2, 7], we have also examined how charge location can affect the structural and transport properties of ionic liquids (Chapter 3) [8]. The model employed consisted of spherical, univalent ions of the same size, with the cation charge displaced from the center of mass (see Fig. 4.1). For “small” charge displacements, the shear viscosity decreases, and the diffusion coefficients, as well as the electrical conductivity, increase. For larger charge displacements, this behavior is essentially reversed, while the diffusion coefficients vary little, the viscosity increases strongly, and the conductivity decreases sharply towards zero. This reversal of behavior can be traced to the formation of significant numbers of long-lived, directional ion pairs. Strong cation-anion correlations, such as ion pairs or other neutral aggregates, decrease the conductivity of some particular RTILs [9–13]. These observations are even more striking when one notes that the diffusion coefficients are not necessarily coupled to the electric conductivity, but RTILs with lower conductivities can have larger diffusion coefficients [9, 11, 12]. Hydrogen bonding has been put forward [14] as a rationalization for the low conductivity of 1-ethyl-3-methylimidazolium bis(trifluoromethanesulfonyl)amide in comparison to the corresponding system where the anion is replaced with tetrafluoroborate.

Another surprising discovery concerning hydrogen bonding in RTILs is worthy of note. While in many cases increasing the hydrogen bonding ability of ionic liquids (by changing the anion type [15–17], or introducing different functional groups [18, 19]), has been shown to increase viscosity, in other instances removal of a hydrogen bond (1-butyl-3-methyl-imidazolium to 1-butyl-2,3-dimethyl-imidazolium) was shown to increase the viscosity [15, 20–22]. A somewhat similar effect is observed in the behavior of our charge-off-center models, and we attempt to draw comparisons at the conclusion of this Chapter.

The present Chapter is a significant extension of our earlier efforts. As a further step towards realistic systems, we consider models where both size disparity and charge displacement occur in the same ionic liquid, and both can be varied independently. The important parameter σ'_{+-} is unconstrained, and will vary as well. Our purpose is to determine how these different molecular features influence each other, and to gauge the relative importance of their contribution to the behavior of ionic liquids.

The remainder of this Chapter is organized as follows. The models and simulation method are described in Chapter 4.2, results are presented and discussed in Chapter 4.3, and our conclusions are given in Chapter 4.4.

4.2 Ionic Liquid Models and Simulation Method

In order to identify the influence of different physical characteristics of the ions, we consider relatively simple models consisting of spherical ions of different size. For all systems considered here, the location of the charge of the anion coincides with the center of mass, but this is not necessarily the case for the cations, a feature consistent with the situation for many ionic liquids [7, 23]. The ion-ion pair potential is given by

$$u(ij) = 4\epsilon \left[\left(\frac{\sigma_{ij}}{r_{ij}} \right)^{12} - \left(\frac{\sigma_{ij}}{r_{ij}} \right)^6 \right] + \frac{q_i q_j}{4\pi\epsilon_0 r'_{ij}}, \quad (4.1)$$

where $\sigma_{ij} = (\sigma_i + \sigma_j)/2$, and ϵ are the Lennard-Jones (LJ) parameters, r_{ij} is the distance between the centers of mass of ions i and j , r'_{ij} is the charge-charge distance, q_i is the charge of ion i , and ϵ_0 is the permittivity of free space. Values for all parameters used in our simulations are given in Tables 4.1 and 4.2.

For description and reference purposes, it is useful to label our charge-centered and charge-off-center models as XCY and $XOCY$, respectively, where X is the size disparity σ_+/σ_- , and Y is the minimum charge separation σ'_{+-} (in Å), when the anion and cation centers of mass are separated by σ_{+-} (see Fig. 4.1). Note that for the XCY systems $\sigma'_{+-} = \sigma_{+-}$.

<i>model</i>	<i>system</i>	$\sigma_+(\text{\AA})$	$\sigma_-(\text{\AA})$	$s_{+-}(\text{\AA})$	$\delta(\%)$
<i>XC5</i>	<i>1C5</i>	5	5	4.85	3
	<i>2C5</i>	6.667	3.333	4.85	3
	<i>3C5</i>	7.5	2.5	4.85	3
	<i>4C5</i>	8	2	4.85	3
	<i>5C5</i>	8.333	1.667	4.85	3
<i>XC5</i>	<i>1C5</i>	5	5	4.85	3
	<i>1.1C4.8</i>	5	4.5	4.6	3
	<i>1.3C4.5</i>	5	4	4.35	3
	<i>1.4C4.3</i>	5	3.5	4.1	3
	<i>1.7C4.0</i>	5	3	3.85	4
	<i>2.5C3.5</i>	5	2	3.35	4
	<i>5C3</i>	5	1	2.85	5
	<i>1CY</i>	<i>1C5</i>	5	5	4.85
<i>1C3.8</i>		3.75	3.75	3.6	4
<i>1C3.4</i>		3.437	3.437	3.3	4
<i>1C3.1</i>		3.125	3.125	3.0	4
<i>1C2.8</i>		2.812	2.812	2.65	6

Table 4.1: Parameters and results for the charge-centered models *XC5*, *XC5* and *1CY*. Here X is the size disparity σ_+/σ_- , Y is σ'_{+-} (rounded), and σ_+ and σ_- are the LJ length parameters for the respective ions. s_{+-} is the position of the first peak in the cation-anion radial distribution function, and δ is the percentage difference between σ'_{+-} and s_{+-} . All ions considered are univalent, and for all particles the LJ energy parameter $\epsilon = 6 \times 10^{-21} J$, the masses $m = 1.99265 \times 10^{-25} kg$.

<i>model</i>	<i>system</i>	l_q/R_+	$s_{+-}(\text{\AA})$	$\delta(\%)$	$D_R(10^{11}Hz)$ ($< 5\%$)	$\tau_\mu(ps)$ ($< 5\%$)	$\tau_{ip}(ps)$ ($< 5\%$)	% p.c. ($< 5\%$)
1OCY	1OC5	—	4.85	3	—	—	—	—
	1OC4.4	0.25	4.7	-7	49.0	1.2	0.04	8
					(27.7)	1.3	0.10) ^a	
					(19.0)	—	0.18) ^b	
	1OC3.8	0.5	3.55	5	7.5	1.3	0.08	20
					(5.7)	1.5	0.13) ^a	
					(4.2)	1.7	0.24) ^b	
1OC3.4	0.625	3.0	13	4.2	1.6	0.17	36	
1OC3.3	0.688	2.75	16	3.2	1.9	0.9	91	
1OC3.1	0.75	2.5	20	2.2	2.9	2.6	95	
				(1.8)	3.3	4.2) ^a		
1OC2.8	0.875	2.0	29	(1.4)	4.2	5.8) ^b	99	
2OCY	2OC5	—	4.85	3	—	—	—	—
	2OC4.2	0.25	4.2	-1	22.0	1.6	0.08	11
	2OC3.8	0.375	3.5	7	6.0	2.1	0.17	22
	2OC3.3	0.5	2.8	16	2.6	3.1	1.0	69
	2OC2.9	0.625	2.15	26	2.2	3.1	2.6	95
3OCY	3OC5	—	4.85	3	—	—	—	—
	3OC4.1	0.25	4.0	2	12.1	1.9	0.30	14
	3OC3.6	0.375	3.2	11	3.5	2.7	0.45	31
	3OC3.1	0.5	2.5	20	2.3	3.5	1.1	68
	3OC2.7	0.625	1.75	34	2.5	1.8	17	99

Table 4.2: Parameters and results for the charge-off-center models 1OCY, 2OCY and 3OCY. σ_+ and σ_- , interaction parameters, and masses are as for systems 1C5, 2C5 and 3C5, respectively (Table 4.1). X , Y , and δ are as in Table 4.1. l_q/R_+ indicates the charge displacement (Fig. 4.1), and s_{+-} is the position of the first peak in CC+- . D_R and τ_μ are the rotational diffusion coefficient and the orientational relaxation time of the cation, respectively, τ_{ip} is the average ion-pair lifetime, and % p.c. is the percentage of paired cations. The superscripts *a* and *b* denote results obtained with cation moments of inertia $I_{xx} = I_{yy} = 2.8 \times 10^{-45}$, and 2.8×10^{-44} kg m², respectively. All other results were obtained using $I_{xx} = I_{yy} = 2.8 \times 10^{-46}$ kg m².

It is appropriate at this point to describe the physical motivations for the particular models we have chosen to study. Considering first the charge-centered systems, we would expect both ion size disparity and σ'_{+-} to significantly influence the properties of ionic liquids, and our models are selected to isolate and understand these effects. In Chapter 2 [4], we examined the influence of size disparity while holding σ'_{+-} fixed at 5 Å. This was achieved by simultaneously enlarging the cation while shrinking the anion (see Table 4.1). In the present notation, this model is labeled *XC5* and its purpose is to highlight the effects of size disparity. However, in many experimental studies one ion is held constant while the counterion is varied, which will in general change both the size disparity and σ'_{+-} . In the charge-centered context, model *XC_Y*, where σ_+ is held fixed at 5 Å, while σ_- is systematically reduced, mimics this situation. Here, the size disparity increases, while σ'_{+-} decreases simultaneously. We also consider model *1CY*, where the ions are of the same size, but σ'_{+-} varies. Comparing models *XC_Y* and *1CY* allows us to separate the influence of σ'_{+-} from that of size disparity. Note that in order to remove effects due to varying packing fraction, in all of our simulations the reduced density $\rho^* = \rho_+\sigma_+^3 + \rho_-\sigma_-^3$, where $\rho_i = N_i/V$ (N_i is the number of ions of species i and V is the sample volume), is held fixed at 0.8. For physically realistic ionic masses, for most of our models $\rho^* = 0.8$ corresponds to liquid densities in the range 0.6 to 2.1 g/mL, with the majority of systems being around 1 g/mL. These densities lie in the range of common RTILs. Other variables, such as the ionic masses and LJ energy parameters, that effect the physical properties, are taken to be the same for all particles (Table 4.1).

Further, since in many real ionic liquids the ionic centers of mass and centers of charge do not coincide, we investigate models where the size disparity, charge location, and σ'_{+-} all vary (Fig. 4.1). Model *1OC_Y*, considered in Chapter 3 [8], consists of spherical ions of the same size but with the cationic charge located a distance l_q from the center of mass. This obviously has the additional effect of decreasing σ'_{+-} . In the present Chapter we extend this approach to include models *2OC_Y* and *3OC_Y*, where the size disparity, charge location, and by consequence σ'_{+-} , are all varied (see Table 4.2). Again, the masses and LJ parameters are held constant for all ions (Table 4.1). For the charge-off-center models

it is also necessary to assign moments of inertia $I_{xx} = I_{yy}$ to the cations, and three values that span the range expected for real ionic liquids are considered [†] (Table 4.2). Of course, for the classical liquids considered here, the equilibrium properties are independent of the masses and moments of inertia, but the transport and other dynamical properties can be influenced. Comparing the results obtained for the charge-off-center systems with those of appropriate *XC**Y* models, allows us to assess the relative influences of size disparity and charge location on the physical properties of ionic liquids, where both effects are present.

All simulations were carried out in the NVT ensemble with the temperature T fixed at 1200 K by means of a Gaussian isokinetic thermostat [24]. This temperature ensures that all of our models are liquid at the density considered. The temperature dependence of various properties of our model ionic liquids was discussed in Chapters 2.3.3 and 3.3.4 [4, 8]. A cubic simulation cell (of length L) with the usual periodic boundary conditions was employed. The LJ potential was cut and shifted at $L/2$ to avoid discontinuity [25], and Ewald sums were used to treat the long-range Coulombic interactions [26]. In the Ewald calculations the inverse length parameter was taken to be $6.0/L$, fifty wavevectors were employed in the k -space sum, and the real space interactions were truncated at $L/2$. Each simulation was started with the ions on a lattice, and was equilibrated with simple temperature scaling for 1 ns, and continued with the thermostat turned on for another 1 ns. Then five production runs of 2 ns each were conducted to calculate the overall average properties (10 ns), and the 2 ns runs were used to estimate standard deviations. The equations of motion were integrated with a fifth order Gear predictor-corrector algorithm [26] with a timestep of 2×10^{-15} seconds, except for systems 1OC2.8, 2OC2.9 and 3OC2.7, where a timestep of 1×10^{-15} seconds was used. Most results were obtained using 216 ions in the simulation cell, but some runs were performed with 512 ions to ensure that the number dependence was not qualitatively significant.

[†]Note that in real RTIL cations there does not appear to be a strong correlation between l_q and the relevant moments of inertia. For example, for the cations 1-butyl-3-methyl-imidazolium (BMIM), and N-hexyl-N,N,N-trimethylammonium (N6111), the l_q/R_+ values are ~ 0.2 and ~ 0.8 , respectively, but their relevant moments of inertia are both $\sim 5 \times 10^{-45}$ kg m².

The usual transport properties (translational diffusion coefficients D_i , shear viscosities η , and electrical conductivities σ_{el}) were calculated via the usual time correlation functions [26, 27], and the details are discussed in Chapters 2.2 [4], 3.2 [8] and Appendix A.3. In addition, for the charge-off-center ions (positive ions in our *XOCY* models) it is interesting to calculate the rotational diffusion coefficients [27]

$$D_R = \frac{1}{2} \int_0^\infty C_\omega(t) dt , \quad (4.2)$$

$$C_\omega(t) = \langle \boldsymbol{\omega}(0) \cdot \boldsymbol{\omega}(t) \rangle , \quad (4.3)$$

and the reorientational autocorrelation function

$$O(t) = \langle \boldsymbol{\mu}(0) \cdot \boldsymbol{\mu}(t) \rangle , \quad (4.4)$$

where $\boldsymbol{\mu}$ is the vector joining the center of mass and the charge of the cation, and $\boldsymbol{\omega}$ is the angular velocity in a coordinate system where the axis of cylindrical symmetry z lies along $\boldsymbol{\mu}$ (and there is no torque about this axis). We know from Chapter 3.3.3 [8], that both D_R and the decay time τ_μ associated with $O(t)$, provide signatures of directional ion pairing in the charge-off-center models.

Directional ion pairing can be further illuminated by calculating the continuously bonded ion pair time correlation function

$$S_{ip}(t) = \frac{\langle h(0)H(t) \rangle}{\langle h \rangle} , \quad (4.5)$$

which describes the probability that an ion pair, which is bonded at $t = 0$, remains continuously bonded up to time t . In Eq. (4.5), $h(t)$ is unity if a tagged pair of ions is defined to be “bonded” at time t , and is zero otherwise. $H(t)$ is unity if the tagged pair remains continuously bonded from time 0 to time t , and is otherwise zero. The angular brackets indicate averages taken over all ion pairs that are bonded at $t = 0$. We define a directional ion pair geometrically. A pair of ions is defined to be bonded if they are closer than the

first minimum in the cation-anion center of charge radial distribution function, and if at the same time the angle between the vector $\boldsymbol{\mu}$ (defined above) and the vector \mathbf{r}_{CM} joining their centers of mass is smaller than 15 degrees. This definition was shown to be physically reasonable in Chapter 3.3.3 [8]. Apart from a short initial period where inertial effects exert an influence, $S_{ip}(t)$ decays exponentially, and its relaxation time τ_{ip} can be regarded as the average “lifetime” of directional ion pairs. We note that the procedure outlined above is analogous to a method sometimes used to investigate the dynamics of hydrogen bonds [28, 29].

4.3 Results and Discussion

4.3.1 Structural Properties

Radial distribution functions are plotted in Figs. 4.2 - 4.7. Both center of mass (CM) and center of charge (CC) functions are displayed, and these are given the obvious notation CM_{ij} and CC_{ij} , where ij refer to the ionic charges.

Influence of Size Disparity and the Distance σ'_{+-}

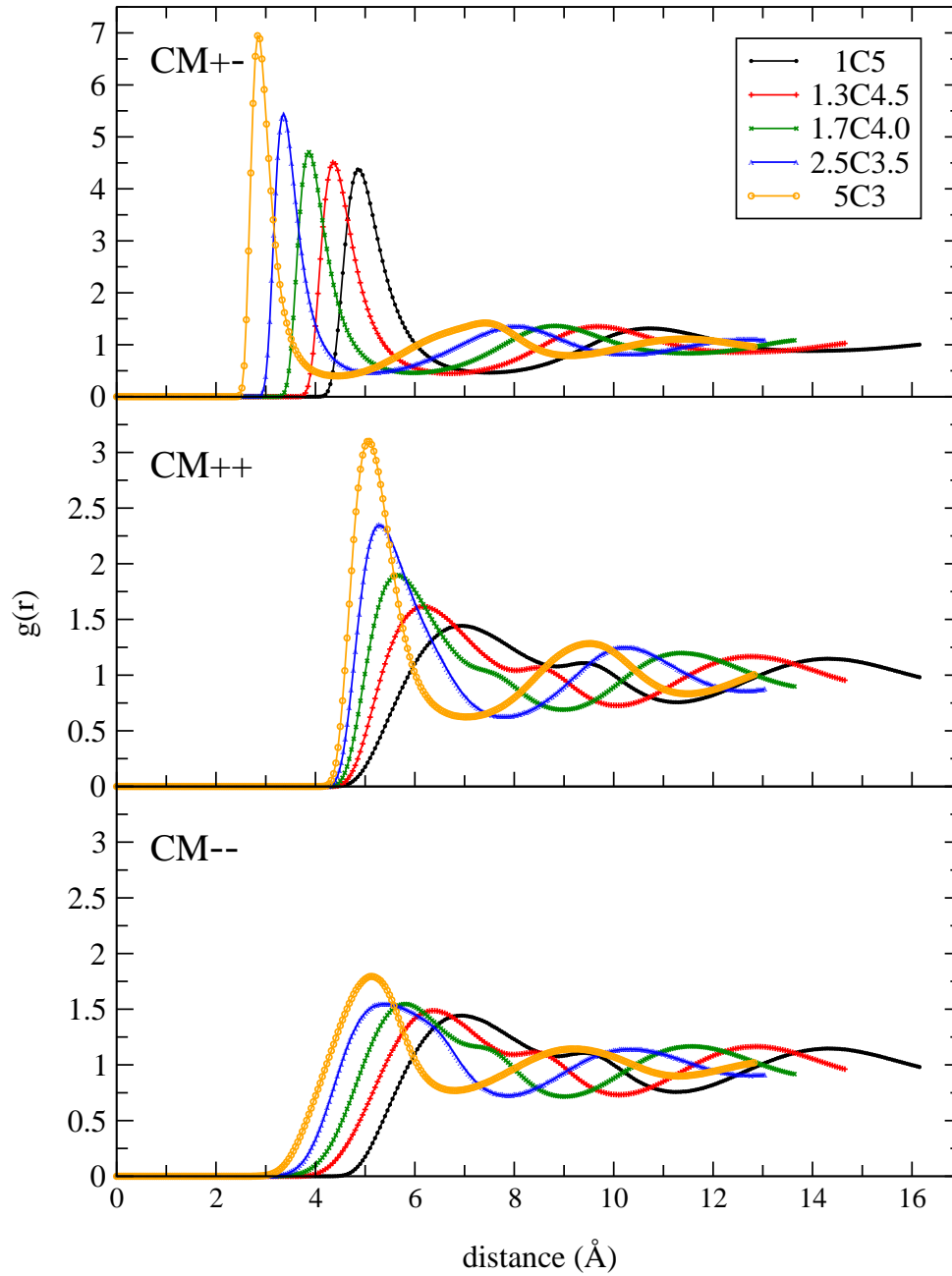
In Chapter 2 [4] we focused on isolating the influence of ion size disparity, and σ'_{+-} (note that, $\sigma'_{+-} = \sigma_{+-}$ for charge-centered models) was held fixed at 5 Å. Here, we refer to this model as *XC5*, and the radial distribution functions obtained are shown in Fig. 2.1. To briefly summarize, because of the constraint on σ'_{+-} , for model *XC5* the position of the first peak in CM_{+-} is essentially independent of the ion size disparity X . As the cation becomes larger, the first peak in CM_{++} moves to larger separations, and becomes more determined by the core repulsions rather than the Coulombic interactions, as one would expect. On the other hand, as the anion becomes smaller, the first peak in CM_{--} moves to *larger* separations, “following” the cation peak. This indicates that the structure of these strongly coupled Coulombic systems is largely determined by the packing of the larger ionic species.

The radial distribution functions for model *XCY* are plotted in Fig. 4.2. We note that the first peak in CM+- now moves to smaller separations as σ'_{+-} decreases from 5 to 3 Å. This effect is expected, but comparing with results (not shown) for model 1CY (ions of the same size but varying σ'_{+-}) we see that the height of the first peak is amplified by ion size disparity. For model *XCY*, the cations are the same size for all systems considered ($\sigma_+ = 5$ Å), but we see from Fig. 4.2, that the first peak in CM++ moves to smaller separations (from 7 to 5.05 Å) as the size disparity increases. Clearly, smaller anions allow the larger cations to approach each other more closely, likely by inserting between them and counteracting some of the direct Coulombic repulsion. The position of the first peak in CM-- moves to smaller separations as the anion decreases in size, but remains completely in step with the first peak in CM++. This again demonstrates the strongly coupled nature of these Coulombic systems. To summarize, in these relatively simple ionic liquids, the structure is very strongly influenced by the strong cation-anion attractions, and the importance of these interactions appears to increase with ion size disparity.

Influence of Size Disparity and Charge Location

A detailed discussion of the radial distribution functions of model 1OCY with displaced charges, compared with model 1CY (same σ'_{+-} as 1OCY, but no charge displacement) is given in Chapter 3.3.1 [8]. Therefore, here we concentrate on models characterized by both size disparity and charge displacement. The relevant radial distribution functions are plotted in Figs. 4.3 - 4.7. In these figures, results for models 1OCY, 2OCY, and 3OCY are displayed in the top, middle, and bottom panels, respectively.

First consider CC+- shown in Fig. 4.3. For all systems with no charge displacement (1OC5, 2OC5, and 3OC5, note that $\sigma'_{+-} = 5$ Å for all three), the first peak is at the same location and the peak heights are nearly the same. A repeating pattern emerges for all models when the charge is displaced. The first peak moves to shorter distances, first becoming wider and lower, then higher and narrower. The high peaks at short distances clearly show the increasing Coulombic counterion attraction. As the cation charge is more “exposed” to the anion, directional ion pairs of increasing strength are formed (see also

Figure 4.2: Center of mass radial distribution functions for model XCY .

Chapter 3.3.1 [8]). The peak height for systems with the same σ'_{+-} is higher for more size disparate systems ($3OCY > 2OCY > 1OCY$). This apparent increase in the counterion attraction is due to size disparity, in accord with Chapter 4.3.1, above.

The effective mean strength of the Coulombic attraction of oppositely charged ions can be assessed by comparing σ'_{+-} with the position of the first peak in $CC+-$, which we will call s_{+-} . These distances (note that σ'_{+-} is included in the system label) together with the percentage difference, $\delta = 100(\sigma'_{+-} - s_{+-})/\sigma'_{+-}$, are given in Tables 4.1 and 4.2. For charge-centered systems (Table 4.1), $\delta = 3 - 6\%$, showing larger increases for systems with smaller σ'_{+-} , as one would expect. For systems with off-center charge (Table 4.2), σ'_{+-} becomes smaller, so at first sight we might expect a corresponding increase in δ . However, from Table 4.2 we see that this depends on how far the charge is displaced from the center. If the displacement is small, we observe a decrease in δ , with negative values for some systems. This indicates that for small charge displacements the distribution of counterions about the positive ion remains nearly spherically symmetric, and hence the mean charge-charge distance is larger than σ'_{+-} . As the charge is moved further off center, the Coulombic attraction becomes stronger, leading eventually to strongly bound directional ion pairs, and large positive values of δ .

Evidence of ion pairing can also be observed in $CM+-$ (Fig. 4.4). Here the first peak again shifts to shorter distances as the charge is displaced, but now, in addition, it splits into two peaks. The new first peak can be attributed to directional ion pairs, the second peak to “non-bonded” counterion neighbors. The peak shift and splitting happens more rapidly as a function of charge displacement for the more size disparate charge-off-center models, showing that ion pairs form more easily and are stronger if there is size disparity.

$CM++$ is shown in Fig. 4.5, and we note that different behavior is observed for $1OCY$ than for the size disparate models. For $1OCY$, the first peak becomes broader and shifts to smaller separations as the charge is moved off center, whereas, for $2OCY$ and $3OCY$ the first peaks exhibits little sensitivity to charge displacement. This is because in $1OCY$ the formation of directional ion pairs with the possibility of different relative orientations influences the center-of-mass distribution of the cations. In $2OCY$ and $3OCY$, directional

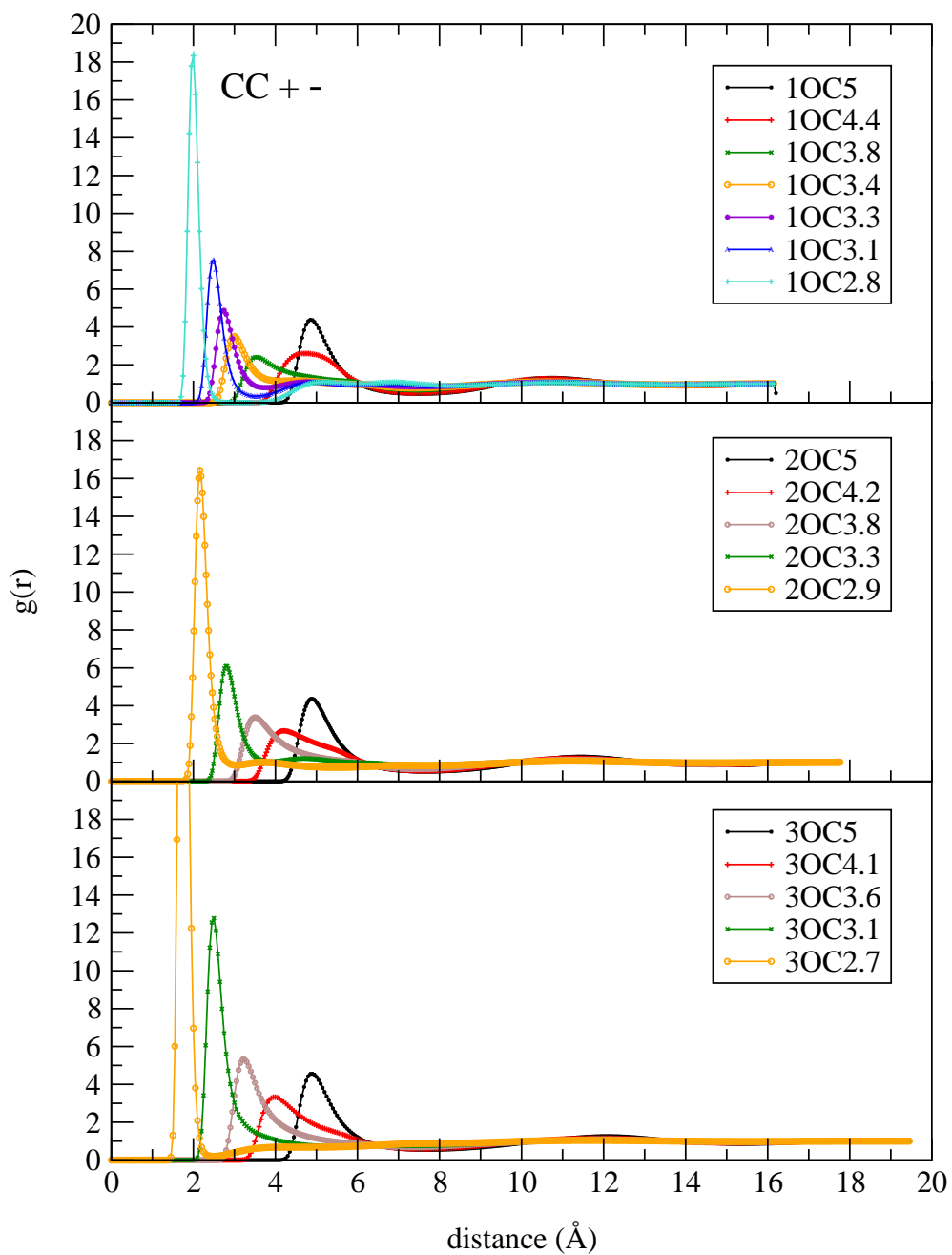


Figure 4.3: Cation-anion center of charge radial distribution functions for models 1OCY (top), 2OCY (middle), and 3OCY (bottom).

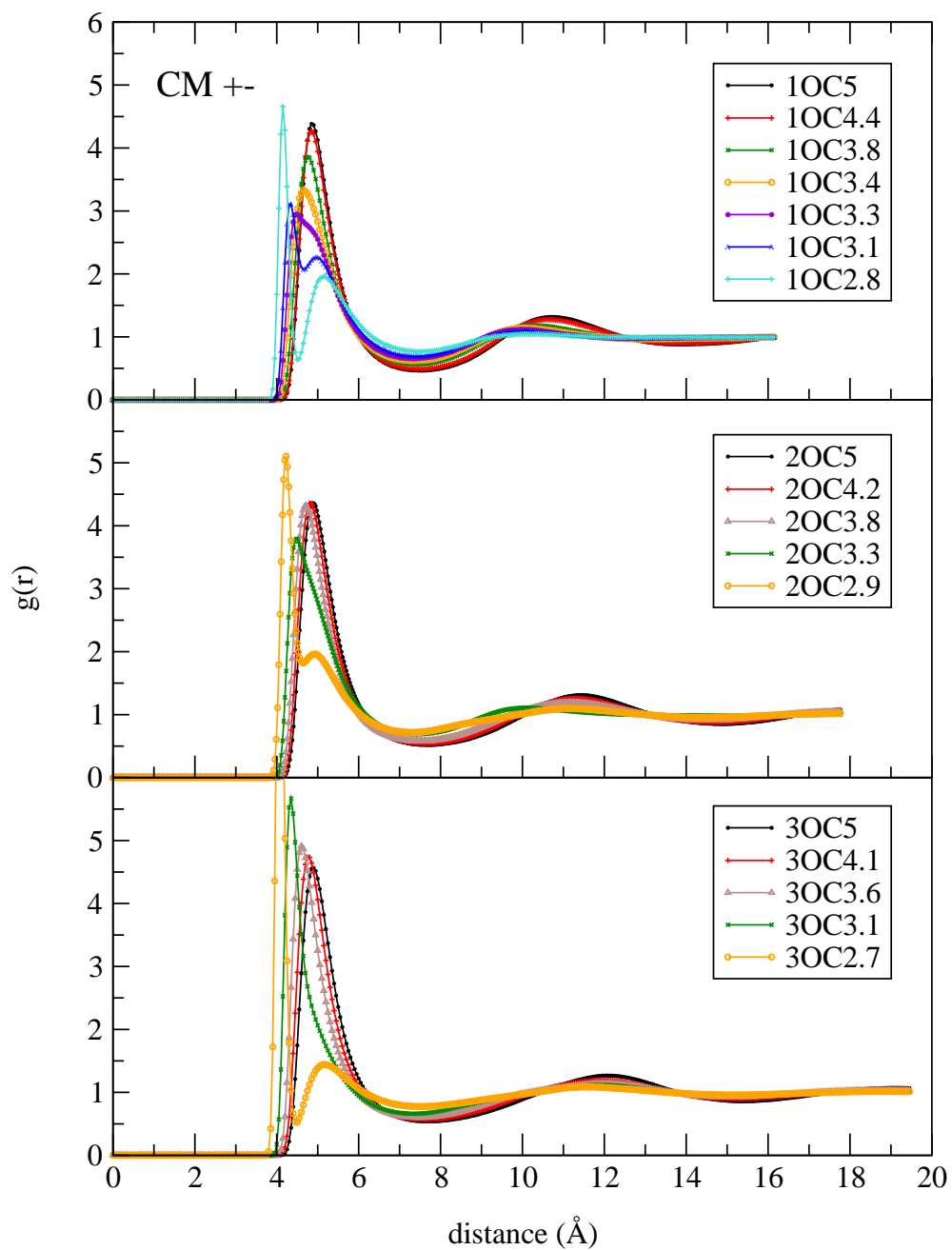


Figure 4.4: Cation-anion center of mass radial distribution functions for models 1OCY (top), 2OCY (middle), and 3OCY (bottom).

ion pairs are also formed (even more readily), but in these systems the cations are so large that their core repulsions dominate the distribution of their centers of mass.

Further structural insight can be obtained from $CC++$ and $CM--$ plotted in Figs. 4.6 and 4.7. It is immediately apparent, particularly for the size disparate systems $2OCY$ and $3OCY$, that $CC++$ and $CM--$ are of similar shape and exhibit the same dependence on charge location. This can be explained by the strong Coulombic coupling and ion pairing in these systems. Qualitatively, one can regard the directional ion pairs as single “units”, with their average separation mainly determined by the core repulsions of the larger cations (see above discussion of $CM++$). This results in distributions of similar shape for the positive and negative charges, but shifted to larger distances for the positive charges, because in an ion pair the positive charge is closer to the cation center of mass.

To briefly summarize, from a structural perspective, charge displacement combined with size disparity leads to varied behavior that can be largely rationalized by considering the shifting importance of the different interactions present in the system. Displacing the charge away from the center of mass strongly influences the importance of the Coulombic attractions. Small displacements weaken its influence, but larger displacements strengthen it leading to directional ion pairs. As pairs are formed, the importance of the Coulombic repulsions are reduced due to cancellation effects of the opposite charges bound in close proximity. This effect is especially pronounced for size disparate systems where the core repulsions of the larger species (the cation in our models) become increasingly important with increasing size disparity.

Further insight into the nature of the Coulombic coupling in our model ionic liquids can be obtained from the radial charge distribution functions defined as [30, 31]

$$Q_{\alpha}^{CM/CC}(r) = \rho_{\alpha} [g_{\alpha\alpha}(r) - g_{\alpha\beta}(r)] , \quad (4.6)$$

where α and β denote the ionic species and $g_{\alpha\beta}(r)$ is either the center of mass [to obtain $Q_{\alpha}^{CM}(r)$] or the center of charge [to obtain $Q_{\alpha}^{CC}(r)$] radial distribution function. Some example $rQ_{\alpha}^{CM}(r)$ plots are given in Fig. 4.8, and we note that all functions of this type

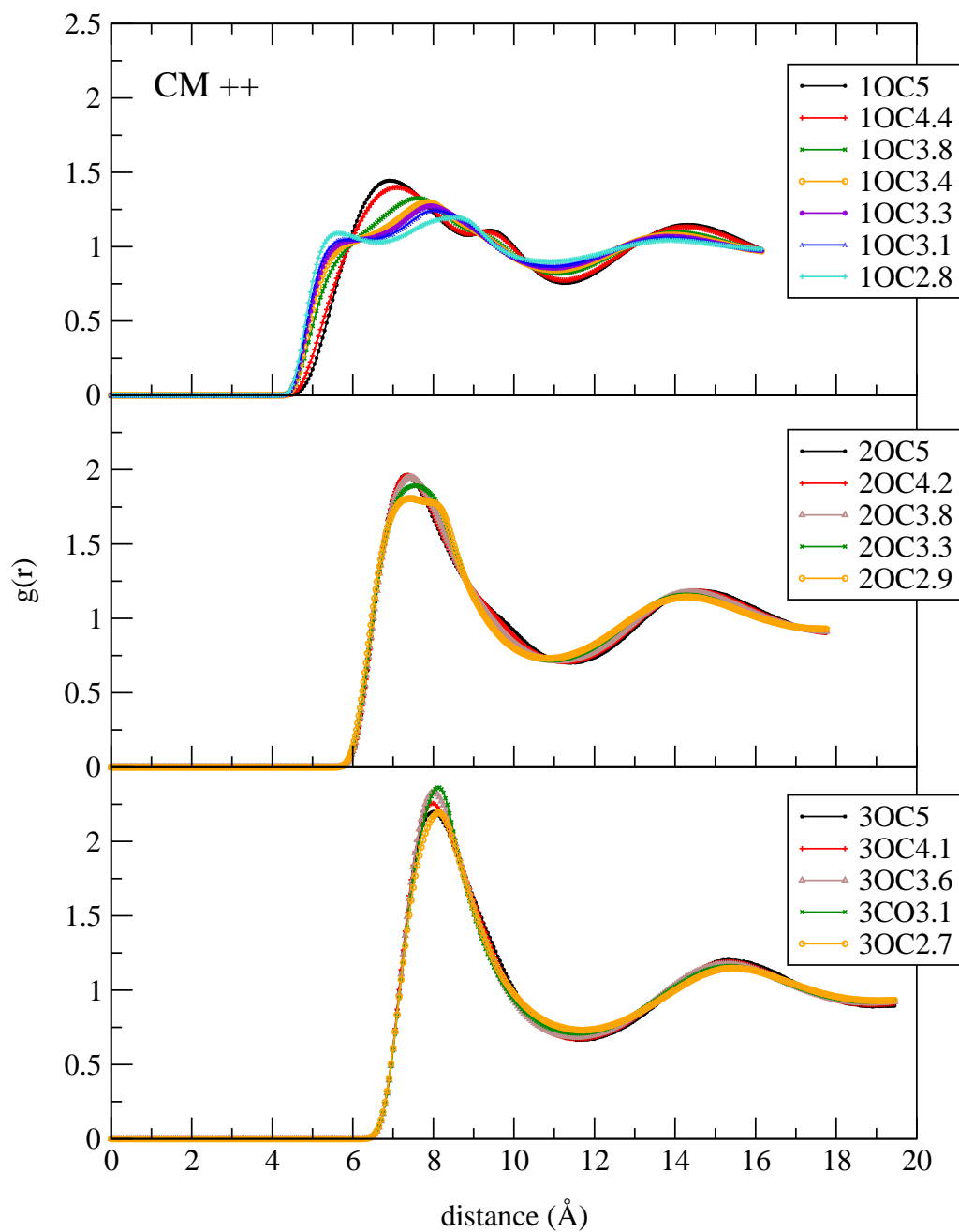


Figure 4.5: Cation-cation center of mass radial distribution functions for models 1OCY (top), 2OCY (middle), and 3OCY (bottom).

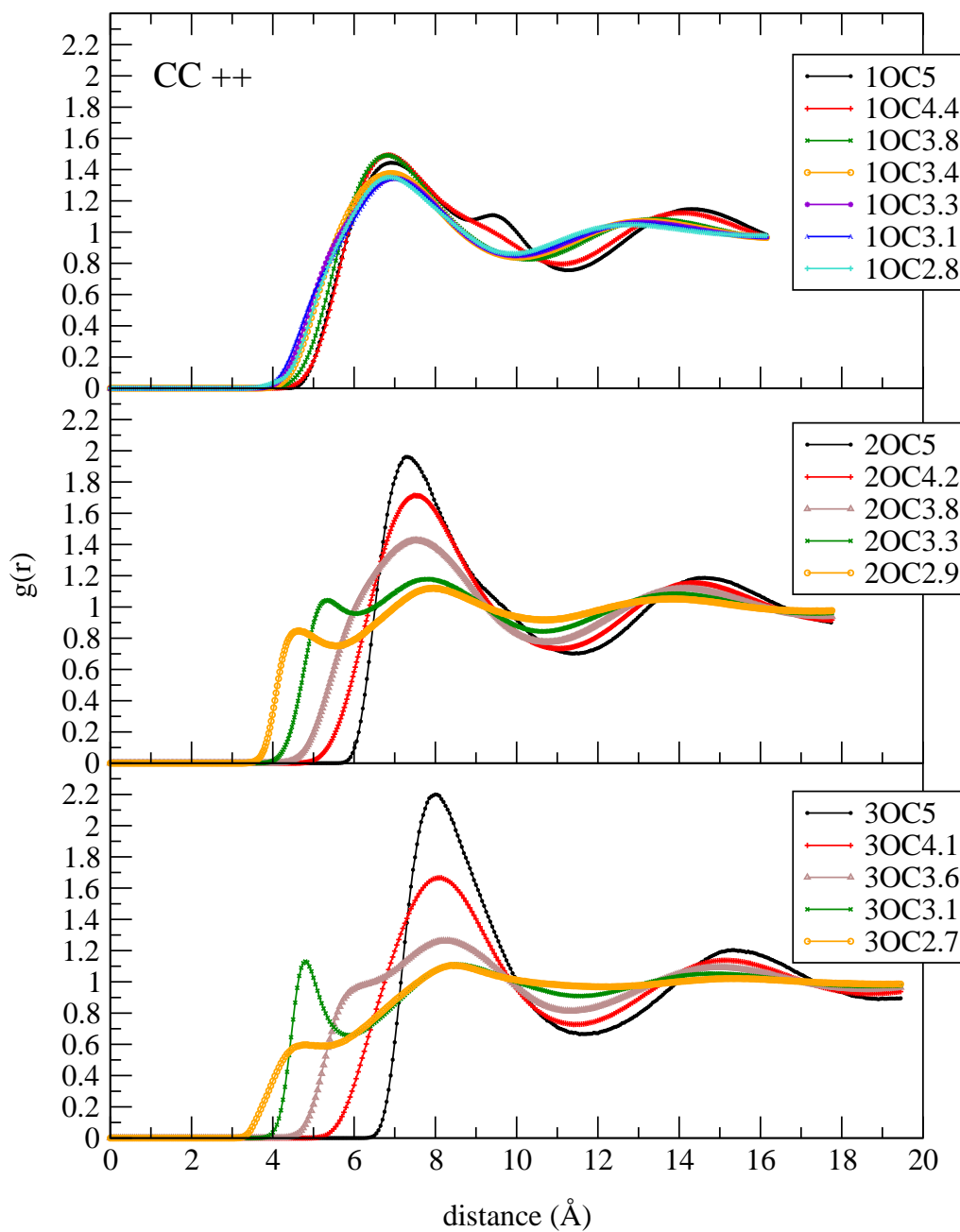


Figure 4.6: Cation-cation center of charge radial distribution functions for models 1OCY (top), 2OCY (middle), and 3OCY (bottom).

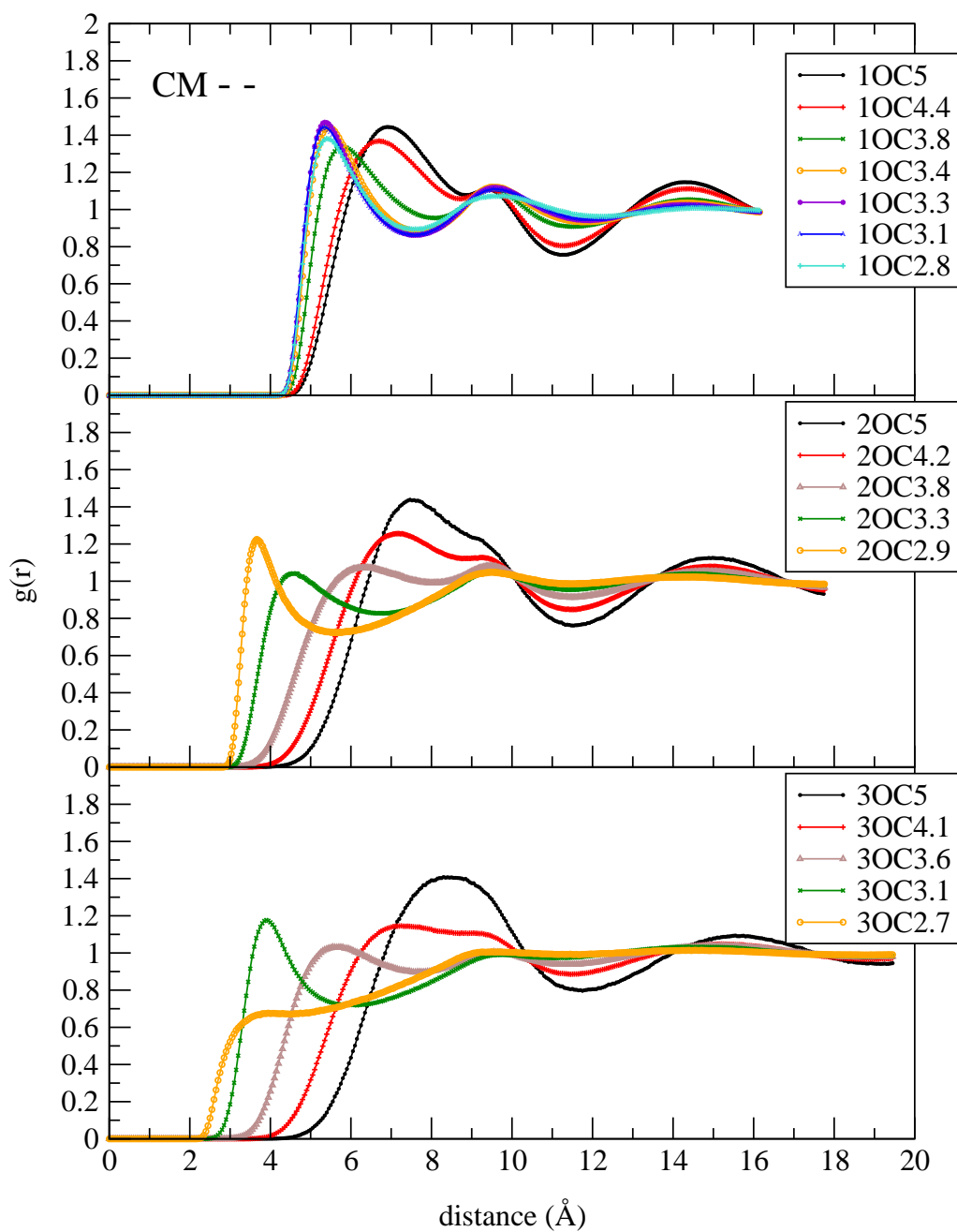


Figure 4.7: Anion-anion center of mass radial distribution functions for models 1OCY (top), 2OCY (middle), and 3OCY (bottom).

have some common features. In particular, all have a deep, sharp minimum at the most probable countercharge separation, and all display the screened oscillatory behavior typical of strongly coupled Coulombic systems. For all models, the first minimum moves to smaller separations as the charge is moved off center, and in most cases the amplitude of the oscillations decreases as well. This behavior can be attributed to the formation of ion pairs; strongly bound opposite charges “neutralize” each other to a large extent, such that less screening from other “unbound” charges is needed. An exception is $rQ_+^{\text{CM}}(r)$ for size disparate systems (e.g., model *3OCY*, middle panel of Fig. 4.8), where the oscillations decrease only slightly in amplitude as the charge is moved off center. This is because in this size disparate system with large cations, the non-Coulombic, cation-cation core interactions tend to determine the cation center-of-mass distribution, even for systems where the charge displacement is large.

To assist with our understanding of the transport properties, particularly the diffusion coefficients, discussed in Chapter 4.3.2, it is useful to consider running coordination numbers defined as

$$CN_\alpha(R) = 4\pi \int_0^R [\rho_\beta \text{CM}\alpha\beta(r) + \rho_\alpha \text{CM}\alpha\alpha(r)] r^2 dr, \quad (4.7)$$

where α and β again denote the ionic species. $CN_+(R)$ results are plotted in Fig. 4.9 for models *XC5* and *XCY* (top panel), and model *3OCY* (bottom panel). We see that for both *XC5* and *XCY*, the coordination numbers decrease significantly with increasing size disparity, at least at the fixed reduced density ($\rho^* = 0.8$) considered here. The results for *3OCY* show that, at fixed size disparity, the coordination numbers are not strongly dependent on the charge location. This is consistent with our earlier observations in Chapter 3.3.1, Fig. 3.3 [8] for model *1OCY*, with off-center charge, but no size disparity. We note that plots of $CN_-(R)$ (not shown) are very similar to those shown in Fig. 4.9, and exhibit exactly the same trends.

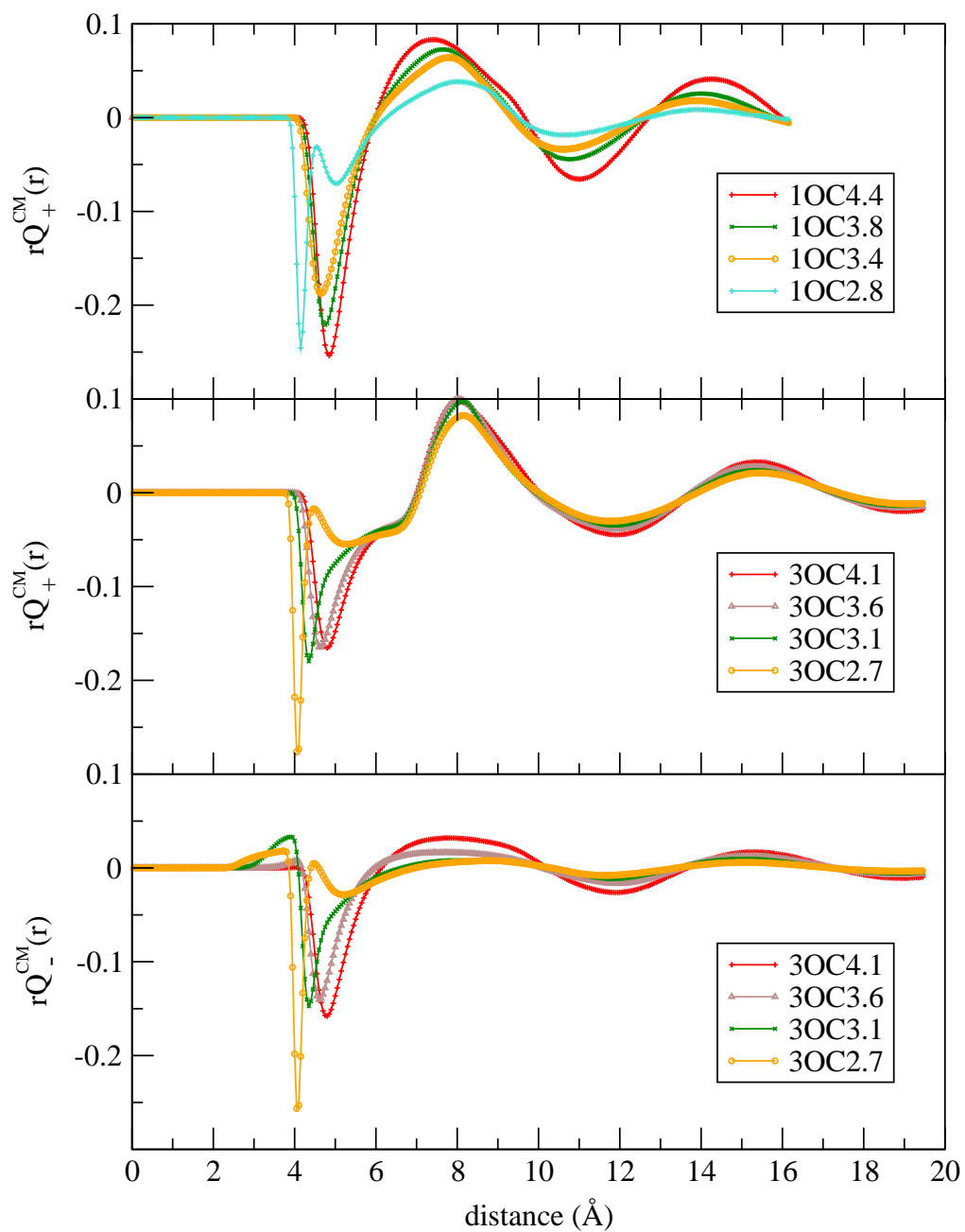


Figure 4.8: Radial charge distribution functions for models 1OCY (top) and 3OCY (middle and bottom).

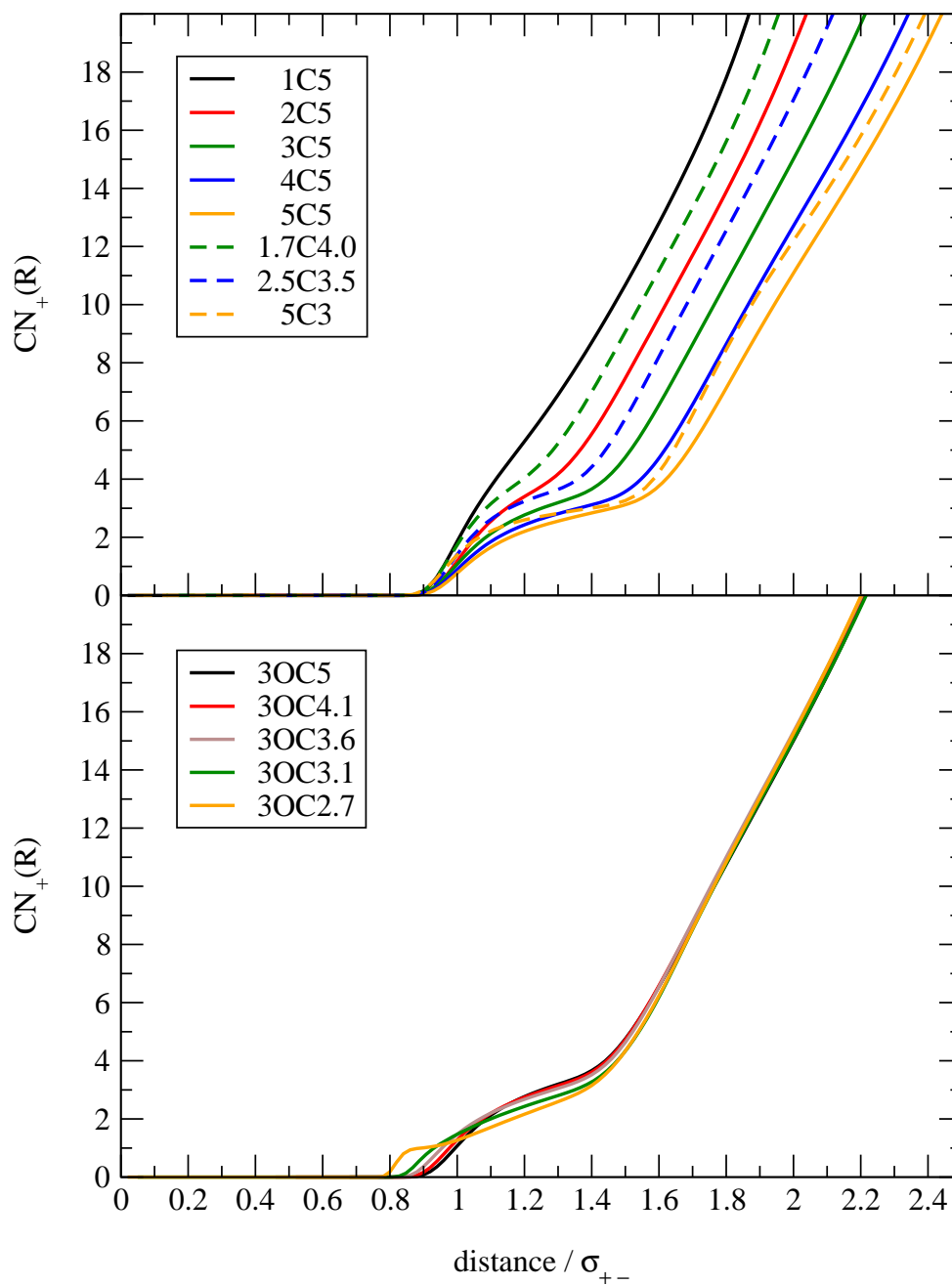


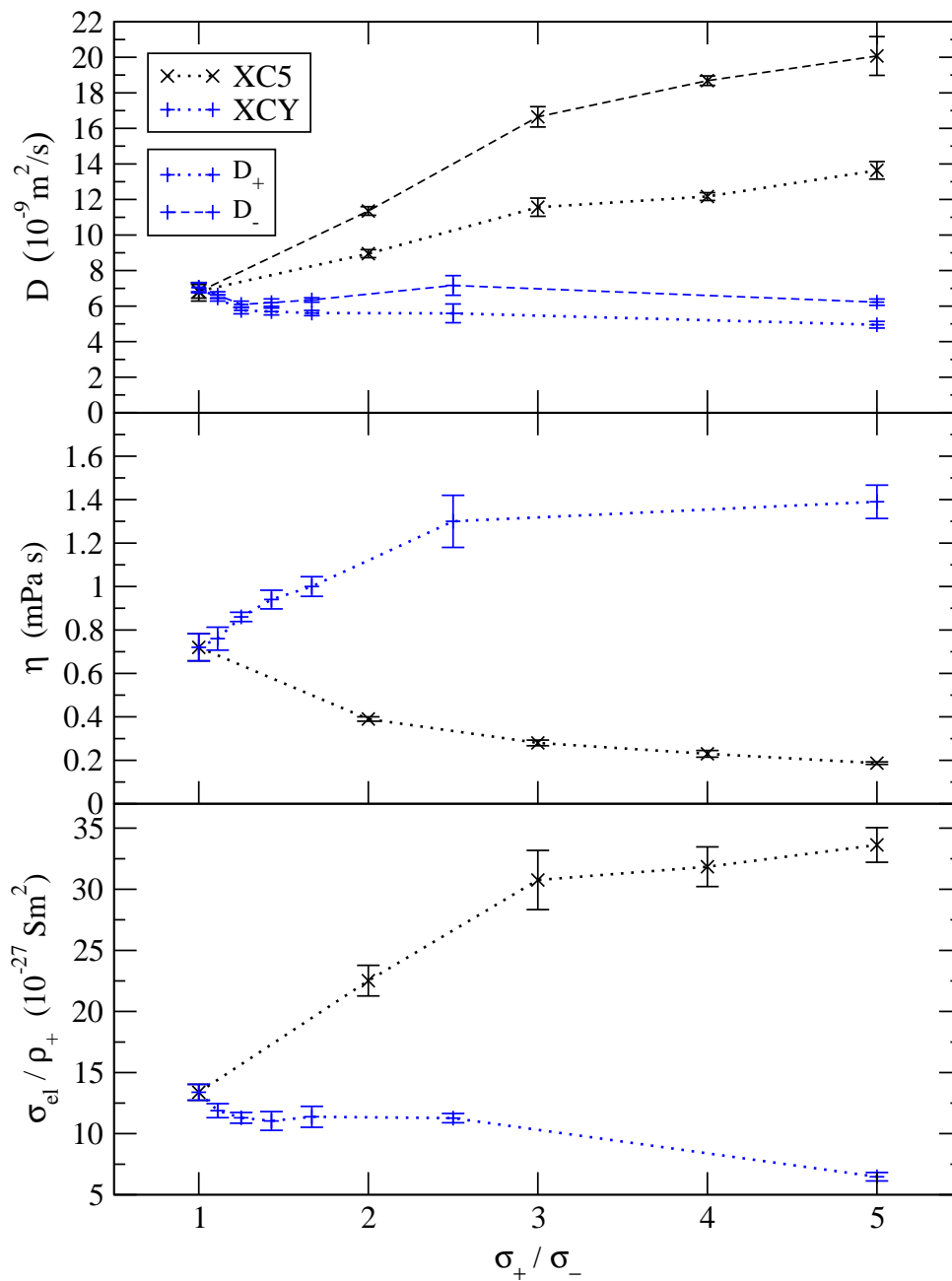
Figure 4.9: Running coordination numbers of the cations for models $XC5$, XCY (top), and $3OCY$ (bottom).

4.3.2 Transport Properties

Influence of Size Disparity and the Distance σ'_{+-}

We first compare model *XC5*, where the size disparity increases but σ'_{+-} remains constant, with *XCY*, where σ'_{+-} decreases as the size disparity increases. The transport properties for both models are plotted in Fig. 4.10 as functions of size disparity. Note that the charge density ($\rho_+ = \rho_-$) varies with size disparity at fixed reduced density $\rho^* = 0.8$. Therefore, to make clear the influence of other factors on the conductivity, $\sigma_{\text{el}}/\rho_+$ is shown in Figs. 4.10-4.13. It can be seen (Fig. 4.10) that for *XC5* the diffusion coefficients increase with increasing size disparity, and the viscosity decreases. Precisely opposite trends are observed for *XCY*. So, increasing size disparity and decreasing σ'_{+-} exert opposite influences on these properties. We note that for both of these charge-centered models, the coordination numbers decrease with increasing size disparity (see above), which helps explain the increasing diffusion coefficients observed for *XC5*. Apparently, for *XCY* this effect is more than offset by the stronger Coulombic interactions associated with the decreasing σ'_{+-} . The situation is similar for the electrical conductivities. For *XC5*, $\sigma_{\text{el}}/\rho_+$ increases with increasing size disparity, whereas a decrease is observed for *XCY*, closely following the behavior of the diffusion coefficients.

Next, we compare *XCY* (increasing size disparity, decreasing σ'_{+-}) with *1CY* (no size disparity, but decreasing σ'_{+-}). For these models, the dependence of the transport properties on σ'_{+-} is shown in Fig. 4.11. For *1CY*, the diffusion coefficients decrease with decreasing σ'_{+-} in a roughly linear manner. For *XCY*, the diffusion coefficients show similar behavior for large σ'_{+-} (where size disparity is small), but then deviate from this trend and show little further decrease with σ'_{+-} . This again illustrates that the influences of σ'_{+-} and size disparity are opposite in nature, and can essentially cancel each other. A similar effect can be seen in the viscosity, where the increase with decreasing σ'_{+-} is much larger for *1CY* than for *XCY*. Clearly, size disparity is a very important variable influencing the viscosity of ionic liquids, and will significantly decrease the viscosity, even if σ'_{+-} is small. For both *XCY* and *1CY*, $\sigma_{\text{el}}/\rho_+$ decreases with decreasing σ'_{+-} , but the decrease is considerably slower

Figure 4.10: Transport properties versus size disparity for models *XC5* and *XCY*.

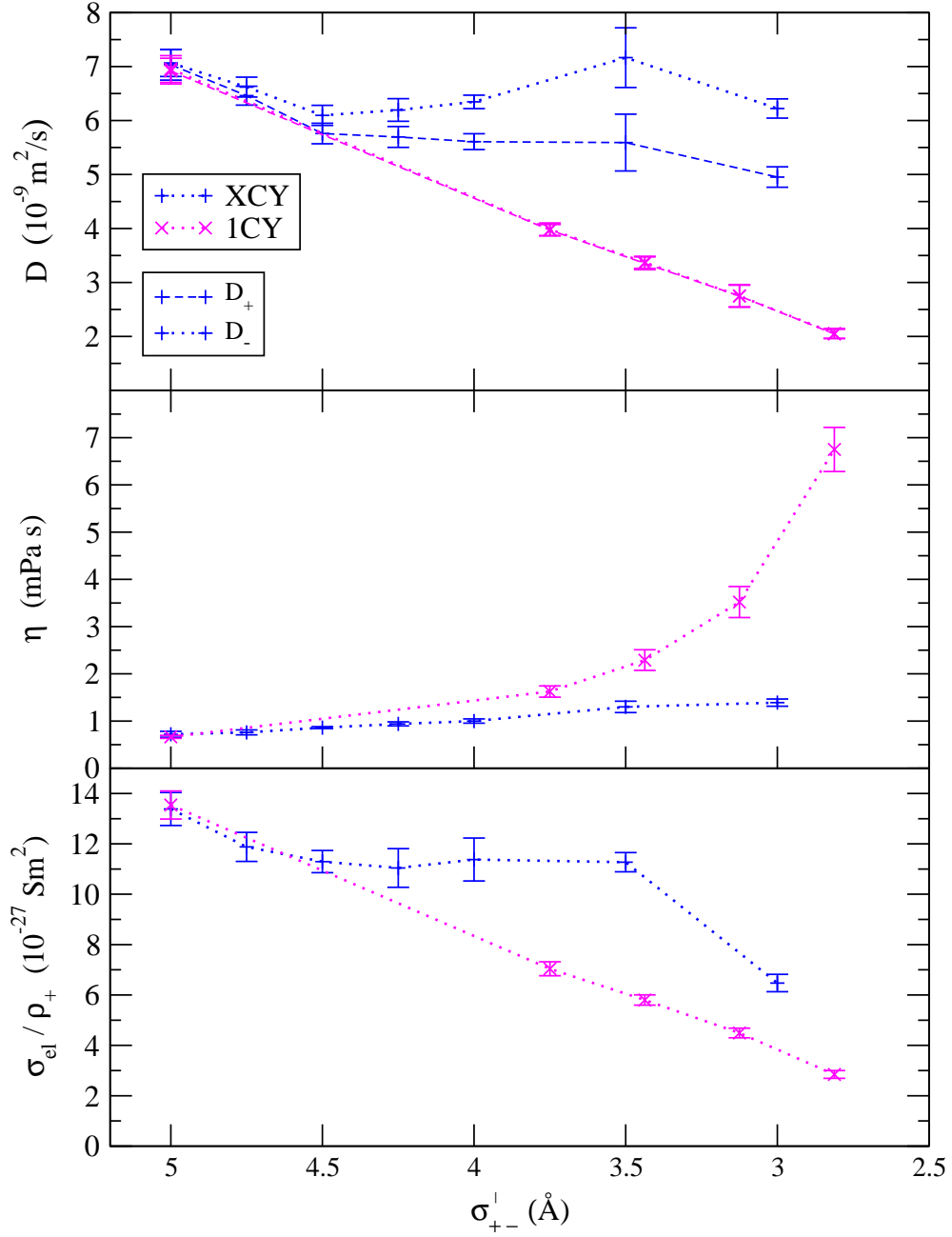


Figure 4.11: Transport properties versus σ'_{+-} for models *XCY* and *1CY*.

for XCY . This is another demonstration of the competing influences of size disparity and σ'_{+-} .

Influence of Size Disparity and Charge Location

For the off-center models ($1OCY$, $2OCY$, $3OCY$), it is instructive to view the transport properties as functions of both l_q/R_+ ($R_+ = \sigma_+/2$) (Fig. 4.12) and of σ'_{+-} (Fig. 4.13). Note that in Fig. 4.13, results for the charge-centered model $1CY$ are included for comparison. Note also that some results obtained with 512 ions (instead of 216) are shown in Fig. 4.13. Except for the viscosity of model $1CY$, the number dependence can be described as small, and clearly in no case does it influence our qualitative conclusions. From Fig. 4.12, we see that for all three models the diffusion coefficients increase as the charge is moved further off center, and also with increasing size disparity. Note that moving the charge off center does not significantly influence the coordination numbers (see Fig. 4.9), so the increase of the diffusion coefficients with increasing l_q/R_+ is not associated with reduced coordination numbers. Rather, the increases are likely due to the increasing asymmetry of the ion-counterion interactions. From Fig. 4.13, we see that the behavior of the diffusion coefficients is not simplified when viewed as functions of σ'_{+-} , but in this plot one can see a clear contrast with the charge-centered model $1CY$, where the diffusion coefficients decrease with decreasing σ'_{+-} . We note also, that for the $XOCY$ models, D_+ and D_- tend to approach each other at small σ'_{+-} (large l_q/R_+), reflecting ion pair formation.

For the charge-off-center models, the viscosity first decreases, and then increases steeply, as functions of both l_q/R_+ and σ'_{+-} . Viewed as a function of l_q/R_+ (Fig. 4.12), the upturn in viscosity occurs at smaller l_q/R_+ values as the size disparity is increased, whereas, when the viscosities are plotted as functions of σ'_{+-} , the results for all $XOCY$ models collapse roughly onto the same curve. This indicates that for all models the upturn in viscosity is mainly associated with directional ion pairs, and that the propensity to form such pairs is mostly determined by σ'_{+-} . This observation is further supported by the fact that an increase in ion pair lifetimes τ_{ip} (Table 4.2) coincides with the increase in viscosity for all models. We note that for $1CY$ the viscosity increases as σ'_{+-} decreases, and is always larger

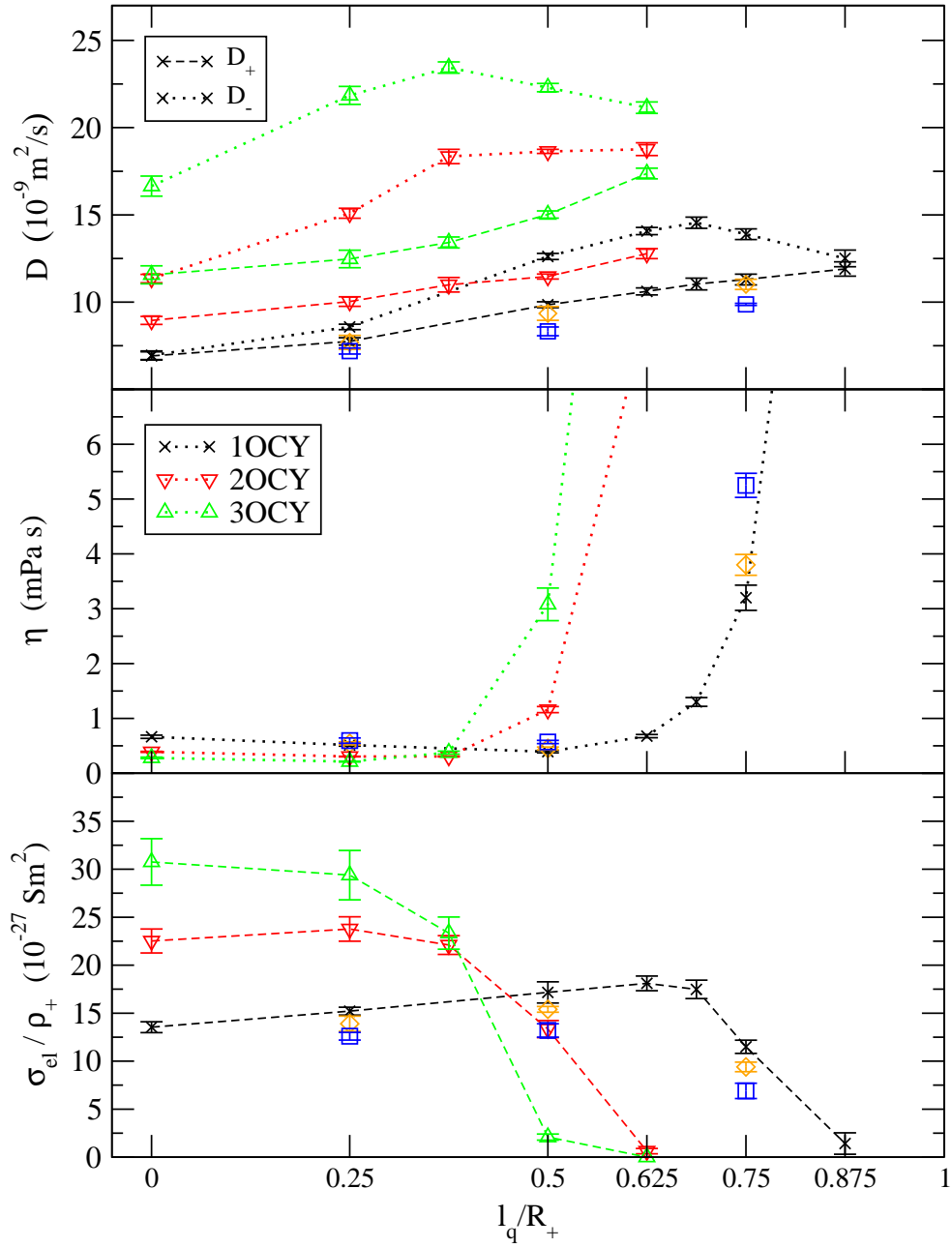


Figure 4.12: Transport properties versus charge displacement for models 1OCY, 2OCY, and 3OCY. The diamonds (orange) and squares (blue) represent the results obtained for model 1OCY with cation moments of inertia of 2.8×10^{-45} , and 2.8×10^{-44} kg m^2 , respectively. All other results were obtained using 2.8×10^{-46} kg m^2 . Note that for clarity the dependence of the diffusion coefficients on the moment of inertia is shown only for the positive ion.

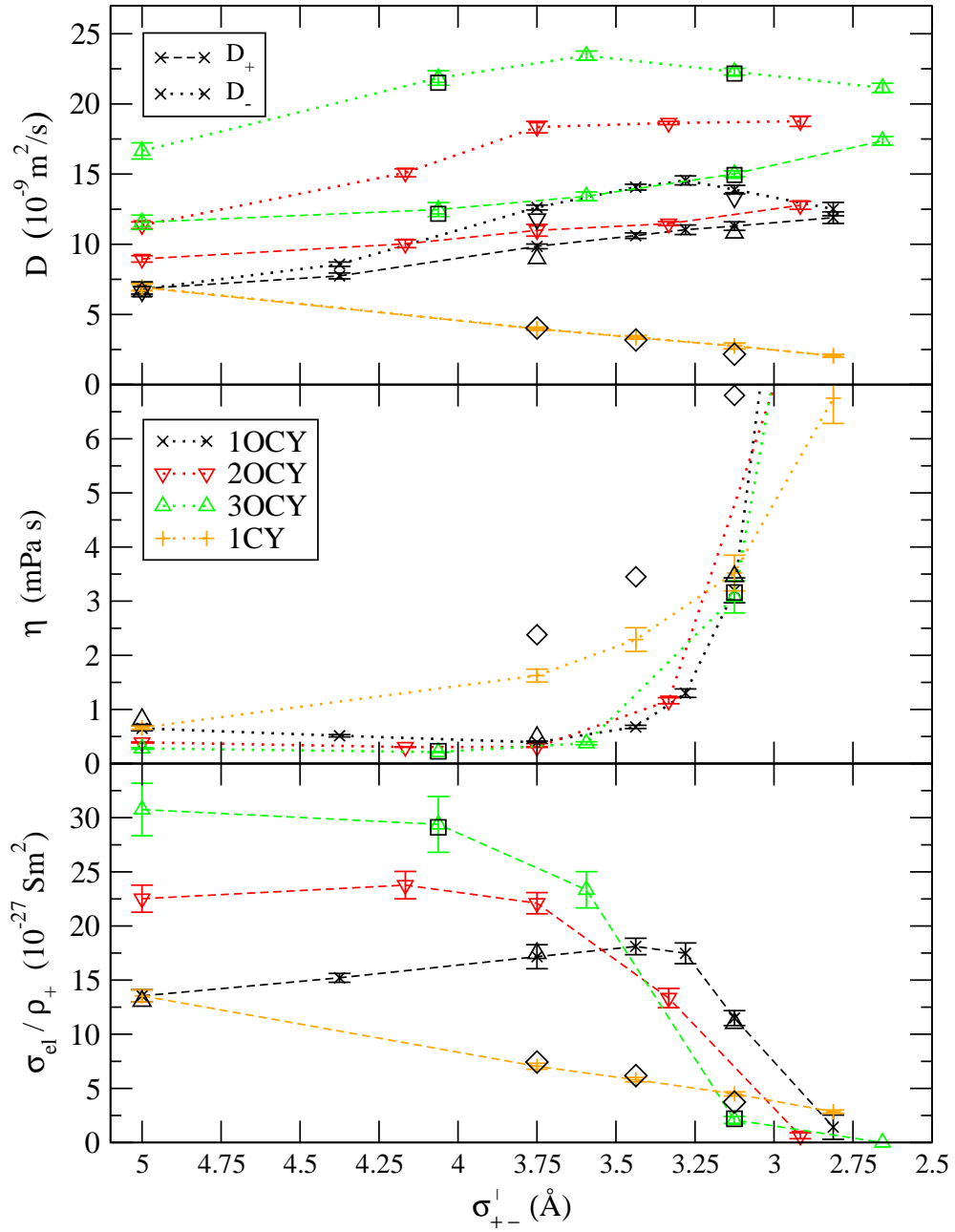


Figure 4.13: Transport properties versus σ'_{+-} for models 1OCY, 2OCY, 3OCY, and 1CY. The open, black diamonds, triangles, and squares indicate results obtained with 512 ions for systems 1CY, 1OCY, and 3OCY, respectively.

than that of the charge-off-center models for $\sigma'_{+-} \lesssim 3.25 \text{ \AA}$.

For the *XOCY* models, $\sigma_{\text{el}}/\rho_+$ shows little dependence on l_q/R_+ or σ'_{+-} until the onset of ion pairing. Ion pairing induces a steep decrease in the conductivity at smaller l_q/R_+ values as size disparity is increased (Fig. 4.12), similar to the increases observed in the viscosity. As a function of σ'_{+-} , there is some collapse of the data towards a single curve (Fig. 4.13), but not to the extent found for the viscosity. We note that in the unpaired regime ($l_q/R_+ \lesssim 0.375$, $\sigma_{+-} \gtrsim 4 \text{ \AA}$) size disparity leads to significantly increased conductivity, likely reflecting the increased diffusion coefficients discussed above. For *1CY*, the conductivity is lower than that of the *XOCY* models at values of σ'_{+-} where ion pairing is not important, but remains larger in the region where directional ion pairs greatly reduce the conductivities of the *XOCY* models.

Angular velocity autocorrelation functions $C_\omega(t)$ and reorientational correlation functions $O(t)$ are shown for the cations of selected size-disparate, charge-off-center models (*3OCY*) in Figs. 4.14 and 4.15, respectively. We note that the behavior of these functions for models *1OCY* and *2OCY* is generally similar (not shown). From Fig. 4.14, we see that $C_\omega(t)$ displays oscillatory behavior with the period of oscillation becoming shorter as the charge is moved further from the center. This behavior leads to decreasing rotational diffusion coefficients, and is clearly associated with the increasing number and lifetimes of directional ion pairs (see Table 4.2).

The functions $O(t)$ (Fig. 4.15) display two modes of decay: (i) a very fast short-time mode, that becomes less pronounced as the charge is moved further off-center, and is likely due to “free” cations and/or the librational motions of cations within ion pairs; and (ii) a much slower decay, consistent with the behavior one would expect for the reorientational motion of directional ion pairs (dipoles). As the charge is further displaced, we see that $O(t)$ decays more slowly for systems *3OC4.1* to *3OC3.1*, but then at *3OC2.7* a reversal occurs, and the decay becomes faster. This is clearly reflected in the relaxation times τ_μ (estimated assuming exponential decay at long times) given in Table 4.2, note the increasing times up to *3OC3.1*, then the decrease for *3OC2.7*. The increasing τ_μ up to *3OC3.1* can be explained by the increasing numbers and lifetimes of directional ion pairs, but what gives

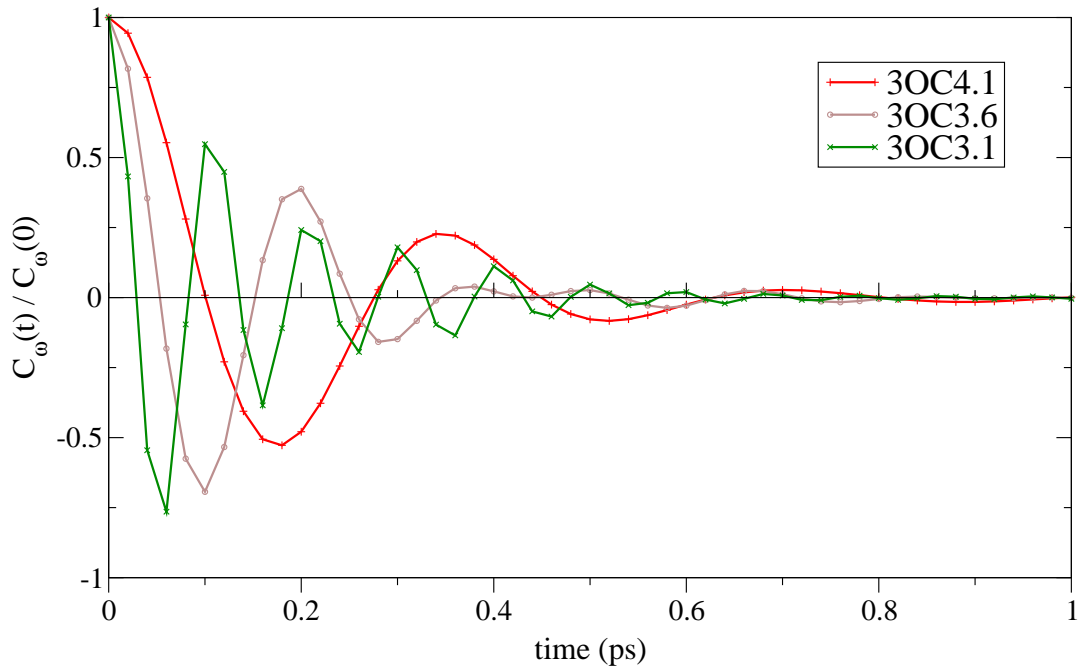


Figure 4.14: Angular velocity autocorrelation functions for model 3OCY.

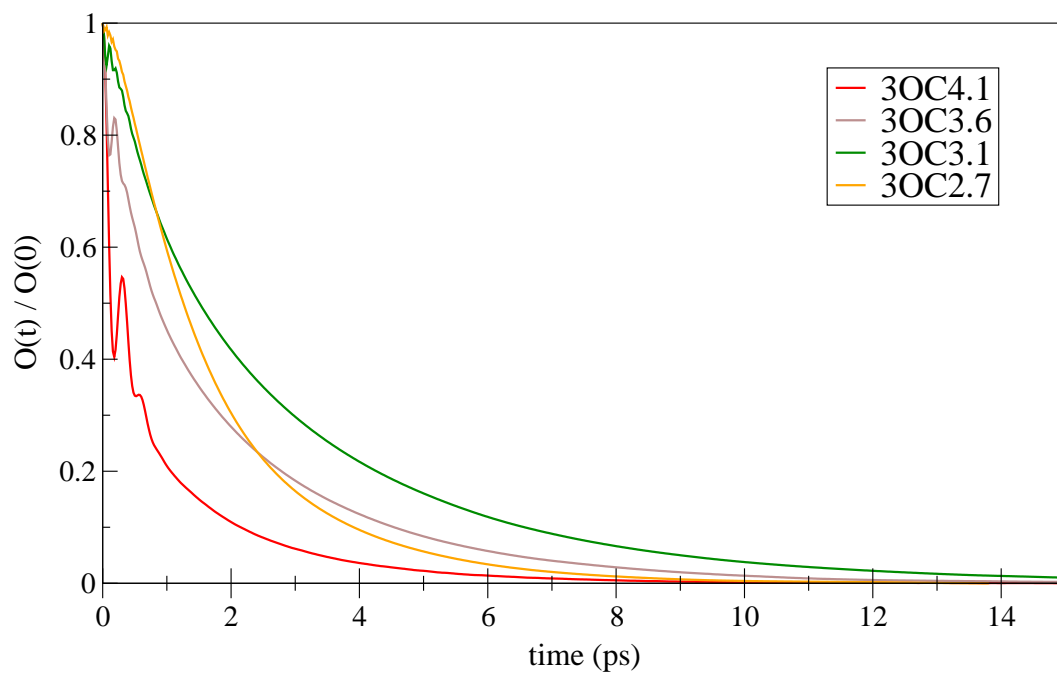


Figure 4.15: Reorientational time correlation functions for model 3OCY.

rise to the substantial decrease for 3OC2.7? One possible explanation is, that while there are more ion pairs (99% of the cations are paired), and their lifetimes are longer (17 ps vs. 1.1 ps for 3OC3.1) for 3OC2.7, because the most probable charge separation s_{+-} is shorter (1.75 Å vs. 2.5 Å for 3OC3.1), the dipole moment of a 3OC2.7 ion pair is significantly smaller than that of 3OC3.1. We would expect the decay of $O(t)$ to depend not only on the numbers and lifetimes of the directional ion pairs, but also on the magnitude of the associated dipole moments, indeed this last factor should dominate the relaxation once nearly all of the ions are paired. Thus, the faster relaxation observed for 3OC2.7 is likely due to smaller dipole moments, and hence weaker ion-pair-ion-pair interactions. We note that this could also account for the slight increase in D_R observed for 3OC2.7 (Table 4.2), which is also a reversal of trend. The reduced dipole moment can also explain the decrease in the first peak of CC++ and CC-- for 3OC2.7 in comparison to 3OC3.1.

The rotational motion of the cations depends on their moment of inertia, and can influence the dynamics of our charge-off-center model. Therefore, in order to check the sensitivity of the transport properties to this parameter, for three 1OCY systems we have carried out calculations with three different values of the cation moment of inertia, spanning two orders of magnitude (Table 4.2). The results obtained are included in Fig. 4.12, and we see that larger moments of inertia lead to reduced diffusion coefficients, larger viscosities, and lower conductivities. However, the variation of the transport properties is relatively small, and does not influence any of the qualitative trends discussed above. As one would expect, increasing the moment of inertia does have a significant effect on the rotational dynamics of the cation, reducing the rotational diffusion constants, and increasing the reorientational correlation times, τ_μ (Table 4.2). Also, as might be expected, the ion pair lifetimes are increased. Nevertheless, we note that these effects do not strongly influence the transport properties, indicating that dynamically the rotational-translational coupling is relatively weak, at least over the range of physically relevant moments of inertia.

4.4 Summary and Conclusions

In this Chapter we report how various molecular features influence the transport properties of ionic liquids. The main variables considered, both alone and in combination, are ion size disparity, charge location, and the characteristic length σ'_{+-} that determines the strength of the crucially important Coulombic attractions. Chapter 4 both extends and generalizes our earlier studies in Chapters 2 and 3 [4, 8] that focused on particular features, but not on how they enforce and/or oppose each other when present in combination.

For charge-centered models, we discuss the influence of varying size disparity for two different physical situations. In one case, as the size disparity is varied, the distance σ'_{+-} , that characterizes the Coulombic attraction, is held fixed. This model (here denoted *XC5*) serves to highlight the influences of size disparity alone, and was discussed in detail in Chapter 2 [4]. In the present Chapter, we also consider the experimentally more usual situation [6], where one ion is held constant while the counterion is changed systematically. In this model (*XC \mathcal{Y}*), both size disparity and σ'_{+-} vary with the changing counterion. We find that both models are similar in that, at fixed reduced density, the coordination numbers decrease significantly with increasing size disparity. For model *XC5*, this leads to predictable changes in the transport properties; the diffusion coefficients, and the electrical conductivity normalized by the density of charge carriers ($\sigma_{\text{el}}/\rho_+$) increase, and the shear viscosity decreases, with increasing size disparity. For model *XC \mathcal{Y}* , the results are less predictable. For this model, despite similar reductions in the coordination numbers, the trends in the transport properties described above for *XC5*, are essentially reversed. Thus, for *XC \mathcal{Y}* the influences of size disparity are opposed, and to some extent overcome, by the increasing Coulombic attraction associated with decreasing values of σ'_{+-} . Nevertheless, comparisons with model *1CY* (varying σ'_{+-} , but ions of equal size), clearly show that the effects of decreasing σ'_{+-} are largely mitigated by increasing size disparity.

For the charge-off-center models (denoted *XOC \mathcal{Y}*), the different influences on the transport properties are less easy to characterize. The behavior of these systems is made more complex by the formation of directional ion pairs, that become the dominant species in all

XOCY systems when l_q/R_+ is sufficiently large. This can have rather dramatic effects on the viscosity and conductivity. The behavior of the diffusion coefficients is relatively simple, these tend to increase with increasing l_q/R_+ , eventually becoming approximately constant, or decreasing slightly in the strongly paired limit. We note that moving the charge off center has only a marginal effect on the coordination numbers in all *XOCY* systems, so the increase in the diffusion coefficients with increasing l_q/R_+ cannot be associated with decreases in the coordination numbers, as is the case for size disparity. Instead, one surmises that the asymmetric nature of the cation-anion interactions facilitates diffusion. Also, comparing different *XOCY* systems, we find that in all cases the diffusion coefficients are significantly increased by size disparity, even in the strongly paired regime.

The behavior of the viscosity and conductivity for the *XOCY* systems is more complicated, and it is necessary to distinguish between weakly paired (or unpaired) and strongly paired regimes, noting that as l_q/R_+ is increased the crossover from one regime to the other occurs rather sharply. In the weakly paired region, the viscosity is reduced, and $\sigma_{\text{el}}/\rho_+$ either remains practically constant, or is slightly increased, as the charge is moved off center. Also, in this regime, the viscosity is decreased and $\sigma_{\text{el}}/\rho_+$ increased by size disparity, consistent with the behavior of the diffusion coefficients described above. At the crossover into the strongly paired regime, the viscosity increases rapidly, and the conductivity decreases rather sharply towards zero. This behavior is qualitatively similar for all *XOCY* models. We would expect the characteristic length σ'_{+-} , which varies both with charge displacement and size disparity, to be important for ion pairing. For all *XOCY* models, the crossover in the viscosity occurs at similar values of σ'_{+-} . However, the agreement is not as good for the conductivity, indicating that other factors are at play.

Although our *XOCY* model is obviously highly simplified, particularly in the assumption of spherical ions, it is possible to make some connection to real RTILs using the volume and l_q estimates available for a number of complex ions, for example, in Ref. [23]. If we make the further assumption of spherical ions, then the estimated l_q/R_+ values range from near zero to ~ 0.8 , which spans the range that we consider. A large majority, but not all, of these ions have l_q/R_+ values that would place them in the regime that we have identified

as weakly paired. However, as discussed in Chapter 3.3.2 [8], the transport properties of some RTILs with larger l_q/R_+ values do show behavior [7] which suggests that they may lie in the strongly paired regime.

Briefly summarized, our calculations show that size disparity, charge location, and σ'_{+-} can all have important influences on the transport properties of ionic liquids. Our results suggest possible strategies for optimizing desirable liquid properties. For example, high size disparity combined with a charge location that is off center, but outside the strongly paired regime, should help lower the viscosity and increase the conductivity of ionic liquids.

Interestingly, directional ion pairing, due to hydrogen bonding [20–22, 32] has been associated with reduced viscosities in some ionic liquids. This is strikingly similar to what we find for our charge-off-center, but not too far off-center, models. In this case, one has ion pairs that are relatively weakly bonded, compared to the far off-center systems where the ion pairs are much more strongly bonded and long-lived. In the weakly bonded regime, we find reduced viscosities consistent with the behavior described above, and we trace its origin to the asymmetric ion-counterion distributions in Chapter 3 [8]. That is, although the ions in a “bonded” pair interact more strongly with each other, they interact less strongly with other neighboring ions, leading to increased diffusion coefficients, and reduced viscosities. We note that in some experimental situations, where a hydrogen bond is introduced by replacing a methyl group with a hydrogen, the interpretation of the results is complicated by associated changes in the molar volume [32]. This is not an issue in our simulations because the ion size does not change as we change the charge location, thus in our case the viscosity changes can be solely attributed to the formation of directional ion pairs. It is important to emphasize, that in our model the directional ion pair bonds become increasingly stronger as the cation charge is moved further off center. In this regime, where long-lived ion pairs dominate the system, the viscosity trend is reversed, and the viscosity becomes an increasing function of charge displacement. This does not appear to have been observed in experiments, and, in fact, it has been suggested that making more strongly hydrogen bonded ion pairs might lead to further viscosity reduction [32]. Given our observations for the strongly bonded regime, it will be interesting to see if this proves to be the case.

Bibliography

- [1] H. Weingärtner, *Angew. Chem. Int. Ed.* **47**, 654 (2008), and references therein.
- [2] M. N. KobraK, *Adv. Chem. Phys.* **139**, 83 (2008), and references therein.
- [3] A. A. H. Pádua, M. F. Costa Gomes and J. N. A. Canongia Lopes, *Acc. Chem. Res.* **40**, 11, 1087 (2007).
M. G. Del Popolo, J. Kohanoff, R. M. Lynden-Bell and C. Pinilla, *Acc. Chem. Res.* **40**, 11, 1156 (2007).
M. Smiglak, A. Metlen and R. D. Rogers, *Acc. Chem. Res.* **40**, 11, 1182 (2007).
Y. Wang, W. Jiang, T. Yan and G. A. Voth, *Acc. Chem. Res.* **40**, 11, 1193 (2007).
- [4] H. V. Spohr and G. N. Patey, *J. Chem. Phys.* **129**, 064517 (2008).
- [5] S. Seki, K. Hayamizu, S. Tsuzuki, K. Fujii, Y. Umebayashi, T. Mitsugi, T. Kobayashi, Y. Ohno, Y. Kobayashi, Y. Mita, H. Miyashiro, and S. Ishiguro, *Phys. Chem. Chem. Phys.* **11**, 3509 (2009).
- [6] H. Shirota, K. Nishikawa, and T. Ishida, *J. Phys. Chem. B* **113**, 9831 (2009).
- [7] M. N. KobraK and N. Sandalow, in *Molten Salts XIV* (The Electrochemical Society, Pennington, NJ, 2006).
- [8] H. V. Spohr and G. N. Patey, *J. Chem. Phys.* **130**, 104506 (2009).
- [9] D. R. MacFarlane, M. Forsyth, E. I. Izgorodina, A. P. Abbott, G. Annat, and K. J. Fraser, *Phys. Chem. Chem. Phys.* **11**, 4962 (2009).
- [10] K. J. Fraser, E. I. Izgorodina, M. Forsyth, J. L. Scott, and D. R. MacFarlane, *Chem. Commun.* 3817 (2009).
- [11] A. Noda, K. Hayamizu, and M. Watanabe, *J. Phys. Chem. B* **105**, 4603 (2001).
- [12] H. A. Every, A. G. Bishop, D. R. MacFarlane, G. Orädd, and M. Forsyth, *Phys. Chem. Chem. Phys.* **6**, 1758 (2004).
- [13] S. Tsuzuki, H. Tokuda, K. Hayamizu, and M. Watanabe, *J. Phys. Chem. B* **109**, 16474 (2005).
- [14] B. Qiao, C. Krekeler, R. Berger, L. Delle Site, and C. Holm, *J. Phys. Chem. B* **112**, 1743 (2008).
- [15] P. Bonhôte, A. Dias, N. Papageorgiou, K. Kalyanasundaram, and M. Grätzel, *Inorg. Chem.* **35**, 5, 1168 (1996).

- [16] M. Buzzeo, R. Evans, and R. G. Compton, *Chemphyschem* **5**, 1106 (2004).
- [17] J. Dupont and J. Braz. *Chem. Soc.* **15**, 341 (2004).
- [18] G. Yu, S. Zhang, G. Zhou, X. Liu, and X. Chen, *AIChE* **53**, 12, 3210 (2007).
- [19] Y. Zhang, S. Zhang, X. Lu, Q. Zhou, W. Fan, and X. Zhang, *Chem. Eur. J.* **15**, 3003 (2009).
- [20] P. Hunt, *J. Phys. Chem. B* **111**, 4844 (2007).
- [21] K. Fumino, A. Wulf, and R. Ludwig, *Ang. Chem.* **47**, 8731 (2008).
- [22] S. Zahn, G. Bruns, J. Thar, and B. Kirchner, *Phys. Chem. Chem. Phys.* **10**, 6921 (2008).
- [23] H. Jin, B. O. Hare, J. Dong, S. Arzhantsev, G. A. Baker, J. F. Wishart, A. J. Benesi, and M. Maroncelli, *J. Phys. Chem. B* **112**, 81 (2008).
- [24] D. J. Evans and G. P. Morriss, *Comput. Phys. Rep.* **1**, 297 (1984).
- [25] D. Frenkel and B. Smit, *Understanding Molecular Simulation: From Algorithms to Applications* (Academic Press, 1996).
- [26] M. P. Allen and D. J. Tildesley, *Computer Simulations of Liquids* (Oxford, Clarendon, 1987).
- [27] J. P. Hansen and I. R. McDonald, *Theory of Simple Liquids*, 2nd ed. (Academic, London, 1986).
- [28] A. Chandra, *J. Phys. Chem. B* **107**, 3899 (2008), and references therein.
- [29] A. Luzar, *J. Chem. Phys.* **113**, 10663 (2000), and references therein.
- [30] P. Keblinski, J. Eggebrecht, D. Wolf, and S. R. Phillpot, *J. Chem. Phys.* **113**, 282 (2000).
- [31] Y. Shim, M. Y. Choi, and H. J. Kim, *J. Chem. Phys.* **122**, 044510 (2005)
- [32] R. Ludwig and D. Paschek, *ChemPhysChem* **10**, 516 (2009).

Chapter 5

The Influence of Water on the Structural and Transport Properties of Model Ionic Liquids *

5.1 Introduction

Room temperature ionic liquids (RTILs) often contain trace amounts of water, owing to the absorption of water vapor from the atmosphere. This common impurity changes the physical properties of RTILs considerably even at low concentrations [1, 2].

For most RTILs the viscosity decreases strongly when a small amount of water is present, but the effect weakens as the mixture becomes water rich [3–9]. This viscosity reducing effect is found to be stronger at lower temperatures. In some particular RTILs, water can have an apparently opposite effect, water induces gelation in RTILs consisting of 1-octyl-3-methyl-imidazolium cations with bromide or tetrafluoroborate anions [10, 11]. The electrical conductivity of RTILs [6–9] increases upon the addition of water up to a maximum value, and this effect is usually ascribed to increased ion mobility due to the decreasing viscosity. In water-rich mixtures, the conductivity decreases as a result of the reduction in the density of charge carriers. Simulation studies [12–15] and experiments [16] have shown that the addition of water increases the diffusion coefficients of the RTIL ions. Also, the addition of water narrows the electrochemical window of RTILs, likely due to the electrolysis of water [6, 16, 17].

A considerable number of experimental [18–24] and simulation [12, 14, 15, 25, 26] studies have focused on the structure of ionic-liquid-water mixtures, particularly on the water-ion interactions. Not surprisingly, a variety of often complex behavior has been reported

*A version of this chapter has been accepted for publication. H. V. Spohr and G. N. Patey, “The Influence of Water on the Structural and Transport Properties of Model Ionic Liquids”, *J. Chem. Phys.* (2010).

[14, 24]. Generally, at low water concentrations ($\lesssim 30$ mol%) only isolated water molecules are detected [12, 18, 19, 25]. (Note that here and elsewhere in this paper mol% is defined as $100 \times N_w / (N_w + N_+ + N_-)$, where N_α is the number of particles of species α .) These water molecules tend to hydrogen bond with one anion [19], or with two anions [14, 18, 19, 25], depending perhaps on the nature of the anion. The strength of the water-anion hydrogen bond is found to increase as the mole fraction of water is decreased [26]. Other studies [15, 22–24] also found that cation-water interactions are of importance. As the water concentration is increased, the dominant, long-range Coulombic interactions among the ions become less important, due at least in part to dielectric screening [15, 26], and ion-water and water-water interactions gain importance. At high water content ($\gtrsim 0.75$ mol%), continuous water networks are found to surround single ions, and ion clusters [12]. Some RTILs act like short chain surfactants and aggregate above a critical micelle concentration [20, 21].

Clearly, the physical property changes that RTILs experience upon the addition of water, can be of advantage in some applications and detrimental in others. Therefore, it is of interest and importance to study the influence of water on RTILs in detail. Our research in this area aims to relate the macroscopic behavior of ionic liquids to the molecular characteristics of the constituent ions, with particular emphasis on transport properties. In previous studies, we considered several relatively simple models that served to single out particular commonly occurring features of RTIL ions. These include ion size disparity in Chapter 2 [27], the displacement of the ion center of charge from its center of mass in Chapter 3 [28], and the characteristic length parameter determining the strength of the obviously important Coulombic attractions in Chapter 4 [29]. All of these variables were shown to have important, often competing, influences on the transport properties, sometimes in easily predictable ways, and sometimes through less obvious mechanisms.

The present Chapter is a systematic investigation of the influence of water on the properties of these model ionic liquids. We consider six model ionic liquids that cover much of the parameter space outlined above, and examine the mixture properties as a function of water concentration up to 50 mol%. Some mixtures where water is replaced by a nonpolar

species are also considered for comparison purposes.

We show that the effect of water on the transport properties can be complex, and can come through several microscopic mechanisms. These include not only variations in the underlying liquid structure of the mixtures, but also effects that are dynamical in nature, stemming from the fact that the molecular mass of water is generally smaller, often much smaller, than that of the ions it replaces in ionic-liquid-water mixtures. This latter point is very important but does not appear to have received much attention, most studies focus almost entirely on structural effects when attempting to explain the strong influence of water on RTILs.

The remainder of this Chapter is divided into three parts. The models and simulation method are briefly described in Chapter 5.2, our results are presented and discussed in Chapter 5.3, and finally our conclusions are summarized in Chapter 5.4.

5.2 Models and Simulation Method

The ionic liquid models and simulation method closely follow our earlier work (see Chapters 2.2, 3.2, 4.2, and Appendix A.1) [27–29]. Two simple models that were originally employed to investigate the influences of ion size disparity, and charge location, on ionic liquid properties are again considered here. The ions are modeled as Lennard-Jones (LJ) spheres of different sizes with embedded point charges, that are not necessarily located at the ion center of mass. For the general case, the ion-ion pair interactions can be written in the form

$$u(ij) = 4\epsilon \left[\left(\frac{\sigma_{ij}}{r_{ij}} \right)^{12} - \left(\frac{\sigma_{ij}}{r_{ij}} \right)^6 \right] + \frac{q_i q_j}{4\pi\epsilon_0 r'_{ij}}, \quad (5.1)$$

where $\sigma_{ij} = (\sigma_i + \sigma_j)/2$ and ϵ are the LJ length and energy parameters, r_{ij} is the distance between the ion centers of mass, r'_{ij} is the charge separation, q_i is the ionic charge, and ϵ_0 is the permittivity of free space. Note that we have assumed that the LJ energy parameter ϵ is the same for all ions.

In this Chapter we consider models where the centers of mass and charge coincide (charge-centered models) as well as systems where this is not true for the cation (charge-off-center models). Following our previous practice in Chapter 4 [29], the charge-centered and charge-off-center models are labeled XCY and $XOCY$, respectively, where C and OC denote charge-centered (C) and charge-off-center (OC) models. Also, in this notation $X = \sigma_+/\sigma_-$ indicates the size disparity, and $Y = \sigma'_{+-}$ (in Å) is the minimum distance between the cation and anion charges, when their center of mass separation is σ_{+-} .

The molecular properties of the ionic liquid models employed here are summarized in Table 5.1. Note that three charge-centered and three charge-off-center systems are considered. The charge-centered models are size disparate, but note that as in Chapter 2 [27], σ_+/σ_- is varied subject to the constraint that $\sigma'_{+-} = \sigma_{+-}$ remains fixed at 5 Å, thus $Y = 5$ in all cases. This is to allow size disparity effects to be distinguished from other, possibly stronger, influences coming through variations in the Coulombic attraction. For the charge-off-center models considered, the ions are of the same size ($X = 1$) in all cases, but Y can vary depending on the distance l_q of the charge from the center of mass. l_q is sometimes called the charge arm [30, 31], and values of the normalized charge arm l_q/R_+ , where R_+ is the cation radius ($\sigma_+/2$), are given in Table 5.1. Note that in our models only the charge of the cation can be located off center, the anion charge is always at the center of mass.

<i>model</i>	$\sigma_+(\text{Å})$	$\sigma_-(\text{Å})$	l_q/R_+
1C5(1OC5)	5	5	–
2C5	6.667	3.333	–
3C5	7.5	2.5	–
1OC4.3	5	5	0.25
1OC3.8	5	5	0.5
1OC3.1	5	5	0.75

Table 5.1: System parameters for the size disparate and charge-off-center models. σ_+ and σ_- are the LJ length parameters, l_q/R_+ is the normalized charge displacement. The LJ energy parameter is $\epsilon = 6 \times 10^{-21} J$ for all ions, the charges $q = \pm 1e$, the ion mass $m = 1.99265 \times 10^{-25} kg$, the moment of inertia of charge-off-center cations is $I_{xx} = I_{yy} = 2.8 \times 10^{-46} kg m^2$. Test simulations were also carried out with $I_{xx} = I_{yy} = 2.8 \times 10^{-45} kg m^2$ and $I_{xx} = I_{yy} = 2.8 \times 10^{-44} kg m^2$.

In order to carry out MD simulations, it is necessary to specify ion masses, as well as moments of inertia for the charge-off-center cations. Here, for simplicity we take all ion masses to be the same at a value (Table 5.1) that is physically realistic for the large molecular ions of which RTILs are usually comprised. The majority of calculations were done with a fixed cation moment of inertia that did not vary with the charge arm (Table 5.1), but, as in Chapter 4 [29], some calculations were carried out with values spanning two orders of magnitude to verify that the transport properties are not very sensitive to this parameter.

In our ionic-liquid-water mixture calculations, the so-called simple point charge (SPC) water model [32, 33] was employed (note that results obtained with the SPC/E water model differed negligibly from those obtained with SPC). This model consists of three point charges embedded in a LJ sphere, and is obviously convenient for use with our model ions. We also investigated the effect of the water mass on the dynamical properties, so we label the regular SPC model as “w18”, and an analogous water model, where we increased the molecular mass of water to 120u, as “w120”. The LJ parameters for the cross ion-water interactions were obtained using the Lorentz-Berthelot rules, $\epsilon_{12} = \sqrt{\epsilon_1\epsilon_2}$ and $\sigma_{12} = (\sigma_1 + \sigma_2)/2$.

All simulations were performed under periodic boundary conditions using a cubic central cell. Most results reported are for systems containing 216 particles in total, but some simulations were carried out with 512 particles to ensure that the number dependence of the transport properties was not qualitatively significant. In all simulations, the volume V of the cell was adjusted such that the reduced density $\rho^* = \sum_i \rho_i \sigma_i^3 = 0.8$, where $\rho_i = N_i/V$, N_i is the number of particles of species i , and the sum is over all species. This means that all systems are compared at fixed packing fraction. We note that this value of ρ^* corresponds to real RTILs in the density range 1.3 – 0.7 g/mL. The LJ potential was cut and shifted at the half the box length L to avoid discontinuity [34]. Ewald summation [35, 36] was used to treat all Coulombic interactions [35], with an inverse parameter length of $6.0/L$, fifty wavevectors, and a real space truncation at $L/2$. The simulations were carried out in the NVT ensemble with a Gaussian isokinetic thermostat [37]. A fifth order Gear predictor-corrector algorithm [35] was used to integrate the equations of motion with a timestep of

1×10^{-15} seconds.

Beginning from a lattice, systems were first equilibrated for 2×10^5 timesteps at 2200 K with simple temperature scaling, then again for 1×10^6 timesteps at 1000 K still with simple temperature scaling, a final equilibration of 1×10^6 timesteps at 1000 K was carried out with the thermostat turned on. We note that 1000 K is obviously much higher than the melting points of RTILs, but it is necessary to ensure that all of our ionic liquid models are in the liquid state. Liquid properties were calculated as averages from five production runs of 2 ns each, resulting in total simulation times of 10 ns. Standard deviations were calculated assuming that the five 2 ns production runs give independent estimates of the quantities of interest. During the production runs, the temperature was scaled to 1000 K every 5000 timesteps for the size disparate and every 1000 timesteps for charge-off-center models. Transport properties are obtained via the Einstein (diffusion coefficients) and the Green-Kubo (shear viscosity, electrical conductivity) relations [35, 38] as described in Chapters 2.2, 3.2, 4.2, and Appendix A.3 [27, 28], with sampling of positions, orientations, and velocities every 20 timesteps.

5.3 Results and Discussion

In the following, we first discuss the structural and then the transport properties of our model ionic liquids. We relate commonly observed trends in the transport properties to the underlying molecular properties. We note when the behavior of our models agrees with experimental observations, as well as where and why deviations may occur.

5.3.1 Structural Properties

Size Disparate Models

Center of mass radial distribution functions (rdfs) are shown in Figs. 5.1 - 5.3 for model *XC5* mixed with water or LJ particles. The cation-anion rdfs are shown in Fig. 5.1 for water-1*C5* (top panel), water-3*C5* (middle panel), and LJ-1*C5* (bottom panel) mixtures. We note that the addition of water decreases the height of the first peak in both cases, but

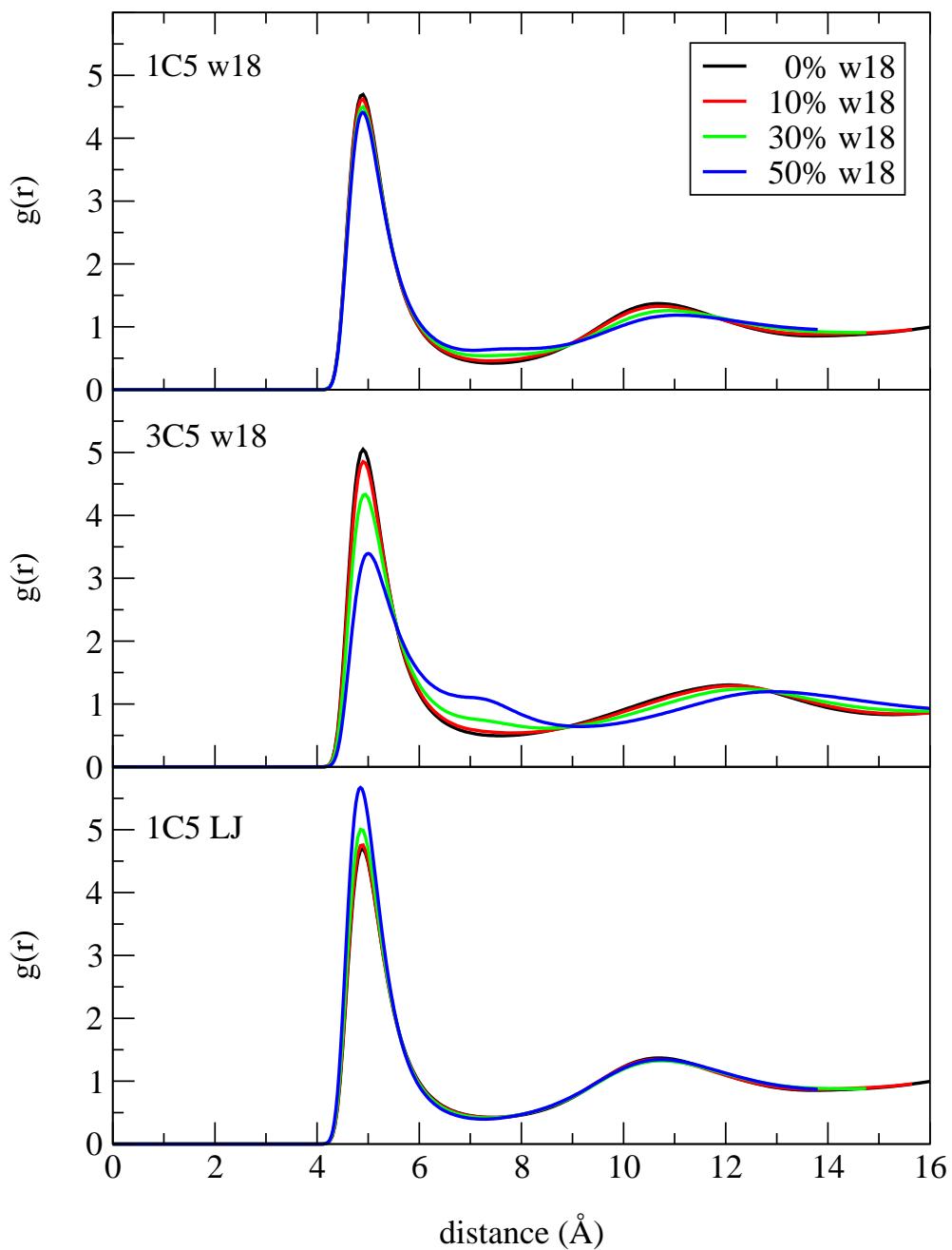


Figure 5.1: Cation-anion rdfs for charge-centered models at different water concentrations. Results are shown for 1C5-water (top panel), 3C5-water (middle panel), and 1C5-LJ-particles (bottom panel).

more strongly in the size disparate system (water-3C5). This simply indicates that water weakens the ion-ion correlations through “solvation”, and that this is more significant when there is a smaller ion present. The cation-anion correlations are somewhat enhanced by the addition of nonpolar LJ particles, which can interact only weakly with the ionic species. The like-ion rdfs (not shown) are only slightly influenced by the addition of water or LJ particles.

Ion-water rdfs for mixtures containing 30 mol% water are shown in Fig. 5.2. As one would expect, the first peak in the anion-water rdf (bottom panel) increases strongly in height, and moves to shorter distances as the anion decreases in size. As the cation becomes larger, the first peak (top panel) moves to larger distances as it must, but somewhat unexpectedly, the peak height increases. Since the direct water-cation interaction is weakened by increasing cation size, this is likely due to strengthening of the indirect water-anion-cation correlations. Not surprisingly, the LJ-particle-ion correlations are weaker than the water-ion case.

Water-water (oxygen-oxygen) rdfs for systems 1C5 (top panel) and 3C5 (bottom panel) with different amounts of water are plotted in Fig. 5.3. The result for pure water at the same ρ^* and temperature is included for comparison. We note that for system 1C5, the water-water rdf is only weakly dependent on the amount of water present, but that a strong dependence is observed for system 3C5. This likely indicates that in system 3C5 water prefers to interact with the anion rather than with itself, leading to a large decrease in the height of the first peak at lower water concentrations. In system 1C5 water interacts with itself as strongly as it does with either ion.

In attempting to understand the behavior of the transport properties discussed in Chapter 5.3.2, it is useful to know how the “occupied” volume about an ion varies with changing water concentration. Therefore, we define the reduced occupied volume $V_\alpha(R)$ as

$$V_\alpha(R) = \frac{V_{occ}(R)}{4\pi\sigma_{+-}^3/3} = 4\pi \int_0^R \left[\rho_\alpha \frac{\sigma_\alpha^3}{\sigma_{+-}^3} g_{\alpha\alpha}(r) + \rho_\beta \frac{\sigma_\beta^3}{\sigma_{+-}^3} g_{\alpha\beta}(r) + \rho_\gamma \frac{\sigma_\gamma^3}{\sigma_{+-}^3} g_{\alpha\gamma}(r) \right] r^2 dr, \quad (5.2)$$

where α , β and γ denote the different species, $\sigma_{+-} = (\sigma_+ + \sigma_-)/2 = 5 \text{ \AA}$, and $g_{\alpha\beta}(r)$ is the

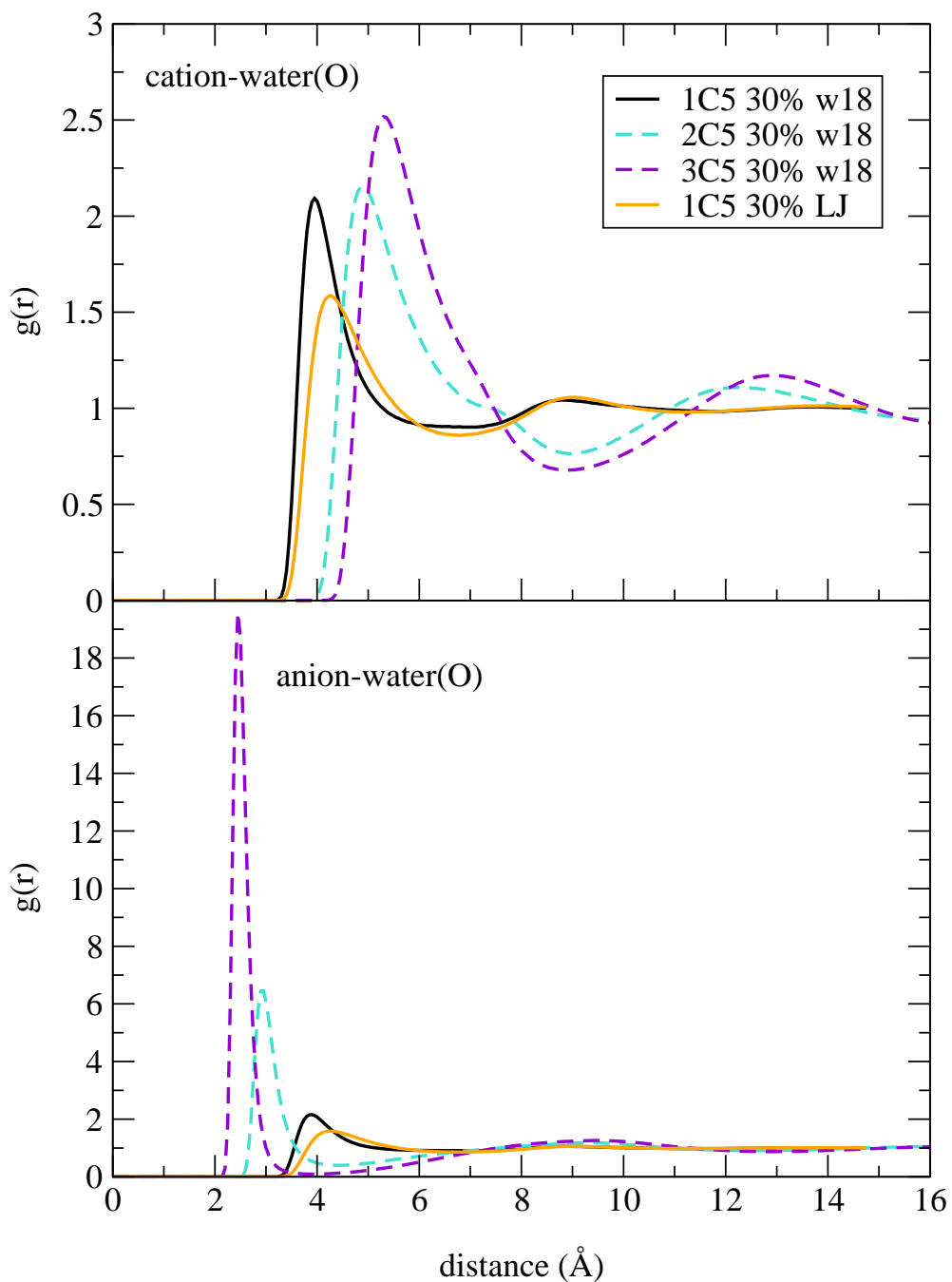


Figure 5.2: Cation-water(O) (top panel) and anion-water(O) (bottom panel) rdfs for charge-centered models at 30 mol% water. For model 1C5, ion-LJ-particle results are included for comparison.

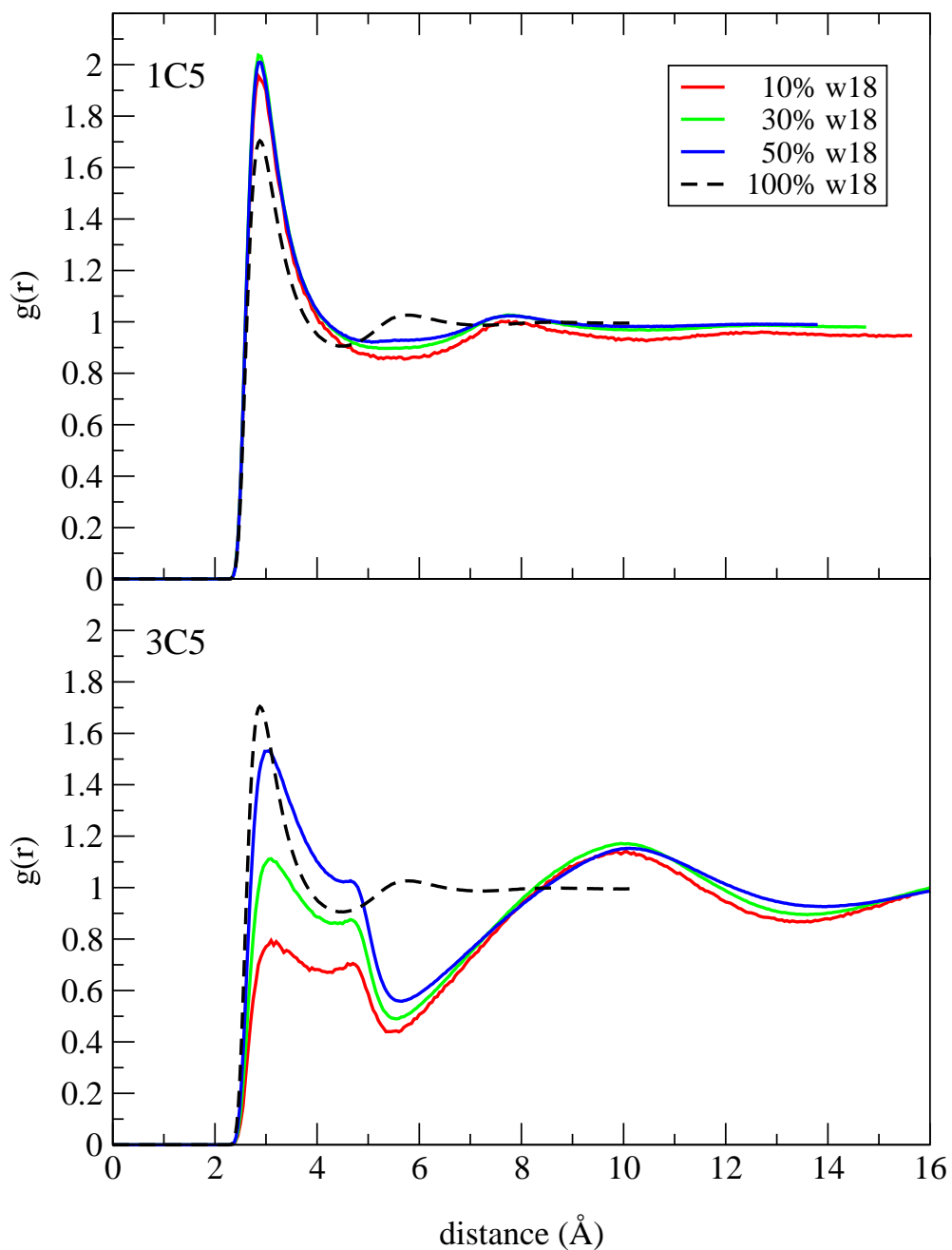


Figure 5.3: Water(O)-water(O) rdfs for 1C5-water (top panel) and 3C5-water (bottom panel) at different water concentrations. The dashed black line is the water(O)-water(O) rdf for pure water at the same ρ^* and temperature.

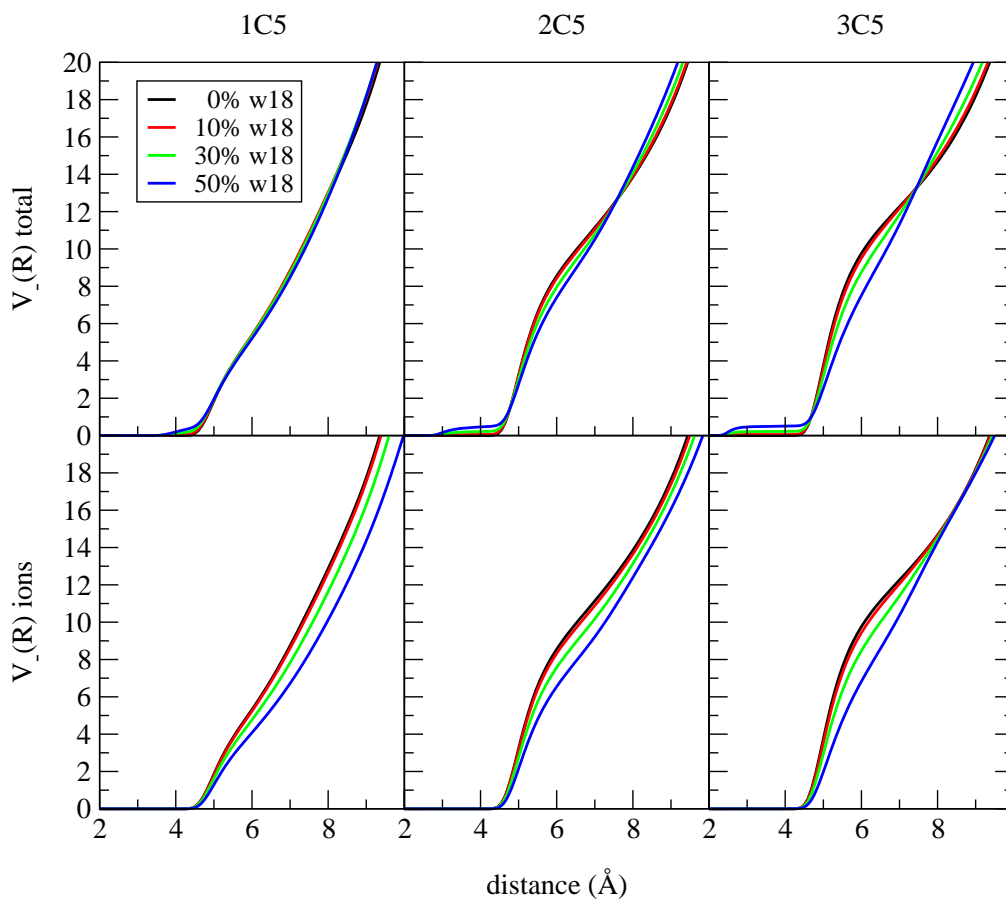


Figure 5.4: The reduced occupied volume $V_-(R)$ [Eq. (5.2)] for charge-centered models at different water concentrations. Both the total $V_-(R)$ (top panel) and its ionic contribution (bottom panel) are shown.

center of mass rdf between species α and β . Note that for an ion, $V_\alpha(R)$ has contributions from the coion, counterion, and water. $V_\alpha(R)$ is similar to a running coordination number, but takes account of the fact that the different species in a coordination shell have different sizes.

$V_-(R)$ for systems 1C5, 2C5, and 3C5 with different amounts of water are shown in Fig. 5.4. Curves are included for the total $V_-(R)$, including cations, anions, and water, as well as for the result obtained when only the ions are included. We note that for system 1CY, the total $V_-(R)$ curves are practically independent of the water concentration, whereas the ion-only curves show a significant variation. This indicates that in this system the ions in the coordination shells are replaced by water, but the total occupied volume remains essentially

constant. This is less true for the size disparate systems, but still the total occupied volume depends only weakly on the amount of water, particularly so for water concentrations less than 30 mol%. The trends for $V_+(R)$ (not shown) are similar.

We noted above that for system 3C5 the anion-water correlations are very strong. Inspection of anion-water running coordination numbers (not shown) indicates that at concentrations less than 33 mol% (at 33 mol% all species are present in equal numbers) each anion tends to have a single water molecule in its first coordination shell. At higher water concentrations, several water molecules can be coordinated to a single anion. We never observe more than one anion in the first coordination shell of a water molecule in systems 3C5 and 2C5, likely due to the strong Coulombic repulsion of the anions.

Models with Charge Displacement

Selected rdfs for model 1OCY mixed with water or LJ particles are plotted in Figs. 5.5, 5.6, and 5.8. All rdfs shown are for the ion centers of mass (CM), except for Fig. 5.8 (top panel), where the cation center of charge (CC) is used.

It is useful to recall that in Chapter 3 [28] we found that charge-off-center models tend to form directional ion pairs, whose strength and lifetime depend on the normalized charge displacement, l_q/R_+ . Furthermore, the dynamical behavior of these ionic liquids can be roughly divided into two regimes, depending on whether the directional ion pairs are weakly or strongly “bonded”. Of the three 1OCY systems considered in the present Chapter (see Table 5.1), 1OC4.3 and 1OC3.8 fall into the weakly paired regime, and 1OC3.1 lies in the strongly paired regime. In the weakly paired regime, the asymmetry introduced by charge displacement reduces the cation-anion correlations (Chapter 3) [28]. We find that in these systems the addition of water has little influence on the ion-ion rdfs (not shown), simply leading to slight decreases in the height of the first peak.

In contrast, in the strongly paired regime water has a significant influence on the cation-anion rdf, as illustrated for system 1OC3.1 in Fig. 5.5. Note that in this system the cation-anion rdf shows two distinct peaks at small separation. The first peak is associated with strongly bound directional ion pairs, and the second peak with “non-bonded” counterion

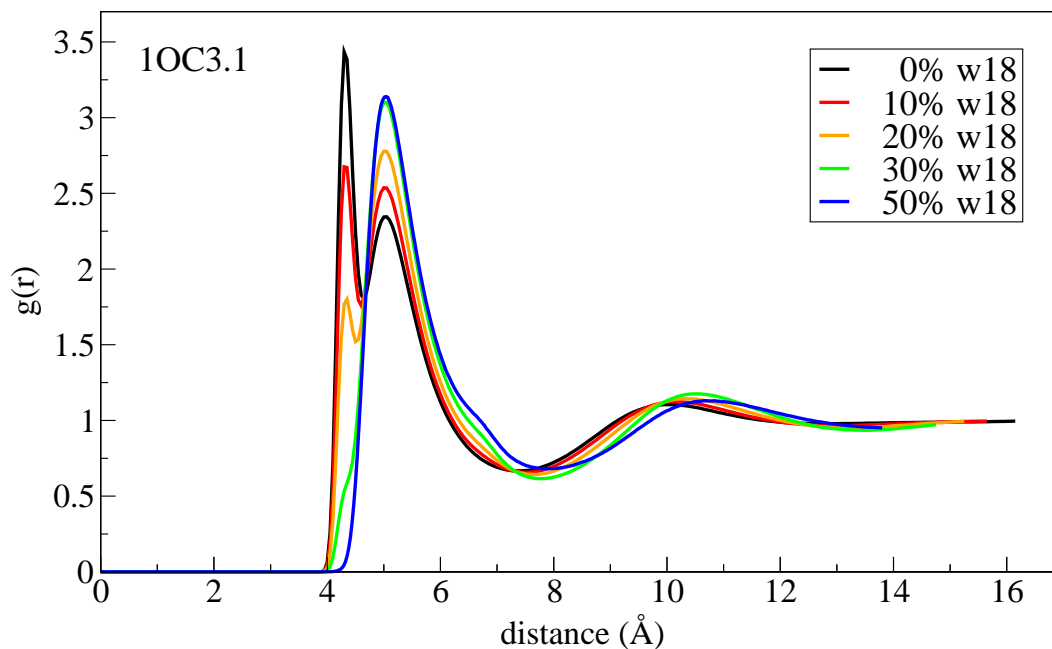


Figure 5.5: Cation-anion center of mass rdfs for 1OC3.1-water mixtures at different water concentrations.

neighbors. As the water concentration increases, the first peak decreases in height, until at 30 mol% it has entirely vanished, never to reappear as more water is added. Essentially, what is happening is that the directional cation-anion pairs are being replaced by cation-water pairs, as evidenced by the cation-water rdfs (Fig. 5.6, top panel) discussed in the next paragraph. Note that at 33 mol% there are just enough water molecules present to replace all of the anions taking part in directional ion pairs.

Ion-water rdfs for the different charge-off-center systems at 30 mol% water are shown in Fig. 5.6, together with some LJ particle results for comparison. First, we focus on the cation(CC)-water(O) rdfs given in the top panel. As the cation charge is moved further off center, the first peak in the rdf initially decreases in height and broadens, then increases in height and narrows. For 1OC3.1, the first peak is much higher and occurs at smaller separations than for the other systems, indicating cation-water(O) “bonds” in this liquid. This is what destroys the directional ion pairs, as discussed above. For system 1OC3.8, the first peak is also shifted to markedly smaller separation, indicating that cation-water(O)

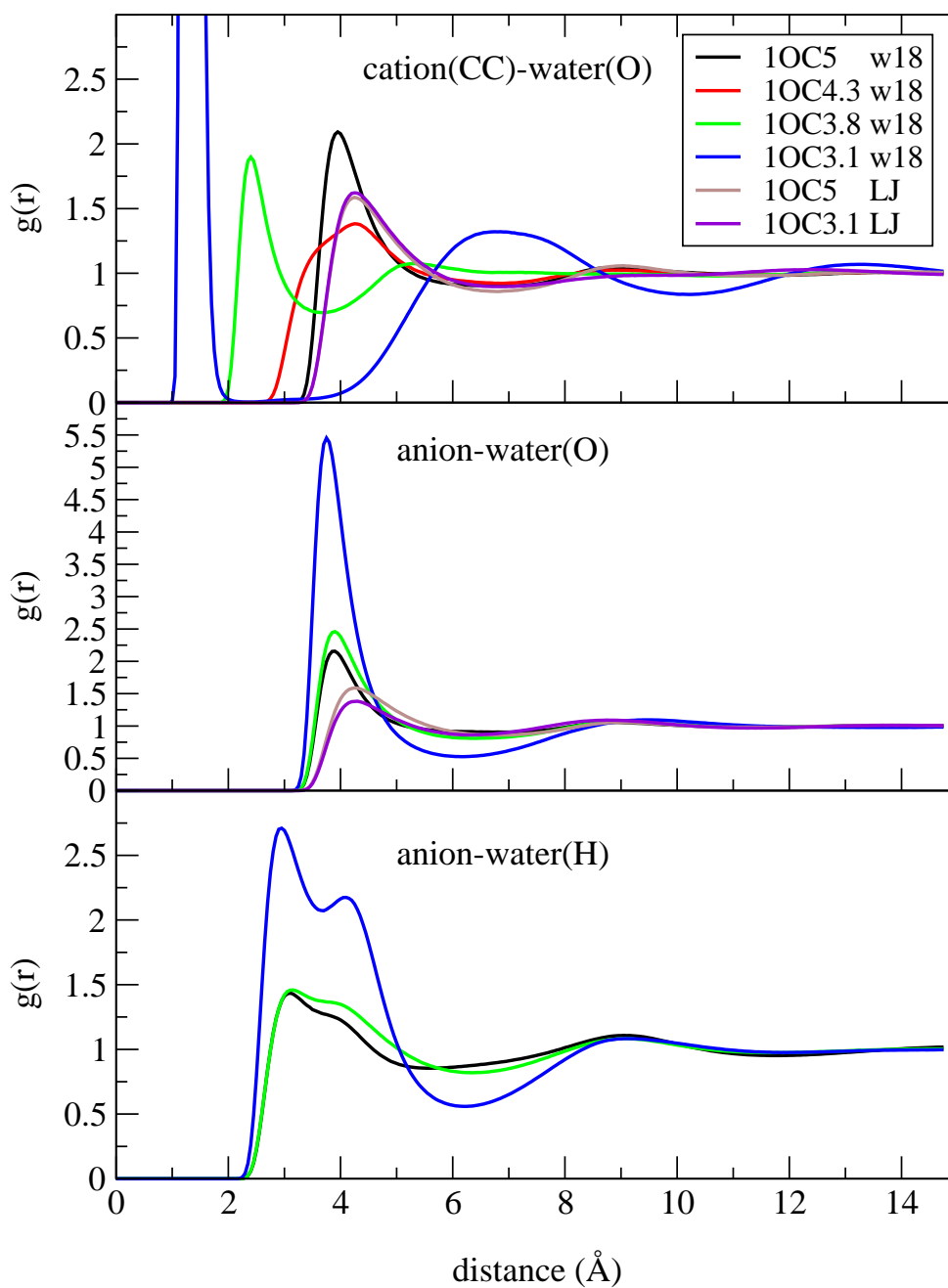


Figure 5.6: Ion-water rdfs for charge-off-center models at 30 mol% water. Included are the cation(CC)-water(O) (top panel), anion-water(O) (middle panel), and anion-water(H) (bottom panel) functions. For 1OC5 and 1OC3.1 some LJ particle results are shown for comparison.

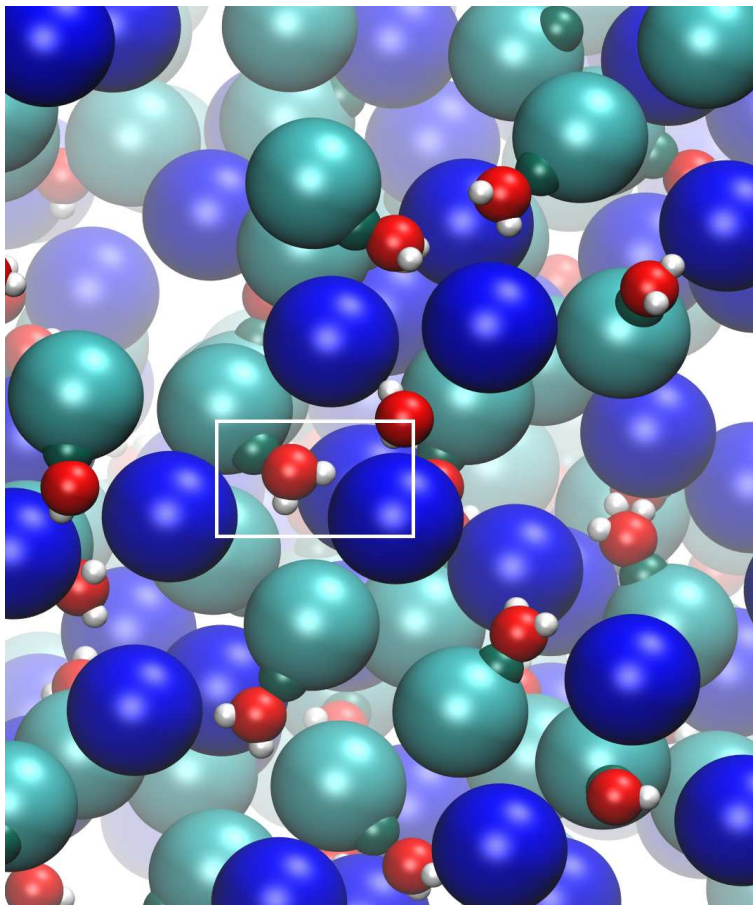


Figure 5.7: A configurational snapshot of the 1OC3.8-water system at 30 mol% water. One cation-water-anion triple is indicated, others can be clearly seen. The anions are blue, the cations turquoise, the water oxygen atoms are red, and the water hydrogen atoms are white. All particles are shown with somewhat reduced diameters to reveal the hydrogen sites of the water molecules, and the charged site of the cations (dark turquoise).

interactions are quite strong in this system as well. For all systems, varying the water concentration does not influence the qualitative behavior of the cation-water rdfs (not shown).

Anion-water(O) (middle panel) and anion-water(H) (bottom panel) rdfs are also shown in Fig. 5.6. The anion-water rdfs do not vary greatly with the amount of water added (not shown), but the dependence is much stronger for 1OC3.1 than for the other models. Also, for 1OC3.1 the anion-water correlations, as measured by the height of the first peak in the rdfs, are clearly stronger than for the other systems. Given that the anion is the same in all systems, this is almost certainly due to the cation-anion attraction indirectly supporting the anion-water correlation. Indeed, in the “snapshot” shown in Fig. 5.7, one can easily

spot cation-water-anion triples in system 1OC3.1. We shall see in Chapter 5.3.2 that these structures likely influence the viscosity as well. Finally, we note that the ion-LJ-particle correlations are relatively weak, and depend only slightly on the charge displacement.

Water-water rdfs for systems 1OC3.8 and 1OC3.1 with varying water concentration are shown in Fig. 5.8. We note that for system 1OC3.8, the dependence of the water-water rdfs on water concentration is relatively small. This is also true of the charge-centered systems as can be seen in Fig. 5.3 (top panel). However, for system 1OC3.1 this is not the case. For concentrations less than 30 mol% water, the first peak in the water-water rdf (compared with pure water) is entirely missing. This is because at 30 mol% and lower all water molecules are strongly bound to cations, and do not interact directly with other water molecules. At higher water concentrations where there are “unbound” water molecules, the first water-water peak reappears.

The total $V_+(R)$ (top panel) and its ionic contribution (bottom panel) for systems 1OC3.8 and 1OC3.1 with varying water concentrations are plotted in Fig. 5.9. We note that for both systems the total $V_+(R)$ curves for different water concentrations are essentially superimposable, whereas the ion-only curves vary significantly. This indicates that for these systems water replaces ions in the coordination shells, but the total occupied volume remains practically constant.

5.3.2 Transport Properties

Size Disparate Models

Diffusion coefficients for the size disparate models with added water are shown in Fig. 5.10. In some cases results for LJ particle mixtures are shown for comparison. For system 1CY results obtained with 512 particles (orange squares) are included, and we note that the system size dependence is not significant.

In Chapters 2 and 4 [27, 29] we found that, for pure ionic liquids, size disparity leads to increased ionic diffusion coefficients, and that this is at least partially due to decreases in the first shell coordination numbers at fixed packing fraction (see Chapter 4.3) [29]. This

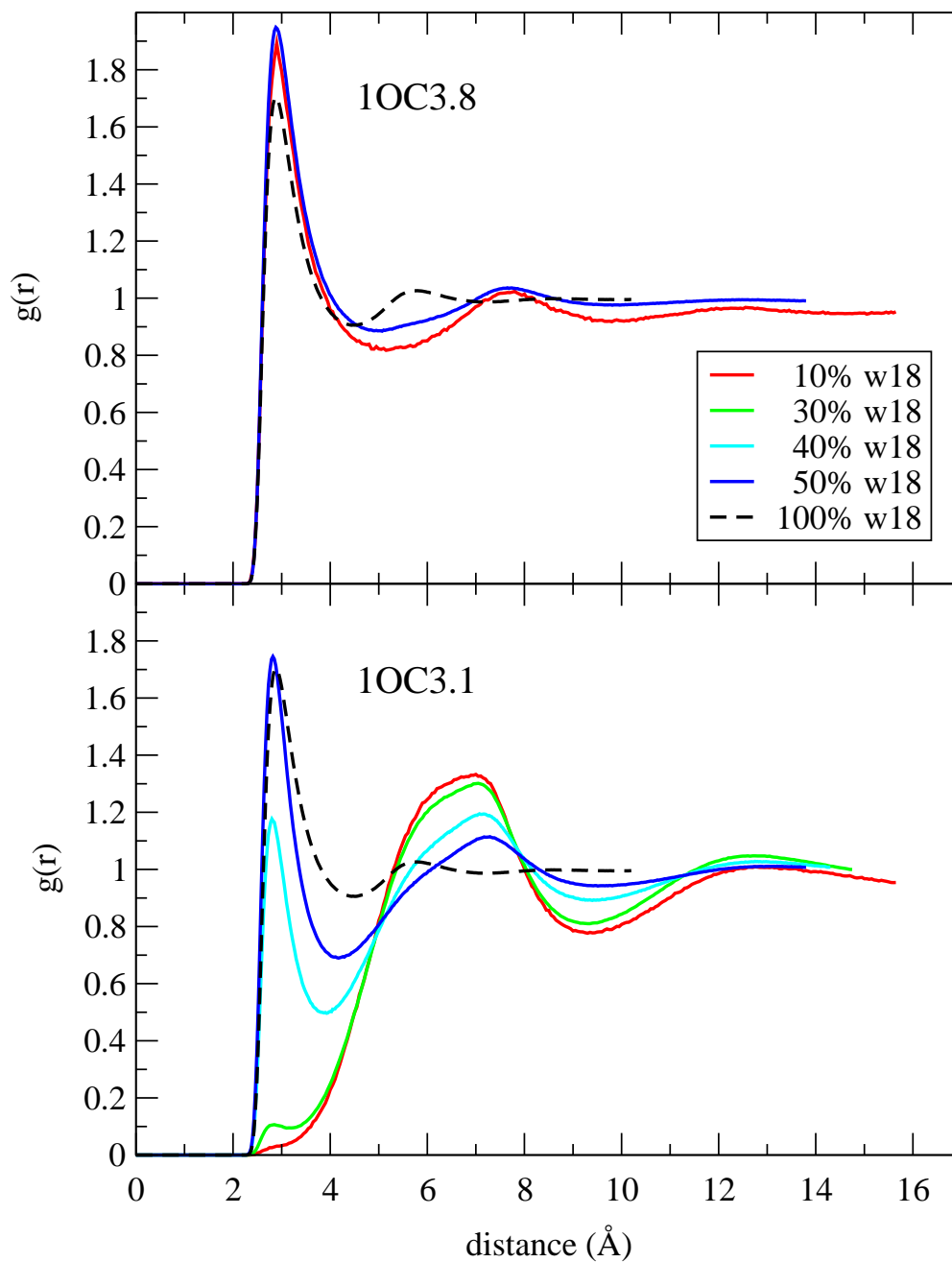


Figure 5.8: Water(O)-water(O) rdfs for 1OC3.8-water (top panel) and 1OC3.1-water (bottom panel) at different water concentrations. The dashed black line is the water(O)-water(O) rdf for pure water at the same ρ^* and temperature.

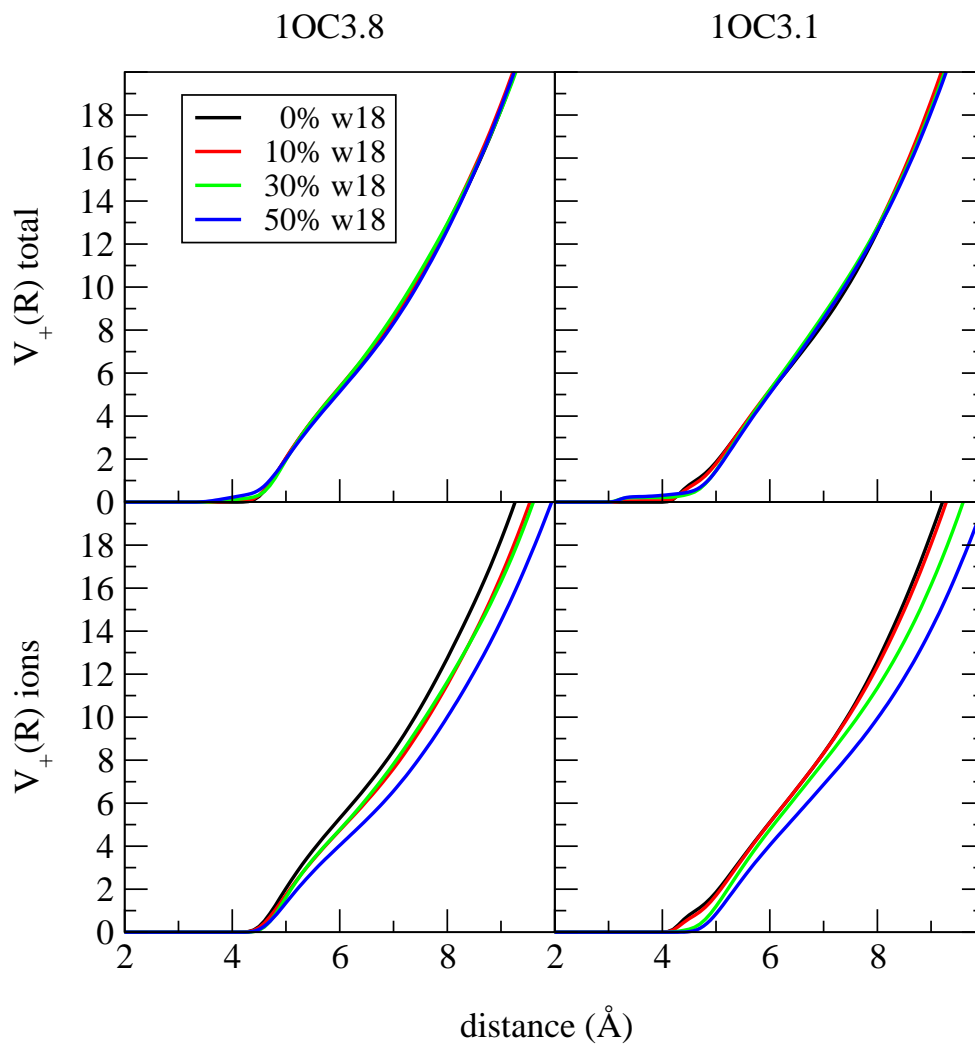


Figure 5.9: The reduced occupied volume $V_+(R)$ [Eq. (5.2)] for charge-off-center models at different water concentrations. Both the total $V_+(R)$ (top panel) and its ionic contribution (bottom panel) are shown.

effect is also observed here for the diffusion coefficients of the ions (top and middle panels), but the diffusion coefficient of the water decreases with increasing ion size disparity. This is in all likelihood due to the strong water-anion interactions, that become stronger as the anion is reduced in size.

For the mixtures containing water, we see from Fig. 5.10 that the diffusion coefficients of the ions and of the water all increase with increasing water concentration, as has been observed in simulations with other models [12–15]. It is interesting to probe a little more deeply into why this is so. We showed above (Fig. 5.4) that the “occupied” volume around the ions does not change much with water content, so simple packing effects cannot explain the increasing diffusion coefficients. The correlations among the ions will be influenced, likely weakened, by the presence of water, so this is a possible contributing factor.

However, in addition to these structural factors, there is a possible dynamical effect that must be considered. In the ion coordination shells, counterions that tend to be heavy are being replaced with lighter water molecules. In our model liquid mixtures the ion/water mass ratio is 120/18. Therefore, to explore the possible influence of mass differences, for systems 1C5 and 3C5 we have carried out simulations with “heavy” water (labeled w120), which is just the same water model, but with the molecular mass increased from 18u to 120u. The results obtained are plotted in Fig. 5.11. We note that in all cases changing the mass of the water particles has a substantial effect on the diffusion coefficients of the ions. For model 1C5 with w120, the diffusion coefficients of both ions still increase with increasing water concentration, but the increase is much smaller than for real water (w18). For model 3C5 with w120, the diffusion constant of the cation is essentially independent of the water present at least up to 50 mol%, and the anion values actually decrease with increasing water concentration. Note that the anion is smaller in this system and interacts more strongly with water. Thus, we conclude that the increase in the ionic diffusion coefficients is in large part not due to water-induced structural changes, but rather to the fact that the water is lighter than the ions it displaces from the coordination shell.

The mass effect can also be clearly seen in the velocity autocorrelation functions. Both cation and anion results for system 3C5 are shown in Fig. 5.12. Curves are included for the

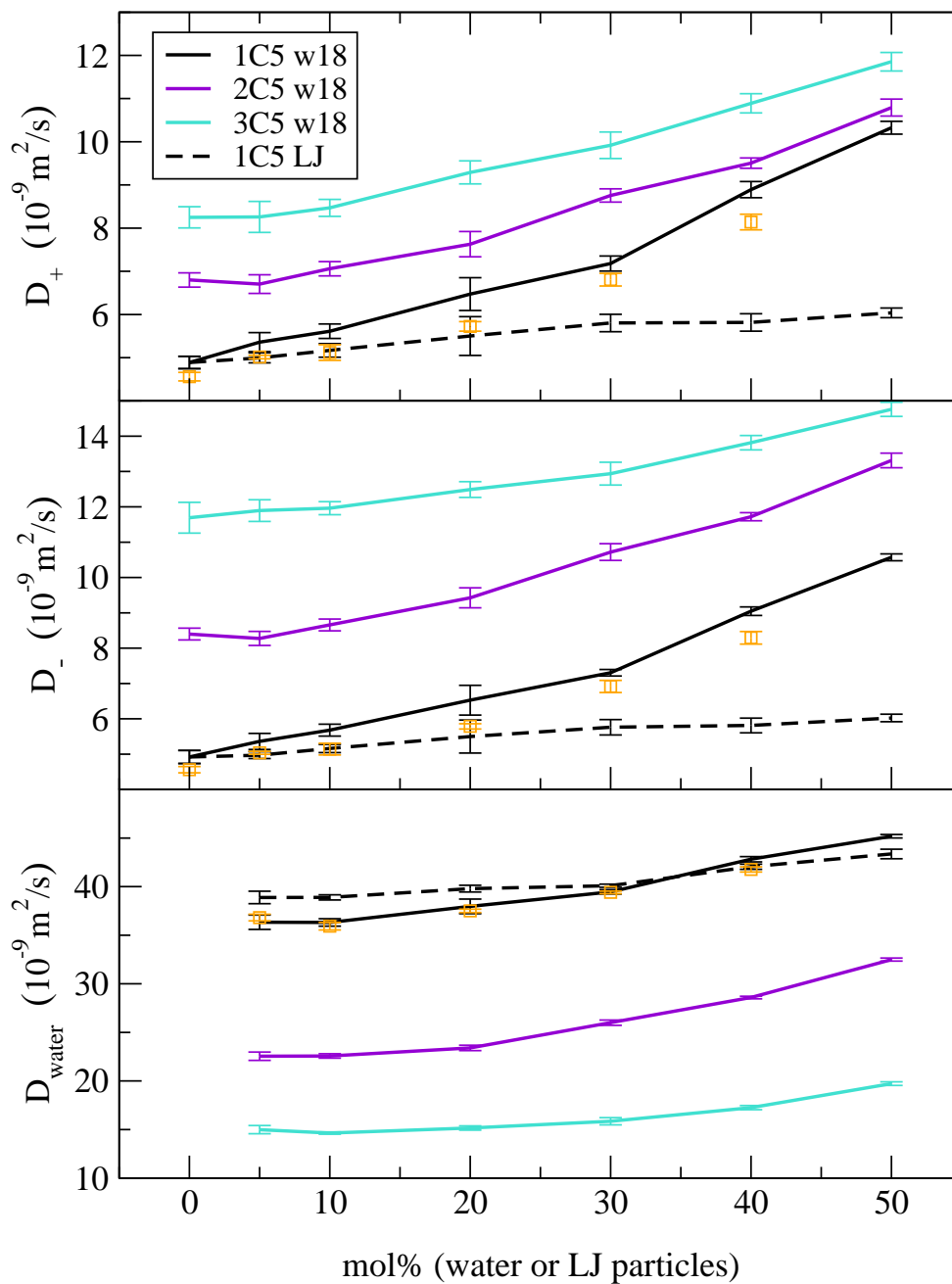


Figure 5.10: Diffusion coefficients versus water (LJ particle) concentration for 1C5-water (or LJ particles), 2C5-water, and 3C5-water systems. Results are shown for the cations (top panel), anions (middle panel), and water (LJ particles) (bottom panel). The orange squares indicate results obtained with a total of 512 particles, all other results shown were obtained with 216 particles. The error bars represent one standard deviation.

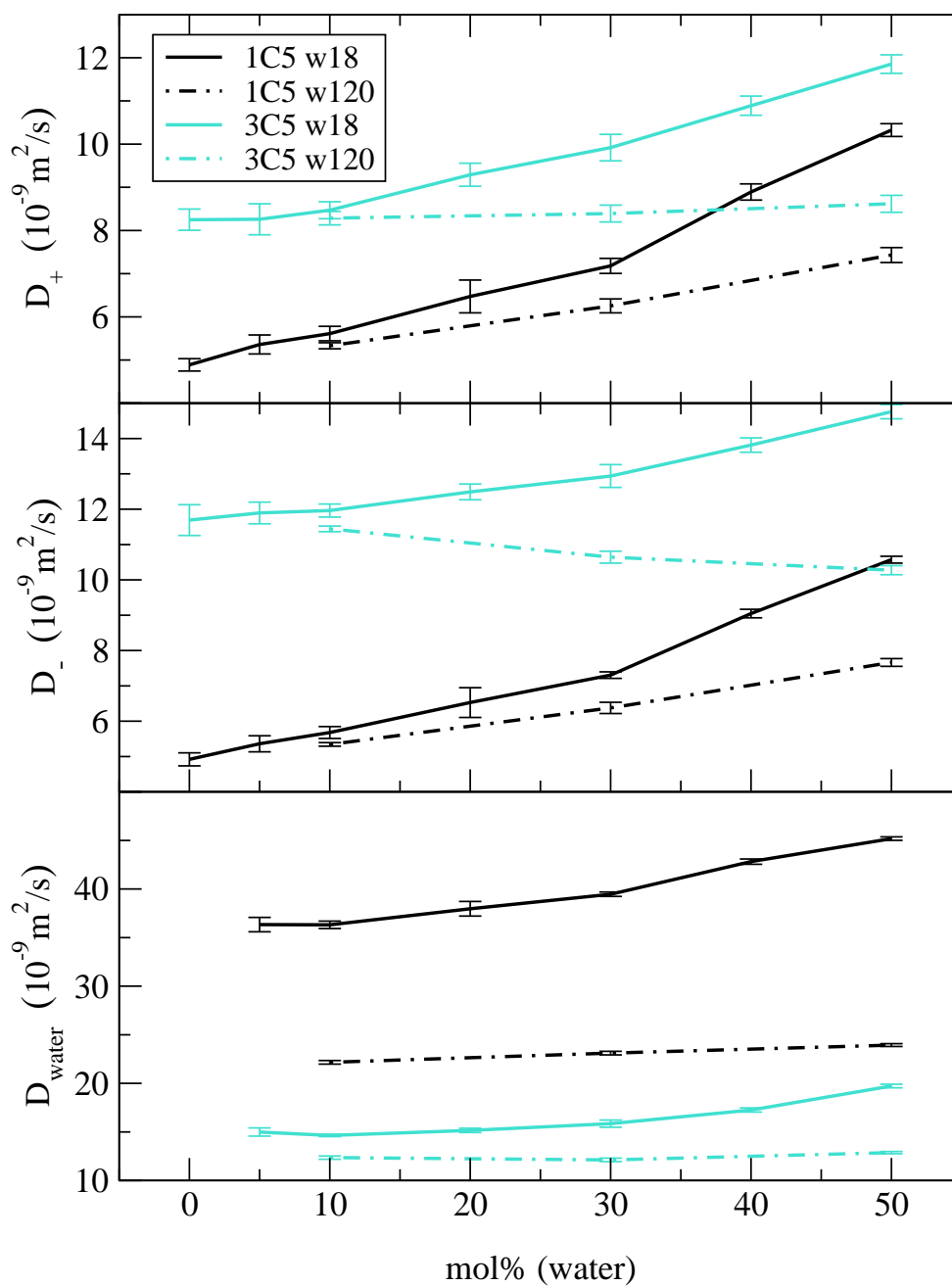


Figure 5.11: Dependence of the diffusion coefficients on the molecular mass of water for systems 1C5-water and 3C5-water. Results are shown for real water (w18, solid lines) and a heavier species (w120, dash-dot lines) having the same molecular mass as the ions. The panels are as in Fig. 5.10. The error bars represent one standard deviation.

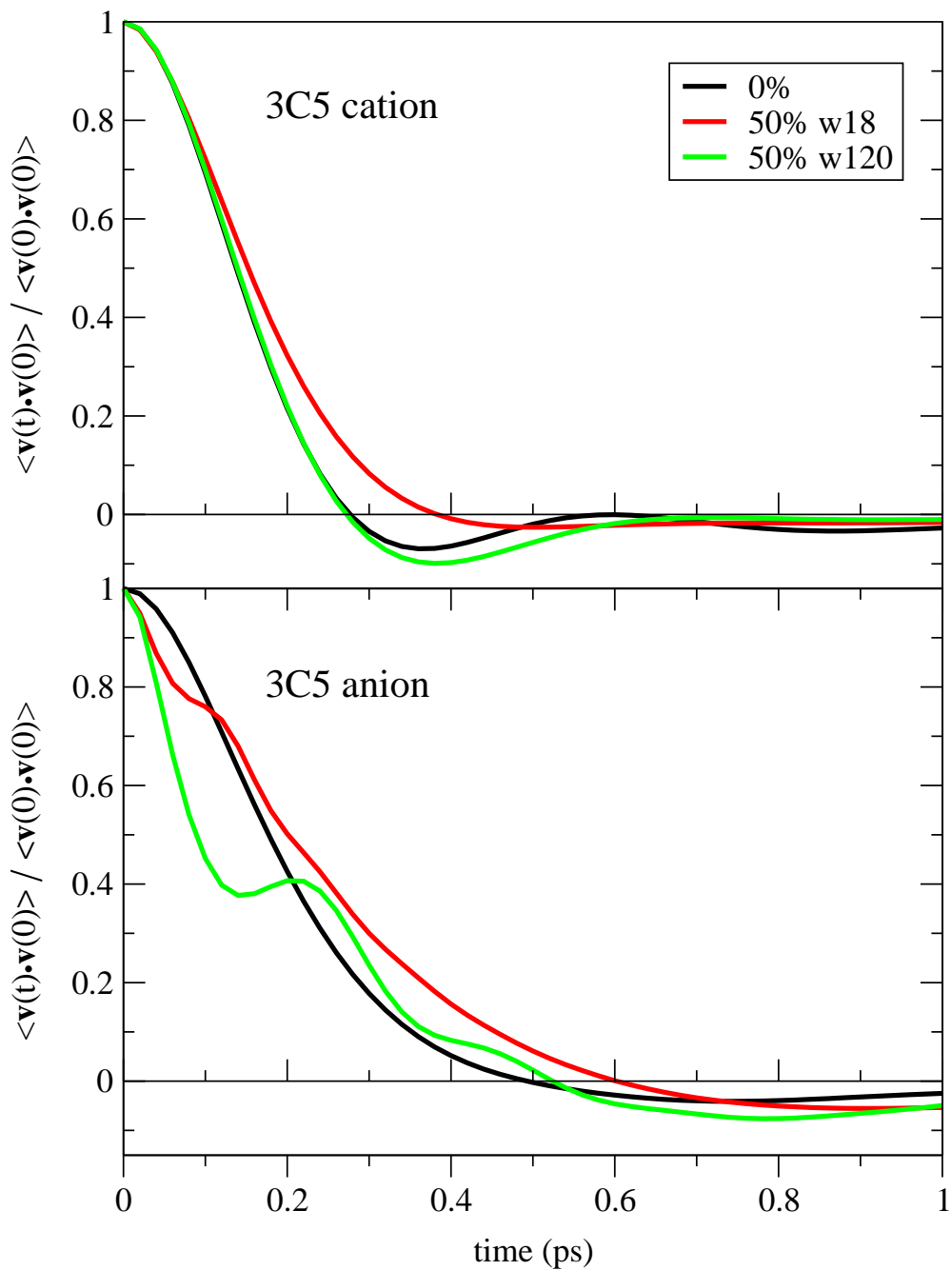


Figure 5.12: Velocity autocorrelation functions for 3C5-water systems at 50 mol% water. The cation and anion functions are shown in the top and bottom panels, respectively. Results are included for real water (w18) and the heavier species (w120). Curves for the pure ionic liquid are shown for comparison.

pure ionic liquid, and for systems with w18 and w120 at 50 mol%. We note that compared with the pure ionic liquid, the “caging” is reduced for w18, but not for w120.

The viscosity (top panel) and the electrical conductivity divided by the density of charge carriers σ_{el}/ρ_+ (bottom panel) are plotted versus the water concentration in Fig. 5.13. Because the total number of particles of all types is fixed in our simulation cell, as more water is added the charge density ($\rho_+ = \rho_-$) is reduced. Therefore, to remove this trivial effect from our consideration of factors influencing the conductivity, we plot σ_{el}/ρ_+ , rather than σ_{el} itself. For system 1C5 some results obtained with 512 particles are included for mixtures with water (orange squares) and LJ particles (orange diamonds). We note that there is a significant number dependence in the viscosity, with the larger systems giving somewhat higher viscosities. However, this appears as a shift of the entire curve, and the trends with increasing water concentration remain the same. The number dependence in σ_{el}/ρ_+ is very small and lies within the error bars.

First, let us consider the viscosities. We see from Fig. 5.13 that for systems 1C5 and 2C5 the viscosity decreases as water is added, but that the slope is considerably smaller for system 2C5. For system 1C5 results for different concentrations of LJ particles are also shown. We note that the viscosity also decreases in this case, but not as much as for corresponding water concentrations. Also, for the LJ particles, the viscosity closely follows the simple ideal relationship, $\eta_{mixture} = X_{IL}\eta_{IL} + X_{LJ}\eta_{LJ}$, where η_{IL} and η_{LJ} are the viscosities of the pure components at the same ρ^* and temperature, and X_{IL} and X_{LJ} are the mole fractions. For 1C5 with water, the viscosity falls faster than the appropriate ideal relationship would imply. We note that a decrease in viscosity when water is added is the usual observation [3–9] for RTILs. Below we show explicitly that the small mass of the water molecules compared to the ions is a significant factor contributing to the water-induced viscosity reduction, just as it is for the increased ion diffusivity discussed above.

Somewhat surprisingly, for the strongly size disparate system 3C5, we do not see the same trend, rather, the viscosity remains practically constant up to 20 mol% water, and then increases up to 50 mol%. This is despite the fact that the diffusion coefficients of all species in this system increase with increasing water concentration, as is also the case

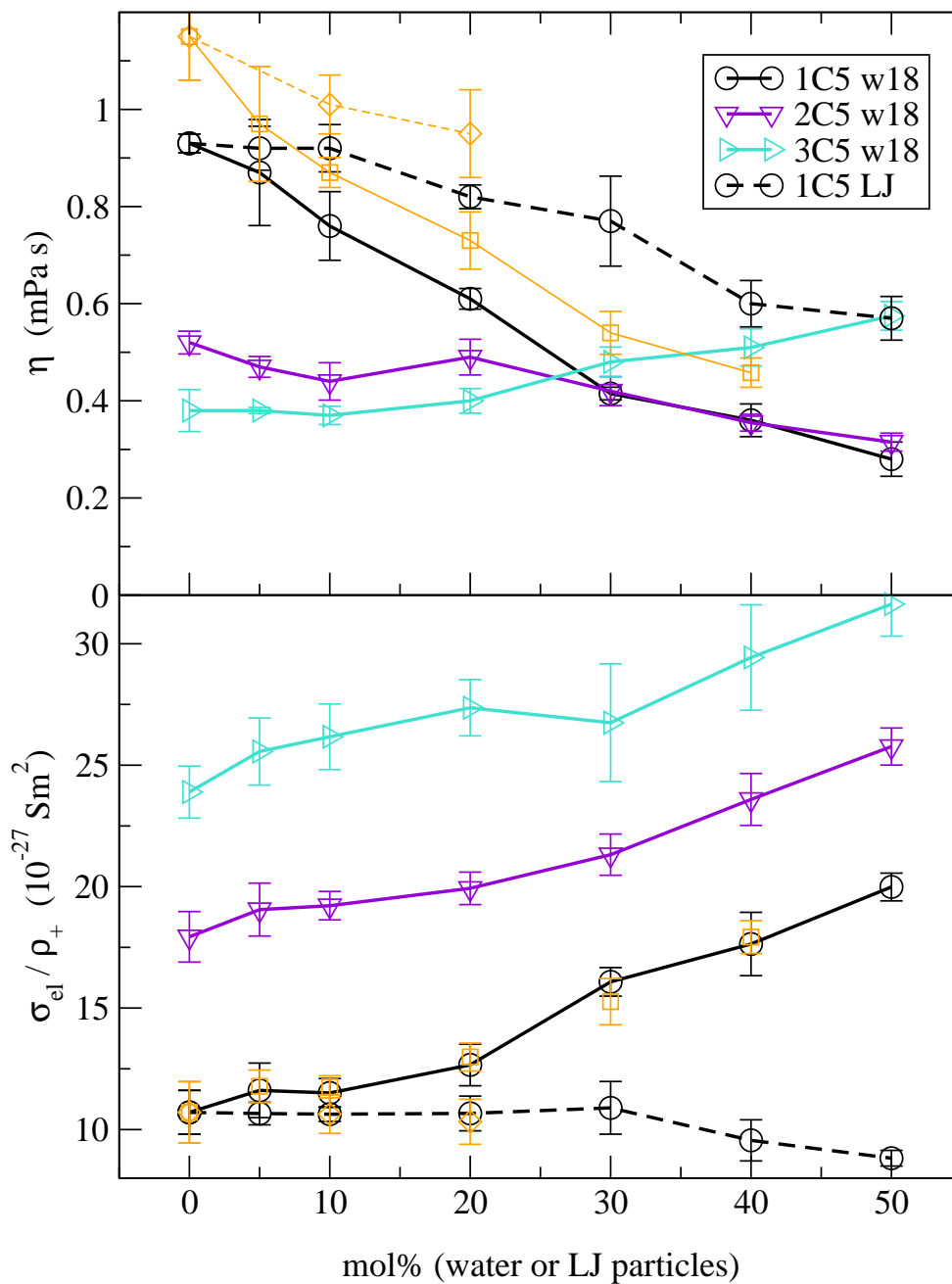


Figure 5.13: Viscosity (top panel) and σ_{el}/ρ_+ (bottom panel) versus water (LJ particle) concentration for 1C5-water (or LJ particles), 2C5-water, and 3C5-water systems. The orange squares (water mixtures) and orange diamonds (LJ particle mixtures) indicate results obtained with a total of 512 particles, all other results shown were obtained with 216 particles. The error bars represent one standard deviation.

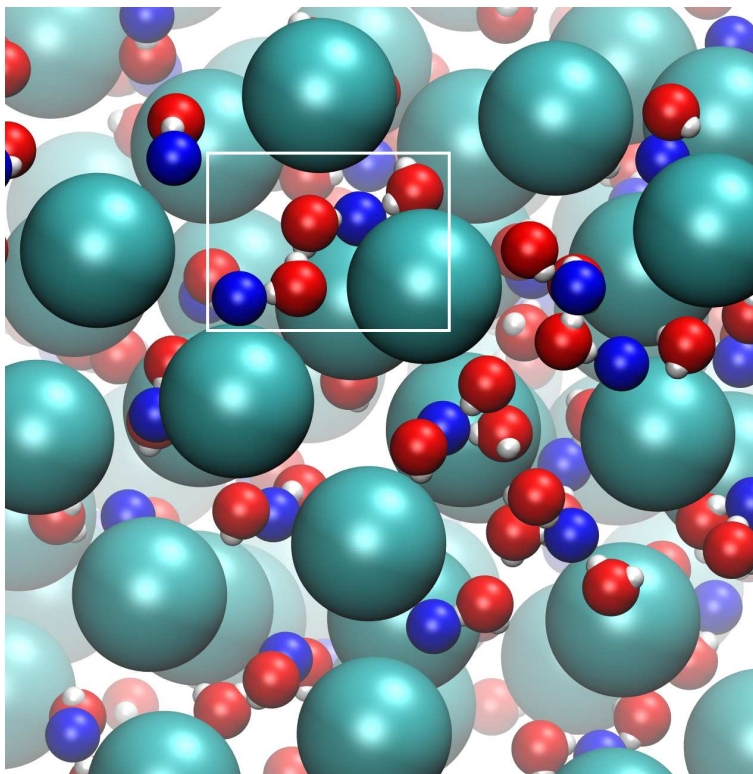


Figure 5.14: A configurational snapshot of the 3C5-water system at 50 mol% water. One of the chain-like, anion-water structures is indicated. The colors are as in Fig. 7, and again the diameters are somewhat reduced to reveal the hydrogen sites of the water molecules.

for the other systems. The likely physical origin of this unusual behavior can be found by inspecting the snapshot of a typical configuration from a 50 mol% solution given in Fig. 5.14. Here we see evidence of chain-like, anion-water structures that fit in among the larger cations. It is likely these associated structures that lead to the increased viscosity as water is added. Clearly, at some water concentration, the viscosity must again decrease, but this does not happen below 50 mol%. Such water-anion structures are not found for systems with 1C5, and, although some association does occur in 2C5, it is less important. Presumably, in these systems the anions are too large for these anion-water structures to form and fit among the cations. We remark that this behavior, a water induced viscosity increase, does not appear to have been reported for any real RTILs.

Turning to the conductivity, we see from Fig. 5.13 that σ_{el}/ρ_+ increases with the addition of water for all systems considered. This is consistent with the behaviour of the

diffusion coefficients discussed above (Fig. 5.10). We note that when LJ particles are added σ_{el}/ρ_+ decreases for concentrations above 30 mol%. This is possibly due to the increased cation-anion correlations in these systems (see Fig. 5.5).

As for the ionic diffusion coefficients discussed above, the fact that the molecular mass of water is considerably less than that of the ions it replaces is a significant contributing factor to the behavior of the viscosity and conductivity as water is added. Results for 1C5 and 3C5 with w18 and w120 are shown in Fig 5.15. We see that for 1C5 the viscosity decreases for both w18 and w120, but that the decrease is less for w120. For 3C5, the viscosity increases with added water, but the increase is larger for w120. The conductivity also shows the now expected behavior. For 1C5, σ_{el}/ρ_+ increases more slowly for w120, and for 3C5 it decreases with added water for w120, whereas an increase is observed for w18.

Models with Charge Displacement

It is convenient to divide this discussion into two parts. First we consider systems 1OC4.3 and 1OC3.8, which are in the weakly paired regime, as discussed above. For these systems, the dependence of the transport properties on water content is generally consistent with experimental observations for ionic liquids. In contrast, the behavior of water-1OC3.1 mixtures (recall that 1OC3.1 lies in the strongly paired region) deviates from commonly observed trends, and we discuss this system separately.

The diffusion coefficients of models 1OC4.3 and 1OC3.8 mixed with water or LJ particles, together with results for the charge-centered model 1OC5 (1C5) for comparison purposes, are plotted in Fig. 5.16. As observed in Chapter 3.3.2 (Fig. 3.8) [28], we see in Fig. 5.16 (top and middle panels) that in the weakly paired regime the diffusion coefficients of all species increase as the cationic charge is moved further off center. We note that in all charge-off-center systems the anions diffuse a little faster than the cations. In the pure ionic liquid case we noted that, since the ions are of the same size and the coordination numbers are very similar, this is most likely due to asymmetries in multi-ion clusters. Considering the simple example of linear ion triples, the two cations in $+ - +$ are both able to bind

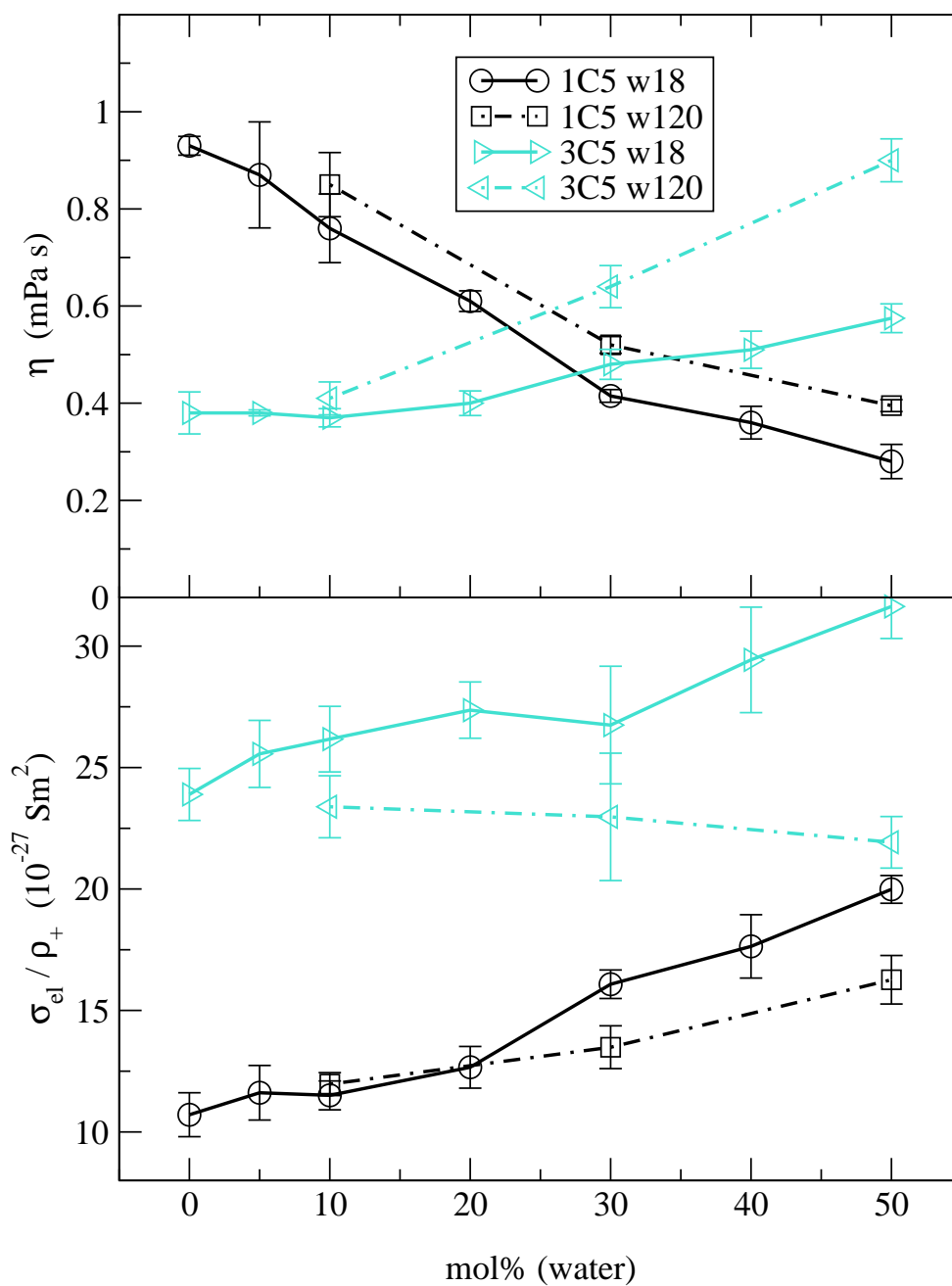


Figure 5.15: Dependence of the viscosity (top panel) and σ_{el}/ρ_+ (bottom panel) on the molecular mass of water for systems 1C5-water and 3C5-water. Results are shown for real water (w18, solid lines) and a heavier species (w120, dash-dot lines) having the same molecular mass as the ions. The error bars represent one standard deviation.

the anion closely, by orienting their off-center charge towards the anion, whereas in $- + -$, the cation will bind closely to one anion, but the other anion will be more weakly bound. Accordingly, linear triples of $- + -$ will be more weakly bound than $+ - +$, “freeing” the anions and enabling them to diffuse faster. Here we see that the same situation persists in the ionic-liquid-water mixtures as well.

Figure 5.16 shows that in all ionic-liquid-water mixtures, the diffusion coefficients of all species increase with increasing water concentration. This is consistent with the usual observation, and the occupied volume plot (Fig. 5.9) strongly indicates that this is not due to near-neighbor packing considerations. Rather, it is largely due to lighter water molecules replacing counterions in the first coordination shell, as discussed above in the size disparate case. We see that the diffusion of water (bottom panel) is as expected reduced by the presence of the ions (For our pure water model at this temperature and density the diffusion coefficient is $\sim 57 \times 10^{-9} \text{ m}^2/\text{s}$). Note also that the diffusion coefficients of water are slightly smaller in *1OC3.8* than in *1OC4.3* reflecting the stronger cation-water interactions when the charge is further off center. The results for LJ particles included for comparison purposes show that the ionic diffusion coefficients are much less affected by these nonpolar particles, with only very small increases observed up to 50 mol%. In system *1OC3.8* the diffusion coefficients remain practically constant over the entire concentration range.

The viscosities and σ_{el}/ρ_+ for systems in the weakly paired regime are plotted in Fig. 5.17. For pure ionic liquids we have shown in Chapter 3.3.2 (Fig. 3.8) [28] that in the weakly paired regime the viscosity is lower for more charge displaced systems because charge displacement leads to spatially nonuniform counterion distributions. Again, we see that the viscosities decrease as water is added. The decrease in viscosity is stronger than the ideal case (dotted line), but the deviation from ideal behavior is less for the more charge off center system *1OC3.8*. The likely reason for this is that as the charge is moved further off center, the cation-water interaction becomes stronger. This effect is also evident above 20-30 mol%, where the viscosities of *1OC3.8*-water mixtures are larger than those of corresponding *1OC5* and *1OC4.3* systems. For LJ particles, the viscosities also decrease with increasing

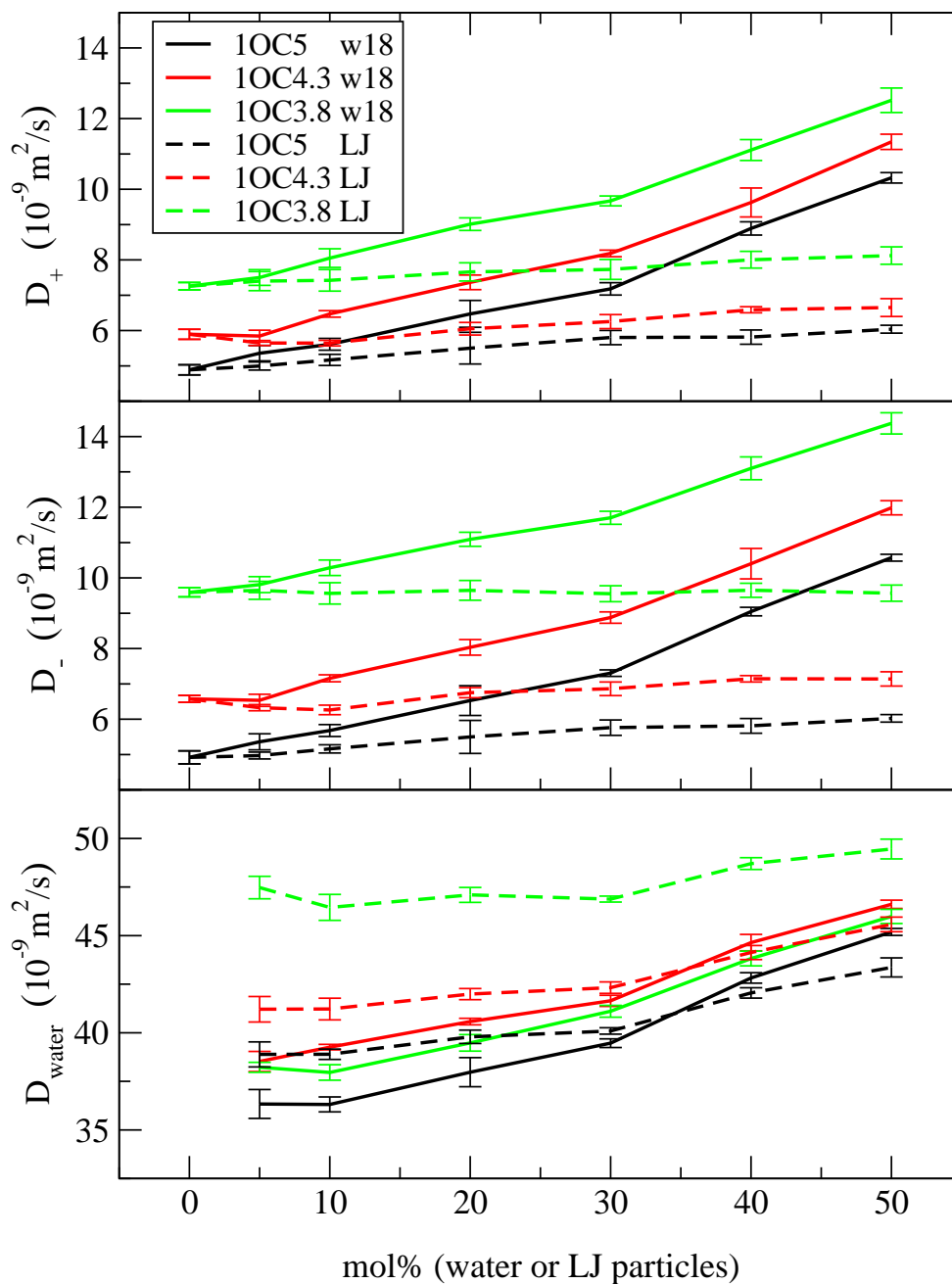


Figure 5.16: Diffusion coefficients of the cations (top panel), anions (middle panel), and water (LJ particles) (bottom panel) versus water (LJ particle) concentration for charge-off-center models mixed with water (solid lines) or LJ particles (dashed lines). The error bars represent one standard deviation.

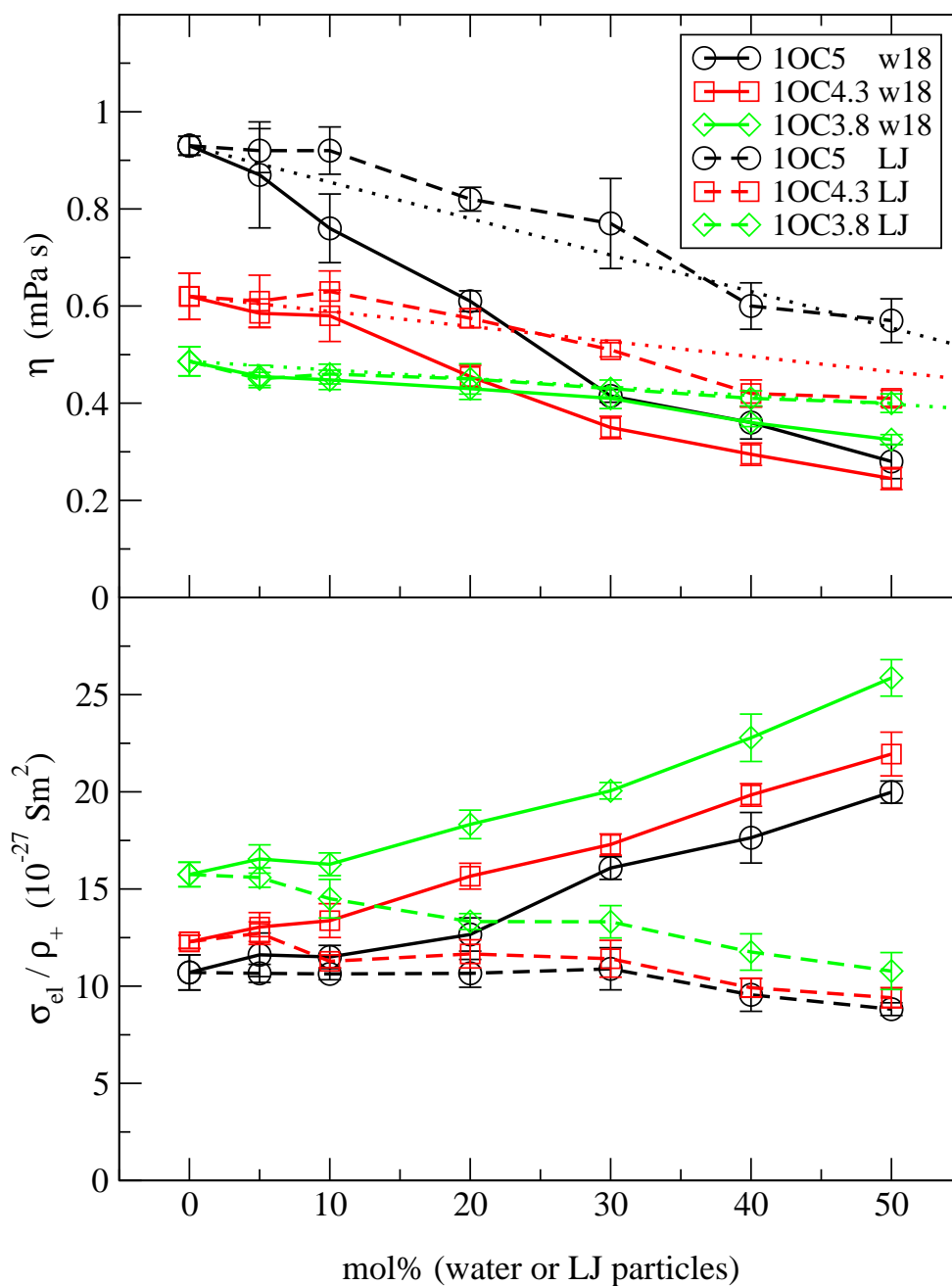


Figure 5.17: Viscosity (top panel) and σ_{el}/ρ_+ (bottom panel) versus water (LJ particle) concentration for charge-off-center models mixed with water (solid lines) or LJ particles (dashed lines). The lightly dotted lines (top panel) show the linear behavior expected for all ideal 1OCY-water mixtures. The error bars represent one standard deviation.

concentration, following the ideal lines (not shown) to a good approximation.

For pure ionic liquids σ_{el}/ρ_+ increases with charge displacement as long as the model remains in the weakly paired regime (Chapter 3.3.2, Fig. 3.8) [28]. Here we see that σ_{el}/ρ_+ increases with added water consistent with the behavior of the diffusion coefficients (Fig. 5.16) discussed above. In mixtures with LJ particles, σ_{el}/ρ_+ decreases with increasing concentration, in all likelihood due to increased cation-anion correlations, as noted above for size disparate systems.

We now consider system *1OC3.1* which has a relatively large charge displacement, and lies in the strongly paired regime. For this system the variation of the transport properties with added water is very different from that described above for systems where the ions are only weakly paired.

Diffusion coefficients for mixtures of *1OC3.1* (blue lines) with water and LJ particles are shown in Fig. 5.18. The corresponding results for models *1OC5* and *1OC3.8* are included in this plot for ease of comparison. For model *1OC3.1*, the ionic diffusion coefficients (solid blue lines, top and middle panels) decrease to a minimum at approximately 30 mol% water, then show a strong increase similar to the other models. The diffusion coefficients of water (bottom panel) are much lower in the *1OC3.1* mixtures than in corresponding systems with the other ionic liquid models. The water diffusion coefficients remain essentially constant up to about 30 mol% water, and then increase strongly. In fact, for $\lesssim 30$ mol% water the diffusion coefficients of water are very close to those of the cations, with those of the anions being slightly larger. These observations can be easily understood in view of the very strong cation-water correlations that appear in the corresponding rdfs, and are discussed above (Chapter 5.3.1). For mixtures that are $\lesssim 30$ mol% water, all water molecules are tightly “bound” to cations and diffuse at the same rate. There are no “free” water molecules below ~ 30 mol% water, and cation-water “bonding” can explain both the minimum in the cation curve, and the constant value found for water at lower concentrations. The corresponding minimum in the anion curve illustrates that the diffusion of both ionic species is very strongly coupled. Above 33 mol%, there are not enough cations to bind all of the water molecules, and the presence of “free” water molecules leads to increasing diffusion coefficients of all

species at concentrations above ~ 30 mol% water. We note that the results obtained with LJ particles do not exhibit these effects, but rather the diffusion coefficients show a small continuous increase with concentration.

The influence of water on the viscosity and σ_{el}/ρ_+ of 1OC3.1-water mixtures is given in Fig. 5.19. Note from the 1OC3.8 results included for comparison, that the viscosities (top panel) of these systems are much larger, and the conductivity (bottom panel) considerably lower than those found in the weakly paired regime. For pure ionic liquids that fall into the strongly paired regime, the strong directional ion pairs are responsible for the high viscosities, compared to those of weakly paired systems (see Chapter 3, Fig. 3.8) [28]. From Fig. 5.19, we see that when water is added to this system, the viscosity (solid blue line, top panel) increases even further reaching a maximum at about 30 mol% water. In contrast, when LJ particles are added a slightly decreasing viscosity is observed over the entire concentration range. We demonstrated above that the directional cation-anion pairs, that are present in pure 1OC3.1, are replaced by cation-water pairs as water is added to the system. The stronger cation-water “bonds” might be a contributing factor to the viscosity increase. However, if we inspect configurational snapshots, such as the example given in Fig. 5.7, we note the presence of more extended structures that are likely significant. In these mixtures one finds cation-water-anion “tethers” that can interact with other tethers to form more extended connections. It is probably these structures that give rise to the rapid increase in viscosity as water is added. The decrease in viscosity above 30 mol% water can be accounted for by the presence of “free” water molecules reducing the influence of the ion-water structures.

For model 1OC3.1, σ_{el}/ρ_+ also displays rather unusual behavior. For pure ionic liquids, the diffusion coefficients for 1OC3.1 are larger than those for charge-centered, or less charge displaced models (see Fig. 5.18), yet, σ_{el}/ρ_+ is lower for 1OC3.1. These apparently contrasting observations for pure ionic liquids are explained by the existence of long-lived directional ion pairs in 1OC3.1, which effectively reduces the number of charge carriers (as also seen in Chapter 3, Fig. 3.8) [28]. From Fig. 5.19, we see that for system 1OC3.1, as the amount of water is increased σ_{el}/ρ_+ increases (solid blue line, bottom panel), whereas

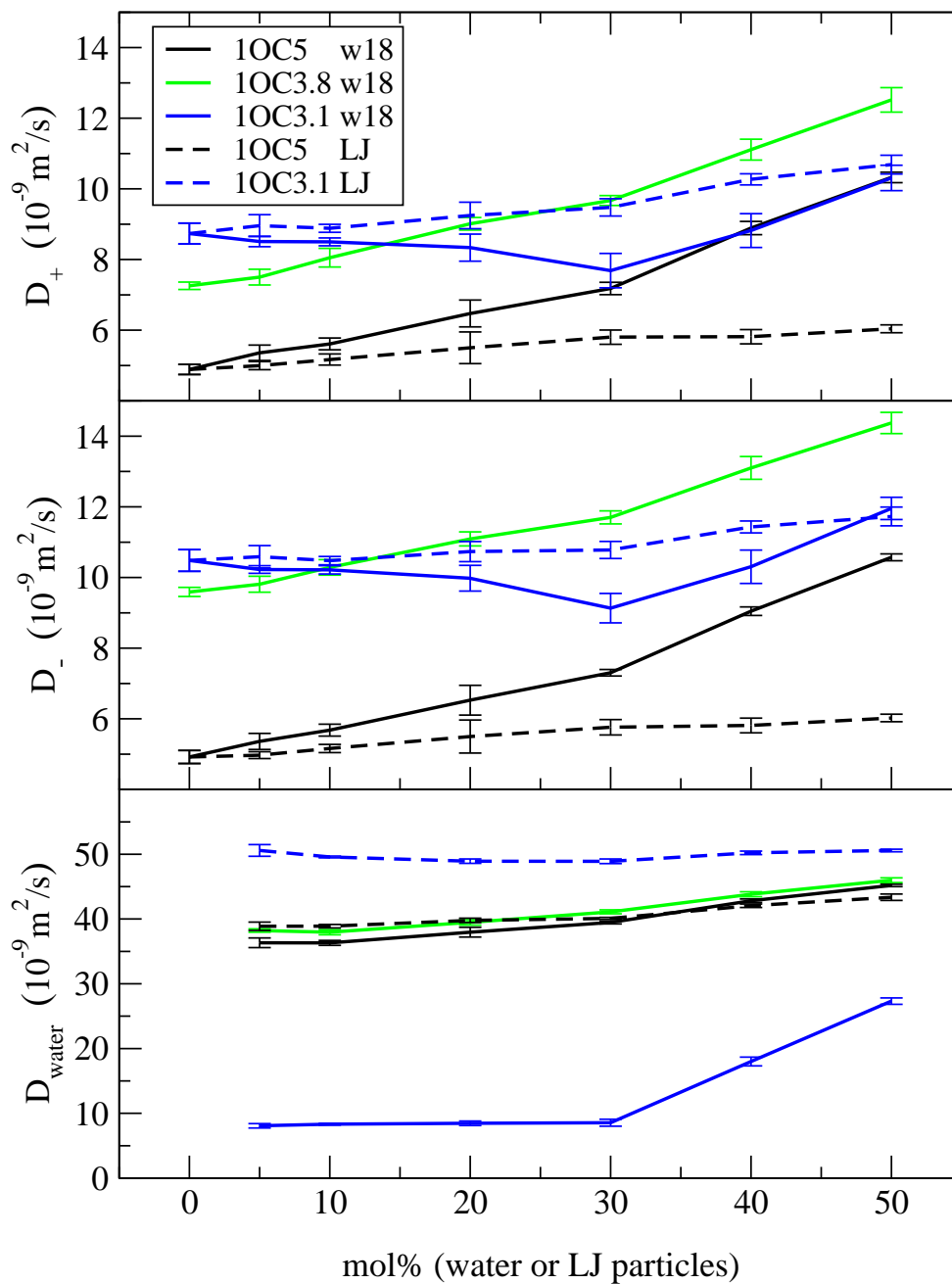


Figure 5.18: Diffusion coefficients of the cations (top panel), anions (middle panel), and water (LJ particles) (bottom panel) versus water (LJ particle) concentration for model 1OC3.1 mixed with water (solid lines) or LJ particles (dashed lines). Results for some corresponding mixtures with the different ionic liquid models indicated on the figure are included for comparison. The error bars represent one standard deviation.

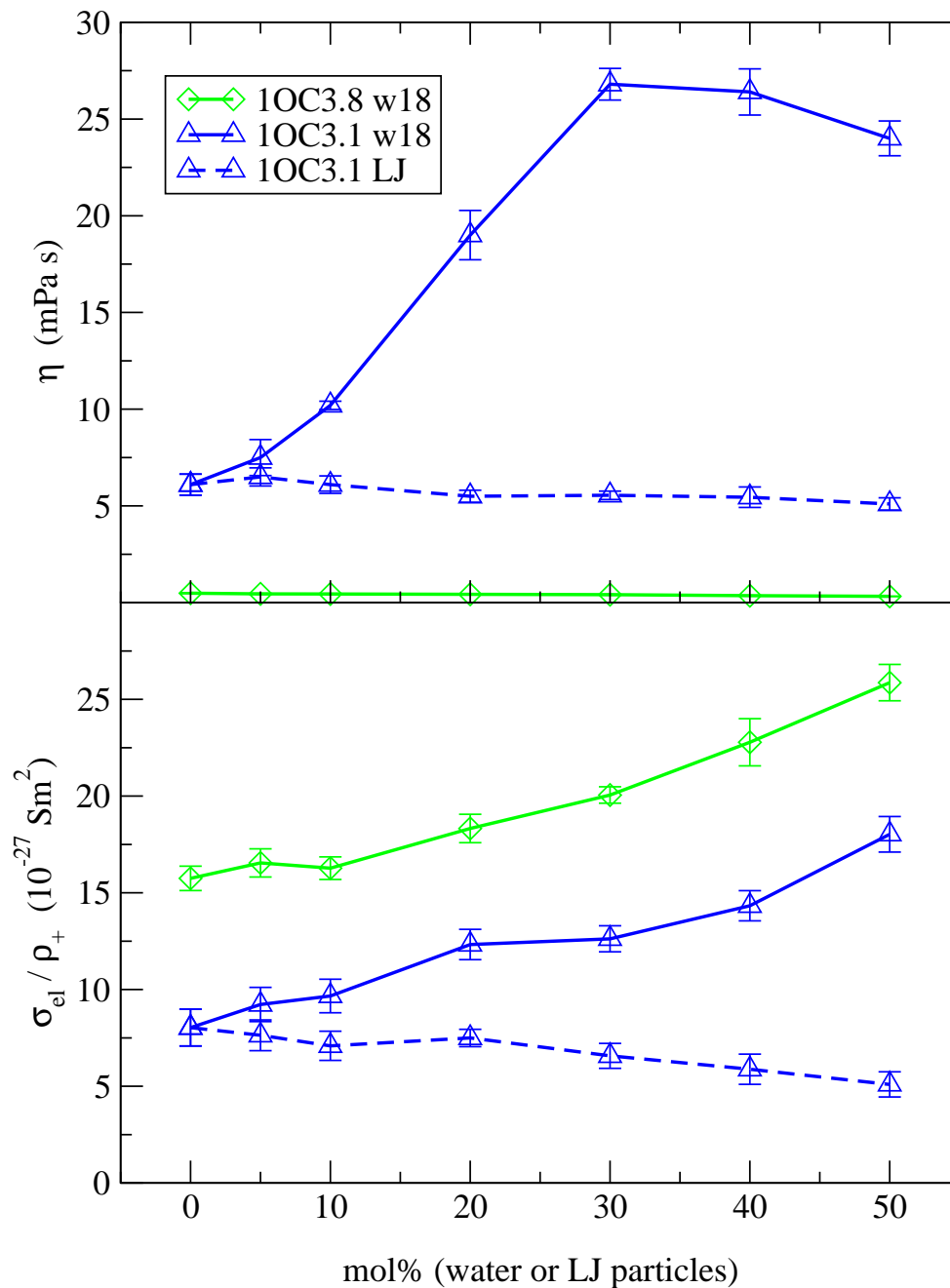


Figure 5.19: Viscosity (top panel) and σ_{el}/ρ_+ (bottom panel) versus water (LJ particle) concentration for model 1OC3.1 mixed with water (solid lines) or LJ particles (dashed lines). Corresponding results for 1OC3.8-water systems are included for comparison. The error bars represent one standard deviation.

the ionic diffusion coefficients decrease for concentrations up to 30 mol% water. The explanation for this unusual behavior is that when electrically neutral water molecules replace the anions in the directional cation-anion pairs, the number of “free” charge carriers is effectively increased. Thus, when water is added, σ_{el}/ρ_+ increases, even though the ion mobility decreases or remains approximately constant. We note that when LJ particles are added, σ_{el}/ρ_+ (dashed blue line, bottom panel) decreases despite that fact that the diffusion coefficients remain nearly constant (Fig. 5.18). As in other situations discussed above, this is likely due to increased cation-anion correlations (pair bonding in this case), when the nonpolar component is added.

It is worth noting, that as in Chapter 4 [29], we did carry out some calculations varying the cation moment of inertia over the physically expected range (see Table 5.1). Consistent with our previous results in Chapter 4.3.2 (Fig. 4.12) [29], we find that larger moments of inertia decrease the diffusion coefficients and electrical conductivity, and increase the viscosity a little. However, the rotational-translational coupling is weak, and does not influence the qualitative trends observed for the transport properties.

5.4 Summary and Conclusions

Water is a common impurity in ionic liquids, it can be absorbed from the atmosphere, and tends to have an important influence on the transport properties of RTILs, even at relatively low concentrations. In the present Chapter, we have investigated the effects of water on the behavior of several model ionic liquids, that capture some of the common characteristics of RTIL ions. Perhaps more importantly, we have attempted to probe the underlying reasons for water’s significant influence on properties such as the shear viscosity, and electrical conductivity, that are of much interest in RTIL research.

The ionic liquid models that we consider vary in ion size disparity, and in the location of the cation charge. We note, that for the models we consider, the pure ionic liquid properties are invariant to exchanging the signs of the ionic charges, due to the symmetry of the Coulombic interactions. However, this invariance to charge exchange does not hold

when water is added, because the water model employed does not interact symmetrically with positive and negative charges. Therefore, the results we report for the water mixtures are in this sense less general than is the case for the pure ionic liquids.

The types of behavior that we observe when water is added to our model ionic liquid can be roughly divided into two classes. For the less “extreme” systems, where the ion size disparity is not too large (cation:anion diameter ratio $\lesssim 2:1$), or the cation charge is not too far off center (weakly paired regime in the pure ionic liquid case), the general trends that we find compare well with those commonly observed in experiments. In particular, the addition of water increases the ionic diffusion coefficients and the electrical conductivity, and decreases the viscosity. In some systems, the water-induced viscosity reduction is much greater than a simple ideal relationship would imply.

We attempted to identify the origin of water’s influence by analyzing our results in some detail. From a structural perspective, we noted that water tends to replace counterions, in the first coordination shell of the ions. This weakens the ion-ion correlations as one would expect, but in some systems, where the ion-ion correlations are affected only slightly by water, there are still large changes in the transport properties. Moreover, we show that while water replaces counterions in the first coordination shell, the occupied shell volume remains practically constant. Therefore, changes in local “density” cannot explain the increased ion diffusivity induced by adding water. Thus, at least at lower water concentrations, structural changes do not appear to offer a convincing explanation of commonly observed water-induced effects.

This motivated us to seek a possible dynamical explanation. If one notes that in typical RTILs the molecular mass of water is generally much less than that of the ions, then one might expect dynamical effects to be significant. Therefore, we carried out simulations with the same water model, to ensure that the equilibrium structural effects are unaltered, but with the mass increased to that of the ions. We find that the larger mass significantly reduces the influence of water on the transport properties, clearly demonstrating that dynamical, rather than equilibrium structural effects, can be dominant. Basically, when counterions are displaced from the first coordination shell by much lighter water molecules, the “caging” of

the ions is reduced. This in turn leads to larger ionic diffusion coefficients, lower viscosity, and increased conductivity. We note that the effects of the molecular mass of water on the dynamical properties of RTIL-water mixtures could be confirmed by carrying out simulations varying the water mass, as we have done, but using all-atom models that are expected to give a more realistic representation of RTILs.

That we are dealing primarily with a first coordination shell effect is clear when one compares the results for water with those for corresponding systems where water is replaced by LJ particles. The LJ particles do not displace counterions from the first coordination shell, their effect on the transport properties is much weaker than that of water, and essentially in accord with the ideal expectations.

In more “extreme” systems with large size disparities, or the cation charge far removed from the center (the strongly paired regime in pure ionic liquids), our models can differ from the commonly observed behavior, and this is especially true of the viscosity. In a size disparate system (3C5) where the cation:anion ratio is 3:1, the diffusion coefficients and the electrical conductivity behave “normally” increasing with increasing water concentration. However, the viscosity deviates, increasing with water concentration, at least up to 50 mol% water. We believe that the reason for this viscosity increase is the formation of chain-like water-anion clusters that can “weave” among the larger anions. These structures do not form for smaller size disparities.

In a pure ionic liquid where the charge is far off center (1OC3.1), there exist large numbers of strongly bonded directional ion pairs, which lead to high viscosities and very low conductivities (Chapter 3) [28]. When water is added to this system, the viscosity increases steeply up to about 30 mol% water, then levels off, and decreases at higher concentrations. The electrical conductivity increases with added water, despite the fact that the diffusion coefficients decrease up to 30 mol%, and only increase slightly at higher concentrations. This peculiar behavior can be readily explained by noting that water replaces the anion in the directional cation-anion pairs to form even more strongly bonded cation-water pairs, until, at 33 mol%, all anions have been replaced by water. In these systems, one finds cation-water-anion triples, and we believe that these structures account for the sharp viscosity

increase, reaching a maximum at approximately 30 mol%, above this concentration the “free” water molecules cause the viscosity to decrease. The increase in conductivity can be explained by the replacement of strongly bound, electrically neutral cation-anion pairs with charged cation-water pairs hence increasing the density of “free” charge carriers.

Bibliography

- [1] T. Welton, Chem. Rev. **99**, 2071 (1999).
- [2] K. R. Seddon, A. Stark and M.J. Torres, Pure Appl. Chem. **72**, 12, 2275 (2000).
- [3] H. Rodriguez and J. F. Brennecke, J. Chem. Eng. Data **51**, 2145 (2006).
- [4] E. Gomez, B. Gonzalez, A. Dominguez, E. Tojo and J. Tojo, J. Chem. Eng. Data **51**, 696 (2006).
- [5] B. Mokhtarani, A. Sharifi, H. R. Mortaheb, M. Mirzaei, M. Mafi and F. Sadeghian, J. Chem. Thermodynamics **41**, 323 (2009).
- [6] J. A. Widegren, E. M. Saurer, K. N. Marsh and J. W. Magee, J. Chem. Thermodynamics **37**, 569 (2005).
- [7] H. T. Xu, D. C. Zhao, P. Xu, F. Q. Liu and G. Gao, J. Chem. Eng. Data **50**, 133 (2005).
- [8] W. W. Liu, L. Y. Cheng, Y. M. Zhang, H. P. Wang and M. F. Yu, J. Mol. Liq. **140**, 68 (2008).
- [9] L. A. S. Ries, F. A. do Amaral, K. Matos, E. M. A. Martini, M. O. de Souza and R. F. de Souza, Polyhedron **27**, 3287 (2008).
- [10] M. A. Firestone, J. A. Dzielawa, P. Zapol, L. A. Curtiss, S. Seifert and M. L. Dietz, Langmuir **18**, 7258 (2002).
- [11] O. Green, S. Grubjesic, S. Lee and M. A. Firestone, Polymer Reviews, **49**, 4, 339 (2009).
- [12] C. G. Hanke and R. M. Lynden-Bell, J. Phys. Chem. B **107**, 10873 (2003).
- [13] C. Schröder, J. Hunger, A. Stoppa, R. Buchner and O. Steinhauser, J. Chem. Phys. **129**, 184501 (2008).
- [14] A. R. Porter, S. Y. Liem and P. L. A. Popelier, Phys. Chem. Chem. Phys. **10**, 4240 (2008), and references therein.
- [15] M. Moreno, F. Castiglione, A. Mele, C. Pasqui and G. Raos, J. Phys. Chem. B **112**, 7826 (2008).
- [16] U. Schröder, J. D. Wadhawan, R. G. Compton, F. Marken, P. A. Z. Suarez, C. S. Consorti, R. F. de Souza and J. Dupont, New J. Chem. **24**, 1009 (2000).

- [17] A. M. O'Mahony, D. S. Silvester, L. Aldous, C. Hardacre and R. G. Compton, *J. Chem. Eng. Data* **53**, 2884 (2008).
- [18] L. Cammarata, S. G. Kazarian, P. A. Salter and T. Welton, *Phys. Chem. Chem. Phys.* **3**, 5192 (2001).
- [19] T. Köddermann, C. Wertz, A. Heintz and R. Ludwig, *Angew. Chem. Int. Ed.* **45**, 3697 (2006).
- [20] J. Luczak, J. Hupka, J. Thöming and C. Jungnickel, *Colloids and Surfaces A: Physicochem. Eng. Aspects* **329**, 125 (2008), and references therein.
- [21] H. Y. Wang, J. J. Wang, S. B. Zhang and Z. P. Xuan, *J. Phys. Chem. B* **112**, 16682 (2008).
- [22] A. Mele, C. D. Tran and S. H. DePaoli Lacerda, *Angew. Chem. Int. Ed.* **42**, 4364 (2003).
- [23] H. C. Chang, J. C. Jiang, W. C. Tsai, G. C. Chen, C. Y. Chang and S. H. Lin, *Chem. Phys. Lett.* **432**, 100 (2006).
- [24] Y. Umebayashi, J. C. Jiang, Y. L. Shan, K. H. Lin, K. Fujii, S. Seki, S. I. Ishiguro, S. H. Lin and H. C. Chang, *J. Chem. Phys.* **130**, 124503 (2009).
- [25] Y. Danten, M. I. Cabaco and M. Besnard, *J. Phys. Chem. A* **113**, 2873 (2009).
- [26] C. Schröder, T. Rudas, G. Neumayr, S. Benkner and O. Steinhauser, *J. Chem. Phys.* **127**, 234503 (2007).
- [27] H. V. Spohr and G. N. Patey, *J. Chem. Phys.* **129**, 064517 (2008).
- [28] H. V. Spohr and G. N. Patey, *J. Chem. Phys.* **130**, 104506 (2009).
- [29] H. V. Spohr and G. N. Patey, *J. Chem. Phys.* **132**, 154504 (2010).
- [30] M. N. Kobrak and N. Sandalow, in *Molten Salts XIV* (The Electrochemical Society, Pennington, NJ, 2006).
- [31] M. N. Kobrak and H. Li, *Phys. Chem. Chem. Phys.* **12**, 1922 (2010).
- [32] H. J. C. Berendsen, J. P. M. Postma, W. F. van Gunsteren and J. Hermans, B. Pullman (ed.) *Intermolecular Forces*, 331 (Reidel, Dordrecht, 1981).
- [33] P. Mark and L. Nilsson, *J. Phys. Chem. A* **105**, 9954 (2001).
- [34] D. Frenkel and B. Smit, *Understanding Molecular Simulation: From Algorithms to Applications* (Academic Press, 1996).
- [35] M. P. Allen and D. J. Tildesley, *Computer Simulations of Liquids* (Oxford, Clarendon, 1987).
- [36] M. Deserno and C. Holm, *J. Chem. Phys.* **109**, 18, 7678 (1998).
- [37] D.J. Evans and G.P. Morriss, *Comput. Phys. Rep.* **1**, 297 (1984).

- [38] J. P. Hansen and I. R. McDonald, *Theory of Simple Liquids*, 2nd ed. (Academic, London, 1986).

Chapter 6

Conclusion

6.1 Analysis

This thesis systematically investigates the influence of some basic RTIL ion characteristics on liquid structure and dynamical properties. The characteristics considered are size disparity, charge displacement from the center of mass, and counterion charge distance. We developed several simple models that isolate these features, while keeping other variables constant. Molecular dynamics calculations are employed to calculate the model structure and its dynamical properties such as diffusion coefficients, viscosity and electrical conductivity (for the computational approach see Appendix A).

In Chapter 2 the influence of ion size disparity on the structural and dynamical properties of ionic liquids is systematically investigated. Ion size ratios are varied over a realistic range (1:1 to 5:1), while other important molecular and system parameters are fixed. In this way we isolate and identify effects that stem from size disparity alone. In Chapter 3 the influence of charge location on the structure and transport properties of ionic liquids is investigated. The model considered consists of univalent spherical ions with the cation charge displaced from its center of mass. In Chapter 4 we extend our work to spherical ionic liquid models where both size disparity and charge displacement are present, and where the characteristic distance σ'_{+-} , determining the strength of the Coulombic attractions, is unconstrained. We consider the interplay among these molecular features, and elucidate their relative importance to the behavior of ionic liquids. Finally, in Chapter 5 we consider mixtures of size disparate and charge displaced models with water or neutral Lennard-Jones particles.

We find that size disparity, charge location, and σ'_{+-} can all have large and often competing effects on the transport properties. Size disparity has the effect of increasing the

diffusion coefficients and electrical conductivity, while decreasing the viscosity. This effect can be mainly traced to a reduction in coordination numbers for more size disparate systems. Reducing σ'_{+-} has an opposite effect of similar magnitude, so that the effects of size disparity and σ'_{+-} can largely cancel each other. A small charge displacement leads to weakly bound, directional ion pairs, the resulting asymmetric ion-counterion distribution gives rise to increased diffusion coefficients, and consequently lower viscosity and increased conductivity. In this regime, the effects of size disparity and displaced charges complement and strengthen each other. σ'_{+-} decreases with increasing charge displacement, but the effects of size disparity and displaced charges outweigh the opposing effects of σ'_{+-} . A large charge displacement and short σ'_{+-} leads to strongly bound, long-lived, directional ion pairs, and in this regime the trends noted above are reversed, increased viscosities and decreased conductivities are observed. Here, size disparity is of little importance for viscosity and electrical conductivity. The strong, directional ion pairing dominates the liquid behavior.

The addition of water to ionic liquid models with moderate size disparities or moderate charge displacement leads to increased diffusion coefficients and electrical conductivities, and decreased viscosities. This agrees with what is commonly observed experimentally for room temperature ionic liquids. This effect of water can not be explained simply with changes in the equilibrium structure. The dominant effect of water is shown to be dynamical in origin. Light water molecules replace heavy ions in the first coordination shell of an ion, thereby reducing caging and increasing ion mobility. If water can form strong associated structures with one of the ions in an ionic liquid model, the liquid property trends can deviate from the common behavior. Water strongly couples to the small anions of strongly size disparate ionic liquid models. The formation of elongated water-anion clusters around the large cations leads to increasing viscosities for mixtures with higher water content. In systems with large charge displacements, where long-lived directional counterion pairs are formed, water inserts itself into the counterion pairs, coupling strongly to the cation. The formation of cation-water-anion triples increases the viscosity strongly and decreases diffusion coefficients up to concentrations of 30 mol% water. At higher concentrations of water, this behavior is reversed due to the presence of water molecules that are not coupled

RTIL characteristic	diffusion	viscosity	el. conductivity
↑ SD	↑	↓	↑
↓ σ'_{+-}	↓	↑	↓
↑ OC, small	↑	↓	↑
↑ OC, large (small σ'_{+-})	↓	↑	↓
↑ water (generally)	↑	↓	↑

Figure 6.1: Schematic overview of all simulation results. The black arrows indicate an increase or decrease in the RTIL characteristic, the red (green) arrows indicate a corresponding increase (decrease) in transport properties. Here, SD stands for size disparity, OC for a displacement of the cation charge from the center of mass (off-center model) and σ'_{+-} is the positive-negative center of charge distance.

to cations. Despite decreasing diffusion coefficients, the electrical conductivity increases as a consequence of the loosening of the directional counterion pairs.

6.2 Comparison with Experimental Work

Comparison with experimental results is attempted throughout the thesis. For example, our predictions about size disparity and varying σ'_{+-} agree qualitatively well with experimental studies of systematic changes in RTIL ions such as those of Seki *et al.* [1] and Shirota *et al.* [2], as described in Chapter 4.1. Seki *et al.* investigate the difference between triethylpentylammonium and triethylpentylphosphonium ionic liquids with the bis(trifluoromethanesulfonyl)amide anion, Shirota *et al.* investigate 1-butyl-3-methylimidazolium with PF_6^- , AsF_6^- and SbF_6^- anions.

Our charge displaced models directly explore the effects of displaced charge to (counter) charge interactions, but the interactions of these models are also analogous to directional interactions such as hydrogen bonds, ion-dipole or dipole-dipole interactions. We can find experimental examples that show the same trends in dynamical properties as our models

(Chapter 4).

In this thesis, an increase in viscosity is observed when comparing a slightly charge displaced to a charge centered system. Similarly, the removal of a single hydrogen bond on imidazolium (R'=methyl instead of hydrogen in Fig. 1.1, 1) was found to increase the viscosity in experiments [3–6]. The imidazolium has the same total charge for either substituent, but the hydrogen substituent has a larger partial positive charge, and so the positive charge is displaced further from the center of mass, leading to an increased charge arm for the cation with a hydrogen substituent. Both our model and the hydrogen bond are directional interactions between a (partial) positive charge that is displaced from the center of mass and an anion. It was also observed that RTILs that are able to form multiple hydrogen bonds have relatively large viscosities [7–9]. These types of ions form “network-like” interactions, whereas a single weak directional interaction has the effect of strengthening interactions in one direction, while weakening interactions in the other directions.

The strongly charge displaced cations lead to the formation of long-lived ion pairs, these systems have high viscosities and low conductivities. The formation of directional ion pair interactions (and also larger aggregates) in RTILs is used to explain experimental observations of anomalously low conductivities of some RTILs that at the same time display large diffusion coefficients [10–13]. Recently, creating more strongly hydrogen bonded, directional ion pairs has been put forward as a possible means of achieving larger viscosity reductions [6]. Our work shows that this might not work in practice, as the viscosity increases when strong counterion pairs are formed.

The temperature dependence of the transport properties is examined for size disparate and charge displaced models in Chapters 2 and 3. In accord with experiment, the temperature dependence of all transport properties is well represented by the Vogel-Fulcher-Tammann equation [14, 15]. Deviations from Arrhenius behavior are found to be most important for the conductivity of strongly charge displaced systems. Based on our results, this possibly indicates that directional ion pairs create an additional “barrier” to charge transport in some ionic liquids. The dependence of the diffusion coefficients on the temper-

ature/viscosity ratio is well described by the fractional Stokes-Einstein relation $D \propto (T/\eta)^\beta$. For many molten inorganic salts, it was shown that the exponential factor $\beta \approx 0.8$ [16]. The deviation of β from one is explained by a difference in the elementary mechanisms of diffusion and viscosity. The self diffusion coefficient is dependant on the motion of the particle itself, whereas the viscosity depends on the interactions among many particles, (and the correlation functions are accordingly one-particle and many-particle functions, respectively). Different energies of activation are needed for these two processes to occur, and it is likely that their ratio determines the factor β (see Appendix A.3.2). Our results are consistent with this physical explanation for the fractional Stokes-Einstein relation. The size disparate models are similar to simple molten salts, and so in agreement with experiments, our size disparate systems do show a fractional Stokes-Einstein dependence with $\beta \approx 0.8$. On the other hand, the charge displaced systems differ substantially in their particle interactions from simple molten salts. For these systems β decreases with increasing displacement. Additional influences of the strong ionic pairs on the viscosity lead to the stronger deviation of the exponential factor in these systems.

A direct comparison of our simple models to experimental RTIL ions (or atomistic RTIL simulation models) with their multiple variables is difficult in many cases. Often changes in size disparity or charge placement are accompanied by changes in other variables. For example, a change of charge placement, through elongating alkane substituents of quaternary amines or imidazoles, changes both molecular shape and the strength of van der Waals interactions among the ions. This simultaneous change of multiple ion characteristics prohibits separation of single influences, an experiment observes the influence of the sum of the changing molecular interactions on transport properties. Our models should only be compared to experiments in which size disparity, charge displacement and/or σ_{+-} are the dominant factors.

The simplicity of our models is both a weakness and a strength. On one hand, our models do not capture all influential characteristics of RTIL ions. If a specific RTIL ion is compared to our model, one might argue that we are missing an important characteristic, for example, a particular ion shape, charge distribution, or effect of substituent variation. On

the other hand, the simplicity of our models allows us to observe the direct effect of a single ion characteristic on the structure and transport properties of the liquid. The variation of single characteristics, followed by an investigation of a combination of them, enables us to judge the interrelationships and relative importance of different characteristics in different regimes.

The simplicity of our models and the strong Coulombic attraction between ions, requires us to use high simulation temperatures to achieve a liquid state, simulation temperatures that are in the range of molten salts rather than around room temperature. At these temperatures, our strongly correlated models have the advantage of relatively fast dynamics, and so the time correlations of the dynamical properties decay quickly. Accordingly, we can calculate the transport properties of our systems accurately. Overall, diffusion coefficients and electrical conductivities are one to two magnitudes higher in our models than in RTILs, and the viscosities are lower by a similar amount. A close quantitative fit of our models to RTIL liquid properties is not the purpose of this work. Our intention of investigating the influence of some of the basic physical properties of the ions was achieved. We are able to make qualitative predictions about the importance of the chosen ion characteristics on ionic liquid properties.

6.3 Future Work

The analysis in the previous paragraph, of the advantages of the models used in this thesis, but also their shortcomings, suggests various new approaches for future simulations of RTILs.

One area of future work should be the investigation of other important RTIL ion characteristics that have not been studied in this work. Here we identify two main areas of interest; ion shape, and ion charge distribution.

The first step in the direction of mimicking RTIL ion shape more closely, would be to better capture the disk-like shape of some common RTIL ions that consist of five- and six-membered (heteroatom) rings, and the rod-like shapes of ions with long substituents. The

influence of prolate/oblate ion shapes on structure and transport properties is currently being investigated in our group. A further convergence to RTILs might be to emulate more complicated ion shapes by merging spheres, disks or rods rigidly into simple shapes. Simple dumbbells, of two same-sized or differently sized spheres, disks with small attached spheres or rods, would be more similar to spherical or disk-like ions with substituents. Even closer to experimental RTILs would be models that consist of linked spheres with flexible “bond” angles, imitating the flexible side chains of some RTILs. This approach could be very similar to coarse grained models, which have been already studied (Chapter 1.3.3).

Charge distributions also play an important role for RTIL liquids [19, 20]. Each ion has an overall charge, which is distributed over all atoms in the RTIL molecule, leading to electrostatic multipole interactions. In aromatic rings, for example, the electron-rich π system above and below the ring is negatively charged, while the ring plane is positively charged, resulting in an electric quadrupole. Many RTILs contain aromatic cations, so a model that includes quadrupole-ion interactions would more closely resemble this type of RTIL. Kobrak *et. al* [20] affirm that the dipolar description of charge and dielectric continuum models commonly used for non-ionic liquids cannot describe RTILs correctly due to their ionic nature. Future work will have to apply more appropriate, newly developed theories to these liquids.

The high melting temperatures of our model ionic liquids in comparison to RTILs lead to the question of the reason for the low melting points of the latter. Low melting points in RTILs are commonly ascribed to large ions, diffuse distributions of charge, asymmetry and weak interactions (Chap. 1.2.1). Future work should investigate the influence of isolated ion characteristics on melting and crystal structures of RTILs. A simulation study of this kind is currently implemented in our group. A genetic algorithm is used to predict crystalline structures of simple ion models. Subsequently, the solid-liquid phase transition of these simple ion models will be investigated.

Of further interest might be systematic computational studies of the transport properties and structure of simple ion models at solid (charged) interfaces. One area of interest in RTILs is their useage in electrochemical processes [23–25]. RTILs are also proposed as

components of devices for the renewable production of energy, such as fuel cells and dye sensitized solar cells [26]. The classical theories for electrical double layers in dilute aqueous electrolytes and also in molten salts were found to be inaccurate for RTILs [27]. Simple models might provide insights about the influence of different ion characteristics on the deviation of RTIL-solid interface properties from that of molten salts.

Bibliography

- [1] S. Seki, K. Hayamizu, S. Tsuzuki, K. Fujii, Y. Umebayashi, T. Mitsugi, T. Kobayashi, Y. Ohno, Y. Kobayashi, Y. Mita, H. Miyashiro, and S. Ishiguro, *Phys. Chem. Chem. Phys.* **11**, 3509 (2009).
- [2] H. Shirota, K. Nishikawa, and T. Ishida, *J. Phys. Chem. B* **113**, 9831 (2009).
- [3] P. Hunt, *J. Phys. Chem. B* **111**, 4844 (2007).
- [4] K. Fumino, A. Wulf, and R. Ludwig, *Ang. Chem.* **47**, 8731 (2008).
- [5] S. Zahn, G. Bruns, J. Thar, and B. Kirchner, *Phys. Chem. Chem. Phys.* **10**, 6921 (2008).
- [6] R. Ludwig and D. Paschek, *ChemPhysChem* **10**, 516 (2009).
- [7] J. Dupont and J. Braz. *Chem. Soc.* **15**, 341 (2004).
- [8] G. Yu, S. Zhang, G. Zhou, X. Liu, and X. Chen, *AIChE* **53**, 12, 3210 (2007).
- [9] Y. Zhang, S. Zhang, X. Lu, Q. Zhou, W. Fan, and X. Zhang, *Chem. Eur. J.* **15**, 3003 (2009).
- [10] A. Noda, K. Hayamizu, and M. Watanabe, *J. Phys. Chem. B.* **105**, 4603 (2001).
- [11] H. A. Every, A. G. Bishop, D. R. MacFarlane, G. Orädd, and M. Forsyth, *Phys. Chem. Chem. Phys.* **6**, 1758 (2004).
- [12] S. Tsuzuki, H. Tokuda, K. Hayamizu, and M. Watanabe, *J. Phys. Chem. B* **109**, 16474 (2005).
- [13] D. R. MacFarlane, M. Forsyth, E. I. Izgorodina, A. P. Abbott, G. Annat, and K. J. Fraser, *Phys. Chem. Chem. Phys.* **11**, 4962 (2009).
- [14] M. N. Kobra, *Adv. Chem. Phys.* **139**, 83 (2008), and references therein.
- [15] H. Tokuda, K. Hayamizu, K. Ishii, A. Susan, M. Watanabe, *J. Phys. Chem. B* **108**, 16593, (2004); **109**, 6103, (2005); **110**, 2833 (2006).
- [16] A. Voronel, E. Veliyulin, and V. Sh. Machavariani, *Phys. Rev. Lett.* **80**, 2630 (1998).
- [17] Y. Wang, W. Jiang, T. Yan and G. A. Voth, *Acc. Chem. Res.* **40**, 1193 (2007).
- [18] B. L. Bhargava and M. L. Klein, *Mol. Phys.* **107**, 4-6, 393 (2009).
- [19] K. Ueno, H. Tokuda and M. Watanabe, *Phys. Chem. Chem. Phys.* **12**, 1629 (2010).

- [20] M. N. Kobraak and H. Li, *Phys. Chem. Chem. Phys.* **12**, 1922 (2010).
- [21] C. P. Fredlake, J. M. Crosthwaite, D. G. Hert, S. N. V. K. Aki and J. F. Brennecke, *J. Chem. Eng. Data* **49**, 954 (2004) and references therein.
- [22] J. Dupont, *J. Braz. Chem. Soc.* **15**, 341 (2004).
- [23] M. Buzzeo, R. Evans and R. G. Compton, *Chemphyschem* **5**, 1106 (2004) and references therein.
- [24] M. Galinski, A. Lewandowski and I. Stepniak, *Electrochim. Acta* **51**, 5567 (2006) and references therein.
- [25] D. R. MacFarlane, J. M. Pringle, P. C. Howlett and M. Forsyth, *Phys. Chem. Chem. Phys.* **12**, 1659 (2010) and references therein.
- [26] J. F. Wishart, *Energy Environ. Sci.* **2**, 956 (2009) and references therein.
- [27] J. Liu, Y. Liu and J. Li, *Phys. Chem. Chem. Phys.* **12**, 1685 (2010) and references therein.

Appendix A

Simulation methods

This Appendix describes the computational model details (A.1) and the methods used to simulate the time evolution of our systems (A.2). Furthermore, it describes the statistical mechanical methods used to calculate the structure and the time dependent properties of the model ionic liquids (A.3).

A.1 The Simulation Model

This thesis uses simple spherical ion models to investigate the influence of RTIL ion characteristics on liquid structure and transport properties. The characteristics of the two main models are described in the introductory Chapter 1.4 (see Figs. 1.2 and 1.3) and in Chapters 2.2, 3.2, 4.2, and 5.2. Here, we give the computational details of the models such as the treatment of different interaction potentials and the rotational treatment of asymmetric bodies.

A.1.1 Interaction Potentials

The interactions of model ions are calculated from interaction potentials, that describe the potential energy, and so the forces, between pairs of particles.

For simplicity, we use a combination of two interaction potentials for our models. We use the Lennard-Jones (LJ) potential $u_{LJ}(r_{ij})$ [1], to include core and dispersion interactions,

$$u_{LJ}(r_{ij}) = 4\epsilon \left[\left(\frac{\sigma_{ij}}{r_{ij}} \right)^{12} - \left(\frac{\sigma_{ij}}{r_{ij}} \right)^6 \right], \quad (\text{A.1})$$

where σ_{ij} and ϵ_{ij} are the LJ parameters, and r_{ij} is the separation between particles i and j . We truncate the LJ potential spherically at a cutoff distance, which introduces an energy

discontinuity for particles entering or leaving the truncation boundary (the total energy is not conserved). To avoid the discontinuity, we shift the LJ potential by a constant amount and use the truncated, shifted LJ potential [1].

LJ parameters for interactions between different species of particles are calculated according to the Lorentz-Berthelot mixing rules, so that $\sigma_{ij} = (\sigma_i + \sigma_j)/2$ and $\epsilon_{ij} = \sqrt{\epsilon_i \epsilon_j}$. The LJ particle size parameters σ_i are listed for different models in Chapter 2.2 (Table 2.1), Chapter 3.2 (Table 3.1 and 3.2), Chapter 4.2 (Table 4.1 and 4.2), and Chapter 5.2 (Table 5.1), the energy parameter $\epsilon = 6 \times 10^{-21} J$ for all models. The LJ parameters are chosen in the range of RTIL sizes, the energy parameter is based on neopentane model parameters [2].

We use the Coulombic potential to account for the ionic interactions [1],

$$u_{Coul}(r'_{ij}) = \frac{q_i q_j}{4\pi\epsilon_0 r'_{ij}}, \quad (\text{A.2})$$

where $q_i = \pm 1e$ is the charge of the ion i , r'_{ij} is the charge-charge distance of ions i and j , and ϵ_0 is the permittivity of free space.

As we are calculating liquid properties of the bulk phase, we employ periodic boundary conditions that periodically repeat the simulation box in all directions to avoid surface phenomena. For the short-range Lennard-Jones interactions it is sufficient to only incorporate interactions with the closest replica (minimum image) of all other particles. However, the Coulombic interactions are long-range and only including the minimum image of the other particles is not sufficient, too many contributions to the potential interactions would be neglected. The total potential energy originating from the Coulombic interactions can be written as

$$u_{Coul,tot} = \frac{1}{8\pi\epsilon_0} \sum_{\mathbf{n}} ' \sum_{i,j}^N \frac{q_i q_j}{|\mathbf{r}'_{ij} + \mathbf{n}L|}, \quad (\text{A.3})$$

where we account for all charges and their interactions with all periodic images \mathbf{n} (where \mathbf{n} is an integer vector denoting the original simulation box $\mathbf{n} = (0, 0, 0)$ and each periodic image $\mathbf{n} = (n_x, n_y, n_z)$). The prime indicates that in the case $i = j$ the term $\mathbf{n} = (0, 0, 0)$ is omitted. In this way, the simulation box is surrounded by a sphere of (simulation box)

periodic images, whose interaction with the ions in the original box are explicitly calculated [3]. To achieve a bulk liquid, this sphere is then surrounded by a homogeneous medium, which is in our case a conductor, the ionic liquid.

The Ewald summation technique is used to account for periodic charge images beyond the simulation cell [1, 3–5]. For our purpose, with small numbers of particles in the simulation cell and simple particle models, the Ewald method is sufficiently fast, but there are more sophisticated, faster summation techniques for simulations with a large number of particles [4–6].

The Ewald method splits the Coulombic interaction into two terms. This can be expressed in a simplified fashion as

$$\frac{1}{r'} = \frac{f(r')}{r'} + \frac{1 - f(r')}{r'} . \quad (\text{A.4})$$

The function $f(r')$ is chosen so that the first term is negligible beyond a cutoff, ideally only the minimum images of particles contribute. The second term should be a slowly varying function, so that its Fourier transform converges rapidly in reciprocal space (only few reciprocal vectors have to be used). For the Ewald method, $f(r')$ is chosen as the complementary error function,

$$\text{erfc}(x) = 1 - \text{erf}(x) = -\frac{2}{\sqrt{\pi}} \int_x^\infty \exp(-t^2) dt , \quad (\text{A.5})$$

but there are many other possible choices for this function.

The total Coulombic potential energy according to the Ewald method is

$$u_{\text{Coul,tot}} = u_r + u_k + u_s + u_d , \quad (\text{A.6})$$

where u_r is the real space term, u_k the reciprocal (k-)space term, u_s a constant self-term correction, and u_d the surface dipole correction. These are described in equations A.7 to A.9. In this work, the last term vanishes, because we are surrounding the considered sphere of charges with a conducting medium and not a vacuum or homogeneous dielectric medium.

The real space term u_r is

$$u_r = \frac{1}{4\pi\epsilon_0} \sum_i q_i \sum_{j>i} q_j \sum_{\mathbf{n}} \frac{\text{erfc}(\kappa|\mathbf{r}'_{ij} + \mathbf{n}L|)}{|\mathbf{r}'_{ij} + \mathbf{n}L|}. \quad (\text{A.7})$$

Physically, we can interpret this as surrounding each point charge with an opposite charge distribution of equal magnitude, so that within a short distance, their influences cancel each other. Typically, the width of the opposite charge distribution, κ , is chosen so that only the original simulation box has to be taken into account in the real space part ($\mathbf{n} = 0$). The size of κ is determined by a series of test calculations, κ is chosen so that the potential energy for both the real space and the reciprocal space terms is converged.

The reciprocal space term u_k is

$$u_k = \frac{1}{V\epsilon_0} \sum_{\mathbf{k}} \frac{1}{|\mathbf{k}|^2} \exp\left(-\frac{|\mathbf{k}|^2}{4\kappa^2}\right) \left[\left(\sum_i q_i \cos(\mathbf{k} \cdot \mathbf{r}_i) \right)^2 + \left(\sum_i q_i \sin(\mathbf{k} \cdot \mathbf{r}_i) \right)^2 \right] \\ + \frac{1}{2V\epsilon_0} \sum_i q_i^2 \sum_{\mathbf{k}} \frac{1}{|\mathbf{k}|^2} \exp\left(-\frac{|\mathbf{k}|^2}{4\kappa^2}\right), \quad (\text{A.8})$$

where V is the simulation box volume, \mathbf{r}_i the position of particle i , and \mathbf{k} a reciprocal space vector. This sum can be interpreted as a charge correction that restores the original charge, it is an equal distribution of charge as that added in the reciprocal space part, but of opposite sign.

The self-term u_s compensates for interactions of the artificially introduced charge-distributions with themselves (first term), and the interactions of charges within the same molecule (second term),

$$u_s = -\frac{1}{4\pi\epsilon_0} \left[\frac{\kappa}{\sqrt{\pi}} \sum_a q_a^2 + \sum_a q_a \sum_b q_b \frac{\text{erf}(\kappa|\mathbf{d}|)}{|\mathbf{d}|} \right], \quad (\text{A.9})$$

where a and b are charges in the same molecule and $|\mathbf{d}|$ is the distance of these charges.

A.1.2 Interaction Site Models and Quaternions

For more complicated simulation models, such as the charge-off-center model and the water model, we include several interaction sites in one molecule. Each site has its specific charge and LJ parameters, and interacts with the sites of all other molecules, but not with the sites on the same molecule. The particle sites are at fixed positions within the particle coordinate system.

The orientation of multiple site particles can be described by Euler angles or by quaternions [1]. Both describe the orientation of the particle's coordinate system around its center of mass with respect to the global coordinate system of the simulation box.

The quaternion \mathbf{Q} of a particle is a set of four scalar quantities,

$$\mathbf{Q} = (q_0, q_1, q_2, q_3) . \tag{A.10}$$

The quaternion uses four parameters to describe a system with three degrees of freedom (rotation around the x , y , and z axis). One of the quaternion parameters is redundant, and the representation of the quaternion is not unique. To achieve uniqueness, the quaternion is constrained by specifying that the sum of the squares of its four constituents must be one. The quaternion can be converted into Euler angle notation, and vice versa,

$$\begin{aligned} q_0 &= \cos \frac{1}{2}\theta \cos \frac{1}{2}(\phi + \psi) , \\ q_1 &= \sin \frac{1}{2}\theta \cos \frac{1}{2}(\phi - \psi) , \\ q_2 &= \sin \frac{1}{2}\theta \sin \frac{1}{2}(\phi - \psi) , \\ q_3 &= \cos \frac{1}{2}\theta \sin \frac{1}{2}(\phi + \psi) . \end{aligned} \tag{A.11}$$

The treatment of the equations of rotational motion through quaternions avoids singularities occurring in the treatment with Euler angles [7, 8], and is therefore applied in this work.

The rotational matrix A ,

$$A = \begin{bmatrix} q_0^2 + q_1^2 - q_2^2 - q_3^2 & 2(q_1q_2 + q_0q_3) & 2(q_1q_3 - q_0q_2) \\ 2(q_1q_2 - q_0q_3) & q_0^2 - q_1^2 + q_2^2 - q_3^2 & 2(q_2q_3 + q_0q_1) \\ 2(q_1q_3 + q_0q_2) & 2(q_2q_3 - q_0q_1) & q_0^2 - q_1^2 - q_2^2 + q_3^2 \end{bmatrix}, \quad (\text{A.12})$$

which transforms coordinates from the global into the particle coordinate system, can be written in terms of the quaternions (or in terms of the Euler angles, by substituting Eqs. A.11 into Eq. A.12). The sites of a particle are located at fixed positions within the particle's coordinate system, and so can be retrieved from the information of the particle's center of mass coordinates and its rotational matrix (and vice versa),

$$\mathbf{r}_s = A^{-1} \mathbf{d}^{pc} + \mathbf{r}, \quad (\text{A.13})$$

where \mathbf{r}_s is the site vector and \mathbf{r} is the center of mass vector in the global coordinate system, and \mathbf{d}^{pc} is the vector from the center of mass to the site in the particle coordinate system.

A.2 Time Evolution of Model Systems

To calculate the time evolution of the model systems, we use molecular dynamics simulations. In molecular dynamics, the forces between a set of particles at time t are calculated. The projected particle positions at time $t + \delta t$ are calculated from the forces (and torques) through equations of motion (e.g. Newton's). These two steps are repeated to generate the time evolution of the system of particles.

A.2.1 The Gear Predictor-Corrector Algorithm

The Gear predictor-corrector algorithm is a numerical method to solve the equations of motion [1, 9]. The equations of motion are ordinary differential equations that describe the motion of particles under the influence of interaction forces. Their solution can be approximated by a finite difference method such as the Gear predictor-corrector algorithm.

The Gear predictor-corrector algorithm predicts the properties $\mathbf{x}^P(t)$ (which include the positions \mathbf{r}^P , the angular velocities $\boldsymbol{\omega}^P$, the quaternions \mathbf{Q}^P and their time-derivatives, with superscript P for predicted) at time t from their values \mathbf{x} at the previous time step $t - \delta t$ with the Taylor expansion

$$\begin{pmatrix} \mathbf{x}^P(t) \\ \mathbf{x}_1^P(t) \\ \mathbf{x}_2^P(t) \\ \mathbf{x}_3^P(t) \\ \mathbf{x}_4^P(t) \end{pmatrix} = \begin{pmatrix} 1 & 1 & 1 & 1 & 1 \\ 0 & 1 & 2 & 3 & 4 \\ 0 & 0 & 1 & 3 & 6 \\ 0 & 0 & 0 & 1 & 4 \\ 0 & 0 & 0 & 0 & 1 \end{pmatrix} \begin{pmatrix} \mathbf{x}(t - \delta t) \\ \mathbf{x}_1(t - \delta t) \\ \mathbf{x}_2(t - \delta t) \\ \mathbf{x}_3(t - \delta t) \\ \mathbf{x}_4(t - \delta t) \end{pmatrix}, \quad (\text{A.14})$$

where the scaled time derivatives of \mathbf{x}^P are $\mathbf{x}_1^P = \delta t \frac{d}{dt} \mathbf{x}^P$, $\mathbf{x}_2^P = \frac{1}{2} \delta t^2 \frac{d^2}{dt^2} \mathbf{x}^P$, $\mathbf{x}_3^P = \frac{1}{6} \delta t^3 \frac{d^3}{dt^3} \mathbf{x}^P$, and $\mathbf{x}_4^P = \frac{1}{24} \delta t^4 \frac{d^4}{dt^4} \mathbf{x}^P$. The matrix is the Pascal triangle matrix. For this prediction, only the particle properties \mathbf{x} and their time derivatives are used, no information about the intramolecular interactions (or the equations of motion) are considered explicitly. The predicted values are moderately accurate for a continuous interaction potential.

Next, the forces and torques are calculated for these predicted properties \mathbf{x}^P by explicitly evaluating the equations of motion and the interaction potentials.

The force \mathbf{F}_s between the site i of one particle and the site j of another particle is calculated from the interaction potential $u(r_{ij})$ described in Appendix A.1,

$$\mathbf{F}_s(r_{ij}) = - \left(\frac{\partial}{\partial x} \mathbf{u}_x + \frac{\partial}{\partial y} \mathbf{u}_y + \frac{\partial}{\partial z} \mathbf{u}_z \right) u(r_{ij}) , \quad (\text{A.15})$$

where \mathbf{u}_α is a unity vector in x , y or z . The total translational force \mathbf{F} on the particle's center of mass is the sum of all interactions of the particle's sites with all other particle sites.

The torque $\boldsymbol{\tau}^{pc}$ on the particle center of mass in the particle coordinate system is

$$\boldsymbol{\tau}^{pc} = A \sum_s \boldsymbol{\tau}_s = A \sum_s \mathbf{d} \times \mathbf{F}_s , \quad (\text{A.16})$$

where A is the rotational matrix expressed in terms of the quaternions (Eq. A.12), $\boldsymbol{\tau}_s$ is the torque, \mathbf{F}_s is the force on site s , and $\mathbf{d} = (\mathbf{r}_s - \mathbf{r})$ is the vector from the center of mass to the site, all in the global coordinate system. (The torque is described in the particle coordinate system because the equations of motion for the rotational acceleration (Eq. A.18) and the quaternion (Eq. A.19) are expressed in the particle coordinate system.)

The forces and torques are used to correct the particle properties \mathbf{x} at time t with the help of the equations of motion. The corrected translational acceleration and the corrected rotational acceleration are

$$\frac{d^2}{dt^2} \mathbf{r}^C = \mathbf{F}/m , \quad (\text{A.17})$$

$$\frac{d}{dt} \boldsymbol{\omega}_\chi^{pcC} = (\boldsymbol{\tau}_\chi^{pc} + \boldsymbol{\omega}_\psi^{pcP} \boldsymbol{\omega}_\varphi^{pcP} (I_{\psi\psi} - I_{\varphi\varphi})) / I_{\chi\chi} , \quad (\text{A.18})$$

where m is the mass, $\boldsymbol{\omega}$ is the angular velocity and \mathbf{I} is the principal moment of inertia, χ , ψ and φ can be the Cartesian coordinates x , y or z (superscript P stands for predicted properties and superscript C for corrected properties). In Eq. A.18 all properties are defined in the particle coordinate system.

The quaternion is treated in a similar manner, its equations of motion are

$$\begin{pmatrix} \frac{d}{dt} q_0^C \\ \frac{d}{dt} q_1^C \\ \frac{d}{dt} q_2^C \\ \frac{d}{dt} q_3^C \end{pmatrix} = \frac{1}{2} \begin{pmatrix} q_0 & -q_1 & -q_2 & -q_3 \\ q_1 & q_0 & -q_3 & q_2 \\ q_2 & q_3 & q_0 & -q_1 \\ q_3 & -q_2 & q_1 & q_0 \end{pmatrix} \begin{pmatrix} 0 \\ \omega_x^{pc} \\ \omega_y^{pc} \\ \omega_z^{pc} \end{pmatrix}. \quad (\text{A.19})$$

Note that Eq. A.17 is a second order equation, whereas Eqs. A.18 and A.19 are first order equations.

The following correction factors $\Delta \mathbf{x}_{corr}$,

$$\Delta \mathbf{r}_{corr} = \frac{d^2}{dt^2} \mathbf{r}^C - \frac{d^2}{dt^2} \mathbf{r}^P, \quad (\text{A.20})$$

$$\Delta \boldsymbol{\omega}_{corr} = \frac{d}{dt} \boldsymbol{\omega}^C - \frac{d}{dt} \boldsymbol{\omega}^P, \quad (\text{A.21})$$

$$\Delta \mathbf{q}_{corr} = \frac{d}{dt} \mathbf{q}^C - \frac{d}{dt} \mathbf{q}^P, \quad (\text{A.22})$$

are used to correct the properties $\mathbf{x}^C(t)$,

$$\begin{pmatrix} \mathbf{x}^C(t) \\ \mathbf{x}_1^C(t) \\ \mathbf{x}_2^C(t) \\ \mathbf{x}_3^C(t) \\ \mathbf{x}_4^C(t) \end{pmatrix} = \begin{pmatrix} \mathbf{x}^P(t) \\ \mathbf{x}_1^P(t) \\ \mathbf{x}_2^P(t) \\ \mathbf{x}_3^P(t) \\ \mathbf{x}_4^P(t) \end{pmatrix} + \begin{pmatrix} c_0 \\ c_1 \\ c_2 \\ c_3 \\ c_4 \end{pmatrix} \Delta \mathbf{x}_{corr}, \quad (\text{A.23})$$

where c_α are the Gear corrector coefficients. These coefficients depend on the order of the differential equation solved, and are $c_0 = \frac{19}{120} \frac{\delta t^2}{2}$, $c_1 = \frac{3}{4} \frac{\delta t}{2}$, $c_2 = 1$, $c_3 = \frac{1}{2} \frac{6}{2\delta t}$, $c_4 = \frac{1}{12} \frac{24}{2\delta t^2}$ for the positions \mathbf{r} and their derivatives, and $c_0 = \frac{251}{720} \delta t$, $c_1 = 1$, $c_2 = \frac{11}{12} \frac{2}{\delta t}$, $c_3 = \frac{1}{3} \frac{6}{\delta t^2}$, $c_4 = \frac{1}{24} \frac{24}{\delta t^3}$ for the angular velocities $\boldsymbol{\omega}$ and quaternions \mathbf{Q} and their derivatives.

The prediction-correction sequence should be iterated until convergence. Due to repeated calculation of the forces, this is costly in computer time. So generally only one prediction-correction sequence is applied per time step.

The Gear predictor-corrector algorithm is fast and allows the use of sufficiently large timesteps, making the calculation of long time trajectories feasible. At the same time, the algorithm is time reversible and conserves momentum and energy well. In this work the energy drift of NVE calculations was $< 1 \times 10^{-3}$ % for 40000 steps with a timestep length of 1×10^{-15} seconds. The Gear predictor-corrector algorithm is also convenient for implementing the equations of motion for asymmetric particles or temperature constrained systems (NVT).

A.2.2 Simulation Constraints

The simulations in this work were carried out under NVT conditions, with a constant number of particles N , constant volume V and a constant temperature T . The temperature is constrained with a Gaussian isokinetic thermostat, that constrains the kinetic temperature by setting its time derivative to zero [1, 10]. It has been shown that the equilibrium time correlation functions (Appendix A.3.2) are independent of the thermostating in the large system limit [10, 11].

The Gaussian isokinetic thermostat is implemented by separately adding an additional constraint term to the correction of the particle accelerations (Eq. A.17) and to the correction of the particle angular accelerations (Eq. A.18). This leads to a new set of equations of motion that are implemented in the corrector part of the Gear predictor-corrector algorithm,

$$\frac{d^2}{dt^2} \mathbf{r}^C = \mathbf{F}/m - \xi \mathbf{p}/m, \quad (\text{A.24})$$

$$\frac{d}{dt} \omega_X^{pcC} = (\tau_X^{pc} + \omega_\psi^{pcP} \omega_\varphi^{pcP} (I_{\psi\psi} - I_{\varphi\varphi})) / I_{\chi\chi} - \zeta \omega_X^{pcP}, \quad (\text{A.25})$$

where ξ and ζ are the correction factors, $\mathbf{p} = m\mathbf{v}$ is the momentum of a particle, and \mathbf{v} the velocity. The equations of motion and the trajectory of the molecular dynamics simulation are perturbed as little as possible from the Newtonian trajectory (in a least squares sense), the magnitude of the overall constraint force is minimal [10]. The correction factor ξ is determined from a sum over all particle momenta and forces of all particles (i),

and correction factor ζ from the angular momenta and torques,

$$\xi = \frac{\sum_i \mathbf{p} \cdot \mathbf{F}}{\sum_i |\mathbf{p}|^2}, \quad (\text{A.26})$$

$$\zeta = \frac{\sum_i \mathbf{L} \cdot \boldsymbol{\tau}}{\sum_i |\mathbf{L}|^2}, \quad (\text{A.27})$$

where $\mathbf{L} = \mathbf{I} \cdot \boldsymbol{\omega}$ is the angular momentum.

For the initialization of a simulation, where a constant temperature is desired to be reached as quickly as possible (and we are not concerned about producing a Newtonian trajectory), we scale the velocities \mathbf{v} and the angular velocities $\boldsymbol{\omega}$ with a simpler method [1],

$$\mathbf{v} = \vartheta \mathbf{v}, \quad \vartheta = \sqrt{\frac{T_{\text{wanted}}}{T_{\text{sys,transl.}}}} = \sqrt{\frac{T_{\text{wanted}} 3Nk_B}{2 \sum_i |\mathbf{v}|^2 m}}, \quad (\text{A.28})$$

$$\boldsymbol{\omega} = \varrho \boldsymbol{\omega}, \quad \varrho = \sqrt{\frac{T_{\text{wanted}}}{T_{\text{sys,rot.}}}} = \sqrt{\frac{T_{\text{wanted}} 3Nk_B}{2 \sum_i \sum_{\chi} I_{\chi\chi} \omega_{\chi}^2}}, \quad (\text{A.29})$$

where T_{wanted} and T_{sys} are the desired and the actual system temperatures (for translational or rotational motion), N is the number of particles, k_B is the Boltzmann constant and the sum over χ is over the x , y , and z coordinates. The system is then equilibrated before the production run is started.

A.3 Statistical Analysis of Model Systems

During the production runs of the simulation, the positions, velocities, angular velocities and the orientations (quaternions) of all particles are collected every 1×10^{-14} s (10 - 20 timesteps). This data for individual particles is accumulated and, through statistical mechanical equations, information can be obtained about experimentally measured many-particle, and single-particle properties.

A.3.1 Structural Properties

Radial distribution functions (rdfs) help us to resolve the average structure of our model systems. The rdf gives the probability of finding a particle at distance r from a selected particle, relative to the probability of randomly distributed particles (it shows the relative particle density). rdfs can be calculated from particle positions as [1]

$$g_{\alpha\beta}(r) = \frac{V}{N_{\alpha}N_{\beta}} \left\langle \sum_i^{N_{\alpha}} \sum_j^{N_{\beta}} \delta(\mathbf{r} - \mathbf{r}_{ij}) \right\rangle , \quad (\text{A.30})$$

where N_{α} is the number of particles of species α , V the simulation box volume, δ the delta-function, and \mathbf{r} the distance of interest. In practice, the rdf is calculated as a histogram, with a grid width of ~ 0.05 Å in this work.

Through integration of a rdf we can obtain a running coordination number $CN_{\alpha}(R)$, that gives the average number of particles at a distance R from particle α ,

$$CN_{\alpha}(R) = 4\pi \int_0^R [\rho_{\alpha}g_{\alpha\alpha}(r) + \rho_{\beta}g_{\alpha\beta}(r) + \rho_{\gamma}g_{\alpha\gamma}(r)] r^2 dr , \quad (\text{A.31})$$

where α , β and γ are the particle species (our models include up to three species) and $\rho_{\alpha} = N_{\alpha}/V$ is the number density of species α .

It can be useful to analyse the occupied volume at a distance R from a particle, for the consideration of the transport properties in mixtures of particles of different sizes. We

define the normalized occupied volume $V_\alpha(R)$ as

$$V_\alpha(R) = \frac{V_{occ,\alpha}(R)}{4\pi\sigma_{+-}^3/3} = 4\pi \int_0^R \left[\rho_\alpha \frac{\sigma_\alpha^3}{\sigma_{+-}^3} g_{\alpha\alpha}(r) + \rho_\beta \frac{\sigma_\beta^3}{\sigma_{+-}^3} g_{\alpha\beta}(r) + \rho_\gamma \frac{\sigma_\gamma^3}{\sigma_{+-}^3} g_{\alpha\gamma}(r) \right] r^2 dr , \quad (\text{A.32})$$

where σ_α is the diameter of particle α , and $\sigma_{+-} = (\sigma_+ + \sigma_-)/2$ the distance between cation and anion.

We also examine the charge ordering and Coulombic screening within a system through the radial charge distribution function [12, 13],

$$Q_\alpha(r) = \rho_\alpha [g_{\alpha\alpha}(r) - g_{\alpha\beta}(r)] . \quad (\text{A.33})$$

A.3.2 Dynamical Properties

The time evolution of the molecular dynamic simulation is used to calculate dynamical properties. We calculate time autocorrelation functions, that evaluate the change of a particle or system property with time. The integrals of certain time autocorrelation functions are directly related to macroscopic transport coefficients.

The diffusion of particles can be investigated through different methods. The Einstein diffusion coefficient $D_{E,\alpha}$ is calculated from the mean square displacement $\langle |\mathbf{r}_\alpha(0) \cdot \mathbf{r}_\alpha(t)|^2 \rangle$ through the Einstein relation [1],

$$D_{E,\alpha} = \frac{1}{6} \lim_{t \rightarrow \infty} \frac{d}{dt} \langle |\mathbf{r}_\alpha(0) - \mathbf{r}_\alpha(t)|^2 \rangle , \quad (\text{A.34})$$

where $\mathbf{r}_\alpha(t)$ is the position vector of a particle of species α at time t . The Green-Kubo diffusion coefficient $D_{GK,\alpha}$ is calculated from the velocity autocorrelation function $\langle \mathbf{v}_\alpha(0) \cdot \mathbf{v}_\alpha(t) \rangle$ through a Green-Kubo relation [1],

$$D_{GK,\alpha} = \frac{1}{3} \int_0^\infty \langle \mathbf{v}_\alpha(0) \cdot \mathbf{v}_\alpha(t) \rangle dt , \quad (\text{A.35})$$

where $\mathbf{v}_\alpha(t)$ is the velocity of a particle of species α at time t . $D_{E,\alpha}$ and $D_{GK,\alpha}$ are formally equivalent [14]. However, in our work we mainly report diffusion coefficients estimated

from the mean square displacement. The velocity autocorrelation functions have long-time asymptotic tails (decaying as $t^{-3/2}$), that would have to be included in the integration to achieve accurate values of $D_{GK,\alpha}$ [14]. Without a correction for long-time tails, the Green-Kubo diffusion coefficients in our work are about 3% smaller than the Einstein diffusion coefficients, which we consider as reasonable agreement between the methods.

Diffusion coefficients can also be estimated from the Stokes-Einstein equation in the hydrodynamic limit (stick boundary conditions) [1],

$$D_{ST,\alpha} = \frac{k_B T}{3\pi\eta d_{ST,\alpha}}, \quad (\text{A.36})$$

where $d_{ST,\alpha}$ is the Stokes diameter of a particle, which is taken to be the LJ parameter σ_α for an ion of species α in this work. For some systems, the fractional Stokes-Einstein equation holds, where

$$D \propto \left(\frac{T}{\eta}\right)^\beta, \quad (\text{A.37})$$

and β is a system dependent exponent [15]. Both diffusion coefficient and viscosity can be expressed as Arrhenius equations [15]

$$D \propto \exp\left(\frac{-E_D}{k_B T}\right), \quad (\text{A.38})$$

$$\frac{T}{\eta} \propto \exp\left(\frac{-E_\eta}{k_B T}\right), \quad (\text{A.39})$$

and the fractional Stokes-Einstein equation can be derived from their division, such that

$$\beta = \frac{E_D}{E_\eta}. \quad (\text{A.40})$$

The coefficient β accordingly is the ratio between the activation energies of the two transport processes, diffusion and viscosity.

The rotational diffusion coefficient D_R for the cation can be calculated from the angular velocity autocorrelation function $\langle \boldsymbol{\omega}(0) \cdot \boldsymbol{\omega}(t) \rangle$,

$$D_R = \frac{1}{2} \int_0^\infty \langle \boldsymbol{\omega}(0) \cdot \boldsymbol{\omega}(t) \rangle dt , \quad (\text{A.41})$$

where $\boldsymbol{\omega}$ is the angular velocity. Only the ω_x and ω_y components are relevant to rotational diffusion, because the cation is cylindrically symmetric around the z-axis, and so there is no torque about this axis.

The reorientational autocorrelation function,

$$O(t) = \langle \boldsymbol{\mu}(0) \cdot \boldsymbol{\mu}(t) \rangle \propto \exp\left(-\frac{t}{\tau_\mu}\right) , \quad (\text{A.42})$$

describes the orientational decay of a charge-off-center ion, where the vector $\boldsymbol{\mu}$ joins the center of mass and the center of charge. τ_μ is the orientational relaxation time.

The shear viscosity η can be calculated from [1, 14],

$$\eta = \frac{V}{k_B T} \int_0^\infty \langle P_{\chi\psi}(0) \cdot P_{\chi\psi}(t) \rangle dt , \quad (\text{A.43})$$

where $P_{\chi\psi}$ represents an off-diagonal element of the pressure tensor. $P_{\chi\psi}$ ($\chi \neq \psi$) is

$$P_{\chi\psi} = \frac{1}{V} \left(\sum_i^N v_{i\chi} v_{i\psi} m_i + \sum_i^N r_{i\chi} F_{i\psi} \right) , \quad (\text{A.44})$$

where the summation on i is over all particles in the simulation system, and $v_{i\chi}$, $F_{i\chi}$, and $r_{i\chi}$ denote the x , y or z components of the velocity, force, and position vectors of particle i . The usual bulk pressure P is obtained from the diagonal elements of the pressure tensor,

$$P = \frac{1}{3} \sum_{\chi=x,y,z} P_{\chi\chi} . \quad (\text{A.45})$$

In periodic boundary conditions particular care must be taken in calculating the pressure tensor of an ionic system [16, 17]. The Ewald method must be applied to the product of $r_{i\chi} F_{i\psi}$, not to $F_{i\psi}$ alone, because the total k-space force on particle i depends not only on

the distance to particle j in the original simulation box, but on various distances to particle j and its images. In periodic boundary conditions, the second term of Eq. A.44 must be calculated as [16, 17]

$$\begin{aligned}
 \sum_i^N r_{i\chi} F_{i\psi} &= \sum_i^{N-1} \sum_{j>i}^N 24\epsilon \left[2 \left(\frac{\sigma}{r_{ij}} \right)^{12} - \left(\frac{\sigma}{r_{ij}} \right)^6 \right] \frac{r_{ij\chi} r_{ij\psi}}{|r_{ij}|^2} \\
 &+ \frac{1}{4\pi\epsilon_0} \sum_i^{N-1} q_i \sum_{j>i}^N q_j \left[\operatorname{erfc}(\kappa |r_{ij}|) + \frac{2\kappa}{\sqrt{\pi}} |r_{ij}| \exp(-\kappa^2 |r_{ij}|^2) \right] \frac{r_{ij\chi} r_{ij\psi}}{|r_{ij}|^3} \\
 &+ \frac{1}{2\epsilon_0 V} \sum_{\mathbf{k} \neq 0} \left[\delta_{\chi\psi} - \frac{2k_\chi k_\psi}{k^2} - \frac{k_\chi k_\psi}{2\kappa^2} \right] \frac{1}{k^2} \exp\left(-\frac{k^2}{4\kappa^2}\right) \\
 &\quad \left[\left(\sum_i^N q_i \cos(\mathbf{k} \cdot \mathbf{r}_i) \right)^2 + \left(\sum_i^N q_i \sin(\mathbf{k} \cdot \mathbf{r}_i) \right)^2 \right].
 \end{aligned} \tag{A.46}$$

The static electrical conductivity is obtained from the current-current correlation function [14],

$$\sigma_{el} = \frac{1}{3k_B T V} \int_0^\infty \langle \mathbf{J}(0) \cdot \mathbf{J}(t) \rangle dt, \tag{A.47}$$

where the current is

$$\mathbf{J}(t) = \sum_{i=1}^N q_i \mathbf{v}_i, \tag{A.48}$$

with q_i being the charge of particle i , and \mathbf{v}_i its velocity. When the cross terms of the current correlation function $\langle \mathbf{J}_i(0) \cdot \mathbf{J}_j(t) \rangle$ are neglected, and only the self-correlation terms $\langle \mathbf{J}_i(0) \cdot \mathbf{J}_i(t) \rangle = \sum_i q_i^2 \langle \mathbf{v}_i(0) \cdot \mathbf{v}_i(t) \rangle$ are integrated in Eq. A.47, the Nernst-Einstein electrical conductivity σ_{NE} [14] is derived,

$$\sigma_{NE} = \sum_\alpha \frac{\rho_\alpha D_\alpha q_\alpha^2}{k_B T}. \tag{A.49}$$

A comparison of σ_{NE} to σ_{el} shows the importance of the current cross correlations to σ_{el} . The current cross correlations generally make a significant (negative) contribution to the electrical conductivity of molten salts. Equations A.47 and A.49 illustrate that the electrical conductivity basically depends on the number of charge carriers and their motion (diffusion

coefficient) at constant volume and temperature.

The directional bonding of one charge-off-center cation to an anion is investigated with a specifically constructed time correlation function, that is similar to one sometimes used to investigate hydrogen-bond dynamics [18, 19]. We construct $S_{ip}(t)$ so that it describes the probability that an ion pair, which is bonded at $t = 0$, remains continuously bonded up to time t ,

$$S_{ip}(t) = \frac{\langle h(0)H(t) \rangle}{\langle h \rangle} . \quad (\text{A.50})$$

$h(t)$ is one if a “tagged” pair of ions are “bonded” at time t and is zero otherwise. $H(t)$ is one if the tagged pair remains continuously bonded from time 0 to time t , and otherwise zero. The average is taken over all ion pairs that are bonded at time $t = 0$. “Bonding” of a pair is defined geometrically, the ions are bonded if they are within a certain distance and angle of each other. For bonding, the ions must have a shorter separation than the first minimum of the center of charge cation-anion radial distribution function. For bonding, the angle between the vector connecting the cation center of mass to center of charge and the vector of the cation center of mass to anion center of mass/charge must be smaller than 15 degrees. Slight variations of distance and angle were shown to not have a significant influence on $S_{ip}(t)$, and other quantities derived from it, see Chapter 3. $S_{ip}(t)$ exhibits an exponential decay at long times, so ion-pair lifetimes τ_{ip} can be estimated from it. We also calculate the average percentage of bonded ion pairs from $h(0)$, averaged over all timesteps.

A.4 Nomenclature Variations in Different Chapters

<i>Chapter 2</i>	<i>Chapter 4/5</i>
<i>system</i>	<i>model – XC5</i> <i>system</i>
1 : 1	1C5
2 : 1	2C5
3 : 1	3C5
4 : 1	4C5
5 : 1	5C5

Table A.1: Different Nomenclature used for the charge-centered size disparate ionic liquid model, with constant σ_{+-} , in Chapters 2, 4, and 5.

<i>Chapter 3</i>	<i>Chapter 4</i>
<i>system</i>	<i>model – 1CY</i> <i>system</i>
C0	1C5
C0.5	1C3.8
C0.625	1C3.4
C0.75	1C3.1
C0.875	1C2.8

Table A.2: Different Nomenclature used for the charge-centered same size ion model, where σ_{+-} decreases, in Chapters 3 and 4.

<i>Chapter 3</i>	<i>Chapter 4/5</i>
<i>system</i>	<i>model – 1OCY</i> <i>system</i>
OC0	1OC5
OC0.25	1OC4.4
OC0.5	1OC3.8
OC0.625	1OC3.4
OC0.688	1OC3.3
OC0.75	1OC3.1
OC0.875	1OC2.8

Table A.3: Different Nomenclature used for the charge-off-center model, with same size anions and cations, in Chapters 3, 4, and 5.

Bibliography

- [1] M. P. Allen and D. J. Tildesley, *Computer Simulations of Liquids* (Oxford, Clarendon, 1987).
- [2] R. A. Kuharski and P. J. Rossky, *J. Am. Chem. Soc.* **106**, 20, 5794 and 5786 (1984).
- [3] S. W. deLeeuw, J. W. Perram and E. R. Smith, *Proc. R. Soc. Lond. A* **373**, 27 (1980).
- [4] A. Y. Toukmaji and J. A. Board Jr., *Comp. Phys. Comm.* **95**, 73 (1996).
- [5] M. Deserno and C. Holm, *J. Chem. Phys.* **109**, 18, 7678 (1998).
- [6] K. Esselink, *Comp. Phys. Comm.* **87**, 375 (1995).
- [7] D. J. Evans, *Molec. Phys.* **34**, 317 (1977).
- [8] D. J. Evans and S. Murad, *Molec. Phys.* **34**, 327 (1977).
- [9] C. W. Gear, *Mathematics of Comp.* **21**, 98, 146 (1967).
- [10] G. P. Morriss and C. P. Dettmann, *Chaos* **8**, 2, 321 (1998).
- [11] D. J. Evans and G. P. Morriss, *Statistical Mechanics of Nonequilibrium Liquids* (London, Academic, 1990).
- [12] P. Koblinski, J. Eggebrecht, D. Wolf, and S.R. Phillpot, *J. Chem. Phys.* **113**, 282 (2000).
- [13] Y. Shim, M. Y. Choi, and H. J. Kim, *J. Chem. Phys.* **122**, 044510 (2005)
- [14] J. P. Hansen and I. R. McDonald, *Theory of Simple Liquids*, 2nd ed. (Academic, London, 1986).
- [15] A. Voronel, E. Veliyulin, and V. Sh. Machavariani, *Phys. Rev. Lett.* **80**, 2630 (1998).
- [16] D. M. Heyes, *Phys. Rev. B* **49**, 755 (1994).
- [17] N. Galamba, C. A. Nieto de Castro, J. F. Ely, *J. Phys. Chem. B* **108**, 3658 (2004).
- [18] A. Chandra, *J. Phys. Chem. B* **107**, 3899 (2008), and references therein.
- [19] A. Luzar, *J. Chem. Phys.* **113**, 10663 (2000), and references therein.
- [20] D. Frenkel and B. Smit, *Understanding Molecular Simulation: From Algorithms to Applications* (Academic Press, 1996).